UNIVERSITY OF LIVERPOOL

Near Real Time Automatic Interpretation of Ground Penetrating Radar Data for Utility Detection

Thesis submitted in accordance with the requirements of
the University of Liverpool for the degree of Doctor in Philosophy

by

Umar Shahbaz Khan

December 2010

Abstract

Ground Penetrating Radar (GPR) is an electromagnetic technique for non-invasive imaging of opaque media, and is commonly used for subterranean surveys for such applications as utility mapping, land mine detection, archeological and geophysical surveys. A typical survey will generate large amount of data, within which only a small percentage represent the actual targets of interest. In this study, these targets are underground utilities such as pipes and cables. GPR data processing relies on skilled operators and involves many computationally expensive and time consuming stages before any information about the subsurface and target can be concluded. The results are often based on broad assumptions and involve human intervention which is a source of inconsistency and error hence rendering the results to be unreliable.

The data processing stage involve pre-processing of data, followed by detecting the areas that contain targets, then extracting the target signature which is interpreted into real world parameters such as depth, dimensions, orientation, dielectric constant of the medium and propagation velocity through the medium. This study automates the data processing stage, suggests improvements in the existing tools and some new data processing tools have been developed which are superior in terms of accuracy and time cost.

A GPR radargram has many unwanted reflections called clutter. In order to successfully extract the target signature, the effect of noise need to be eliminated. Though clutter cannot be completely removed, background removal techniques suppress their effect to quite an extent. Usually, mean subtraction is used as a background removal technique but in this study a newly developed Eigenvalue based background removal technique is presented. This method decreases the effect of clutter and the output is relatively more refined and clear.

The target signature needs to be extracted from the data for correct estimation of parameters. Usually, multi-stage neural classifiers in conjunction with different statistical and regional features are used to distinguish between desired targets and redundant data. In this study, a novel neural network based classifier has been developed that classifies targets on the basis of polynomial shaping coefficients and Mel Frequency Cepstral Coefficients (MFCC). This classifier performs well in

data with low or high signal to noise ratio and is able to successfully classify weak reflections.

Signature from cylindrical targets are in the form of a hyperbola. A fitting algorithm is used to extract the hyperbolic parameters. This study has combined two different fitters that give good performance over a wide range of hyperbolas hence resulting in correct estimation of the hyperbolic parameters. The results from both the fitters are compared to the target hyperbola and the one closest to the signature is selected.

The study makes use of an existing general equation that models GPR hyperbolic reflections from buried cylinders. The information extracted from the model has slight error due to some initial assumption and this error can be reduced by using a 3D iterative cycle. The information from the GPR model of consecutive scans are plotted in a 3D space and aligned points are extracted using 3D line detection techniques. Changes have been made in order to automate and reduce the processing time of an existing 3D line detection technique known as the Adaptive Non-Accumulative Hough Transform (ANHT). But the amount of time needs to be reduced further for a near real time application, hence another novel 3D line detection technique is developed which is known as the Angle-Based 3D line detection. This approach reduces the computation time significantly to just a few seconds and is robust as well as accurate.

All the stages presented can be combined in order to produce a near real time automated procedure for correct target parameter estimation. The data had been collected at the University of Liverpool campus and the suggested techniques have been applied to this data. The newly developed tools have been used in underground utility investigations, however their use can also be extended to other GPR applications such as land mine detection and archaeological surveys.

To my father Col(R) Khaista Gul, mother, brothers, sisters, wife Sadaf and son Aadil.

Acknowledgements

I am grateful to Allah All Mighty for giving me an opportunity to do this degree. I want to express my deep gratitude to my supervisor Dr. Waleed Al-Nuaimy for his continuous guidance and encouragement. I am also grateful to Dr. Yi Huang for his support and Dr. Fathi E. Abd El-Samie for his help in my research. I am especially grateful to National University of Science and Technology (NUST) and Higher Education Commission (HEC) Pakistan for sponsoring me for this study.

I am thankful to Zetica for providing me with the radar for data collection. Thanks are also due to all the staff at the Department of Electrical Engineering and Electronics and University of Liverpool administration especially Miss Rebecca Morton for their support and assistance.

Special thanks are to my father Col (R) Khaista Gul, mother Irshad Bibi, grandma Makhmaru jaan, brothers Sajjad and Junaid, sisters Assia, Aisha and Lubna, Bhabi Fatima, brother in law's Aarif, Ilyas, Zeeshan, Adnan, Sharukh, uncle Zulfiqar and his family, uncle Khalid and his family, wife Sadaf, father and mother in law Ashraf khan and Bachazameen, sister in law's Sadia, Sania, Shahtaaj, colleagues Nayel, Abdur Rahman, Lina, Ali, Bala, Shekhar, Muhammad and friends Jalal, Clement, Nesan, Dayani, Kristel, Madiha, Carlos, Raajini, Shafiq-ur-Rahman, Aijaz, Moin, Sidra, Hassan, Deen, Zubair, Tariq, Umair, Aftab, Zubair, Kalim and Shafique and others whom names I might have missed out for their patience, encouragement, support and prayers.

At the end I would like to thank Ali Al-Ataby for proof reading my thesis and giving his valuable comments and suggestions.

Contents

List of Figures

List of Tables

Acronyms

GPR	Ground penetrating radar
MAD	Mean absolute deviation
$STFT$	Short-time Fourier Transform
ED	Equivalent diameter
CPU	Central processing unit
SIR	Surface impulse radar
$GSSI$	Geophysical survey systems Inc
RBF	Radial basis function
HT	Hough transform
$ANHT$	Applied non-accumulative Hough transform
EMI	Electromagnetic Induction
SAR	Synthetic aperture radar
$FMCW$	Frequency modulated continuous wave
$CW-SF$	Continuous wave-stepped frequency
$MFCCs$	Mel frequency cepstral coefficients
$ORFEUS$	Optimised radar to find every utility in the street
IIR	Infinite impulse response
UWB	Ultra wide wand
WVD	Wigner-ville distribution
NN	Neural network
SVD	Singular value decomposition
SNR	Signal to noise ratio
DCT	Discrete cosine transfrom
DWT	Discrete wavelet transform

DST	Discrete sine transform
MLP	Multi-layer perceptrons
$AWGN$	Additive white Gaussian noise
PS	Parameter space
MH	Modified Hubert

Nomenclature

j_{bg}	Scan number corresponding to background clutter
$s(t)$	Analytic signal
$\sigma(s)$	Variance or the second moment of a signal $s(t)$
s_i	The i^{th} element in a vector s
$\bar{s}$	The mean value of a vector s
MAD	Mean absolute deviation of a signal $s(t)$
m_4	Fourth moment of a signal $s(t)$
$R^2(p_1, p_2)$	Euclidean distances between the two points $p_1 = (x_1, y_1)$ and $p_2 = (x_2, y_2)$in a plane
$\text{STFT}_s^w(i,p)$	Short-time Fourier Transform of time series s using window w
$\text{SPEC}_s^w(i,p)$	Spectrogram of time series s using window w
$P(c)$	Periodogram power spectral density estimate
$S(c)$	Discrete Fourier Transform of time series
B	Number of Discrete Fourier Transform bins
b	Length of time series scan in samples
$W_s(t,f)$	Wigner-Ville distribution of time-series s
$R_s(\tau,t)$	Instantaneous autocorrelation function
$D_s(f,t)$	Instantaneous spectral density
N_h	The number of horizontal windows of size $x \times y$ across the image
N_v	The number of vertical windows of size $x \times y$ down the image
p	Fractional degree of overlap between windows
A_R	Area of a region
ED_r	Equivalent diameter
R_k	The k^{th} region in an image that contain N regions

net	Neuron activation signal
w_i	Neuron input weight values
in_i	Neuron input values
out	Output value of neuron
f_{sig}	Logistic neuron transfer function
$f_{\tan}$	Hyperbolic tangent sigmoidal transfer function
$\hat{t}$	The two-way travel time
$\hat{v}_s$	Velocity of propagation of GPR electromagnetic waves
z_0	Depth to the top of a buried cylinder
z	Apparent depth of the reflection from a buried cylinder at a position x displaced from the position of the cylinder x_0
R	Radius of a buried cylinder
d	Depth of target
α	Azimuthal orientation of a buried cylinder with respect to the direction of scanning
β	Vertical inclination of a buried cylinder with respect to the plane that contains the ground surface
γ	The angle that combines both α and β via the relation $\cos\gamma = \cos\alpha \cdot \cos\beta$
θ	Azimuth orientation angle in spherical coordinates and is related to α via: $\alpha = \theta - 90°$
ϕ	Vertical orientation angle in spherical coordinates and is related to β via: $\beta = 90° - \phi$
ϵ_r	Relative permittivity of the medium
ϵ_s	Relative permittivity of the soil or transmission medium
$F(\mathbf{m};\mathbf{x})$	An implicit second order polynomial representing a general conic

$\mathbf{D}$	The design matrix for the least-square hyperbola fitter
$\mathbf{S}$	The scatter matrix for the least-square hyperbola fitter
$\mathbf{C}$	The constraint matrix for the least-square hyperbola fitter
D_i	Maximum depth of interest
$S_{m)}$	Two way slowness of subsurface material
μ_i	ith Eigenvector of $X^T X$
υ_i	ith Eigenvector of XX^T
C	Positive symmetric covariance of matrix X
$P_x[n]$	Power cepstrum of a signal
$C_x[n]$	Complex cepstrum of a signal
m	Unit Mel on the Mel scale
C_j	Mel frequency cepstral coefficient MFCC
$a_j(t)$	Slope of C_j in the t^{th} frame
$b_j(t)$	Curvature of C_j in the t^{th} frame
λ	Lagrange multiplier
c	Speed of electromagnetic propagation in free space
r	Position vector relative to the origin O
$\overrightarrow{l}$	Direction vector in spherical coordinates

Chapter 1

Introduction

Subsurface information is a crucial requirement in the modern day as there are many applications that rely on existing underground structures. Excavation for new utilities and building purposes require knowledge of existing pipes and cables as accidental damage could lead to disastrous consequences in terms of risk to life, property and could lead to heavy law suits. Many other applications also require subsurface knowledge such as land mine detection, archeological surveys and other geophysical investigations. Subsurface imaging is therefore a means of gaining this knowledge. Ground Penetrating Radar (GPR) is a non destructive tool used for subsurface imaging. There are many different types of radars commercially available. The difference in radars is based on the manner in which the data is collected as data is collected either in time domain or in frequency domain. There are two common categories of radar one is impulse radar that operates in time domain and the other is continuous wave and stepped frequency radar that operates in frequency domain [4].

GPR is a rapidly growing sector in the geophysics industry and there is an increasing demand of its use due to its ability to be used as a non-destructive tool [5], [1]. The post processing suffers from many problems which are due to many factors such as reliance on operator intervention, manual systems, scan-by-scan processing, assumptions made regarding the nature and geometry of targets and non real time scanning.

A GPR display is a two-dimensional image of the sub-surface. In order to get this image, the radar itself has to perform some pre-processing steps, but these steps are not sufficient to comprehend the data into layman terms. Therefore, a number of post processing operations need to be carried out. Often these processes are done off site in a laboratory environment by trained human operators, thus consuming inconsiderable amount of time and effort along with the human error intervention. It is thus necessary to devise a system that gives the output results with as less human involvement as possible.

The post processing steps involves background removal, detecting targets, characterising, mapping and interpreting GPR data. There exist techniques that perform these operations, but most of them require extensive time and efforts along with human intervention at every stage. Besides these, the results are not consistent as they may give acceptable results for some data sets but fail when applied to different data sets.

The proposed study has investigated many techniques that can be used as stages towards the final data interpretation. This research has not only chosen the best technique that would give better results but also suggested improvements along with development of new ideas and concepts that can replace some important existing methods. Each method has been tested on a variety of data set, thus

demonstrating its robustness and time efficiency. All these stages when combined together produce an automatic system with no human intervention.

GPR uses a range of radio frequencies from 20 MHz to 2 GHz. The frequency is chosen according to the required depth of penetration. The lower the frequency the higher will be the depth of penetration. GPR has a transmit and a receive antenna, a series of electromagnetic pulses typically of the amplitude 100 V to 1000 V and a duration between 1 ns and 10 ns is applied to the terminals of the antenna and launched into the transmission medium. In accordance with the laws of classical electromagnetism, as the pulses propagate downwards through the ground, they interact with subsurface materials in a variety of ways, including attenuation, reflection, refraction, diffraction and scattering. The reflections of these pulses from the subsurface anomalies are received by the receiving antenna. GPR has the ability to detect metallic as well as non metallic targets. Each received reflection is known as an A-scan. When the radar is progressed forward, the next A-scan is stacked side by side to the previous one, thus resulting in a two-dimensional image known as a B-scan having the vertical axis as the time in nano-seconds and the horizontal axis as the scan number.

The B-scans, also known as radargrams, are difficult to interpret and thus require a skillful operator for interpretation. Observations drawn from the radar are combined with knowledge of the transmission medium, nature of the targets, environmental conditions along with limited automated processes in order to get an idea of the subsurface.

The post processing involves clutter and background removal, target classification, segmentation, signature extraction, fitting and modeling into target parameters.

The processing tools for data interpretation involve either complex geophysical inversion tools, image processing, forward modeling or iterative migration which are computationally very expensive and thus are inadequate for on-site applications. In underground utilities identification, such as pipes and cables, the B-scan shows an inverted hyperbola for the target. The shape of the hyperbola is dependent on the target radius, depth, dielectric of the transmission medium and its orientation. Usually, some of these parameters are assumed which results in inaccurate values of the other parameters as the shape of the hyperbola is equally dependent on all the parameters combined.

1.1 Commercial Systems

All GPR systems work on the same principle of sending electromagnetic waves into the ground and recording the reflected traces side by side in a time-depth profile. The system hardware is composed of a main CPU powered by a 12 V battery and a transmit and receive antenna. The choice of antenna is important and is dependent on the required penetration depth. A low-frequency antenna is able to provide greater penetration depth, but lower resolution, on the other hand, a high frequency antenna is able to provide high resolution images but on the expense of less penetration depth. The antenna frequency choice not only determines the penetration depth but also the minimum size of the target that could be seen using that frequency. Table 1.1 shows a range of antenna frequencies along with their applications and the typical depth and range [6].

GPR has a wide range of applications ranging from planetary explorations to the detection of buried cylinders such as pipes and tanks. The selection of a

range of frequency operations, modulation scheme and type of antenna and its polarisation, depends on a number of factors, including the size and shape of the target, properties of the transmission medium and the characteristics of the surface [1]. For a GPR to operate successfully, the radar should achieve adequate signal-to-noise ratio, signal-to-clutter ratio, spatial resolution and depth resolution of the target.

Two radar systems have been used in this study; the Geophysical Survey Systems Inc Surface Impulse Radar System-2 (SIR-2) shown in Figure 1.1 (a) and the Geophysical Survey Systems Inc Surface Impulse Radar System-3000 (SIR-3000) shown in Figure 1.1 (b). Figure 1.2 is a site survey taken using the SIR-2 system. The system specifications of the SIR-2 and SIR-3000 are given in Appendix A. The SIR-2 system is the predecessor of SIR-3000. Both systems comprise of a digital control unit, the antennas mounted in a shielded casing, a portable battery and a co-axial cable connecting the control unit and antennae. The control unit is usually stationary and contains the transmitting and receiving circuitry and a computer that runs the data collection software, does the online processing, displays and stores the data. The SIR-3000 system can be either carried or mounted on a cart. This cart is specially designed to have the main unit placed on top, the antenna attached to the bottom and one of the wheel has a survey wheel attached to it that is calibrated before the survey. This wheel records the movement and sends it to the main control unit, hence the horizontal axis of the B-scan is calibrated in terms of distance as scans per meter.

The antennas used are typically twin dipole or bow-tie antenna with fractional bandwidth in the region of 100%, *i.e.*, possessing a centre frequency equal to the half-peak power bandwidth. The angular width of the main radiation lobe

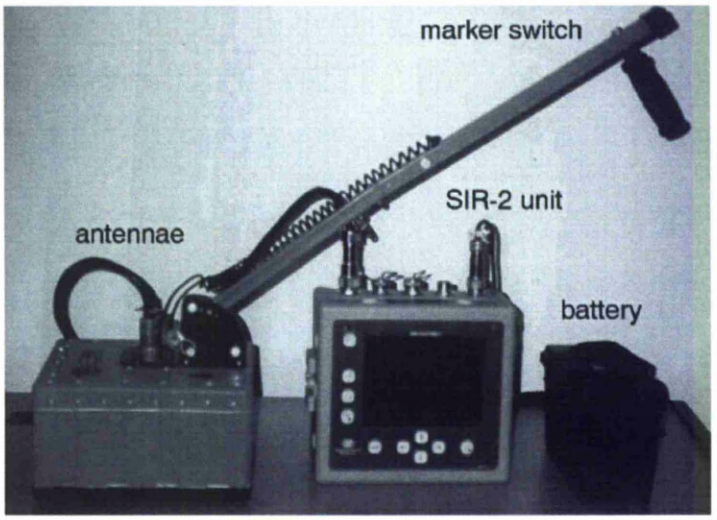

(a) The GSSI Surface Impulse Radar System-2 [1]

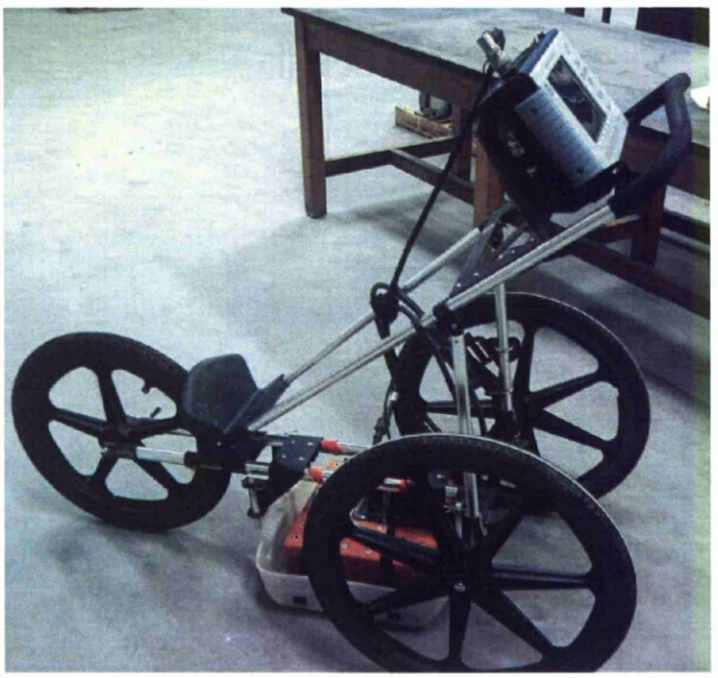

(b) The GSSI Surface Impulse Radar System-3000

FIGURE 1.1: SIR radar systems

TABLE 1.1: Antenna frequencies with application and penetration depth

Frequency	**Sample Application**	**Depth Ft (m)**	**Range(ns)**
1.5 GHz	Concrete, Roadways, Bridge Decks	1.5(0.5)	10-15
1000MHz	Concrete, Shallow Soils, Archaeology	3(1)	10-20
400MHZ	Geology, Utilitity, Archaeology	12(4)	20-100
200MHz	Geology, Environmental	25(8)	70-300
100MHz	Geology, Environmental	60(20)	300-500

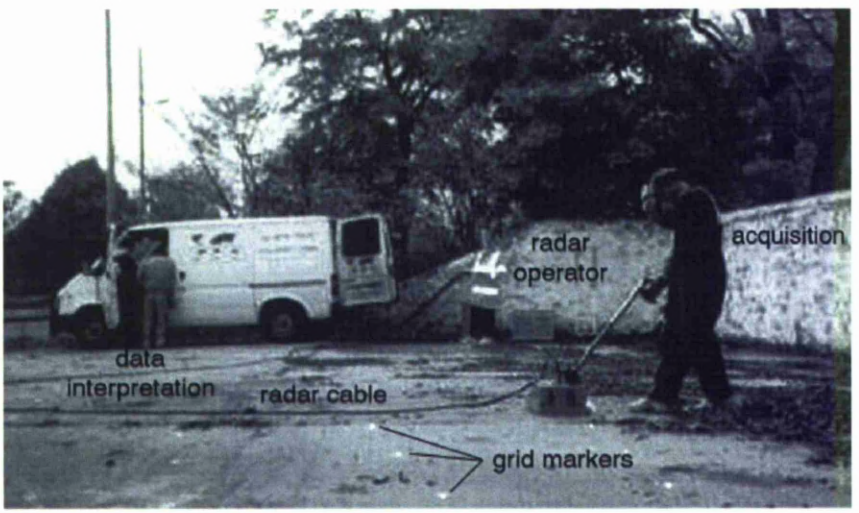

FIGURE 1.2: Data acquisition with the SIR-2 at a former service station [1]

beneath the surface is approximately 90^0 from back to front (along the direction of movement) and 60^0 from side to side. The physical dimensions of the antenna casing and shielding vary [1]. Antennas with larger centre frequency are smaller in size and as the frequency goes down the size of antennas gets bigger.

1.1.1 Propagation Velocity

The propagation velocity is a direct measure for the depth of an object and the relation is given by

$$d = \frac{\hat{v_s}\hat{t}}{2} \tag{1.1}$$

where d is the depth of the target, $\hat{v}$ is the velocity through the medium and $\hat{t}$ is the two way travel time. Unfortunately, in real world scenario, the velocity of the electromagnetic wave through the material medium is unknown. The propagation velocity through a medium is dependent on the relative permittivity of the medium and is given by

$$\hat{v_s} = \frac{c}{\sqrt{\epsilon_r}} \tag{1.2}$$

where c is the speed of electromagnetic propagation in free space[1] and ϵ_r is the relative permittivity of the medium.

In most practical cases, the relative permittivity of the medium is unknown as the subsurface could be composed of many layers or could have objects like rocks, bricks, buried rubbish etc. The normal procedures of estimating the velocity is done by direct measuring to a physical layer or estimating the value of the dielectric having knowledge of the medium type.

A method of estimating depth of a target is by using the common depth point technique, in which both the transmitter and the receiver antennas are moved at equal intervals from the top of the target which is the common centre point, and

[1]The speed of light is approximately 0.299792458 mns^{-1}.

the idea that the same apparent reflection position should be maintained is used to estimate the depth [7].

Another issue in determining the permittivity of a material is the environmental affects on a materials permittivity. Wet mediums have higher relative permittivity than dry materials, therefore the velocity of propagation through them changes. Materials exhibiting this characteristic are known as dispersive. Similarly, propagation characteristics also change through anisotropic mediums. Such material exhibit different propagation velocity depending on their directions such as coal. Prior to coal excavation, the propagation characteristics parallel to the bedding plan are different than that normal to the bedding plane.

The estimation of the propagation velocity is an important step towards GPR data interpretation as an error in the velocity would results in error in the depth and this could lead to disastrous consequences especially in applications such as mine or utility detection.

1.1.2 Clutter

An electromagnetic wave transmitted by a GPR undergoes reflection, diffraction, refraction and scattering. The reflected A-scans recorded by the receiving antenna are stacked side by side to give us a radargram. This radargram gives us information of the subsurface layers and anomalies. Unfortunately, these reflections are also caused by non-targets such as rocks, cavities, buried rubbish, local variations in the characteristic impedance of the ground, breakthrough between transmit and receive antennas and multiple reflection between antenna and ground as well as reflections from targets above the ground within the side lobe range of the radar

[7], [8]. These unwanted reflections are known as clutter. Clutter that affects GPR data can also be defined as the set of signals that are not related to the target but they have similar spectral characteristics as the target reflections. The effect of clutter is more near the surface of the ground and decreases at longer range in the ground, therefore clutter is a serious issue for near-range GPR applications such as mine and utility detections. The effect of clutter can be reduced by careful antenna design and proper shielding. Some post processing tools can also be used to reduce the effect of background and clutter, which will be discussed in detail in Chapter 3.

1.1.3 Data Representation

GPR data consists of reflected electromagnetic waves, these are one dimensional traces and are known as A-scans. The objective is to display this data in such a way that it could easily be interpreted as a subsurface image with the target objects and anomalies located in their proper spatial positions. For this purpose, the A-scans can be stacked side by side in order to produce a two-dimensional image of the underground. This representation is known as a B-scan or radargram. Multiple B-scans taken in an orthogonal grid can be placed in a 3D format to give a three-dimensional interpretation of the scanned area.

The raw data that is acquired from a GPR system is in the form of a B-scan. That is a lateral ensemble of sampled time series with horizontal axis as the number of scans referenced to time or distance and the vertical axis as the two way travel time for the electromagnetic wave. The basic two-dimensional display is colour coded which means that each waveform is represented as a vertical line with the

amplitude represented by a pixel intensity level or a colour within a colour-map. The number of colours and the colour table can be customised according to the user requirement to enhance the visibility. The two-dimensional display can be displayed in other formats as well such as a waterfall or wiggle plot. The density of waterfall traces can also be varied for better data representation. Contour plots showing points of equal amplitude is also commonly used. Other means of varying the data representation can be performed by using arithmetic transformations that emphasise or suppress certain features, such as taking square root of absolute values. The square root, for example, enhances the sensitivity of display of lesser reflections by assigning a low amplitude samples a larger range of colours than higher amplitude samples. The different 2D displays are shown in Figure 1.3.

Three-dimensional views are also known as 3D blocks, and are constructed by placing the 2D radargrams in their scaled spatial position within a 3D format. For this representation, the data collection could be a continuous recording system or discrete points on the surface in fixed-mode recording, but it is critical to know the accurate location of each trace. The three-dimensional blocks thus constructed can either be viewed as solid blocks or sliced and viewed. Figure 1.4 shows a 3D representation of GPR data.

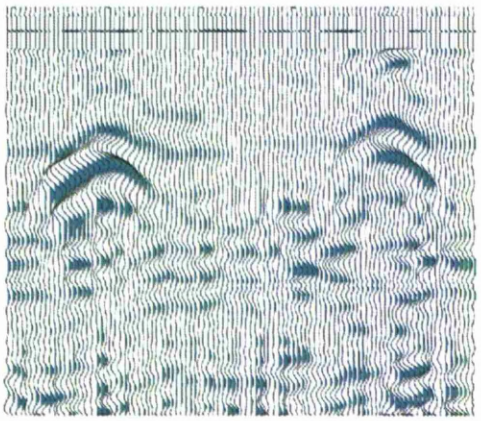

(a) "waterfall" display (close-up)

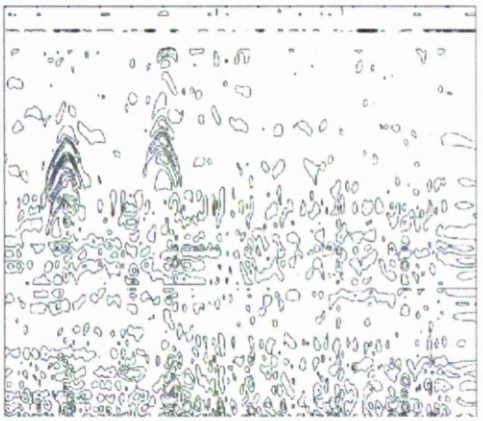

(b) contour display

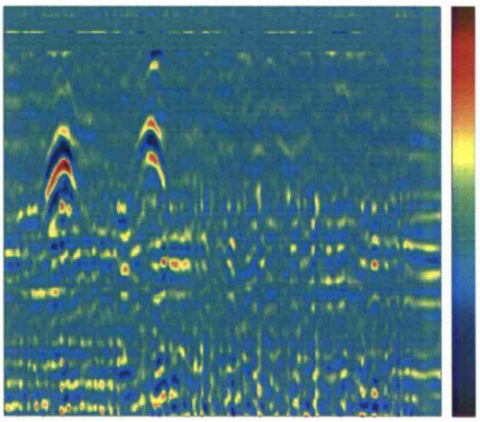

(c) colour-amplitude format (128 colours)

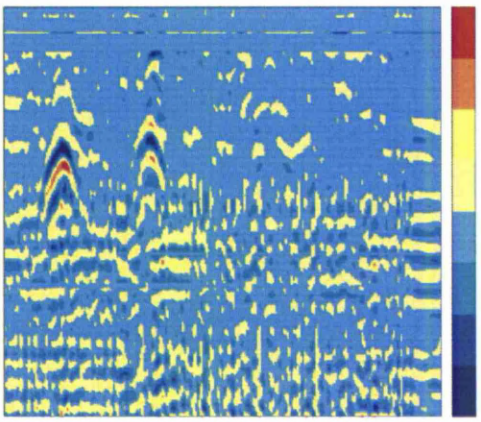

(d) 8 colour display

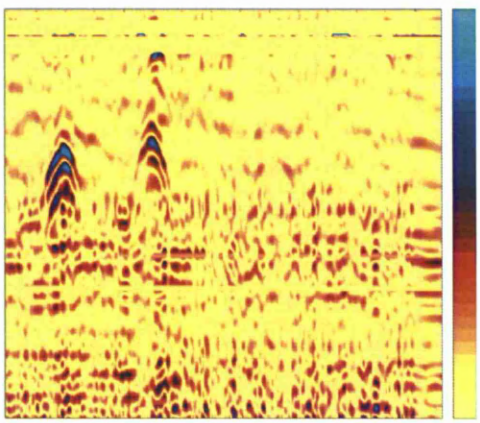

(e) absolute value

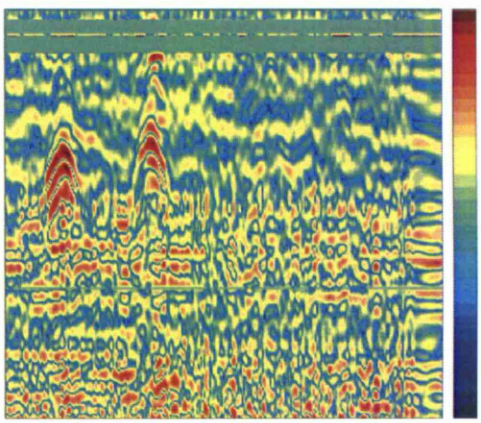

(f) square root

FIGURE 1.3: Effects of various B-scan display options [1]

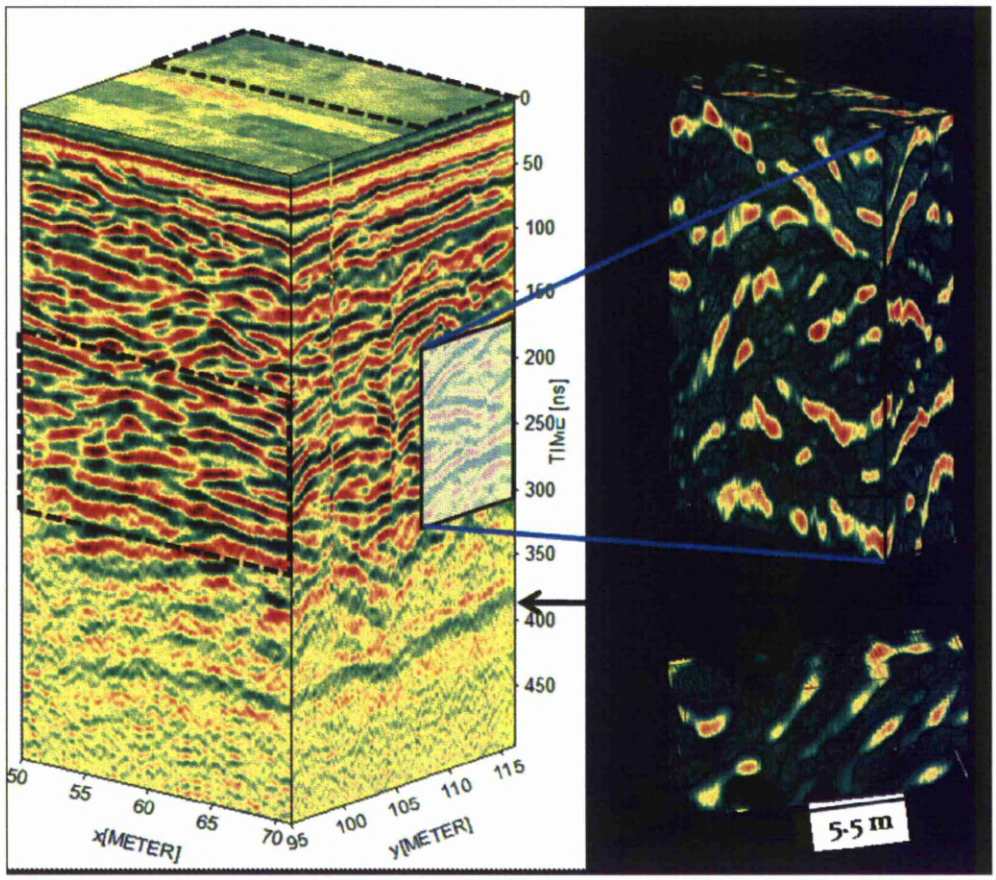

FIGURE 1.4: Three-dimensional display of an orthogonal grid of B-scans [2]

1.2 Previous Work

Over the past two decades a lot of work has been done in the area of GPR and utility detection. Various research work has been outlined here as follows; a general overview of GPR has been given, some important work in data processing and antenna arrangement is described after which research on utility detection has been described in the order of 2D processing, clutter removal, target identification, classification, hyperbola processing, parameter estimation, real time interpretation, 3D processing, surface reconstruction and mapping.

A general overview of GPR introduction, background, theory, various system designs, modelling and modulation techniques, signal processing and applications are presented by Daniels [7], [9], [10].

Costello *et al.* [11] gave an overview and discussion of different underground utility investigations technique such as magnetometers, electromagnetic line locators, Ground penetrating radars, infrared thermography, acoustic location systems and location of targets by these technologies combined.

Cassidy [12] threw light on GPR data processing, modelling and analysis. Different basic GPR data processing steps are discussed along with advanced imaging and analysis tools and data visualisation.

Radzevicius and Daniels [13] discussed the phenomenon of GPR antenna polarisation and the scattering from cylindrical objects such as pipes, wires, re-bars etc, from the perspective of designing a survey. They showed that metallic pipes and low impedance dielectric pipes are best imaged by using linearly polarised antennas on the other hand high impedance, dielectric pipes visibility can be enhanced with the long axis of the dipoles oriented orthogonal to the long axis of the pipes.

Allred *et al.* [14] used different GPR systems covering different frequency ranges in determining the position of drainage pipes in farmlands. A properly chosen system, frequency band and processing method could significantly enhance the detection capability even under difficult ground condition.

Sai and Ligthart [15] presented a two-dimensional preprocessing technique using an ultra wideband impulse ground penetrating radar. The objective was to produce an enhanced GPR image by suppressing the effects of the direct coupling between

the transmit and receive antenna and the surface reflections. The operations include removal of DC-offset, frequency filtering, gain compensation, background removal and data interpolation.

Merwe *et al.* [16] presented a signal processing technique to reduce clutter produced due to ground bounce in GPR data. The method is beneficial especially in case where the targets are land mines. An equation is derived that has contribution from the targets as well as clutter. The equation derivation is then applied to the data in an iterative way so that it takes into consideration the clutter effect leaving the effect of the subsurface inhomogeneities. The disadvantage of this method is that it is based on estimating the values of the desired signal and neglecting the clutter effects. Also the method is time consuming.

Carevic *et al.* [17] presented a Gaussian mixture modelling procedure along with Baysian classification technique to identify mine like targets. This method is used for target specific feature extraction.

Ulug *et al.* [18] described the application of radial basis function (RBF) for feature based automatic target recognition. A performance comparison between this classifier and several other classifiers had been shown and they concluded that RBF network performs better than the other feature based classifiers that they had considered. This paper did not show any quantifiable measure for results and the time cost issue had not been addressed.

Nagashima *et al.* [19] presented a crude trace addition processing algorithm for immediate on-site detection of buried pipes by locating the peaks of 'humps' in the radar data. The simplicity of the technique and the lack of any signal processing or image enhancement restrict the practical utility of this system to only the

most ideal of cases. Chignell *et al.* [20] combined migration and three-dimensional mapping, but without an effective target detection and characterisation stage their systems suffer from effects of clutter and false alarm.

The capability of neural networks to detect concrete reinforcement bars was initially proposed by Molyneaux *et al.* [21] by investigating the properties of radar images generated with the aid of an oil-water emulsion to mimic the electrical properties of real concrete, but the technique is not applicable to the highly cluttered urban environment associated with utilities.

Lotlikar and Kothri [22] presented a dimensionality reduction technique based on using a neural network classifier to produce a reduced image containing the regions of interest in utility mapping. In both papers however, the efficiencies of the proposed classifiers are not quantified and the time cost issue is not addressed.

Gamba and Lossani [23] used a robust spatial approach to pipe signature detections using a feed forward neural network to detect a hyperbolic shape in the images. The network decides whether the certain shape is part of a pipe or not.

Al-Nuaimy [5] presented various neural network based classifiers and pattern recognition techniques for the investigation of buried utilities and solid objects. The authors in [24] presented a novel texture classification technique based on unsupervised neural networks that would identify four different types of textures, but the process has a high time cost.

Youn *et al.* [25] presented an automatic buried pipe detection algorithm applying two steps neural networks in the fully polarimetric GPR.

Grandjean and Durand [26] presented an algorithm that generates hyperbolas and

compare them with the hyperbolic signature in the GPR image to get a perfect or reasonably close match. The program is iterative in nature and is used for off line processing as doing so for a large database would require considerable amount of time. This program also requires human involvement hence making it unsuitable for an automatic near real time requirement. The paper lacks any specific example indicating its efficiency in dealing with real data.

Chaudhuri and Samanta [27] Presented the moment of inertia to fit a hyperbolic target reflection while Illingworth and Kittler [28] used Hough transform for hyperbola fitting. These two methods are usually applicable for fitting simple models as they are computationally expensive and are not suitable for on site data processing. Conic fitting algorithms however are fast but they are only able to identify one conic in each image and are sensitive to outliers hence can not be applied to practical applications as real data is contaminated by noise as presented by the work of authors in [29], [30],[31], [32].

Chen and Cohn [33] used a probabilistic hyperbola mixture model for interpretation of GPR hyperbolas, a hyperbola fitting algorithm based on orthogonal distance fitting is employed for real time detection of buried infrastructure, results of four different algorithms have been discussed for simulated GPR data however results of real GPR data have not been discussed in much detail.

O' Leary and Zsombor Murray [34] explained Fitsgibbon's [30] modified least square method for hyperbola fitting in further detail but this method did not characterise the hyperbola in terms of major and minor axis. Shihab and Al-Nuaimy [35] modified Fitzgibbons ellipse specific direct least square fitting technique to develop a constrained least square method for specifically fitting hyperbolae. The

most important feature of this method is its ability to calculate hyperbolic parameters that are used to calculate target information and hence minimising the inaccuracy of weak estimation. This modified method uses Booksteins [29] quadratic constraint in order to solve by rank deficient generalised eigenvalue system however when tested on simulated hyperbolas of various major and minor axis it was seen that the method performed well with major axis 'a' greater than minor axis 'b' but when value of major axis was less than the minor axis the method tend to fail.

Shihab [1], [36] presented a GPR model for estimating the parameters of underground utilities. This model takes into account the target depth in terms of two way travel time and velocity of propagation through the host medium, radius, orientation with reference to the scan angle thus giving better estimation as the models used before would assume either zero radius or estimate the dielectric.The authors [37], [38], [39] in developed a neural network based target identification technique that does not need operator supervision and hence can be used in automatic detection of underground utilities in GPR data. Al-Nuaimy *et al.* in [40] showed a three dimensional iterative technique that can be used to correct the errors in the parameters.

Bernold *et al.* [41] presented a novel technology for detecting and locating buried utilities, that was attached to the digging equipment, and utilised both EMI (Electromagnetic Induction) and a GPR. Efforts were put into developing a performance analysis algorithm to detect and extract features and characteristics of these utilities, such as their orientation, diameters etc. The two sensory systems were fused to create a multi sensory approach to 3D mapping of the utilities without a priori knowledge of location.

Stolte and Nick [42] presented a relationship between the cylinder radius and the eccentricity of the hyperbola for the purpose of migration. Olhoeft in [43] derived the radius from the curvature of the hyperbola apex. This method requires human intervention.

Ristic, Petrovacki and Govedarica [44] use the same GPR model as Shihab to estimate the radius of a cylindrical object and the propagation velocity simultaneously. The only difference is that the propagation velocity resulting from the model is reduced to a pre defined minimum velocity which is said to be the optimum velocity. This value is then used to calculate the cylinder radius.

Capineri *et al.* [45] developed an image processing technique for real time interpretation of GPR images which uses Hough Transform to locate straight lines and hyperbolic arcs in 2D images. This method can not be used in an automated system as it requires human intervention. Also the method has high computational cost.

Olhoeft [46] presented an automated system for processing and modelling the thickness of pavements in real time. Algorithm was developed to obtain the data from system attached to a moving vehicle and automatically calibrate, position, process and model it without operator intervention.

Torrione, Throckmorton and Collins [47] presented a two stage 3D algorithm for land mine detection in which first a 3D data set is processed and flags are set at potential areas of interest and then the flagged locations are passed onto a feature based processor that further distinguish target like anomalies. The objective is to distinguish targets from naturally occurring clutter from 3D GPR data.

Roberts and Cits [48] used orthogonal profile line data as a method of GPR data-imaging. A 3D image that is generated from a migrated and concatenated data-file is used to detect linear and finite targets. This method can not be used for near real time on site processing as migration techniques require high time consumption.

Binningbo *et al.* [49] performed a three-dimensional processing of radar data and apply a three-dimensional migration algorithm on data with a switched antenna array. This technique is based on the assumption that the wave velocity is the same throughout the soil. The system could resolve the size and location of targets in dry sand with an error range of 5cm.

Al-Nuaimy *et al.* [50] used a 3D iterative model for target parameter correction. A 3D line detection technique called Applied Non-Accumulative Hough Transform (ANHT) was used in this study. ANHT has been found to be much more efficient in terms of time consumption and storage than the traditional Hough transform however it is still very time consuming and hence not suitable for near real time detection.

Sato *et al.* [51] presented a pulse-compression filter which works in conjunction with an aperture synthesis stage to present a high-resolution reconstruction of the subsurface. The success of this system relies on the assumption of the existence of at least one isolated target in the radar image, and several of the parameters require manual adjustment to minimize spurious responses, thus undermining the system's effectiveness as an automatic interpretation tool.

Shanker and Ikuo [52] used super resolution technique algorithm called MUSIC using SAR (Synthetic Aperture Radar) for signal processing and image reconstruction of GPR images of land mines. Jiang *et al.* [53] used a windowed FFT

MUSIC algorithm called W-MUSIC in Non-linear Frequency Modulated/Continuous Wave (FMCW) GPR Signal Analysis to detect closely spaced targets under noisy conditions.

Zarkhidze and Lemenager [54] used 3D GPR technology to map utilities in a complex urban location in Paris. A series of modeling, interpretation and processing tools were used to extract the relevant information. A 3D GPR tool was used to map the complex pipe network and a finite difference time domain model was used to verify the assumptions.

Petrovacki and Ristic [55] used GPS along with GPR for data acquisition and mapping of gas pipe lines at city of Kikinda and surrounding areas. The two technologies were combined to map an underground mid-pressure gas line network.

A large number of case studies, site investigations and processing tools have been developed to correctly estimate the target parameters but there has not yet been a fully operational on site real-time investigation system. The main reason is the time consumption of data processing. Moreover, broad assumptions being made about the various parameters broaden the error range. For this reason, research is needed in order to provide more robust and reliable tools for automatic data processing. In order to make real-time systems, further developments are needed especially to reduce the time cost. The system in this study have addressed the two serious issues: automated processing and time efficiency.

1.3 Objectives and Scope of Work

This study addresses the problem of interpretation of GPR data for underground utilities and evaluates most of the post processing, modeling and parameter estimation methods available. The study has suggested vital improvements in some existing methods and developed new techniques for improved outputs. The main objectives were to enhance the robustness, accuracy and efficiency of the available techniques, and to reduce the time consumption as much as possible. The resulting stages can thus be put in a sequential order to construct an automated system of GPR data interpretation with as minimum operator intervention as possible. Even though, the study has emphasised mostly on estimating target parameters such as depths, dimensions and orientation of underground utilities. The techniques developed can be used for other applications such as mine detection and archeological investigations as well.

The subject has been covered by performing each step of the GPR interpretation method. The remaining chapters of this thesis discuss each and every aspect in detail. Chapter 2 gives a detailed overview of the data acquisition performed for the study. Data was collected around the University of Liverpool campus. In 2007 a large project was undertaken by the University of Liverpool to lay pipes within the campus. Real target parameters, measurements and pictorial data had been collected through out the process thus resulting in a very large database for a GPR site. The radar data for this site has also been collected in orthogonal grid and varying angle scans. This site and the detailed database has not only been used in this study but is also available for future GPR research. Chapter 3 discusses the existing post processing tools that are usually used in GPR data processing. Chapter 4 discusses the improvements to the existing post processing methods

along with some newly developed tools such as Eigen based background removal, MFCC based classification and combined hyperbola fitting technique. Chapter 5 discusses a GPR model for parameter estimation and two methods of GPR radius correction that involves processing of multiple radargrams. The process is used iteratively to correct the target parameters. Chapter 6 discusses a near real time GPR system that incorporates all the findings of this study put in a sequential order. Finally, chapter 7 is the conclusion along with some recommendations for the future work.

1.3.1 Contribution of Work

The personal contribution of this study to the general body of knowledge in this area can be summarised briefly as follows.

- Development of a novel Eigenvalue based background removal technique, which not only results in a refined output with reduced clutter but also highlights the positive and negative target reflections, hence making it easier to classify the target in later stages.
- Development of a novel classification approach that uses targets Mel Frequency Cepstral Coefficients (MFCCs) and polynomial coefficients in a neural classifier for target classification.
- Development of a hyperbola fitter which combines two distinct fitting algorithms that gives good fits for a wide range of hyperbolas.

- Improvements in existing 3D line detection technique called ANHT in order to make it more efficient and accurate while removing operator intervention thus automating it.

- Development of a novel 3D line detection technique called angle based 3D line detection that is far more superior than existing techniques in terms of time consumption and accuracy.

- Sequencing the proposed techniques together in order to make a near real time automatic system for GPR data interpretation of underground utilities.

1.3.2 Published Work

Since this study was started the following papers were published in scientific journals and proceedings of international conferences:

1. Umar S. Khan, W. Al-Nuaimy, "Angle-based 3D line detection and its application for radius correction of underground utilities in GPR data", Proceedings on the 5th International Workshop of Advanced Ground Penetrating Radar IWAGPR, 247-252, 2009 [56].

2. Umar S. Khan, W. Al-Nuaimy and H. Lu, "3D line detection using adaptive non-accumulative Hough transform and its application for radius correction of underground utilities in GPR data", Proceedings of the 5th International Workshop on Advanced Ground Penetrating Radar IWAGPR, 253-258, 2009 2009 [57].

3. Umar S. Khan, Abd El-Samie. Fathi, W. Al-Nuaimy, "Detection of Land mine and Underground Utilities from Acoustic and GPR Images with a Cepstral Approach", Journal of Visual Communication and Image Representation, JVCI, 21:731-740 [58].

4. Umar S. Khan, W. Al-Nuaimy, "Background removal from GPR data using Eigenvalues", 13th International Conference on Ground Penetrating Radar, Lecce, Italy, June 2010 [59].

5. Al-Nuaimy W, Shihab S, Khan U, Huang Y, "An Iterative Technique for the Characterisation of the Geometry of Buried Utilities in a Non-uniform Medium", Proceedings of the 12th International Conference on Ground Penetrating Radar - University of Birmingham.Birmingham, 2008 [60].

1.4 Summary

This chapter describes the GPR system used in this study and presents the rationale for the development of advanced signal and image processing techniques for reliable and robust automated processing and interpretation of radar data in near real time. The scope of the work to be presented in this thesis is outlined, detailing previous research in this area as well as the objectives and scope of the work.

Chapter 2

Data Acquisition

Data collection is a very important step towards GPR data processing as the quality of the collected data is crucial in order to interpret it correctly. Radar system settings, grid layout, ground conditions, antenna arrangement, survey speed and electromagnetic interference from other sources are all important aspects that can affect the quality of data. The operator should take all these options in to account and decide the best approach.

In this study, a large amount of data was collected using the SIR-2 and the SIR-3000 radar systems. Many surveys were taken around the University of Liverpool campus. Also, radar surveys were taken using a newly developed ORFEUS Radar system which is a CW-SF (Continuous Wave-Stepped Frequency) Radar as well as with a commercially available state of the art pulsed radar called DUO. The objective of this survey was to compare the two radars and demonstrate the superiority of the new developed radar in terms of data resolution and penetration depth.

The chapter has been outlined such that the University of Liverpool test site has been explained in detail. The radar settings, parameters and data collection procedure has also been explained. Field trials of the ORFEUS and DUO radar systems and survey of the Harrison Hugh building at University of Liverpool have also been presented.

2.1 University of Liverpool Survey

In the year 2007, an extensive project was given out by the University of Liverpool that involved laying of water pipes within the departments throughout the campus. This gave an ideal opportunity for GPR data collection as the process involved digging of trenches, laying of new pipes and backfilling with standard material.

2.1.1 Test Site Specifications

An ideal site for GPR survey is the one that has a wide variety of target objects within material of different dielectric properties at varying depths. If the actual target parameters are known in advance, it would be beneficial because the results can be verified after data processing. During year 2007, metallic pipes had been laid all around the University campus. The pipes were laid over a wide area within different departments, thus they had to intercept different surfaces such as grass, concrete, roads, pavements, bricks and granite tiles. The campus had been divided into three sites *i.e.* the north campus, south campus and central campus. Appendix B shows the maps of these three sites.

TABLE 2.1: Nominal diameters of pipes used in the site

Inner Dia (mm)	Outer Dia (mm)	Outer Casing Dia (mm))
20	26.9	90
25	33.7	90
32	42.4	110
40	48.3	110
50	60.3	125
65	76.1	140
80	88.9	160
100	114.3	200
125	139.7	225
150	168.3	250
200	219.1	315

The inner portion of the target pipes are metallic and they are covered by insulated material. The outer section of the pipes is hard rubber. Figure 2.1 shows a sample of these target pipes. The pipes that had been laid through out the campus are of different dimensions. Table 2.1 shows the inner and outer diameter of the steel pipe and the outer diameter of the outer casing.

(a) Target pipes

(b) Target and intersecting pipes

FIGURE 2.1: Sample of target pipes

The trenches that had been dug for the pipes are of varying depth and have an average width of 3-5 feet. Two pipes about 5-9 inches apart from each other have

been laid at the bottom of the trenches. The depth of the pipes vary from place to place from 2.5 to 5 feet. These pipes are then covered by red sand. On top of that, four hollow plastic pipes were laid for electric cables. These hollow pipes were again covered by a thin layer of red sand and on top of that a layer of gravel was spread out. These layers were pressed and leveled. Then the original surface was remade, for example if the surface was a road before the dig, then the road was remade. Similarly surfaces were remade for pavements walkways and grassy areas. Figure 2.2 shows one section where the trench is being backfilled. The

(a) Backfilling (b) Closeup view

FIGURE 2.2: Backfill in progress

two most important physical conditions that affect electromagnetic waves are the materials dielectric properties and conductivity. The velocity of electromagnetic wave is determined by the dielectric constant of the material. Propagation speed is faster in low dielectric constant material and vice versa. A sudden reduction in the relative permittivity of a geological boundary causes a corresponding increase in

the velocity of the wave and some of the energy is reflected back into the surface, on the other hand a sudden increase in the relative permittivity of the material results in slowing down the wave and some energy loss. Different materials have different dielectric properties, and since this site is spread out over a very large area, the ground conditions vary extensively. The dielectric constants of the material being scanned in this study is shown in Table 2.2 along with the propagation velocity of electromagnetic wave within that material.

The conductivity of the subsurface is important factor in determining the rate of signal attenuation. An electromagnetic wave when passing through a high conductive material would excite the ions within that medium and transfer some of its energy as heat into the medium. This causes dissemination of the transmitted pulse. It has been observed that signal loss is greater in clayey or wet soil. The surface over trenches were also made of different material, so even though the backfill material was the same, the original surfaces of different material would give different results for GPR scans. In some areas, the surface was grassy clay which when wet would not give penetration depth, on the other hand at some areas the surface was made of reinforced concrete, thus the re-bars in the concrete would interfere with the radars performance. Similarly, some areas were tiled with granite others with brick thus giving a variety of surfaces and severe conditions that the radar could be tested on. The electrical properties of different materials is given in Appendix D.

All the details of the site were recorded both in pictorial format and practical measurements for every section. Pictures of each section were taken through out the pipe layout process for future referencing. These involve pictures of the empty

TABLE 2.2: Material dielectric constant and propagation velocity

Material	Relative dielectric constant	V(mm/ns)
Sand(dry)	3-6	122-173
Sand(wet)	25-30	55-60
Clay(wet)	8-15	77-105
Clay soil(dry)	3	173
Average soil	16	75
Sandstone	6	122
Coal	4-5	134-150
Concrete	6-30	55-122
Asphalt(dry)	2-4	150-212
Asphalt(wet)	6-12	86-120
Granite(dry)	5	134
Granite(wet)	7	114

trenches, pipes being laid in the trenches and the backfilling. Measurements involving the depth of target pipes, their separation from each other and distance from trench boundary were recorded in detail. Besides these, the GPS position exactly on top of the target pipes were recorded. Therefore, the location of any part of the pipe system can be accurately found.

Another benefit of this test site is that the trenches were being intersected by the existing utilities in different areas as shown in Figure 2.3. These utilities were pipes and cables of different sizes and materials.The measurements of their diameters and depth at the trench intersections were also recorded, therefore, creating a very large database for an underground utility site.

2.1.2 Setting Up the Grid

The grid is a very important step in data acquisition, it does not only prove to be helpful in organizing the data files with respect to each other but also the files can be organised accordingly for 3D processing. The grid depends on the scanning order. There are two types of scanning orders; one is the normal profile order in

FIGURE 2.3: Trench being intersected by other pipe

which data is collected in one direction only, that is, either the X or Y axis. In this method the starting line of the scan which is also known as the baseline should be straight. The scan is started at the baseline and continued till the end line after which the radar is returned to the baseline for the next scan. The scan should be exactly perpendicular to the baseline. Another scanning method is known as the zigzag method, in which the first profile is collected from the baseline to the end line and then the second profile starts from the end line to the baseline in the opposite direction of the previous one. To collect data in the zigzag order both the start and the finish baseline should be straight and parallel to each other and the grid corners should be exactly right angles.

There are different ways to set up a grid; the simplest way is by using the ABC right angled triangle method. To make a square grid of 10 X 10, first of all the origin (0,0) is marked. Then a tape measure is pulled 10 units to mark the point (10,0), this is the baseline A. Another tape measure is pulled 10 units from (0,0) in a direction perpendicular to the base line to mark (0,10), which is line B. By using pythagoras theorem for a right angle, if the base and perpendicular of a right

angle triangle are 10 units, then the hypotenuse is calculated to be 14.4. Hence, by pulling a tape measure of length 14.4 from (10,0) at line A and joining it with (0,10) at line B such that C is 14.4, it can be said that the corner (0,0) is at 90^0 because this method produces a right angle triangle. Other ways to make a right angled grid is to use optical square, dumpy or quickset level with horizontal circle.

In the current study, a quickset level with horizontal circle as shown in Figure 2.4 was used to set up the grid. The quickset level with horizontal circle has a zooming lens and a horizontal circle at the base marked 360^0. The quickset is first set steady at a point that is to be the origin (0,0) of the grid. A marker pole is moved at the required distance away from the quickset, so that the red mark on the pole can be seen at the center of the zooming lens. The base of the pole is marked as the end of the baseline, and a line is then drawn from the origin to this point which is the baseline. After that, the quickset is rotated exactly 90^0 in the direction towards which the grid is to be spread out and fixed. The pole marker is then moved at the required distance away from the quickset until the same red marker on the pole is seen in the middle of the lens. The base of the pole is marked, which is the other end of the grid. A line is drawn from the origin to this point, which is the grid line. Afterwards, lines are drawn parallel to the grid line and the base line. The grid can be marked using chalk, spray paint, rope, wire or a tape measure. The density of the grid lines and grid spacing depends on the operator. For high resolution, lines can be drawn closer to each other. In this study, the grid spacing was set to be one meter or half meter apart depending on the requirements.

FIGURE 2.4: Quickset level with horizontal circle

2.1.3 Antenna Arrangement

The antenna arrangement with respect to each other and the direction in which it is pulled over the target specifies the shape of the target in the GPR scan. The most common antenna arrangement is with the electrical field of the transmitter and receiver antenna parallel to each other and parallel to the surface of the earth. This arrangement when pulled perpendicular to the direction of the electrical field results in a wave propagating into the earth perpendicular to the surface. The angle at which the scan direction intercepts a target such as a pipe, cable or rebar determines the shape of the target in the scan, such as if the angle between the target and the antenna movement is 90^0 the target act as a perfect reflector and results in a hyperbolic shape. This shape is the result of the antenna pattern and geometry of the traverse motion. If the angle between the scan direction and the target is reduced the hyperbolic shape expands until the angle is close to 0^0 *i.e.*, scan is being taken along or close to the length of the target in which case hyperbola disappears and a straight shape is seen. Usually, three sets of

measurements can be taken with antennas oriented relative to the electric field and parallel to the surface of the earth. The antennas could be parallel to each other and perpendicular to the scan direction, parallel to each other and parallel to the scan direction and perpendicular to each other, this last arrangement is such that the antennas are cross polarised.

2.1.4 Acquisition Parameters

The SIR-3000 system provides a data acquisition setup facility in which the user can set up different parameters according to the ground conditions, and target location. These settings control the on-site signal processing operations such as filtration, range gain function and the receiver operation such as the range and quantisation level. These settings are also stored in the header of the radargram file and maybe different for different radargrams depending on the operator's settings, but they can be retrieved later at any stage during data processing by reading the header file. The structure of SIR-3000 `dzt` radar data format is detailed in Appendix C.

2.1.5 Signal Conditioning Parameters

The digitised signal is selected by setting the number of samples per scan and the number of bits per sample. The samples per scan depends upon the volume of data and storage limitations and a typical value for that is 512. The resolution of the data is determined by the bits per sample and could be set to either 8 or 16. The horizontal sampling rate along the ground is controlled by the scans per second value, the higher the value of this parameter, higher will be the density of the

scans in the radargram. On-foot surveying 32 scans/second is usually adequate. The SIR-2 system did not have a survey wheel, therefore in order to get a relation of horizontal sampling in terms of distance, a clicker was attached to the system. This is a simple push button arrangement that the operator can press manually with respect to markers set at equal intervals. If markers are set every meter, then the operator would press the push button whenever the antenna passes over the marker during a scan. Each time the push button is pressed, a pulse is sent into a system that records a peak within the B-scan second row. These peaks are helpful in determining the position of the target in real time in the post processing stage. This method of data collection is continuous, therefore, the operator should move the antenna with steady uniform pace and can not stop during a scan.

The SIR-3000 system used in this survey had a wheel cart with a survey wheel installed. The survey wheel needed to be calibrated first. To calibrate the survey wheel the survey wheel calibration tab can be selected from the menu, within which a calibration distance is inserted say, 10 meters. A tape measure is spread out to a 10m distance. The cart is moved from on end to the other and the radar records the distance with respect of the survey wheel rotation. Once the calibration is done, the horizontal sampling rate can be set as scans_per_meter. The radar then automatically distributes that number of scans with respect to the distance in meters. The advantage of this method of scanning is that the data collection is not dependent on time but on distance, therefore, even if the operator stops during the survey the data collection process is also paused as the survey wheel is not moving. Also, if the operator moves backward the survey line moves back over the data respectively.

Usually the received signal is significantly diminished in amplitude then the transmitted signal because of attenuation caused by propagation medium, path and spreading losses. A digital range gain function is available to process the A-scans to make the signal strength independent of depth or travel-time, thus improving the detection of deeper reflections [1]. The sample signal in time is multiplied by a time-varying gain function. The value of these node points can either be adjusted manually by the operator or automatically by the software. A better method is to set the gains on "auto" and then fine tune them manually. This information is also stored in the radargram header so that the gain can be later compensated for and modified in the post processing if needed. Figure 2.5 shows the effect of a radar signal before and after the application of a range gain function.

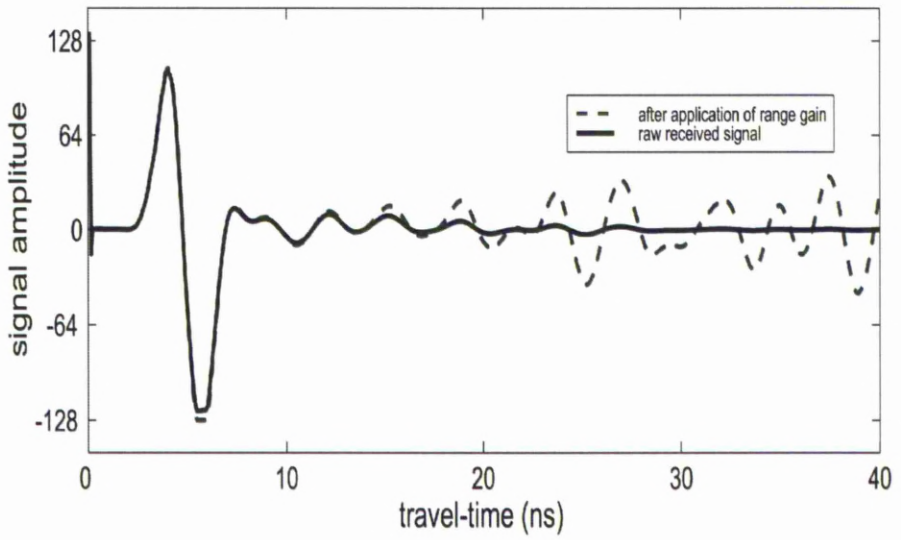

FIGURE 2.5: A-scan before and after application of range gain function[1]

2.1.6 Range Parameter

The range of a GPR is the maximum depth to which the radar signal can penetrate to and can be detected by the receiving antenna. The range is mainly dependent on the total path loss, less path losses give greater range and vice versa. Path losses are mainly caused by target's reflection loss, spreading loss, scattering loss or material loss [7]. The radar itself can not determine specific depth to which it can penetrate, it requires a time limit from the operator till which it can record reflections for a particular scan. The operator can decide this value by evaluating the ground conditions and looking at the initial reflections. The digital range gain function can be used to amplify the signal response, but only to certain extent, as if the path is lossy then the signal return will be un-interpretable. The resolution and quality of the data is also dependent on the range and varies from application to application. In cases where detection of the shape of a target is involved such as utilities and land mines, high resolution images are a crucial demand as the data processing relies on the clarity of the reflection of the targets. On the other hand, where the detection of objects is more important rather then clarity of the obtained image high resolution can be compromised for deeper penetration depth such as detection of soil disturbances, voids, cavities, glacier depths etc. For any antenna frequency, there is always a maximum range that the signal can penetrate into, hence there is a maximum range beyond which the data quality is un-interpretable and hence is useless. The ground condition is another factor that determines the range, for example GPR signals can not penetrate in salt water or through metals. The maximum range value for a particular site can be set by using the formula

given by Equation 2.1.

$$Range = D_i \times S_i \times 1.5 \tag{2.1}$$

where D is the maximum depth of interest and S is the two way slowness of the subsurface material. This is the time taken by the radar wave to travel down and back through one meter of a particular material. The two way slowness of different material is given in Appendix D.

The samples per scan can also be used as a measure of the maximum permissable range. The range should not be increased from this value as by doing so the data will be under sampled and the resolution will be lost. If the data is set to have 512 samples per scan, then for each antenna frequency there is a maximum value that should be set as the range. If the operator requires to increase the range the samples per scan should also be increased. The maximum permissable range can be calculated for 512 samples per scan using Equation 2.2.

$$Maximum\ Range = \frac{(512 \times 100)}{Antenna\ Frequency} \tag{2.2}$$

where the antenna frequency is in MHz.

2.1.7 On Site Data Processing

The SIR-2 and SIR-3000 systems have the option of data playback and reviewing. The operator can review any of the collected data files on screen and there are a limited number of processing tools that can be applied on the data such as gain and filtration. The gain function can be used to apply additional gain constant to

the data in case the signal acquired is low in amplitude and difficult to interpret. The gain values are in decibels (dB) and every 6 dB increase is equivalent to doubling the amplitude of all points in the signal [61].

There are few filters available for on site processing such as vertical high pass, vertical low pass, horizontal smoothing and horizontal background removal filters. These filters can be used to improve the signal clarity. The vertical low-pass and high-pass filters, both of which are three-pole IIR (infinite impulse response), are used to band-pass the input digital data. These filters operate on each incoming vertical A-scans. The high-pass filter eliminates the low frequency noise and some of the system ringing from the data. It is set in MHz and is recommended to be one sixth of the antenna centre frequency [62]. The low-pass filter eliminates the high frequency noise that appear as 'snow' from the data. The cutoff frequency is set in MHz. The recommended settings are twice the antenna centre frequency [5]. The horizontal smoothing filter smooths the data by applying an IIR running average filter and eliminating random noise. The higher the value set for this filter, the smoother will be the output image. It is recommended that a high value of this filter is not used as it will smooth out the small targets in the data. The horizontal background removal filter is used to improve the recognition of small targets when the data is dominated by noise bands [61]. This filter is an IIR running subtraction filter, which works by taking an average of the data and subtracting it from each scan. The filter has more effect when its value is set to be small.

2.1.8 Radar Display

The radar can display the data in three forms; Linescan, Wiggle and Oscope. The linescane can be displayed in colour or grey shade. The trace is represented as a line with varying colour intensities depending on the amplitude of the signal. If a colour scan of 16 is selected, then eight colour will represent the positive value while the other eight will represent the negative values. The screen is filled with vertical coloured lines to generate an image of the subsurface. This form of display is good for most applications especially to identify buried point targets such as pipes, cables, drums and voids. The linescan colour or greyscale display is also good for displaying geological boundaries. The linescan greyscale display is more suitable for identifying buried pipes. During data acquisition different colours and greyscale linescans should be tried in order to determine which one would be the best in data interpretation. The Wiggle displays, on the other hand, are good for interpreting layering in stratigraphic or hydrological surveys. The Oscope display is the display of the A-scans only.

2.2 ORFEUS Field Trials

ORFEUS, which is short for Optimised Radar to Find Every Utility in the Street is a European-wide project undertaken by a consortium of nine organisations consisting of academic institutes, equipment developers and user organisations. The intension was to develop a new radar system and then subject it to Europe-wide field trials on a range of carefully selected test sites to evaluate the performance of the new system to a present day state of the art equipment. The ORFEUS project had two main goals [63]:

- To improve the performance of GPR deployed on the surface to provide underground maps.
- To develop a new radar to provide a look-ahead capability for Horizontal Directional Drilling Equipment.

Two radars were thus developed: one was a surface radar and the other was a bore-head radar that could be installed in the drilling head of a horizontal directional drilling equipment [63]. The technical and scientific objectives of the ORFEUS surface radar were to develop a GPR radar system able to enhance the state of the art performance by a factor of 1.5, to develop a very fast microwave transceiver so that rapid surveys are possible, to develop an innovative hardware active background canceller able to cancel the effects of the soil at the microwave transceiver and to develop an Ultra Wide Band (UWB) antenna with radiation characteristics that enable it to operate in most soil types [63]. The developed radar uses a continuous wave stepped frequency (CW-SF) system because technical analysis shows that impulse radars penetration depth is limited to about 1m when the soil is highly conductive (clay with 50 dB/m two-way attenuation) and a detection rate of about 80% could be expected with a confidence of 90%. In such conditions, it is extremely difficult to detect small objects over the depth of 0.5 meter and the GPR application is strongly limited [64]. The ORFEUS radar can achieve greater dynamic range and penetration depth as compared to a pulse radar. The CW-SF radar also provides reduced receiver noise because it operates in very small instantaneous bandwidths consequently giving an increase in dynamic range. A unique advantage of the ORFEUS surface radar system is its ability to manage very large bandwidth which is from 100 MHz to 1 GHz. Most of the current GPR

systems on the other hand have an effective bandwidth of some hundred MHz, therefore the ORFEUS radar gives better resolution.

The disadvantage of the ORFEUS radar system is that it takes more time than the pulse radar system. This is because it uses CW-SF, which is slow for two reasons *i.e.*, its low spectral efficiency and the temporal efficiency of the synthesiser used for sweeping across the frequencies in steps.

Initially, the test site at Gaze De France was chosen to be the test site for this radar [65], but after the development phase was complete the system was ready to be tested on other sites as well. The University of Liverpool site was one of many sites suggested for the trials. The test site had to be made of different surfaces covering a wide range of utilities with original measurements for the results to be compared to. University of Liverpool campus site offered all these aspects, therefore it was chosen as one of the sites for the ORFEUS trials along with a few other test sites at newcastle, Paris, Nice, Milan, and Sardinia.

The ORFEUS team arrived at the site in August 2007 surveys were done in areas of interest around the campus with the developed radar system and another commercially available pulse radar known as DUO. The DUO radar uses two antennas in the same casing having center frequency of 200 MHz and 600 MHz. The 200 Mhz antenna is used for greater penetration depth while the 600 MHz antenna is used for shallower depths and better resolution. The objective of the trials were to compare the results from both the radars and evaluate the performance of the new radar system in terms of data quality and penetration depth.

The target pipes around the campus were chosen for performance assessment. The trial site was divided into five sections. A dense grid of sweep was taken for each

site. The first site was a pedestrian walkway covered by granite tiles. The second site was covered up by concrete tiles, some of which were reinforced. The third site was a meadow with tall grass, since it had rained some days earlier,the clay was still slightly wet. The fourth and fifth sites were covered up with asphalt. The radars were tested on four different ground conditions. Figure 2.6(a) shows a survey scene at one of the sites with a meadow having tall grass, the radar on the left is the ORFEUS radar while the one on the right is the DUO radar. The survey scan is taken in parallel with the survey line marked by the tape measure. After each scan the data is observed and stored in the hard drive of a portable computer attached to the system. The laptop also carries the necessary software to view and analyse the data.

2.2.1 Results of ORFEUS Field Trials

A comparison of the results from the ORFEUS radar and the DUO radar operating at 200 MHz and 600 MHz frequency is shown in Figure 2.8. It is clear by looking at the images that the ORFEUS radar is not only giving better resolution and quality but also has more penetration depth than the DUO radar. The ORFEUS radar shows more detailed hyperbolic reflections. Also the two targets pointed out as target 2 and target 3 can only be seen in the results from the ORFEUS radar and is not visible in any of the scans of the DUO radar.

The pulsed GPR system is affected by high noise levels due to ultra wide band receiver architecture. Evidence of this can be seen in the B-scan of the DUO radar in which when the radar signal went deeper the target detection capability was compromised by the salt and pepper noise. On the other hand the ORFEUS

(a)

(b)

FIGURE 2.6: Data acquisition with the ORFEUS and DUO radars

surface radar had a tuned receiver architecture hence showing very low levels of noise. In this case it is also seen that the noise appears in the DUO 200 and DUO 600 at about 1.5 m to 1.2 m depths respectively while this level is about 2 m in the ORFEUS scans.

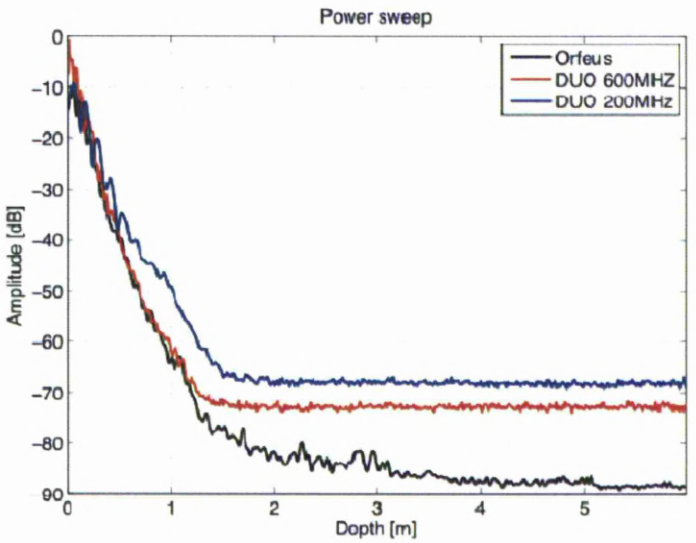

FIGURE 2.7: Power sweep of the DUO 200 DUO 600 and ORFEUS radar [3]

Another instrument to compare the overall performance of the radars was the power sweep graph. This graph represented the mean signal level measured during a whole B-scan coming from each depth layer. The power level is an integral contribution due to many factors such as antenna coupling, targets, ground clutter, cell noise, thermal noise, antenna ringing effects etc. Figure 2.7 shows the power sweep of both the radars and it is seen that the dynamic range of the ORFEUS radar is increased about 10 dB at 3 m depth and about 20 dB at greater depths. Detailed survey report of the trials is attached in Appendix F.

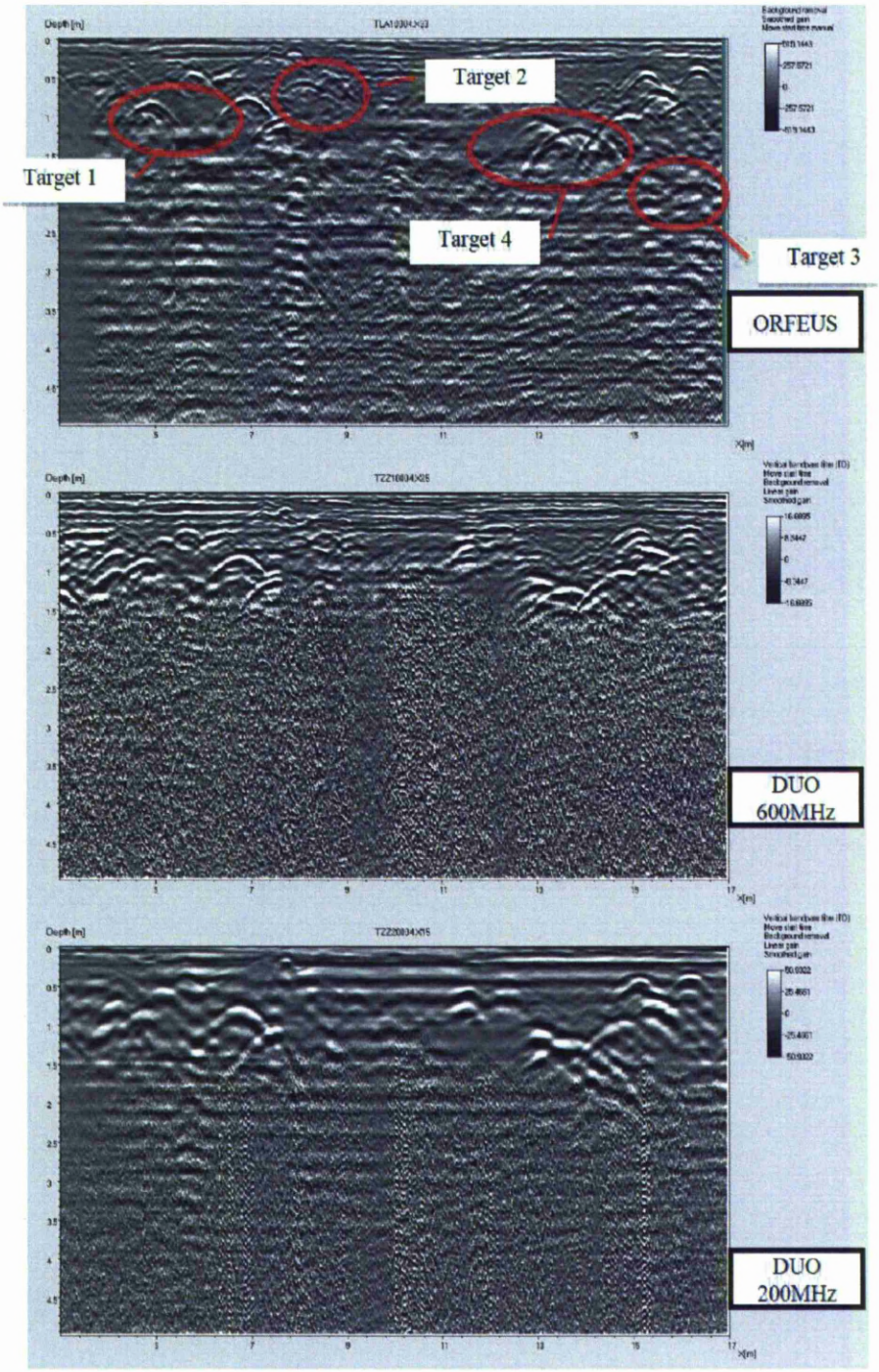

FIGURE 2.8: ORFEUS and DUO radar results [3]

2.3 Harrison Hugh Building Survey

An approximate 1 m by 3.5 m area has collapsed at the basement of the Harrison hugh Building at University of Liverpool as shown in Figure 2.9. It was initially assumed that the collapse was because of voids under the surface and if that was the case then the rest of the floor was at the risk of collapse as well. Therefore, it was decided that a GPR survey be taken of the area in order to determine the cause of the collapse. This site gave a real world scenario of GPR data acquisition and processing.

FIGURE 2.9: Collapsed region in the basement of Harrison Hugh building

2.3.1 Equipment Specifications

Two GPR systems were used in the survey. The first system was the SIR-2 system with a 900 MHz antenna. Since 900 MHz is a high frequency antenna, it was not able to penetrate deeper into the concrete surface. The maximum depth in concrete

assuming a dielectric of 5.5 was around 0.7 m to 1 m (12 ns), however it provided good near surface resolution. The second system was the latest SIR-3000 with a survey wheel and two antennas of 900 MHz and 400 MHz. The 400 MHz antenna could reach a depth of 2.6 m - 3.2 m (50 ns) depending on the ground condition. Scans were taken on an orthogonal grid.

2.3.2 Survey Results

The initial scan made with the SIR-2 system showed presence of rebar in the non affected area and no rebar was seen in the collapsed area. Both the areas required different gain settings for the radar. A very high gain was required in order to extract comprehensible information from the collapsed area, the same gain settings were extremely high for the rest of the floor due to the presence of rebar as the reflections from the rebar were too high and clipped off.

Figure 2.10 shows a GPR scan taken with the SIR-2 system using a 900MHz antenna of the collapsed and the non-affected area. It is clearly seen that there is rebar in the non-affected area and no traces of rebar can be seen in the collapsed area.

In order to get a better understanding, scans were taken with the SIR-3000 radar and similar results were found. An interesting question thus arises: why was this one rectangular section without rebar and the rest of the floor reinforced with rebar? The answer to this question is still unknown. Having analysed that specific room, there was a possibility that the floor in the gallery and the neighbouring room might also show similar behaviour. Therefore, scans were taken in the gallery

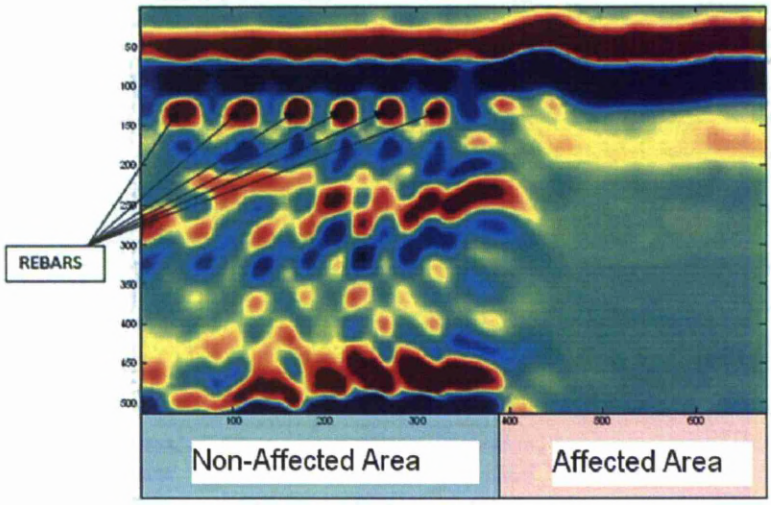

FIGURE 2.10: GPR scan of the collapsed area vs. non-collapsed area

and the other rooms. Figure 2.11 shows a scan taken in the gallery, it can be clearly seen that there is continuous rebar throughout the floor.

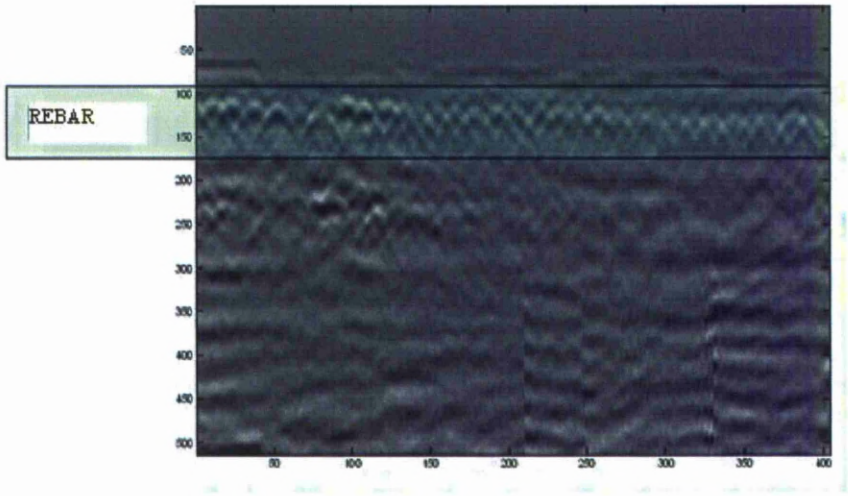

FIGURE 2.11: GPR scan taken in the gallery showing continuous rebar

The scans taken in the neighbouring room showed interesting results. It was observed that similar behaviour to the collapsed area was found in this room. Two anomalies that were also rectangular in shape were seen that showed no

rebar. The GPR scan in Figure 2.12 shows the two areas marked in red. Section A was calculated to be 0.5 m X 1.35 m while section B was calculated to be 1 m X 2 m.

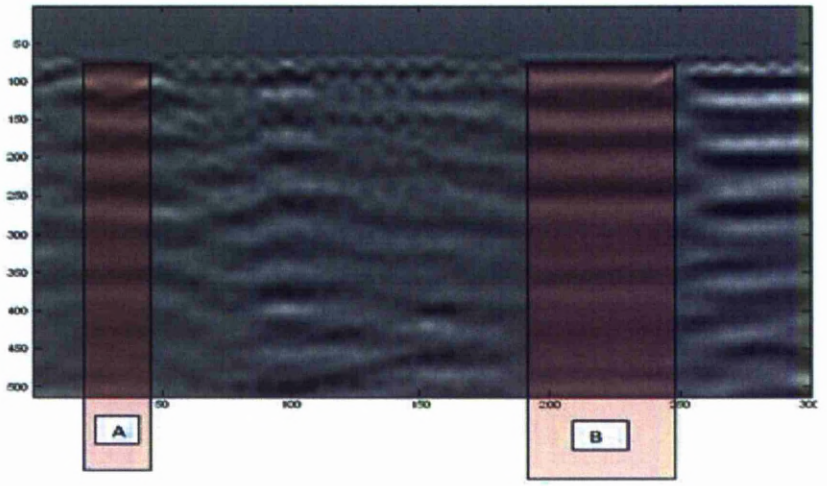

FIGURE 2.12: GPR scan taken in the next room

The survey indicated that the reason for the collapse is the absence of rebar in the collapsed area. Stress caused by heavy machinery placed there could have caused the collapse. No indications of large voids were seen in the survey throughout the rest of the floor scan. Areas were pointed out in the neighbouring room that also did not have reinforced concrete and was recommended that no heavy machinery be placed there as by doing so they might also collapse. Figure 2.13 is a CAD drawing of the three rooms that show the exact locations of the collapsed area and section A and B. The dimensions are in cm.

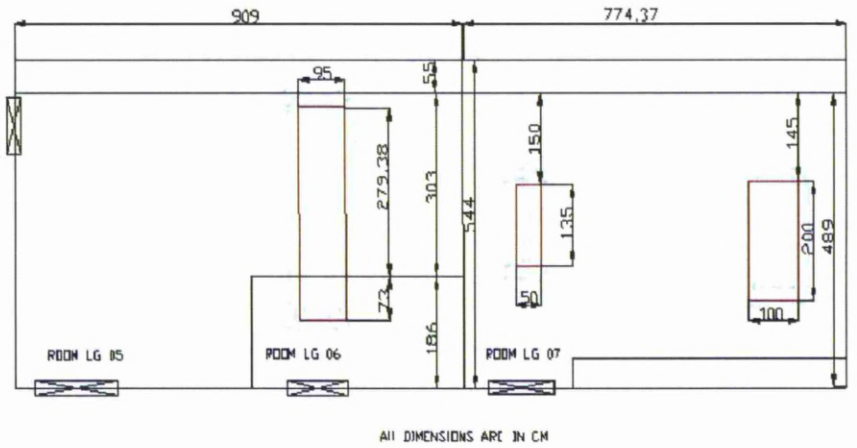

FIGURE 2.13: CAD drawing of the rooms and target areas

2.4 Summary

This chapter described the data acquisition sites, procedure and the associated acquisition and processing parameters. A large database was created around the University of Liverpool campus. This database is composed of pictorial images of the site before, during and after the utility installation. Record of detailed measurement of the dimensions and depth profiles of all target utilities along with non target intersecting utilities had been made. GPR scans have been taken over different surfaces such as granite tiles, bricks, grassy lawns, concrete slabs, reinforced concrete and asphalt roadways with two different radars the SIR System-2 and the SIR-3000. Two case studies of radar surveys have also been presented: the first one involves data collection using the newly developed ORFEUS surface radar that uses continuous wave stepped frequency and its results have been compared with a commercially available pulsed radar DUO 200 and DUO 600. The second case study is about a collapsed area in the basement of the Harrison Hugh building and after the survey the reason of the collapse has been concluded as absence of reinforcement in the concrete tiles underneath.

Chapter 3

GPR Data Processing

The interpretation of GPR data involves many post processing tools after which an acceptable parameter estimation can be achieved. These tools are distance normalisation, background removal, classification, segmentation, feature extraction, edge detection, region completion, skeletonisation and hyperbola fitting. The data is then introduced to the GPR model which is presented in Chapter 4. Artificial neural networks is used in the classification stage that replaces the role of expert interpreters in recognising potential targets and rejecting the unwanted data. In the following sections a detailed description of the post processing tools is given.

3.1 Introduction

To understand GPR data for target parameter estimation the data has to undergo many preprocessing and post processing tools. Usually these tools are applied manually by an operator which involves human intervention and consumes large

amount of time and effort. It is therefore necessary that an efficient, smart and automated process be created to remove the operators intervention and to perform the desired operations resulting in correct parameter estimation.

Typically, GPR data is interpreted off-line by an operator using various manual and automatic techniques. A skillful expert is required to separate potential targets and distinguish them from clutter and background noise taking into account the various system effects, environmental effects and subsurface information. Since a typical GPR survey yields a large volume of data, this processing requires significant time, skill and experience not to mention the cost of the techniques.

GPR data is in the form of both ensembles of time series and image. Hence it requires different signal and image processing techniques to get correct interpretation. Less then 2% of total GPR data would correspond to actual data. Therefore, it requires an intelligent automated system that would collect the essential data and remove the redundant data in order to save computational space and time.

This chapter outlines important stages that the data has to go through in order to get to a stage where the GPR model can be applied. The problem of distance normalisation and background removal is discussed, after which feature detection and classification techniques to extract target reflections from both A-scans and B-scans are discussed. The remaining data is discarded and image processing tools such as edge detection, hyperbola completion and skeletonisation are used to get a completed hyperbolic signature of the target. Fitting algorithms are then applied on the signature to get suitable inputs to the GPR model. A block diagram of the automated process is shown in Figure 3.1.

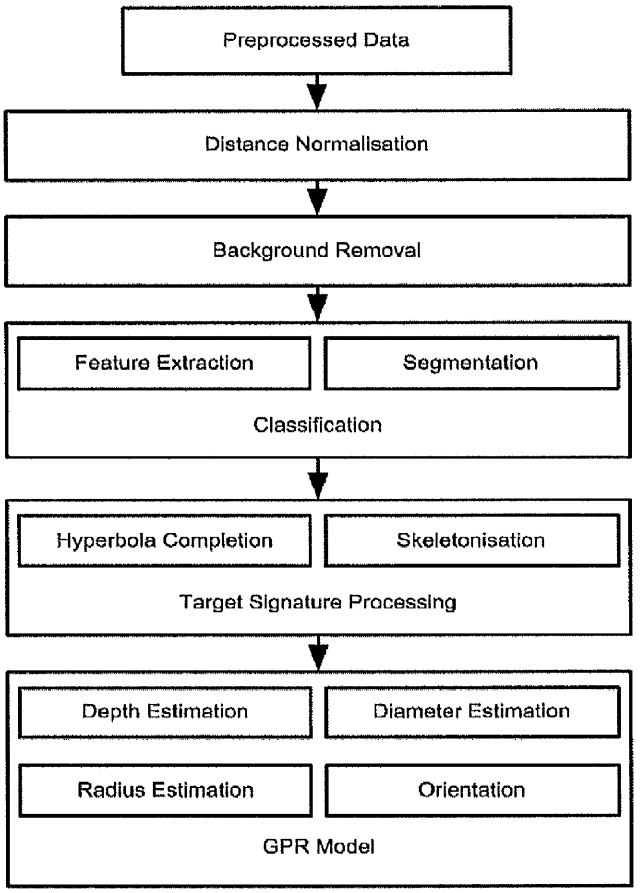

FIGURE 3.1: Automatic detection and interpretation system

3.2 Distance Normalisation

In GPR the targets are stationary and the antennas are moved with respect to the surroundings. The target position must be given in reference to a grid on the ground surface. To get any practical data, there has to be sufficient spatial positioning information in the data to correlate any detected features with the surface coordinates. Event markers are introduced within the data to incorporate spatial positions. These markers are often introduced by a manual switch button that is controlled by the operator. During the grid layout markers are placed at equal intervals and the operator is required to press a manual switch button when passing over these markers, which places fiducial markers within the data.

The SIR-2 system records these fiducial markers as spikes of 90% of the maximum dynamic acquisition range at the second sample of the time series. The spacing between consecutive markers depends on the speed of the survey, even with a survey wheel. If the scans per meter value of the radar setup is set very high and the scan pace is fast, then the spacing between the markers would be distorted.

A process of distance normalisation can be used to remove these distortions by stacking or interpolating the data according to the true survey coordinates and to render a regular scan spacing. This normalisation is also sometimes referred to as "rubber band" processing or "rubber sheeting". The distance normalisation procedure is also used to reduce the size of the radar file to facilitate processing and storage, on the other hand, stacking several radar signals average over the same point reduces the random noise effect.

3.3 Background and Clutter Removal

A typical radargram contains many unwanted reflections that need to be excluded from the data set. These reflections are caused by breakthrough between transmit and receive antenna, ground coupling, reflections from non targets such as rocks or buried rubbish, geological layers, antenna ring-down or radar system effects. The antenna ringdown effect occurs when the characteristic impedance does not match with the transmission medium hence some energy is stored as standing waves in the antenna elements and is radiated over extended period causing the antenna to ring. This effect is made worse when combined with breakthrough, coupling and surface reflections making it difficult to see less intense reflections from targets near to the surface.

The most classic and simplest background removal technique is the mean subtraction method. Here it is assumed that the target material properties vary randomly about a location independent mean and that the target indications are present in a relatively small number of measurements, thus the mean of a large number of measurements can be considered as the measurement of the system clutter [1]. Mean subtraction can be performed in a number of ways, *i.e.*, the mean average of the whole B-scan subtracted from individual A-scans, the average mean of only the area around the desired signal being subtracted from the A-scans or estimating the background and subtracting that from the data by using either moving average filter or median filter [66]. Another method of clutter removal is the likelihood ratio test in which a maximum likelihood approach is used to estimate unknown model parameters [66]. In this method a hypothesis test is taken for the measured signal containing the background signal, target and noise. A log likelihood test of the probability density functions of the hypothesis is taken in order to get a certain threshold value. Unfortunately this method gives bad results for plastic targets. The detailed formulas for the maximum likelihood approach are given in [66]. System identification method for clutter removal uses two different system models for clutter reduction. The first model is the convolution model in which the GPR image is considered as a convolution of the clutter impulse response and the target impulse response. An auto-regression moving average is used to derive an estimate of the transfer function of the clutter and the clutter is removed by passing the image through an inverse clutter filter [66]. In certain cases Wavelet transform is also used for background clutter removal [66].

Li and Ling-Jiang used a symmetry filter for clutter removal in which a weighting matrix for the target was designed to reduce the unsymmetrical clutter [67]. Huo used KL transform to remove effects of direct waves from GPR data [68]. Eigen

vectors corresponding to highest Eigenvalues were used to perform the transformation. Ulrych and Cagnoli used singular value decomposition to remove flat horizontal reflection from GPR data of base surge deposits [69].

The proposed system is a two-step method. The first step is a combination of the last two methods stated above and the second step uses mean background removal on the output from the first step. The first step uses the singular value decomposition of the GPR radargram. The covariance of the original image is then taken and the highest and lowest Eigenvalues are used to construct two Eigen images. This method not only removes the flat horizontal reflections but the effect of the system clutter is also removed thus producing a clearer image. In certain cases there still remains slight traces of the horizontal reflections, therefore applying mean subtraction as stage two reduces this effect. The final output of the proposed method gives remarkable results showing a clear superiority over the existing methodologies.

Figures 3.2 and 3.3 show a radargram, containing two target pipes, before and after background removal. The radargrams used in this study have been collected using the SIR-3000 system from the University of Liverpool test site.

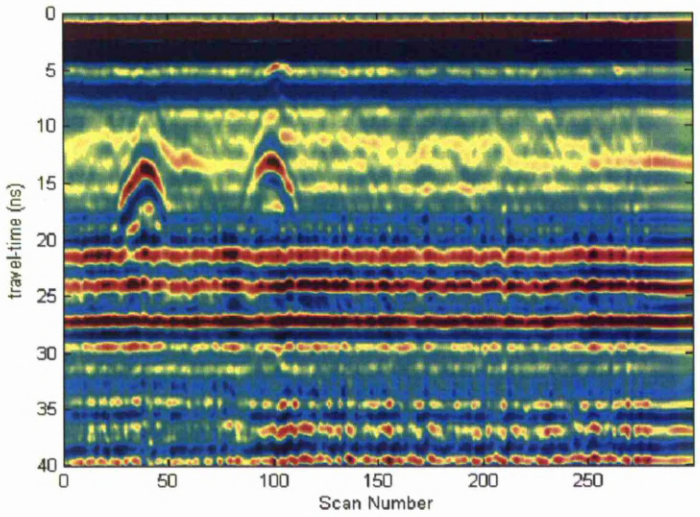

FIGURE 3.2: Radargram before background removal

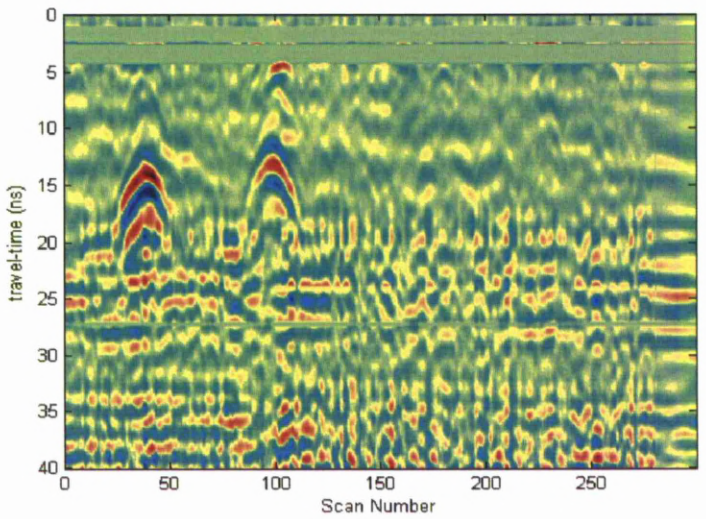

FIGURE 3.3: Radargram after mean background removal

3.4 Feature Extraction

A typical GPR radargram has reflections from targets as well as non targets. It is therefore necessary to extract these reflections and distinguish target reflections

from undesired reflections. The remaining data can thus be discarded to save computation space and time cost. Figure 3.2 is a typical radargram which shows two strong reflections from targets in the form of inverted hyperbolas, the remaining of the data is redundant.

GPR data is considered in both A-scan and B-scan form. Therefore, based on the way the data is viewed there are different segmentation techniques. Two major categories of segmentation are:

1. Time-series features
2. Spatial features

These categories will be discussed further in the following sections.

3.5 Time-Series Features

The A-scans contain all the information about the subsurface but human operators usually prefer the B-scans as they are easier to interpret. It is impossible for an operator to distinguish between two A-scans one of which is from a target and the other one from a non target as shown in Figure 3.4. Besides this visual observation, an A-scan does contain the necessary information for a target. Therefore, it is important to find features, also known as descriptors, that could discriminate between targets and non targets.

In order to chose a suitable descriptor for a signal, it should be kept in mind that the descriptor should emphasise a feature of the signal which is unique to that

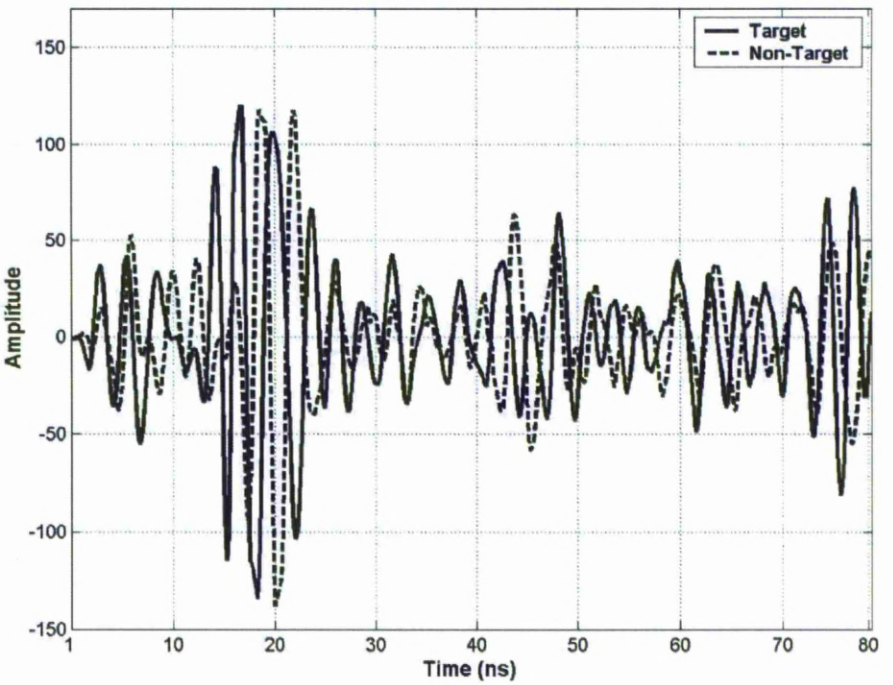

FIGURE 3.4: GPR scans of target and non-target [1]

specific class of signals so that it could be differentiated from other signals. Also, some descriptors may be useful in certain applications and not in others. Besides these, the time consumption factor should also be kept in mind. There are several features of the reflected signals out of which the following are considered:

1. Statistical Features
2. Spectral Features
    - Periodogram
    - Time-frequency

3.5.1 Statistical Features

The selection of a statistical feature depends on the type of the signal and the ability of that feature to discriminate the signal from other types. Some first order statistical features have therefore been extracted from the radar reflections to present basis of discrimination between genuine targets and reflections representing noise and clutter. It has been seen that the effective data contents of targets and non-targets exist in an average 64-pixel of the A-scans. Therefore the data set is segmented to 64-pixel long segments [1]. Investigations have shown that the following three descriptors give a good discrimination between signals returned from targets and other reflections such as clutter, shallow reflections, noise and attenuation [70] [71].

1. Variance (second moment):

$$\sigma = \frac{1}{n-1}\sum_{i=1}^{n}(s_i - \bar{s})^2 \tag{3.1}$$

   where s_i is the i^{th} element in the vector s of length n, and $\bar{s}$ is the mean value of s.

2. Mean absolute deviation (MAD):

$$\text{MAD} = \frac{1}{n}\sum_{i=1}^{n}|s_i - \bar{s}| \tag{3.2}$$

3. Fourth moment:

$$m_4 = \frac{1}{n-1}\sum_{i=1}^{n}(s_i - \bar{s})^4 \tag{3.3}$$

3.5.2 Spectral Features

The reflections from buried targets and non-targets can be differentiated using pattern recognition techniques. The pattern recognition task is performed by extracting different features from the signals. Frequency domain representation of the A-scans facilitates this task. Different spectral representations have been investigated as follows:

3.5.2.1 Periodogram

The power spectral density (PSD) is a measure of the distribution of the average power in a time series. Periodogram is an estimate of the PSD and is given in [1], [5] as:

$$P(c) = \frac{S(c)S^*(c)}{B} \qquad c = 0, 1, \cdots, \frac{B}{2} \tag{3.4}$$

where $S(c)$ is the B-bin Discrete Fourier Transform (DFT) of the b-sample time-series $s(n)$, and is given by

$$S(c) = \frac{2}{b}\sum_{n=0}^{b-1} s(n)e^{-j\frac{2\pi}{B}} \qquad c = 0, 1, \cdots, \frac{B}{2} \tag{3.5}$$

where the global domain is that of frequency and (*) indicates the complex conjugate.

The significant spectral information in a signal can be captured by retaining the first 12 spectral bins in a 64-bin DFT [5]. Each 512 sample A-scan is transformed into a 12 point PSD estimate.

Each scan is divided into eight continuous 64-sample segments as shown in Figure 3.5. For each segment the logarithm of the 64-point windowed PSD is extracted as the discriminating feature. Hanning window is chosen for this application which is given by:

$$w(n) = \begin{cases} \frac{1}{2}\left(1 + \cos\frac{n\pi}{J}\right) & |n| \leq win \\ 0 & |n| > win \end{cases} \tag{3.6}$$

where win is the length of the window.

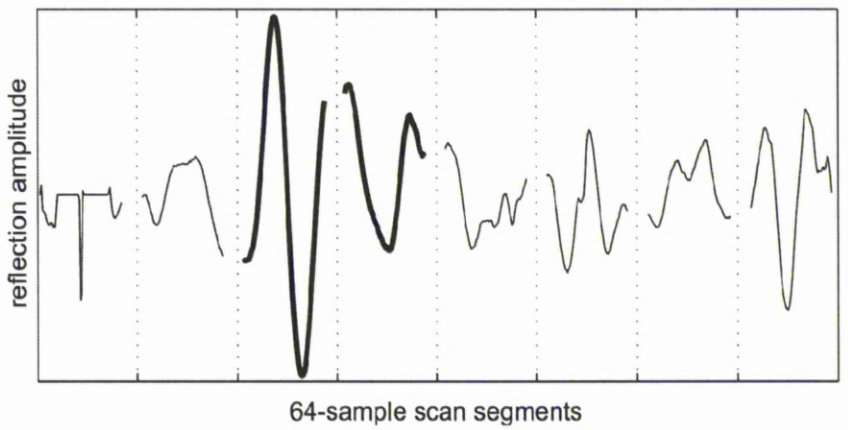

FIGURE 3.5: An A-scan sectioned into eight 64-sample segments [1]

Periodogram has many drawbacks, one of which is excessive variance [72]. Bartlett [73] suggested that the variance would be reduced if the time-series segment is divided into subsets, with the periodogram then computed for each subset and the average energy density obtained for each frequency in order to obtain a greater reduction in variance. By applying this the segmentations become more sensitive to the presence and location of the targets.

3.5.2.2 Time-frequency Techniques

Wigner-Ville distribution (WVD) [74] is a widely applied time-frequency technique in a number of applications and is given by:

$$W_s(t,f) = \int_{-\infty}^{+\infty} s(t+\tau/2)s^*(t-\tau/2)e^{-j2\pi f\tau}d\tau \tag{3.7}$$

Knowing that the instantaneous autocorrelation function $R_s(\tau,t)$ of a signal $s(t)$ is given by:

$$R_s(t,\tau) = s(t+\tau/2)s^*(t-\tau/2) \tag{3.8}$$

The Fourier transform of $R_s(t,\tau)$ provides the instantaneous spectral density function:

$$D_s(t,f) = \int_{-\infty}^{+\infty} e^{-j2\pi f\tau}d\tau R_s(t,\tau) \equiv W_s(t,f) \tag{3.9}$$

WVD of a signal can be viewed as an instantaneous spectral density. WVD can characterise the signal's frequency change better than any other scheme thus making it superior to other methods [75]. A major drawback of WVD is its high time cost which makes it unsuitable for automatic real time processing.

Another analysis technique is the Short-time fourier transform (STFT) [76]. Fourier analysis allows passage from the time domain to the frequency domain. Therefore, its use is mainly concerned with stationary signals whose properties do not evolve with time. The two domains are not allowed to combine and most temporal information cannot be seen in the frequency domain. The spectrum shows the overall

strength of each frequency contained in the signal but is unable to provide the time localisation of spectral components [77]. Fourier transform is based on global information which is inadequate for study of compact or local patterns. That is why non-stationary signal analysis require more than the fourier transform [75]. STFT is one of the commonly used techniques which is defined by

$$\mathrm{STFT}_{s}^{w}(t,f) = \int_{\tau} s(\tau)w(\tau - t)e^{-j2\pi f\tau}\, d\tau \tag{3.10}$$

and in discrete form for a time-series $s(n)$ consisting of b samples,

$$\mathrm{STFT}_{s}^{w}(i,p) = \sum_{n=0}^{b-1} s(n)w(i-n)e^{-j\frac{2\pi ci}{b}} \tag{3.11}$$

where $i, p = 0, 1, 2, \cdots, b-1$. The STFT, or windowed Fourier transform introduces a frequency dependence with time by filtering a signal "at all times" with a band-pass filter centred at each individual frequency and whose impulse response is that of the window function $w(i-n)$. This produces a "local spectrum" of the signal $s(n)$ around the analysis time i. The ensemble of the corresponding power spectra for all times produces a two-dimensional time-frequency representation known as a *spectrogram* [1].

$$\mathrm{SPEC}_{s}^{w}(i,p) = \left|\mathrm{STFT}_{s}^{w}(i,p)\right|^2 \tag{3.12}$$

This is a very common tool in signal analysis because of its ability to provide a signals energy distribution in the time frequency plane. The choice of the window size is very critical in this form of study. By reducing the window size the time resolution increases but the number of discrete frequencies that can be represented in the frequency domain is reduced.

The features extracted from this analysis are the frequency and the magnitude of the largest peak of the spectrum at each point on the time axis [1].

3.6 Spatial Features

The GPR radargram is an ensemble of time-series and the manner in which the stacked A-scans are displayed by using intensity-mapped images lends the targets and clutter to be interpreted visually. The operator can manually point out areas of interest relying on certain visual clues in order to pass judgement. Visual texture is the most important feature to identify target regions [78]. Studies in psychophysics have investigated the visual processes that allow humans to separate features in images using texture clues [79]. It is therefore an area of interest to identify and quantify the qualities of texture for an automatic image interpretation system. The term texture is used to represent the visual texture of the images, not the physical texture of the underground medium.

There are different definitions for texture [70], [80] and there are many approaches for its interpretation [81], [82], [70]. The most successful texture interpretation techniques are the statistical and regional methods.

3.6.1 Statistical Features

Statistical feature analysis computes local features at each point in the image and calculates a set of statistics for the distribution of the intensity levels [1]. These statistics classified into first order, second order and higher order statistics. The decision of choosing the right order of statistics is based on the complexity of

the system, the number of classes to distinguish, minimum accuracy and type of texture.

First order descriptors are computed from the local pixel statistics of the intensity histogram, the radargram is scanned vertically and horizontally using a rectangular window and each window's histogram is characterised using statistical descriptors. These descriptors are a function of the pixel intensity distribution $h(i)$ within the windowed region centred at an arbitrary point (x,y). If g is the number of data points (pixels) in the scanning window, and μ_h is the mean of the pixel intensity distribution in the window then these descriptors are given by

1. Variance (second moment):

$$\sigma_h^2 = \sum_{i=1}^{g} (i - \mu_h)^2 \, h(i) \tag{3.13}$$

2. Skewness (third moment):

$$\sum_{i=1}^{g} (i - \mu_h)^3 \, h(i) \tag{3.14}$$

3. Kurtosis (fourth moment):

$$\sum_{i=1}^{g} (i - \mu_h)^4 \, h(i) \tag{3.15}$$

4. Entropy:

$$-\sum_{i=1}^{g} h(i) \, \log h(i) \tag{3.16}$$

The discrimination capability between targets and non targets is tested by performing hierarchial tree unsupervised clustering. Vertical and horizontal window overlaps are used to further reduce any unnecessary regions that do not contain targets. the overlap percentage for the window can be set so that in the subsequent neural network classification stage each region is classified more than once making the selected regions include only the targets of interest as the overlapping percentage increases. The right percentage of the window overlap should be chosen as increasing the percentage would involve more loops, calculations and memory size, hence increasing the time cost.

3.6.2 Regional Features

This approach aims at selecting the hyperbolic shape generated by the scan of a buried cylinder. The radargram is treated as an image containing different shaped regions and the hyperbolic shaped regions are to be differentiated from others. This process is known as image segmentation. The automatic segmentations techniques can be categorised into four types:

1. Thresholding techniques
2. Boundary-based techniques
3. Region-based techniques, and
4. Hybrid techniques

Thresholding is a popular technique to detect discontinuities and is an easy and convenient way to perform segmentation on the basis of differentiating between

various intensities or colours between regions in an image. In this study a simple thresholding is performed that generates a binary image with the resulted segments as an output. Black pixels as the background and white as the segments or vice versa. The segmentation cut-off is performed by a single value (certain percentage of the peak value) known as the intensity threshold and all the pixel values are compared to this value. If the values of the pixels is higher, then they are set to white and if the values of the pixels is lower, they are set to be black. Figure 3.6 shows the result of thresholding a typical radargram.

Edge detection is another approach used to detect meaningful discontinuities as edges are located and used to represent most frequently appearing boundaries within the images in comparison to point and line boundaries [70].

The regional based technique involves regional features that could be best used to describe hyperbolic shapes and are able to distinguish them from non-hyperbolic shaped regions. There are various regional descriptors suitable for identifying the above mentioned two classes but the following features are found to be best in distinguishing hyperbolic shapes [1].

1. Area: represents the actual number of pixels in the region, and is given by

$$A_R = \sum_{i}^{n} \sum_{j}^{m} R(i,j) \tag{3.17}$$

where A_R is the area of a region which represents the actual number of pixels in that region.

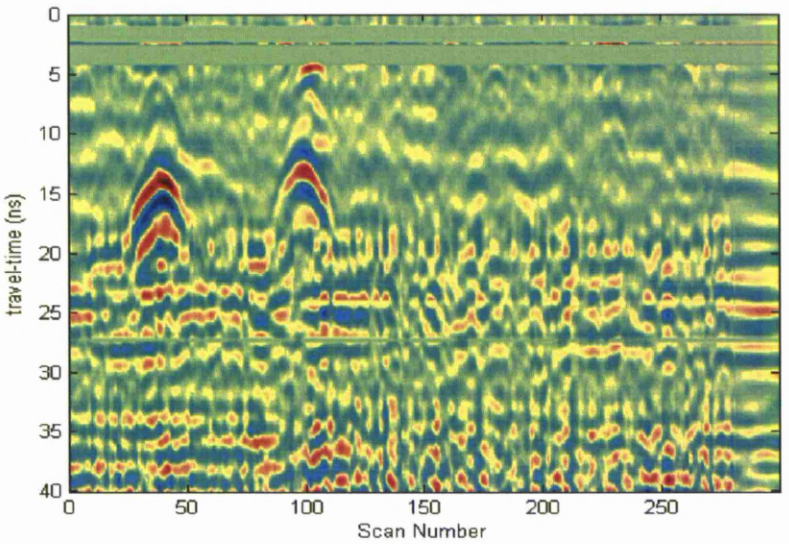

(a) Background removed radargram

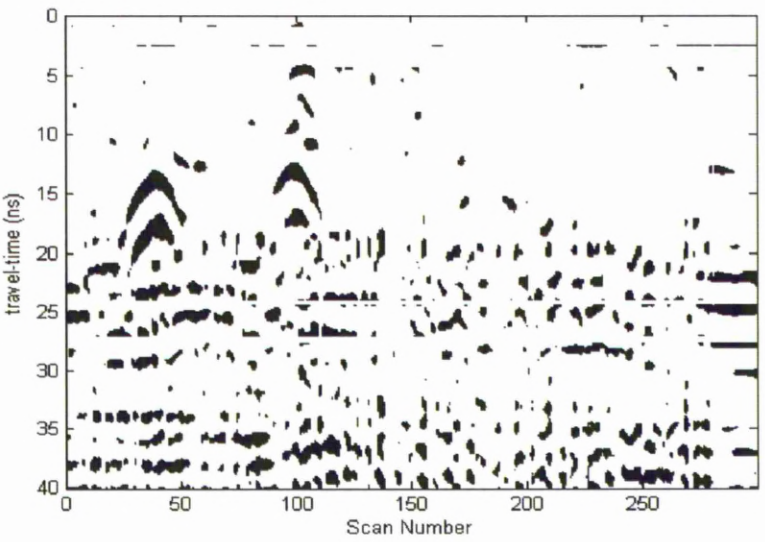

(b) The radargram after applying simple thresholding

FIGURE 3.6: Result of applying thresholding

2. Equivalent Diameter: represents the diameter of a circle with the same area as the region, and is given by

$$ED_R = 2\sqrt{\frac{A_R}{\pi}} \tag{3.18}$$

where ED_R is the equivalent diameter which represents the diameter of a circle with the same area as a chosen region

3. Extent: represents the area of the region divided by the area of the smallest rectangle containing that region, and is given by

$$\text{Extent}_R = \frac{A_R}{A_{rectangle}} \tag{3.19}$$

where $A_{rectangle}$ is given by

$$A_{rectangle} = (i_{max} - i_{min})(j_{max} - j_{min}) \tag{3.20}$$

4. Major axis length: represents the length of the major axis of the ellipse or hyperbola that has the same second moment as the region.

5. Minor axis length: represents the length of the minor axis of the ellipse or hyperbola that has the same second moment as the region.

6. Convex area: represents the area of the smallest convex polygon containing the region.

7. Solidity: the area of the region divided by the area of the smallest convex polygon containing that region.

3.7 Target Classification

After the segmentation techniques, the selected features need to be incorporated into a classification mechanism for the extraction of the hyperbolic features from the data. Neural networks [83] are one of the most successful approaches that have proven to be rapid, accurate and consistent in classing and simplifying complex data.

3.7.1 Neural Networks

Neural networks have the ability to derive meaning from complicated and imprecise data, and they can be used to extract patterns and detect trends that are unnoticeable by either humans or other computer methods. A neural network is trained to be an expert in recognising certain patterns and this expert can then point out similar patterns in new situations.

All artificial neural networks take numeric input and produce numeric output. To capture the essence of biological neural systems, an artificial neuron receives a weighted number of inputs, and responds by producing an activation signal. The activation signal is passed through a transfer function to produce the output of the neuron. This is based on the original model for the neuron proposed by McCulloch and Pitts [84].

To illustrate this, consider a neuron with n inputs $in_1, in_2, \cdots, in_n$ and corresponding weights $w_1, w_2, \cdots, w_n$. The activation net is given by

$$\text{net} = w_1 in_1 + w_2 in_2 + \cdots + w_n in_n = \sum_{i=1}^{n} w_i in_i \tag{3.21}$$

This activation is subjected to a (usually) nonlinear activation function, and the result is the output of the neuron. This transfer function is selected so as to accept input of an unlimited range, and produce output on a restricted range. One common example of such saturating nonlinearity is the *logistic* S-shaped (*sigmoidal*) function shown in Figure 3.7.

$$\text{out} = f_{\text{sig}}(\text{net}) = \frac{1}{1 + e^{-\text{net}}} \tag{3.22}$$

In addition to being bounded, it also has the desirable properties of being both smooth and easily differentiable. The hyperbolic tangent function is very similar to this but with an output range of -1 to 1. Indeed f_{sig} and f_{tan} are related, thus

$$f_{\text{tan}}(\text{net}) = 2f_{\text{sig}}(2\text{net}) - 1 \tag{3.23}$$

Neural networks can be trained using two types of learning strategies one is the supervised and the other is unsupervised learning. In supervised learning, also known as associative learning, the network is trained by providing it with matching output patterns. In unsupervised learning, also known as self organisation, no priori set of classification is provided to the system, and the system learns by detecting statistically salient features of the papulation. Figure 3.8 shows a typical feed forward network where the neurons are arranged in distinct layered topology. The neural network provides a measure of confidence of whether the radargram

sections is from a target or a non target. Radargram sections with measure below a certain threshold are rejected hence reducing the computational burden for subsequent stages significantly.

In a supervised neural network the user assembles a set of data consisting of vector training pairs to train the neural network.The training pair is composed of an input vector and a target vector. The target vectors are the desired outputs of the input

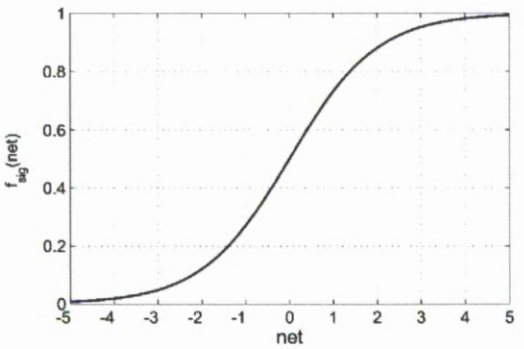

FIGURE 3.7: Sigmoidal transfer function `logsig`

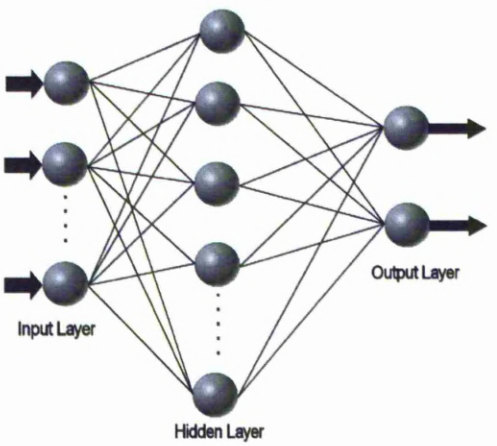

FIGURE 3.8: Feedforward multi-layer perceptron neural network with one hidden layer

data. The training set must be accurate representative samples of the problem. The network is then trained using a supervised learning algorithm that adjusts the network weights according to the data such that the error is minimised. After the training the network would have learned how to model the function that could relate the input to the output variables and can be used for predictions on the same lines where the output is unknown.

The features extracted in the previous sections can be used to train a neural network. A simple example would be a three layer feed forward neural network trained using back propagation algorithm. The time-series, spatial first order or regional feature methods can be used to train the network and if trained properly the neural network is able to classify features representing targets and non-targets.

3.7.2 Double Stage Classifiers

In a double stage classifier two feature extraction techniques that have been previously discussed are combined together in order to get optimum results. B-scan statistics and regional feature techniques are combined together to make one such classifier that uses the strong points of both techniques. The radargram is subjected to the classification procedure twice using the B-scan statistics first and then the regional features. The outputs of both methods, known as the resulting mask, can then be compared to each other and the features that have been detected by both techniques are selected while the others are ignored.

This technique required more time as two procedures are used instead of one but since both the techniques are quite fast in their own perspective a tradeoff is made

since the robustness of the two methods combined is far more than individual techniques.

3.8 Image Reduction

In practical GPR data, the area of interest is only a small portion. Therefore, the segmentation and classification techniques are implemented to point out the target reflections. Once these regions have been selected they need to be isolated and the rest of the data is discarded. The image reduction process performs this task.

Image reduction is performed on the binary mask which is the result of the segmentations and classification process as shown in Figure 3.9. The pixels of the areas of interest are set to one and the rest of the data is set to zeros. When this mask is multiplied to the original data only the region of interests will remain with their original intensities and the rest of the data is discarded. Figure 3.10 shows the multiplication result and how the processing area is just reduced to the area of interest.

3.8.1 Edge Detection

Edge detection is used to find the boundary of the shape in order to perform further detection and characterisation of the desired shape. Edge detection finds the edges by locating the abrupt intensity changes associated with the edges of the reflections. Several edge detection techniques can be found in image processing literature [70]. In GPR data processing most researchers use less sophisticated and

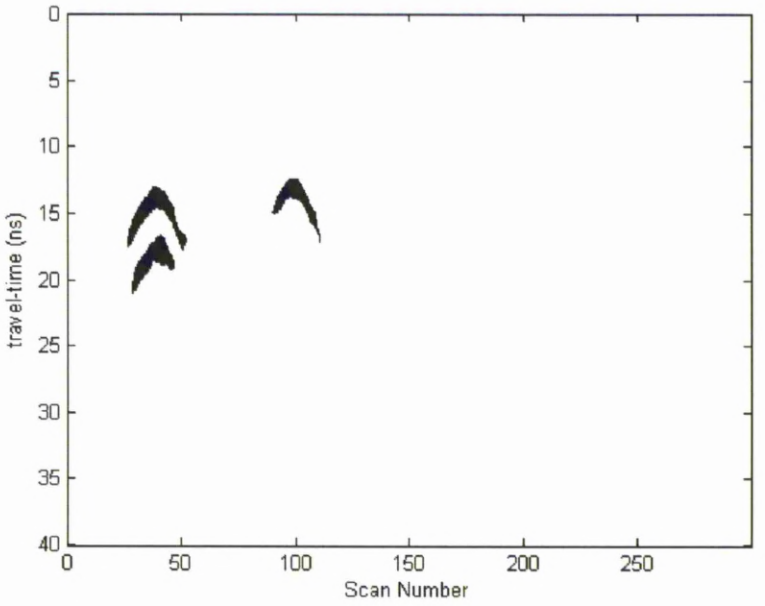

FIGURE 3.9: Binary mask resulted from regional-features classification method

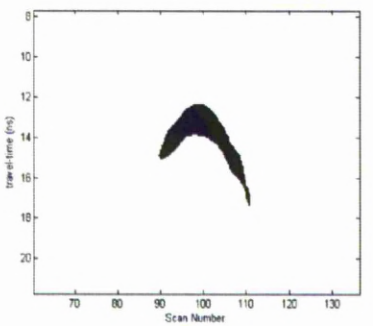

FIGURE 3.10: Sectioned out region of interest for further processing

simple techniques and hence these methods lack efficiency and drawbacks caused by noise and other effects of sub-surface surveys.

Nagashima [19], for instance simply assigns values of $+1$ and -1 to all the peaks

and troughs in the image, while Sato [51] takes this one step further and "extrapolates" in the vicinity of each local maximum in order to locate continuous edge peaks corresponding to wavefront crests.

The present regional feature techniques short cut extra processing as the results are already separated regions, and not windowed areas of mixed regions, but these hyperbolas would require additional processing. The hyperbolas in GPR data are not perfect hyperbolas. Their shape is usually distorted because of various factors such as system noise, subsurface layers complexity and resolution and quality of reflections from the target. Therefore, the already detected edges would need edge processing that involves regions completion, also known as hyperbola completion and skeletonisation.

3.8.1.1 Region Completion

As discussed above, in some GPR cases, the extracted signature is not a perfect hyperbola and some parts of the hyperbola are missing. These regions need to be completed for further processing.

This procedure is performed by checking the hyperbola for symmetry. The Apex of the hyperbola is considered to be the mid point of the symmetry axis. If symmetry does not exist then the shortest side is located using a horizontal search. Once located a part from the longer side which starts at the same horizontal point is copied and the last stage required both sides to be mirrored. The hyperbola completion process can be seen in Figure 3.11.

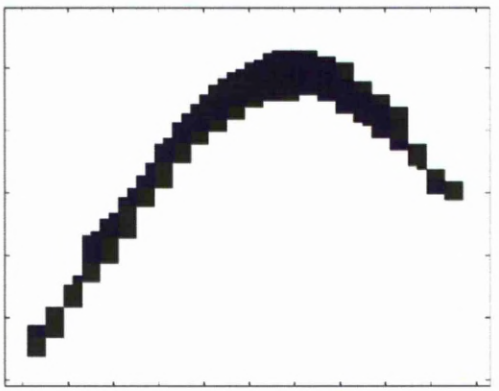

(a) Incomplete hyperbolic region

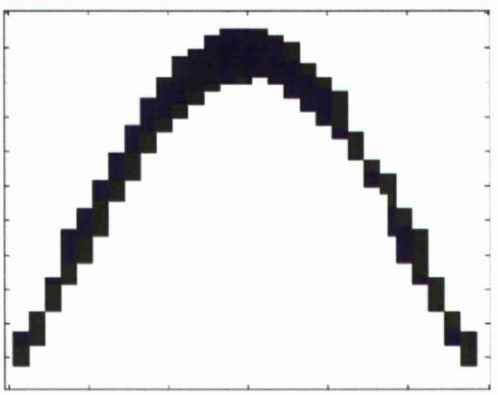

(b) Completed region

FIGURE 3.11: Region completion process

3.8.1.2 Skeletonisation

The skeletonisation algorithm extracts one-pixel thick segments out of the detected hyperbolic region. This is performed by first multiplying the completed region to the original data in order to get the original pixel values for that region. A vertical search is performed from left to right through the columns to obtain pixel value of each column. These pixel values are then replaced by a single value that represents the mean of the values. Skeletonisation performs extremely well when applied to gradient images, the results are shown in Figure 3.12.

3.9 Hyperbola Fitting

There are a variety of fitting procedures, some are Hough transform based approaches that are not only computationally expensive but have a high time cost as well, others are least square fitting to general conics and rejecting non-hyperbolic fits, which are much faster and give good performance when applied to data that has hyperbolic shapes and they can also be refined using iterative procedures [30]. Unfortunately, they do not characterise the hyperbola in terms of major and minor axis that is needed in the hyperbolic model used in this study.

Shihab [1] used a novel fitting technique developed from Fitzgibbons ellipse-specific direct least square fitting technique [30] that uses constrained least square method for specifically fitting hyperbolae. The most important feature of the technique is its ability to estimate the hyperbolic parameters.

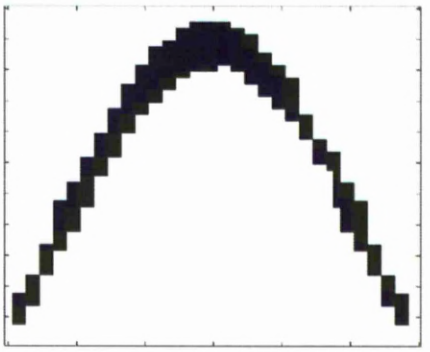

(a) Detected region

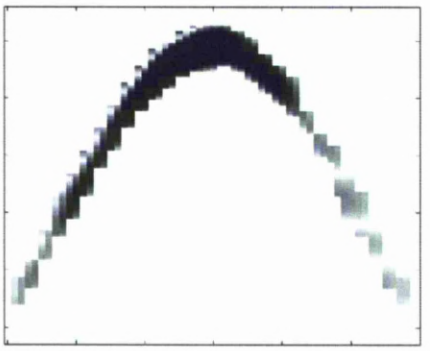

(b) Retrieving original pixels values

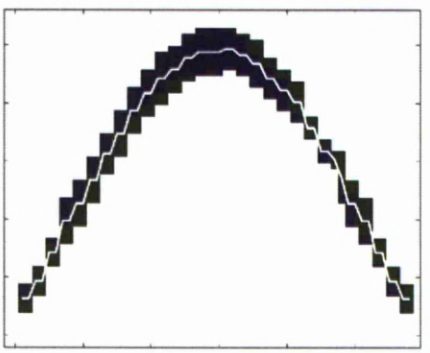

(c) Skeletonisation result

FIGURE 3.12: Skeletonisation process

3.10 Summary

This chapter has addressed the post processing tasks that are necessary for an automatic hyperbolic signature extraction procedure from GPR data. A number of techniques involving background removal, distance normalisation, various segmentation and classification techniques, image reduction and fitting methods were discussed. Techniques that could be applied to time-series discrimination and B-scan pattern recognition were also shown.

Although time-series discrimination techniques can perform well in distinguishing targets from non targets, but on the expense of high time consumption, thus it is impractical to involve them in a near real time automatic application where a large amount of GPR data is involved. Also, they would not perform well in conditions where data has greater variability and where target zones might have more subtle properties. Higher order statistic would perform better in such conditions but at the expense of more time cost. The region completion techniques would be a big improvement in the automatic segmentation process especially where hyperbolic shapes need to be extracted. This technique has many advantages such as its speed, accuracy, robustness and noise immunity.

This chapter also discusses a fitting technique that can be applied on hyperbolic signatures in order to extract hyperbolic parameters in terms of major and minor axis. These values are required for interpretation of the target parameters. The model that incorporates these values is discussed in Chapter 5.

Chapter 4

Advanced Post Processing

The post processing techniques discussed in Chapter 3 are able to successfully extract target reflections from GPR data. However, in order to get automated, real time and more accurate data interpretation, further improvements are required. This chapter addresses the three critical and major sections of the post processing techniques which are background and clutter removal, hyperbola classification, and hyperbola fitting. Novel techniques have been developed in order to get more accurate results. These techniques are called Eigen-based background removal, target classification using MFCC's, combined hyperbola fitting technique and angle-based 3D line detection for parameter correction.

4.1 Introduction

Clutter and background removal is the first step of GPR data processing. It is nearly impossible to extract target reflections from data having clutter and

background effect. Although there exist many background removal techniques, a novel Eigenvalue based background removal technique has been developed and used in this study. This method produces more refined and clear GPR images than traditional methods. The methodology is discussed in detail in the remaining sections along with an overview of traditional background removal techniques.

The second most important aspect of GPR data processing is the segmentation and classification of the hyperbolic signature. The approach used in this study is completely novel to GPR data and it involves extraction of Mel Frequency Cepstral Coefficients (MFCCs) and polynomial coefficients from the radar images and using neural networks to classify the target signatures.

The classified hyperbola is then subject to hyperbola completion, thinning and skeletonisation. Afterwards, it is fitted with a hyperbolic fitter in order to extract the hyperbolic parameters. There are various hyperbola fitting methods, but some are computationally expensive, some do not characterise the hyperbola in terms of major and minor axis which are the key components in the mathematical model for estimation of target parameters and others are able to determine the major and minor axis, however, their performances deteriorate over a wide variety of hyperbolas. In this study two distinct hyperbolic fitters have been combined to give accurate results. The combined effect of these fitters has the ability to determine the hyperbolic parameters for a wide range of hyperbolas. The results have been verified on simulated data and successfully tested on real GPR hyperbolas. Even though the proposed method uses two hyperbolic fitters instead of one and would consume slightly more time, the results are much more precise and accurate. Therefore, making the proposed fitting solution an important step towards correct GPR target parameter estimation.

4.2 Eigen Based Background Removal

The proposed method has two steps. The first step takes into account the singular value decomposition (SVD) of the GPR radargram and uses the Eigen images corresponding to the highest and the lowest Eigenvalues of the covariance of the original image. In the second step the output of the first step is subject to mean subtraction.

The SVD is the factorization of a rectangular matrix X into orthogonal matrices given as $X{=}UDV^T$, where T is the transpose and D stands for a diagonal matrix whose positive entries are the singular values of X, U and V are two identity matrices [85]. These values are distributed along the main diagonal in descending order and are equivalent to the positive square root of the Eigen values of the covariance matrix given by XX^T and X^TX [69]. Freire and Ulrych et al [86], [87] showed the application of singular value decomposition in seismic profile but Ulrych and Cagnoli explained its application on GPR data in [69] as Equation 4.1

$$X = \sum_{i=1}^{r} \sigma_i \mu_i \vartheta_i \tag{4.1}$$

where r is the rank of X, μ_i is the *ith* Eigen vector of X^TX and ϑ_i is the *ith* Eigen vector of XX^T σ_i is the *ith* singular value of X and μ_i σ_i is an mXn matrix of unitary rank called the *ith* Eigen image of X. The highly correlated parts of the GPR traces form the flat reflections in the profile and the high-pass Eigen images act as filters that discard these flat reflections. Therefore, the energy of the Eigen images appears to be an index of the waviness of the reflections. The low pass Eigen images act as filters that suppress the clutter as the clutter seem to saturate in the background. The target reflections are also slightly affected by

this saturation effect, but results indicate that the hyperbolic shape is still intact and much more visible than the background.

The proposed technique produces two images, one is from subtracting the normalised highest Eigenvalue image from the normalised original image and the other one is from the normalised lowest Eigenvalue image subtracted from the normalised original image. The final output is the dot product of the two images having their combined effect. Mean subtraction is then applied onto this image.

4.2.1 Eigen Background Removal Methodology

Let us assume $\boldsymbol{X}$ is a GPR data image of the rank r. The first step is to find the covariance of X given by Equation 4.2

$$C = \mathbf{X}.\mathbf{X}^T \tag{4.2}$$

C is a positive symmetric covariance matrix of X, therefore there must be an orthogonal matrix L that would satisfy Equation 4.3

$$\mathbf{L}^T\mathbf{X}\mathbf{L} = \mathbf{M} \tag{4.3}$$

where diagonal values of $\boldsymbol{M}$ denote the Eigenvalues of the covariance matrix. In the next step the Eigen images *u1* and *u2* of the covariance matrix X^TX and XX^T respectively are calculated, the column vectors of these Eigen images are the Eigen vectors corresponding to the Eigenvalues. The singular value decomposition value is stored in a vector S. The row of the maximum Eigenvalue in the Eigen matrix $\boldsymbol{M}$ is found and the corresponding Eigen column vectors are extracted from the

Eigen images *u1* and *u2* which have been sorted out in ascending order. The same is done for the singular value decomposition vector S. An image can now be created by the product of these three given in Equation 4.4

$$P = S(val) \times u1(:, val) \times u2(:, val)^T \tag{4.4}$$

Where *val* is the row of the maximum Eigenvalue in the Eigen matrix $\boldsymbol{M}$. It can be seen that this image P constitutes most of the background noise with the effect of ground coupling, direct wave and clutter. Normalised value of P subtracted from normalised value of X gives us one of the output "out1", the same procedure is repeated but in the second case the Eigen images *u1* and *u2* are sorted out in descending order and instead of the highest Eigenvalues the algorithm searches for the lowest Eigenvalues and constructs another output image say *P2*. Subtracting the normalised value of *P2* from the normalised value of X gives the second output "out2". The dot product of both the output images is taken and the resulting image is the required background removed output image.

This process serves three purposes. First of all, it reduces most of the clutter within the image refining the results. Secondly, if there are any horizontal reflections remaining in the image, their values are within the image mean range, and applying the mean subtraction removes these residual effects. Thirdly, the proposed method is able to produce an image in which the positive and negative peak reflections from the target are easily distinguishable from the background. Therefore, when the resulting image is passed on to the segmentation and classification stage for the extraction of the target signature, the results will be more accurate and efficient. The complete background removal process is given in the flowchart shown in Figure 4.1.

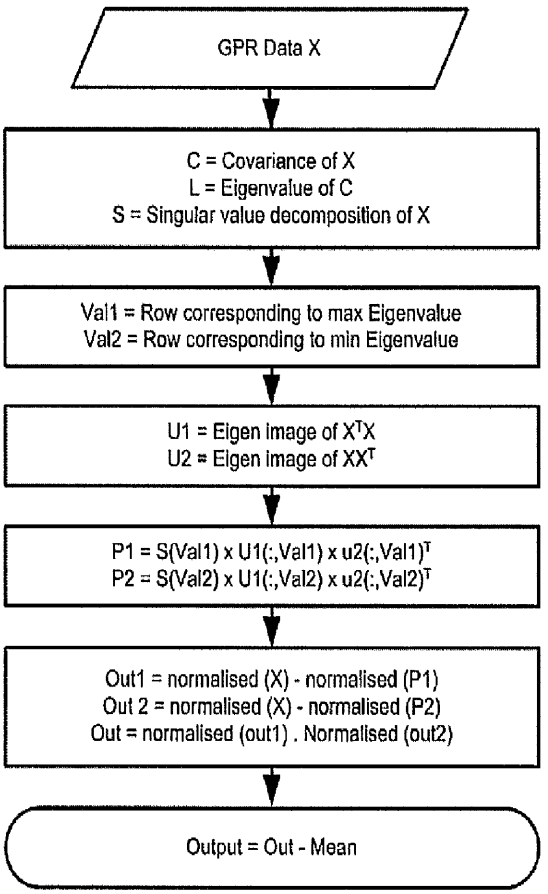

FIGURE 4.1: Flowchart of background removal process

4.2.2 Results for Eigen Background Removal

The proposed method has been applied to a number of different data sets and a few examples are shown below. Figure 4.2(a) is the original GPR radargram with background and target signature, Figure 4.2(b) is the result after conventional background removal technique applied, Figure 4.2(c) is the output of the proposed background removal technique. It can be seen that the proposed method has removed the coupling effect and the clutter effect is significantly reduced as compared to the conventional background removal method. It can also be seen that in the proposed method the positive and negative reflections from the target

are clearly highlighted therefore can easily be extracted in the segmentation and classification process.

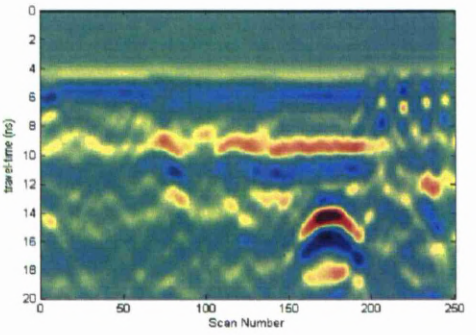

(a) Original Image with background

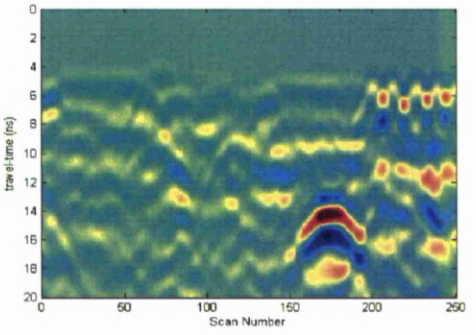

(b) Image from subtractive background removal

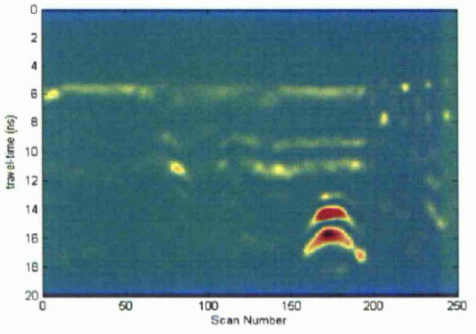

(c) Image after proposed background removal

FIGURE 4.2: Background removal process on actual GPR data

Gray-scale is a much better form of visualizing underground utility data therefore another example is shown, the original gray-scale radargram is in Figure 4.3(a), the result from traditional background removal is shown in Figure 4.3(b) and Figure 4.3(c) shows the result from the proposed background removal technique. It can be seen that the proposed method has not only produced a refined output that has a reduced clutter effect but the target reflections are also clearly seen. On the other hand, the traditional background removal technique is able to remove the horizontal reflection completely, but the target reflections are not as clear and are also not very distinct from the background, hence, making it difficult to extract in the later processing stages.

Eigen based background removal needs the input radargram to be a square matrix. Practically this is not the case, the radargram can be of different dimensions based on the length of the scan. In order to solve this issue the radargram needs to be divided into square images and the process needs to be applied separately on each section. Afterwards the radargram can be combined together to form a single image. This test has been done on the radargram shown in Figure 4.4 and it is seen that the results are the same.

The proposed method has been applied to a number of GPR radargrams and the results are compared to mean subtractions background removal. Table 4.1 gives the signal-to-clutter ratio in dB of the results obtained from ten different GPR radargrams. It can be seen that the results of the proposed method have a much higher signal to clutter ratio as compared to the mean subtraction method.

The proposed method has been tested on a variety of data sets collected throughout the test site. The collected data is of pipes of different sizes buried at different depths. The medium hosting the targets is also changing from place to place.

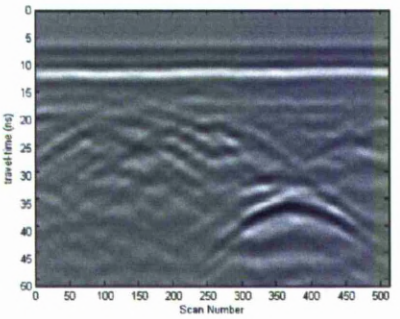

(a) Original gray-scale Image with background

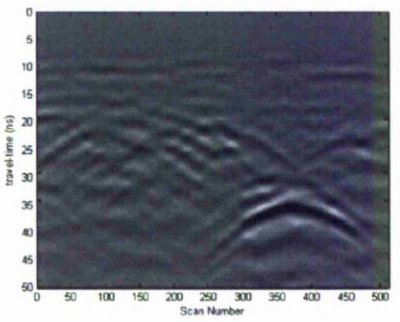

(b) Gray-scale image from subtractive background removal

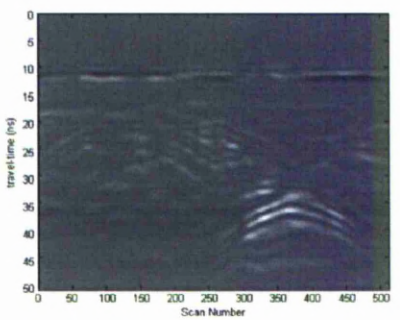

(c) Gray-scale image after proposed background removal

FIGURE 4.3: Background removal process in Gray-scale

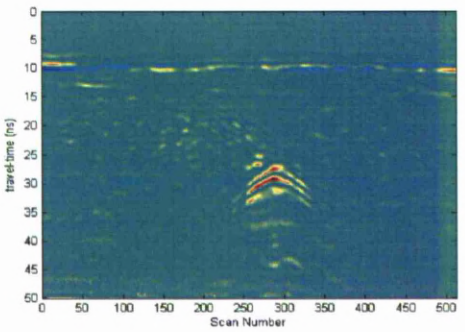

(a) Results from first half of radargram

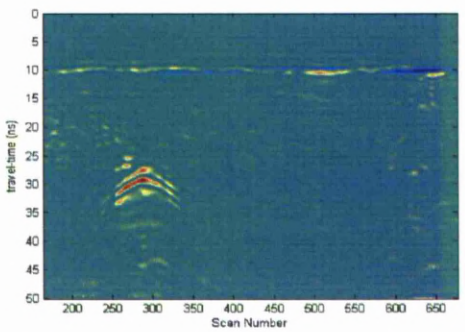

(b) Results from second half of radargram

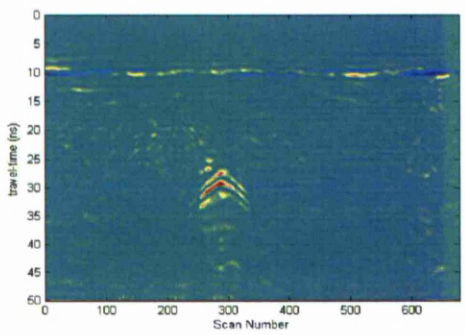

(c) Both radargrams combined together

FIGURE 4.4: Background removal process on a non-square image

TABLE 4.1: Signal-to-clutter ratio in dB for the original image, mean subtraction and proposed method

S/No.	Original Image	Mean Subtraction	Proposed Method Stage 1	Proposed Method Stage 2
1	20.1258	34.4940	31.3656	41.7189
2	21.3786	28.7940	29.7783	31.966
3	18.3589	32.1901	35.4819	45.6320
4	19.2912	30.5295	34.5855	41.2069
5	20.6911	29.3671	33.3536	37.4747
6	20.0907	30.8404	33.4886	37.2865
7	21.8055	28.2373	33.2771	39.9249
8	21.5027	28.5775	33.8287	41.3551
9	20.3346	28.5148	34.4586	40.7710
10	21.3619	28.4460	31.9787	33.5691

Data had been collected for areas with different surfaces such as concrete tiles, granite tiles, grassy loans and asphalt roads. In nearly all cases the proposed method shows a higher signal-to-clutter ratio than the mean subtraction method. However, in certain cases where the target reflection is very weak the result from stage 2 of the proposed method saturates the target reflection to the background along with the clutter which makes the target extraction very difficult. In such cases it is advisable to stop the process at stage one.

4.3 Proposed Classification Approach

The dependence on object shapes for underground utilities detection has several limitations as mentioned in the previous section. In this section, a new approach for detection which does not depend on geometrical shapes is presented. The proposed approach has two phases; a training phase and a testing phase. A database of regions containing target signatures is used in the training phase. Different hyperbolic shapes originating from potential targets within real GPR data are extracted. After background removal, normalisation and conversion into 1D signal, the MFCC and polynomial features are extracted from them in the DCT domain, which are then used to train a neural network. In the testing phase, a background removed normalised B-scan is thresholded to a binary image, the resulting blobs are passed through a miniature deletion filter to eliminate the very tiny targets and a boxed region is extracted from the B-scan of the remaining blobs. This creates a number of regions of both targets and non-targets with their original intensities. Each region is converted into a 1D signal by lexicographically ordering and features are extracted from each blob, a feature matching step is performed

to decide whether these features belong to a target or not. A schematic diagram of the steps of the proposed detection system is shown in Figure 4.5.

The time and space complexity of the algorithm depends upon the size of the data and the number of blobs resulting from the miniature deletion filter.

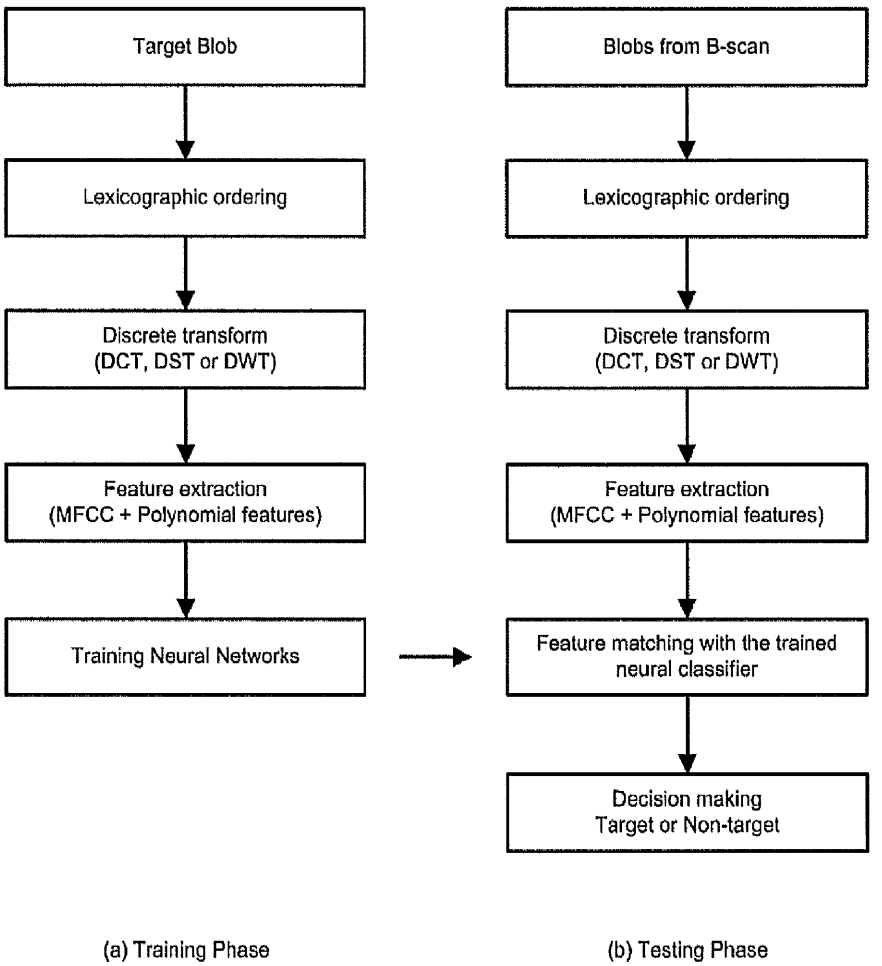

FIGURE 4.5: Schematic diagram of the proposed detection system

4.4 MFCC Approach

MFCC is widely used in speaker identification in sound processing, these features are robust to noise and insensitive to time shifts signals. As a result, there is no need for registration of images, and the extracted features have been found to be very suitable for underground utility detection in the presence of degradation. MFC is a representation of short term power spectrum of a sound based on a linear cosine transform on a non linear mel scale of frequency. Details of use of MFCC in sound processing can be seen in [88], [89], [90]. It contributes in identifying speaker even in very noisy and low level data thus making it a robust technique. In this study the GPR images are converted into 1D signals and are treated as speech signals. In the following subsections the extraction of MFCC and polynomial coefficients is discussed in detail.

4.4.1 Cepstrum Analysis

Cepstrum can be seen as the rate of change in different spectral bands. In order to use power spectrum as a feature for representing human voice the spectrum is first transformed using mel scale to get mel frequency cepstrum. The power cepstrum of a signal $x[n]$ is given by the following equation

$$P_{x[n]} = |F(\log(|F(x[n])|^2)|^2 \tag{4.5}$$

where F is the Fourier transform.

A complex cepstrum of a signal $x[n]$ is defined in terms of its Z-transform and is given by

$$C_{x[n]} = Z^{-1}\log(Z[x[n]]) \tag{4.6}$$

The process of complex cepstrum and power cepstrum calculation are shown in Figures 4.6 and 4.7

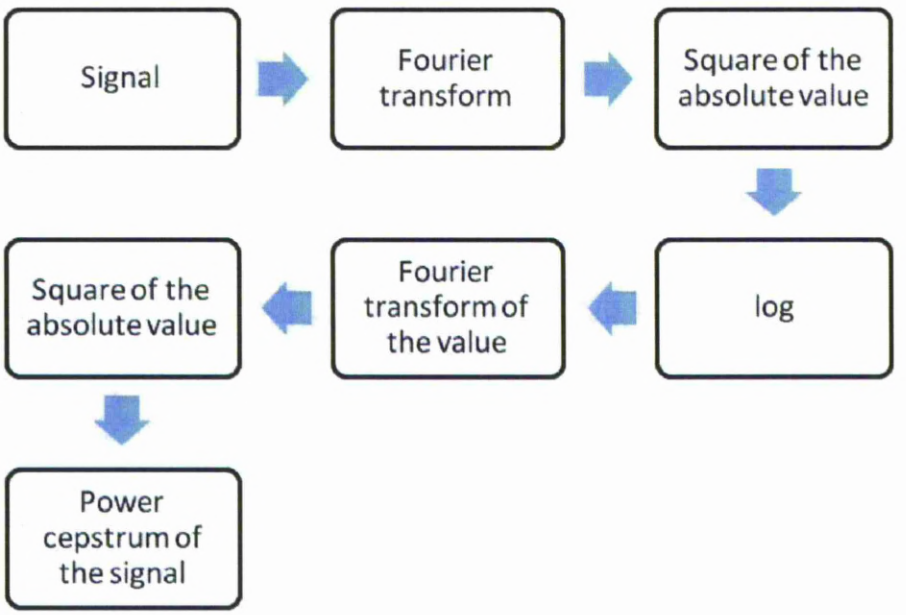

FIGURE 4.6: Power cepstrum calculation process

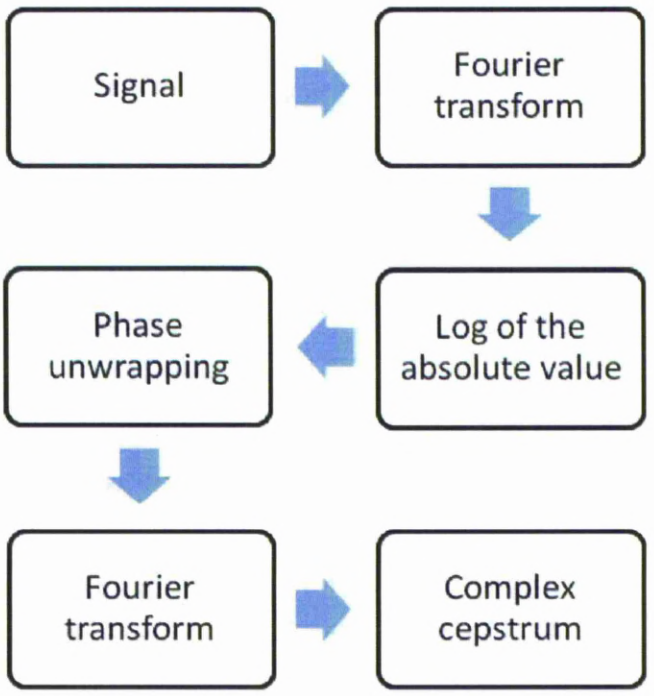

FIGURE 4.7: Complex cepstrum calculation process

4.4.2 MFCC Extraction

the MFCC's are extracted by transforming the image into 1D signal using lexicographic ordering. The input signal is framed and windowed then the Fourier transform is taken and the magnitude of the resulting spectrum is warped by the Mel-scale. The log of this spectrum is then taken and the DCT is applied instead of the IDFT stage for increasing the computational efficiency [91], [92]. The Mel scale is a perceptual scale of pitches and the following equations are used to convert from Frequency (Hz) to mel (m):

$$m = 2595 \log_{10}\left(\frac{f}{700} + 1\right) \tag{4.7}$$

$$m = 1127 \log_{e}\left(\frac{f}{700} + 1\right) \tag{4.8}$$

To convert back into Hz

$$f = 700\left(10^{\frac{m}{2595}} - 1\right) \tag{4.9}$$

$$f = 700\left(e^{\frac{m}{1127}} - 1\right) \tag{4.10}$$

The calculation of the MFCCs is based on the short term analysis, and thus for each frame, the MFCCs vector is computed. In this process, the 1D signal is pre-emphasised to remove blurring effects which might affect the image. The pre-emphasis is implemented by a first order finite impulse response (FIR) filter of the form [93]:

$$H(z) = 1 - az^{-1} \tag{4.11}$$

where $0.9 \leq a \leq 0.99$.

The 1D signal must first be broken up into small sections. These sections are called frames and the motivation for this framing process is the quasi-stationary nature of the 1D signals. However if we examine the signal over discrete sections which are sufficiently short in duration, then these sections can be considered as stationary and exhibit stable characteristics [91], [92]. To avoid loss of information, frame overlap is used.

For each frame, a windowing function is usually applied to increase the continuity between adjacent frames. Common windowing functions include the rectangular window, the Hamming window, the Blackman window and flattop window. Windowing in time domain is a point wise multiplication of the frame and the window function. According to the convolution theorem, the windowing corresponds to a

convolution between the short term spectrum and the window function frequency response. A good window function has a narrow main lobe and low side lobe levels in its frequency response. The most commonly used window function is the Hamming window which defined as [91], [92]:

$$w_H(n) = 0.54 - 0.46\cos\left(\frac{2n\pi}{N-1}\right) \tag{4.12}$$

where n=0, 1, ..., N-1, and N is the number of frames the signal has been broken into.

The DFT of a windowed frame of the 1D signal is computed to obtain the magnitude spectrum. The DFT is mathematically defined as [91], [92]:

$$S(k) = \sum_{n=0}^{N-1} s(n)e^{\frac{-j2\pi}{N}kn} \tag{4.13}$$

where $s(n)$ is a time sample of the windowed frame.

The IDFT is defined as [91], [92]:

$$s(n) = \frac{1}{N}\sum_{k=0}^{N-1} S(k)e^{\frac{j2\pi}{N}kn} \tag{4.14}$$

The magnitude spectrum is frequency warped in order to transform the spectrum into the Mel-frequency scale. The Mel-frequency warping is performed using a Mel-filter bank composed of a set of bandpass filters with constant bandwidths and spacings on the Mel-scale. The bank consists of one filter for each desired Mel-frequency component, where each filter has a triangular filter bandpass frequency response. The triangular filters are spread over the entire frequency range from zero to the Nyquist frequency. The number of filters is one of the parameters which

affect the recognition accuracy of the system. The last stage involves performing a DCT on the log of the Mel-spectrum. If the energy of the *mth* Mel-filter output is $\tilde{S}(m)$, the MFCCs will be given as follows [91], [92]:

$$c_j = \sqrt{\frac{2}{N_f}} \sum_{m=1}^{N_f} \log(\tilde{S}(m)) \cos\left[\frac{j\pi}{N_f}(m - 0.5)\right] \tag{4.15}$$

where j= 0,1,. . . . . ., J-1 , with J being the number of MFCCs, N_f is the number of Mel-filters and c_j are the MFCCs. The number of the resulting MFCCs is chosen between 12 and 20, since most of the signal information is represented by the first few coefficients. The 0th coefficient represents the average log energy of the frame.

Figure 4.8 shows the MFCC calculation process from a 2D image.

4.4.3 Polynomial Coefficient Extraction

The MFCCs are sensitive to mismatches or time shifts between training and testing data. Therefore, other coefficients need to be added to the MFCCs in order to reduce the sensitivity. Polynomial coefficients can be used to help increase the similarity between the training and testing signals. If each MFCC is modeled as a time waveform over adjacent frames, the polynomial coefficients can be used to model slope and curvature of this time waveform for each MFCC. Therefore, adding these polynomial coefficients to the MFCC vector will be helpful in reducing the sensitivity to any mismatch between the training the testing data [94].

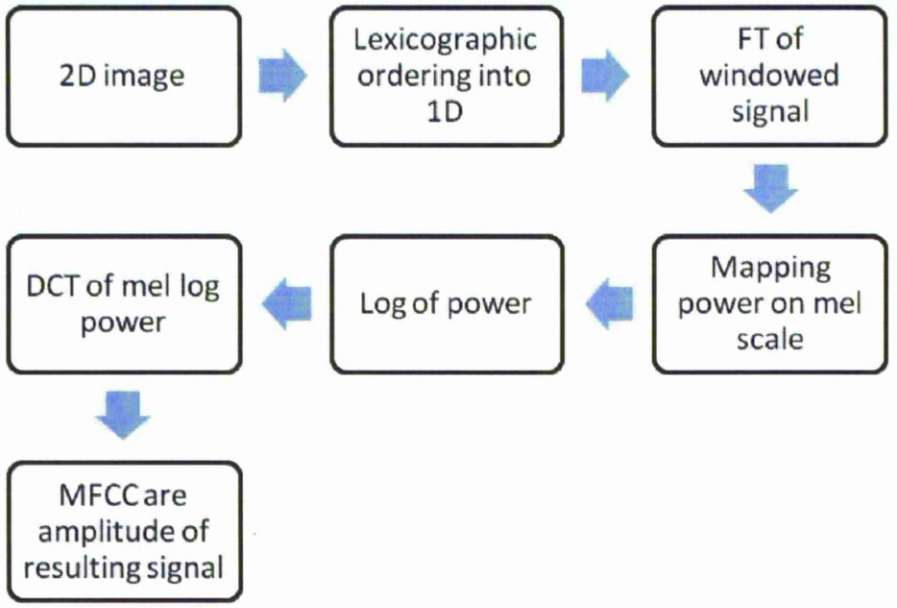

FIGURE 4.8: Process showing MFCC calculation

To calculate the polynomial coefficients, the waveform of the cepstral coefficients are expanded by the orthogonal polynomials. The following two orthogonal polynomials can be used [94]:

$$P_1(\iota) = \iota - 5 \tag{4.16}$$

$$P_2(\iota) = \iota^2 - 10\iota + \frac{55}{3} \tag{4.17}$$

To model the shape of the MFCC time function, a nine-element window at each MFCC is used. Based on this window assumption, the polynomial coefficients can

be calculated as follows [94]:

$$a_j(t) = \frac{\sum_{i=1}^{9} P_1(\iota) c_j(t+\iota-1)}{\sum_{i=1}^{9} P_1^2(\iota)} \tag{4.18}$$

$$b_j(t) = \frac{\sum_{i=1}^{9} P_2(\iota) c_j(t+\iota-1)}{\sum_{i=1}^{9} P_2^2(\iota)} \tag{4.19}$$

where $a_j(t)$ and $b_j(t)$ are the slope and curvature of c_j in the t^{th} frame respectively. The vectors containing all c_j, a_j and b_j are concatenated to form a feature vector.

4.4.4 Feature Matching Using Neural Networks

The classification step in the proposed detection approach is in fact a feature matching process between the features of a new image and the features saved in the database. Neural Networks are widely used for feature matching. Multi-layer perceptrons (MLPs) consisting of an input layer, one or more hidden layers and an output layer can be used for this purpose [95], [96].

Each neuron in the neural network is characterised by an activation function and its bias, and each connection between two neurons by a weight factor. In this study, the neurons from the input and output layers have linear activation functions and the hidden neurons have sigmoid activation function F(u) = 1/(1+ e-u) . Therefore, for an input vector X, the neural network output vector Y can be obtained according to the following equation [95], [96]:

$$Y = W_2 \times F(W_1 \times X + \mathbf{B}_1) + \mathbf{B}_2 \tag{4.20}$$

where W_1 and W_2 are the weight matrices between the input and the hidden layer and between the hidden and the output layer, respectively, and $\mathbf{B}_1$ and $\mathbf{B}_2$

are bias matrices for the hidden and the output layer, respectively.

Training a neural network is accomplished by adjusting its weights using a training algorithm. The training algorithm adapts the weights by attempting to minimize the sum of the squared error between a desired output and the actual output of the output neurons given by [95], [96]:

$$E = \frac{1}{2}\sum_{o=1}^{O}(D_o - Y_o)^2 \tag{4.21}$$

where D_o and Y_o are the desired and actual outputs of the O^{th} output neuron. O is the number of output neurons. Each weight in the neural network is adjusted by adding an increment to reduce error as rapidly as possible. The adjustment is carried out over several training iterations until a satisfactorily small value of E is obtained or a given number of epochs is reached. The error back-propagation algorithm can be used for this task [95], [96].

4.4.5 Experimental Results on Simulated Data

In this section, several experiments are carried out, on data with simulated noise, to test the performance of the proposed cepstral detection approach. Time and transform domains are used for feature extraction. The degradations considered are additive white Gaussian noise (AWGN), impulsive noise, speckle noise and poisson noise with and without blurring. These degradations are severe cases which are not studied by researchers in the field of underground utility detection. In the training phase of the proposed detection system, a database is first composed. Twenty target images are used to generate this database. The MFCCs and

polynomial coefficients are estimated to form the feature vectors of the database. In the testing phase, similar features to that used in the training are extracted from the degraded target images and used for matching.

The features used in all experiments are 13 MFCCs and 26 polynomial coefficients forming feature vectors of 39 coefficients for each frame of the image. Seven different methods for extracting these features are adopted in the study. In the first method, the MFCCs and the polynomial coefficients are extracted from the time domain signals only. In the second method, the features are extracted from the discrete wavelet transform (DWT) of these signals. In the third method, the features are extracted from both the original signals and the DWT of these signals and concatenated in single feature vectors. In the fourth method, the features are extracted from the discrete cosine transform (DCT) of the time domain signals. In the fifth method, the features are extracted from both the original signals and the DCT of these signals and concatenated in single feature vectors. In the sixth method, the features are extracted from the discrete sine transform (DST) of the time domain signals. In the last method, the features are extracted from both the original signals and the DST of these signals and concatenated in single feature vectors.

A comparison study is held between all these extraction methods for the above mentioned degradation cases, and the results are given in Figures 4.9 to 4.11 for underground utility data. From this comparison, it is clear that the features extracted from the DCT of the 1D signals help in achieving the highest detection probability or recognition rate. This is attributed to the energy compaction property of the DCT, which enables accurate feature extraction from the first frames of the 1D signals after the DCT, which can characterise each signal. It is also

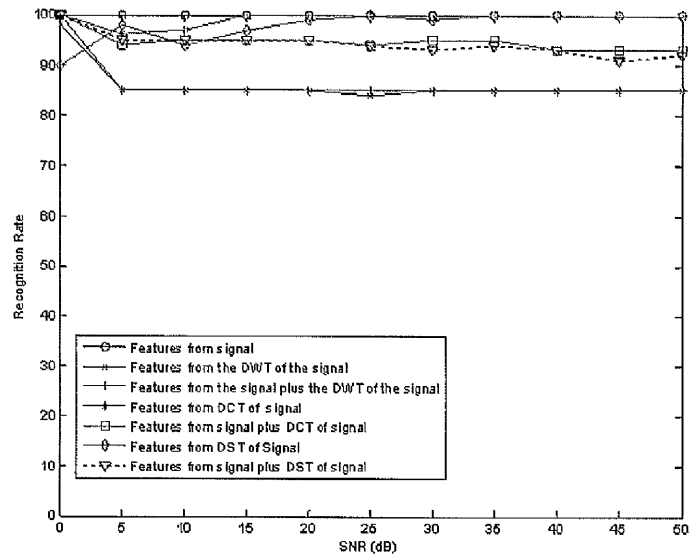

(a) Recognition rate vs. SNR for images contaminated by AWGN

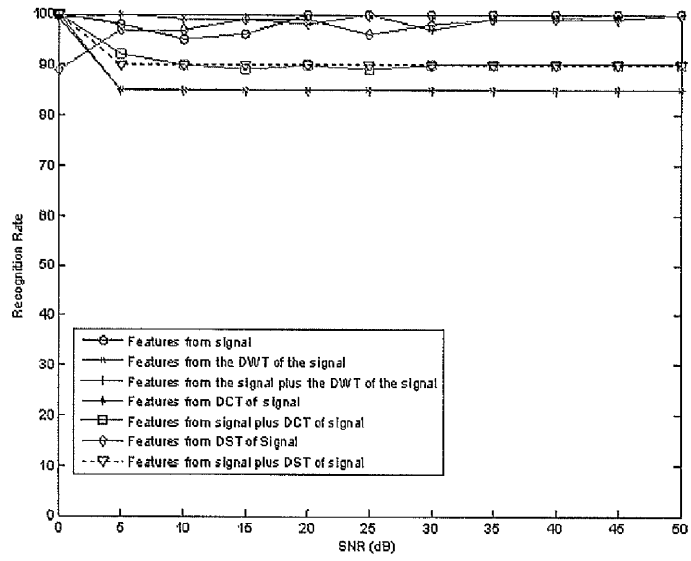

(b) Recognition rate vs. SNR for blurred images contaminated by AWGN

FIGURE 4.9: MFCC Results a

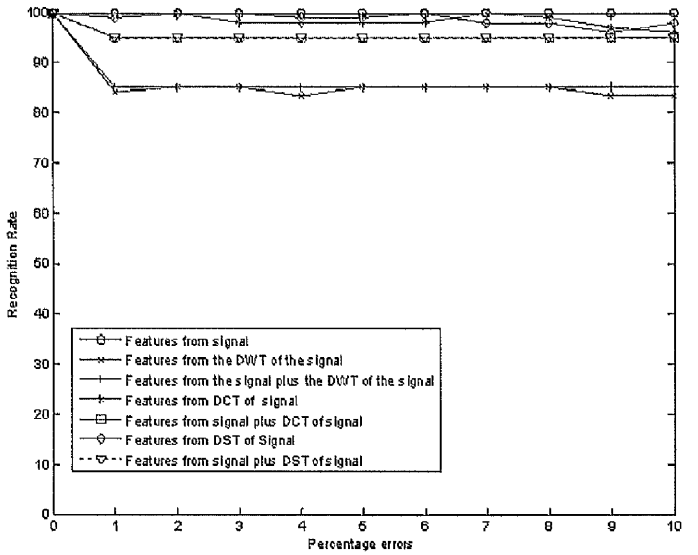

(a) Recognition rate vs. the percentage error for images contaminated by impulsive noise

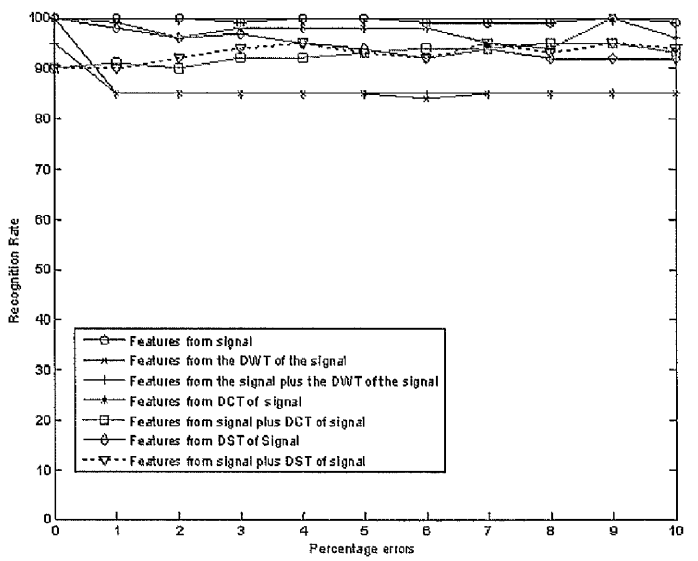

(b) Recognition rate vs. the percentage error for blurred images contaminated by impulsive noise

FIGURE 4.10: MFCC Results b

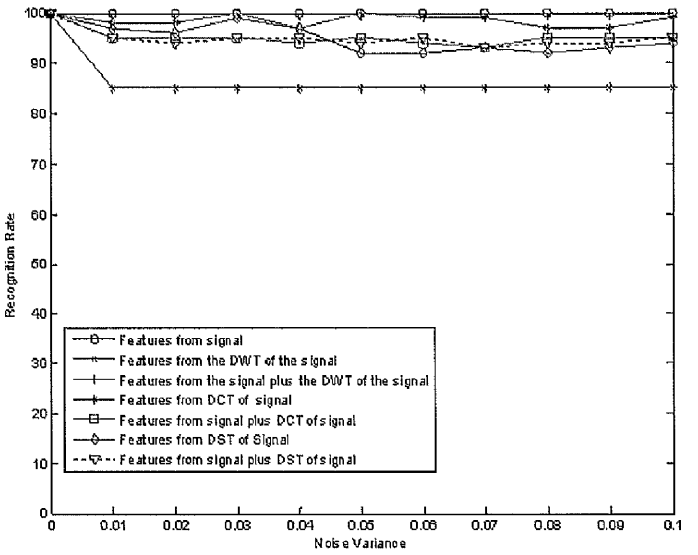

(a) Recognition rate vs. the noise variance for images contaminated by speckle noise.

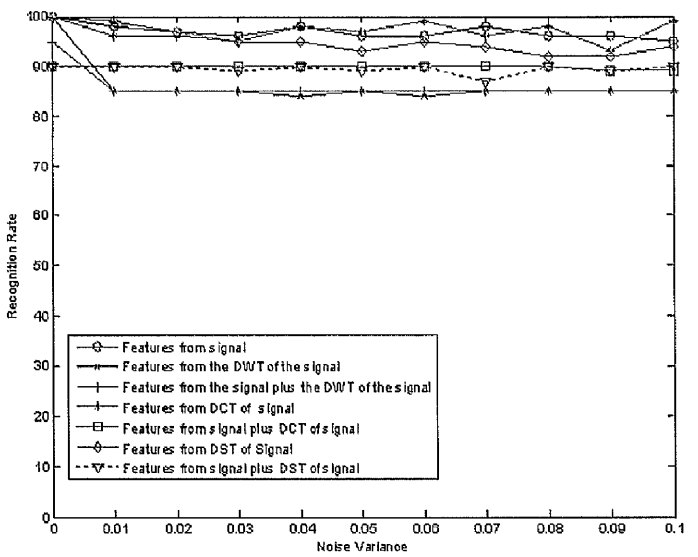

(b) Recognition rate vs. the noise variance for blurred images contaminated by speckle noise

FIGURE 4.11: MFCC Results c

clear that a recognition rate of about 100% can be achieved with the proposed approach at low degradation cases.

4.4.6 Experimental Results on GPR Data

The proposed target detection approach cannot be applied directly to raw GPR data. The data needs to undergo certain processing stages before the data is ready to be classified. These stages are described in the following sections followed by the results obtained by applying the proposed method on real GPR data.

4.4.6.1 Pre-processing

The raw radargram shown in Figure 4.12 needs to go through certain pre processing stages before it could be classified using MFCC. The radargram shown in Figure 4.13 is the result of Eigen based background removal. The data is then converted into a binary image by applying an adaptive threshold, hence retaining the significant reflections as shown in Figure 4.14.

The binary image contains of many blobs, most of them are very small in size that would not qualify as a target, but when they are subjected to a classification procedure they would consume nearly equal amount of time. Classification is the most time consuming process in GPR data processing and is considered as a bottle neck in the time consumption for a near real time system. The data is thus passed through a miniature deletion filter before the classification is performed. This filter determines the length and height of each blob. There is a size limit which is set by the user depending upon the resolution of the image. If a blob is smaller

then the filter size it is rejected from the data set. The binary image shown in Figure 4.14 has a total of 419 blobs, after applying the miniature deletion filter this count comes down to 43 as shown in Figure 4.15.

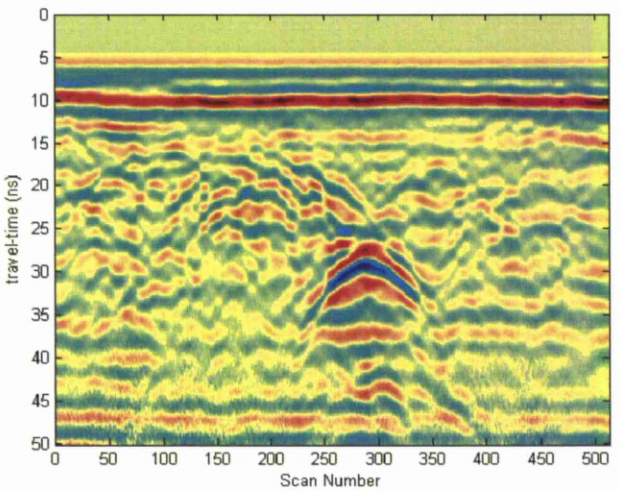

FIGURE 4.12: Raw GPR Data

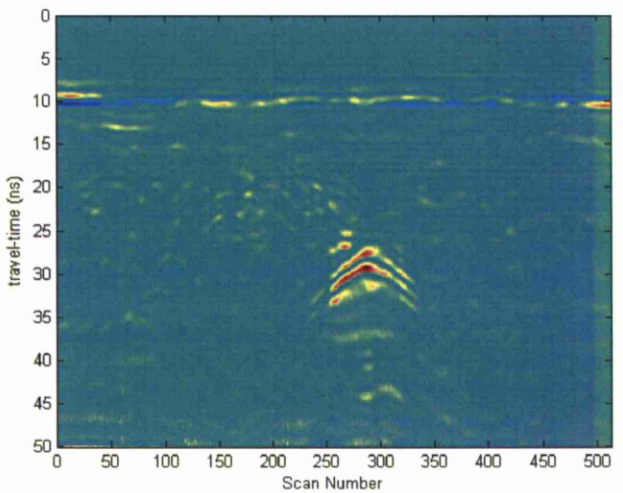

FIGURE 4.13: GPR data after background removal

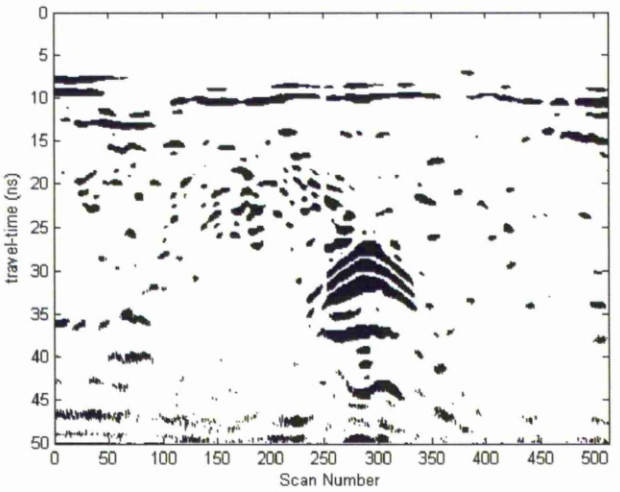

FIGURE 4.14: Binary image

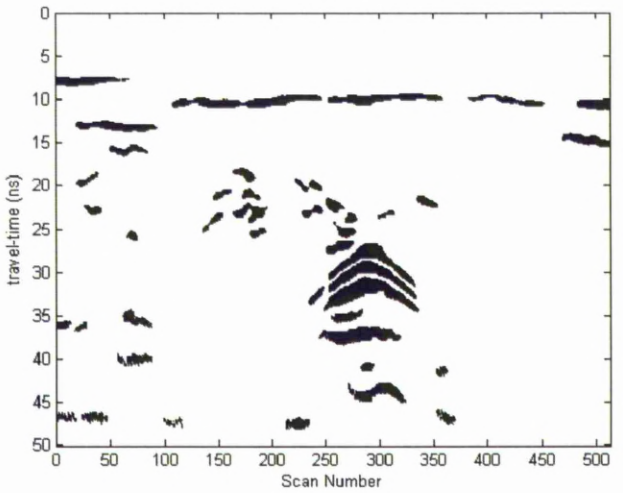

FIGURE 4.15: Binary image after application of miniature deletion filter

4.4.6.2 Real GPR Data Classification Results

The classification approach has been implemented on different GPR data sets successfully. Results indicate that the classifier is able to extract the hyperbolic target shapes as well as some other shapes that have hyperbolic resemblance.

The position of the blobs in the binary image is located and a boxed region around the blob is extracted from the original B-scan. Each region is then converted into 1D signal and the MFCC and polynomial coefficients are extracted as features. These features then go through a feature matching process in a trained neural network and the output determines the blob as target or non target. If the target is classified as non-target that blob is eliminated from the binary data set. The final output is an image that only consists of blobs which had qualified as targets. The resulting image is again converted into binary as shown in Figure 4.16 (a). The output masked on the original image is shown in Figure 4.16 (b).

4.4.7 Performance Quantification

With the increased reliance on automated segmentation techniques for GPR interpretation, it is no longer sufficient to judge the performance of a classifier solely by its ability to detect a given target as this figure can be grossly misleading. Here it is proposed that a standardised approach to performance quantification be adopted to avoid such ambiguity.

The classifier presented here produces a mapping of a finite set of input parameters into an output set of two classes, a discrete class label indicating only the predicted class for each input; hyperbolic (positives) or non-hyperbolic (negatives). When the classification process is performed, there are four possible outcomes:

1. True Positive (T_p): This is when the input is positive and it is classified as positive. It is also referred to as a hit.

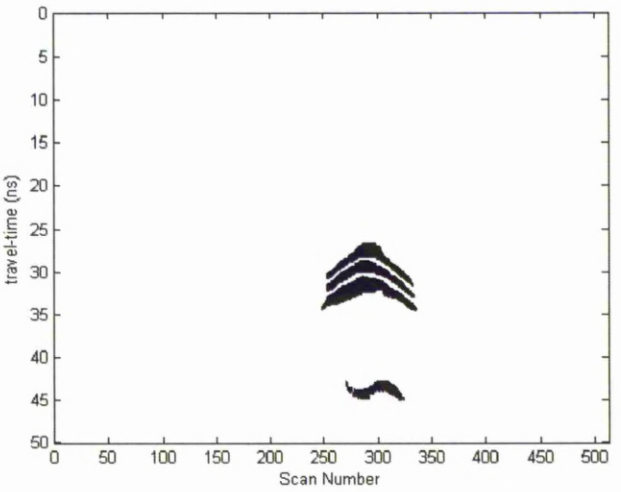

(a) Binary Output of the classified blobs.

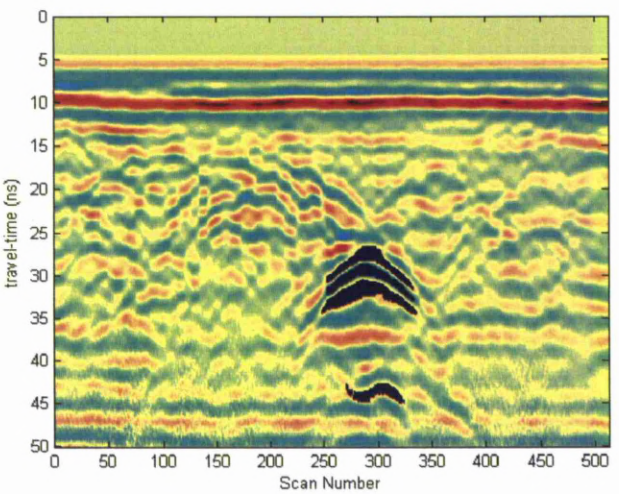

(b) Output superimposed on original raw image

FIGURE 4.16: Final classified output

2. False Negative (F_n): This is when the input is positive but it is classified as negative (*i.e.*, as non-hyperbolic). It is also referred to as a false dismissal.

3. False Positive (F_p): This is when the input is negative and it is classified as positive. It is also referred to as a false alarm.

4. True Negative (T_n): This is when the input is negative and it is classified as negative.

The following classifier performance measures were adopted to assess the suitability of the classification system [97]:

1. The true positive rate (also called hit rate or recall) represents the proportion of hyperbolic shaped blobs correctly identified:

$$T_p \text{ Rate} = \left(\frac{T_p}{T_p+F_n}\right) \times 100\% \tag{4.22}$$

2. The false positive rate (also known as the false alarm rate) represents the proportion of non-hyperbolic shaped blobs incorrectly classified as hyperbolic:

$$F_p \text{ Rate} = \left(\frac{F_p}{F_p+T_n}\right) \times 100\% \tag{4.23}$$

3. The false negative rate (also known as false dismissal rate) represents the proportion of hyperbolic shaped blobs incorrectly classified as non-hyperbolic:

$$F_n \text{ Rate} = \left(\frac{F_n}{T_p+F_n}\right) \times 100\% \tag{4.24}$$

4. The true negative rate represents the proportion of non-hyperbolic shaped blobs correctly classified as non-hyperbolic:

$$T_n \text{ Rate} = \left(\frac{T_n}{T_n + F_p}\right) \times 100\% \tag{4.25}$$

5. Accuracy represents the proportion of the total number of predictions that were correct:

$$Accuracy = \left(\frac{T_p + T_n}{T_p + T_n + F_p + F_n}\right) \times 100\% \tag{4.26}$$

6. The error rate is given by:

$$ErrorRate = 100 - Accuracy \tag{4.27}$$

7. Precision represents the proportion of the predicted positive cases that were correct:

$$Precision = \left(\frac{T_p}{T_p + F_p}\right) \times 100\% \tag{4.28}$$

8. Specificity measures the proportion of actual negative which are correctly identified:

$$Specificity = \frac{T_n}{T_n + F_p} \tag{4.29}$$

9. Sensitivity measures the proportion of actual positives which are correctly identified:

$$Sensitivity = \frac{T_p}{T_p + F_n} \tag{4.30}$$

10. The score is given by:

$$Score = \frac{Precisionrate}{100} \times \frac{T_pRate}{100} \tag{4.31}$$

Based on these quantification measures, the performance of the classifier was assessed and quantified using the above metrics. A batch process of 15 radargrams was processed by the classifier having 76 hyperbolic signatures. The total blobs within the data set after thresholding were 5613. This count came down to 586 after application of the miniature deletion filter. The classifier was successfully able to detect 93.42% of the target signatures with very low false rate. The quantified figures of the proposed method are compared in Table 4.2 with performance measures using regional feature technique described in [98]. The data set used in this analysis consisted of eight B-scans with strong target reflections both regional feature technique and proposed methods were able to detect 100% of the targets. The remaining seven B-scans consisted of very weak target reflections even difficult for human operators to interpret. The regional feature technique failed to detect many of the targets on the other hand the proposed technique was able to distinguish most of the reflections caused by targets. This is because the proposed technique looks at the spectral features of the A-scan reflections and is able to determine whether they are caused by targets or non targets.

TABLE 4.2: Quantitative comparison between the performances of proposed and regional feature classification technique

Method	True Positive %	True Negative %	False Positive %	False Negative %	Accuracy %	Error %	Precision %	Specificity %	Sensitivity %	Score
Regional features [1]	75	99.51	0.48	25	99.18	0.81	67.85	0.995	0.75	0.508
Proposed Method	93.42	99.69	0.307	6.57	99.60	0.391	80.68	0.996	0.934	0.753

4.5 Hyperbola Fitter

Hyperbola fitting is an important step towards the correct estimation of underground utility target parameters. There are different hyperbola fitting techniques. Hough transform based fitting are computationally expensive. Least square fitting to general conics and rejecting non-hyperbolic fits are fast and of good performance but they do not characterise the hyperbola in terms of the major and minor axis, hence, they are not able to provide the necessary information for target identification. Shihab *et al.* [35] presented a fitter developed from Fitzgibbon's ellipse-specific direct least-square fitting technique [30] which uses a hyperbolic constraint to specifically fit a hyperbola. The advantage of this fitter is that it has the ability to calculate the features of a hyperbola that are required to calculate target information.

The fitter used by Shihab is able to calculate the hyperbolic parameters required to calculate target parameters which are the major axis 'a', minor axis 'b' and center coordinates but the hyperbolas from GPR data are not usually perfect in shape. A number of hyperbolas can fit to it which would result in different values of depth and radius. This fitter however when tested on simulated hyperbolas of various major and minor axis, performed well with major axis 'a' greater than minor axis 'b' but when value of major axis was less than the minor axis the method tend to fail. On the other hand, when the hyperbolas were solved without application of the quadratic constraint the results tend to improve for minor axis greater than major axis, but tend to deteriorate the other way around.

The proposed system in this study hence uses both of the fitting techniques mentioned above. This way hyperbolas having wide range of major and minor axis

can be fitted accurately. Results from both methods are compared to the original hyperbolic points and those having maximum likelihood are selected.

The two fitting techniques discussed in this study are referred to as 'modified direct least-square fitter' and 'hyperbola fitter without quadratic constraint'. These methods are discussed in detail in the following subsection.

4.5.1 Modified Direct Least-Square Fitter

A general conic can be represented by the following second order polynomial equation

$$F(\mathbf{m};\mathbf{x}) = \mathbf{m}\cdot\mathbf{x} = a_c x^2 + b_c xy + c_c y^2 + d_c x + e_c y + f_c = 0 \tag{4.32}$$

where $\boldsymbol{m} = [a_c\ b_c\ c_c\ d_c\ e_c\ f_c]^T$ and $\boldsymbol{x} = [x^2\ xy\ y^2\ x\ y\ 1]^T$. $F(\boldsymbol{m};\boldsymbol{x}_i)$ is called the *algebraic distance* of a point (x, y) to the conic $F(\boldsymbol{m};\boldsymbol{x}) = 0$. The fitting of such a general conic can be achieved via minimizing the sum of squared algebraic distances

$$D_A(\mathbf{m}) = \sum_{i=1}^{N} F(\mathbf{x}_i)^2 \tag{4.33}$$

of the curve to the N data points x_i [99]. The parameter vector $\mathbf{m}$ is required to be constrained in a manner that avoids solution of $\mathbf{m} = 0$, and recognises that any multiple solutions of $\mathbf{m}$ represents the same conic [30].

It was shown by Bookstein [29] that if a quadratic constraint is set on the parameters, then Equation 4.33 can be solved by the rank-deficient generalised eigenvalue

system

$$\mathbf{D}^T\mathbf{D}\mathbf{m} = \mathbf{S}\mathbf{m} = \lambda\mathbf{C}\mathbf{m} \tag{4.34}$$

where $\mathbf{D} = [x_1 x_2 ... x_N]^T$ is called the *design matrix*, $\mathbf{S} = \mathbf{D}^T\mathbf{D}$ is called the *scatter matrix* and $\mathbf{C}$ is the matrix that expresses the constraint.

In order to fit a hyperbola specifically to produce a highly efficient solution of the linear least- squares problem of Equation 4.33, the parameter vector $\mathbf{m}$ is to be constrained so that the conic it represents is forced to be a hyperbola. This constraint happens to be the *discriminant* ${b_c}^2 - 4a_c c_c$.

It is very difficult to solve this constraint inequality problem in general as there is no guaranteed solution. Instead the parameters can be scaled arbitrarily via imposing the equality constraint ${b_c}^2 - 4a_c c_c = 1$.

This constraint may be expressed in the matrix of the form $\mathbf{m}^T C\mathbf{m} = 1$ as [1]

$$\mathbf{m}^T \begin{pmatrix} 0 & 0 & -2 & 0 & 0 & 0 \\ 0 & 1 & 0 & 0 & 0 & 0 \\ -2 & 0 & 0 & 0 & 0 & 0 \\ 0 & 0 & 0 & 0 & 0 & 0 \\ 0 & 0 & 0 & 0 & 0 & 0 \\ 0 & 0 & 0 & 0 & 0 & 0 \end{pmatrix} \mathbf{m} = 1 \tag{4.35}$$

minimizing

$$E = \|\mathbf{D}\mathbf{m}\|^2 \tag{4.36}$$

subject to the constraint

$$\mathbf{m}^T\mathbf{C}\mathbf{m} = 1 \tag{4.37}$$

This system was solved by calculating the generalised eigenvectors of Equation 4.34 and thus the parameters of the hyperbolae are obtained.

Using this hyperbola-specific conic section least squares fitter, the values of a and b can be extracted, as the angle between the two asymptotes is $(2\arctan\frac{b}{a})$. This angle, in conjunction with either the focal length or the distance from the centre to the apex, together uniquely characterise a hyperbola [1].

4.5.2 Hyperbola Fitter Without Quadratic Constraint

The above method performs well in the case where *'a'* is greater than *'b'*, but when the value of *'a'* goes less then *'b'*, which might be the case in certain practical scenarios the above method tends to fail. However it is observed that when the hyperbolic parameters are extracted without applying the quadratic constraint the results are improved. The conic equation used is given as

$$F(\mathbf{m};\mathbf{x}) = \mathbf{m}\cdot\mathbf{x} = a_c x^2 + b_c xy + c_c y^2 + d_c x + e_c y = 0 \tag{4.38}$$

Where $\boldsymbol{m} = [a_c\ b_c\ c_c\ d_c\ e_c]^T$ and $\boldsymbol{x} = [x^2\ xy\ y^2\ x\ y]^T$. In this case, the scatter matrix is obtained as $\boldsymbol{S}=x^T.x$. Fitting is achieved by minimizing the sum of the

algebraic distance of the curve to the N data points given as D:

$$D = \sum_{i=1}^{N} x_i \tag{4.39}$$

Instead of applying the quadratic constraint, D is multiplied to the inverse of the scatter matrix

$$K = DS^{-1} \tag{4.40}$$

The subsequent values of a_c, b_c, c_c, d_c and e_c are extracted such that a_c=K(1), b_c =K(2), c_c=K(3), d_c=K(4) and e_c=K(5).

The hyperbolic parameters are estimated using the following equations:

$$F = 1 + \frac{d_c^2}{4a_c} - \frac{e_c^2}{4c_c} \tag{4.41}$$

$$a = \left| \sqrt{\frac{F}{c_c}} \right| \tag{4.42}$$

$$b = \left| \sqrt{\frac{F}{a_c}} \right| \tag{4.43}$$

where a and b are the major and minor axis of the hyperbola.

4.5.3 Fitter Results

In order to check the performance of the two fitters a set of ten hyperbolas were simulated with major axis constant at 100 units and minor axis varied from a value of 20 units to 200 units with 20 units interval. The results from both the methods along with error rate are shown in Table 4.3. It can be seen here that when the major axis is greater than the minor axis the modified least square method has the least error on the other hand when the value of the minor axis tends to go greater than the major axis the hyperbola fitter without quadratic constraint method tends to give better results. The results are shown in graphical form in Figure 4.17, it can be seen clearly for the minor and major axis in Figures 4.17 (a) and (b) respectively that when the major axis is greater than the minor axis the curve of the modified least square fitter tends to be close to the true value and when the minor axis tends to go greater than then the major axis the modified least square fitter tends to deviate away from the true values but the hyperbola fitter without quadratic constraint method curve converges towards the true values. In general the values closest to the true values with the least error are selected as the final hyperbola fitting results in the proposed study.

The results on real GPR data are shown in Chapter 5 where the fitting results are incorporated into a mathematical model to estimate the target parameters.

TABLE 4.3: Hyperbola results of two fitters and selected fitter

True axis		Modifies least Sq method		Error		Fitter without quad constraint		Error		Selected axis	
a	b	a	b	a	b	a	b	a	b	a	b
100	20	99.92	19.98	-0.08	-0.10	381.98	76.40	281.98	282.00	99.92	19.98
100	40	100.35	40.11	0.35	0.27	216.18	86.35	116.18	115.88	100.35	40.11
100	60	99.52	59.77	-0.48	-0.38	164.89	98.69	64.89	64.48	99.52	59.66
100	80	91.01	75.54	-8.99	-5.57	135.31	110.70	35.31	38.38	91.01	75.54
100	100	86.54	91.74	-13.46	-8.26	127.41	126.95	27.41	26.95	86.54	91.74
100	120	75.00	101.40	-25.00	-15.50	128.92	148.66	28.92	23.88	75.00	101.40
100	140	49.47	93.94	-50.53	-32.90	110.21	158.00	10.21	12.86	110.21	158.00
100	160	34.33	87.25	-65.67	-45.47	114.89	180.95	14.89	13.09	114.89	180.95
100	180	21.54	74.93	-78.46	-58.37	97.14	185.30	-2.86	2.94	97.14	185.30
100	200	14.19	65.27	-85.81	-67.31	99.61	206.77	-0.39	3.39	99.61	206.77

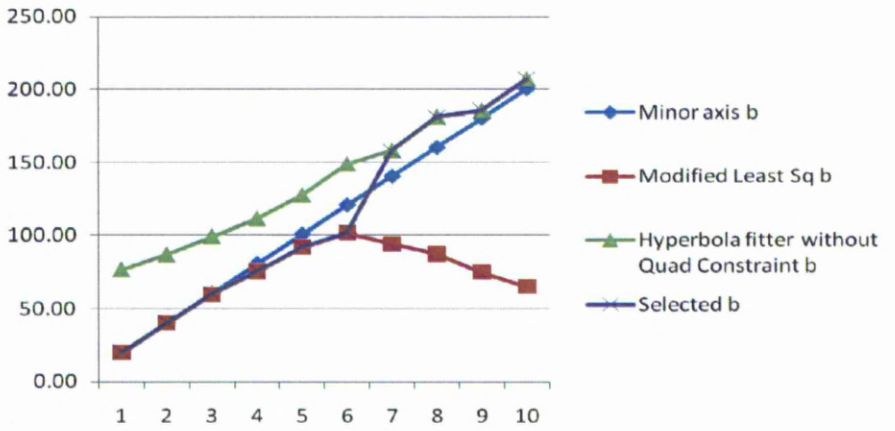

(a) Minor axis chart

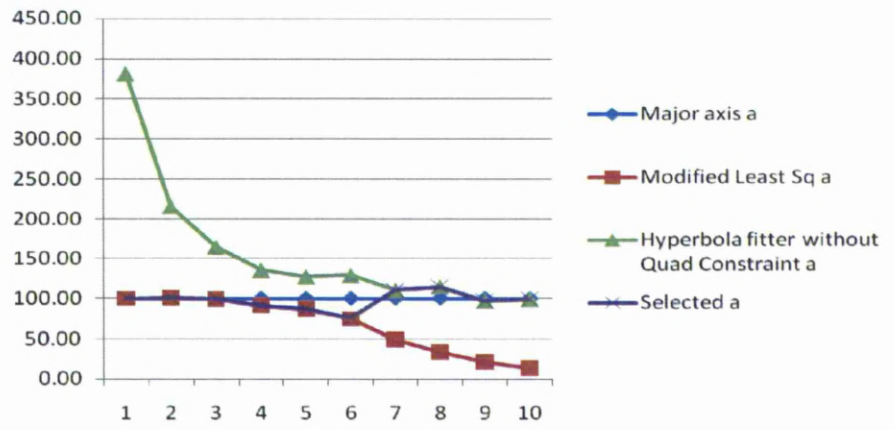

(b) Major axis chart

FIGURE 4.17: Major and Minor axis of the fitting techniques along with the true and selected values

4.6 Summary

This chapter addresses three crucial stages of the GPR post processing and have introduced novel and efficient approaches to perform them. The three areas of study are background removal, hyperbola classification and hyperbola fitting.

The Eigen based background removal technique is an effective and much more efficient background and clutter removal technique. The method has been tested on several data set and the results indicate that the proposed method is superior to the traditional techniques in three ways. First of all the method is able to serve the main clutter reduction purpose extremely well, secondly the method is a two stage process that applies mean subtraction as stage two so if there are any horizontal reflections left as residue from stage one, they are removed in stage two of the process and the third aspect is the refined output image in which the target positive and negative peak reflections are quite distinguishable then the background. Since this is a two stage process therefore it consumes slightly more time than the mean subtraction process but it should also be noted that the results give a distinct target signature and the effect of extra clutter is reduced significantly so in the later GPR processing stages of target segmentation and classification less time will be consumed hence the proposed method is reducing the overall time consumption. Considering all the advantages, the proposed system can easily qualify as a strong candidate for preliminary post processing tool of an automated near real time GPR processing system.

The cepstral approach for underground utility detection from GPR data is a completely novel approach. In this approach the image is first converted into binary image. Afterwards, a miniature deletion filter is applied that eradicates the reflections that would not classify as targets based on their small size, by doing so the overall classification time consumption is reduced tremendously. The remaining reflections are then indexed and their location within the B-scan is determined. A boxed region of this location is then extracted from the original GPR B-scan. Each region is then transformed to 1D signals and the MFCCs and polynomial

features are extracted from the signals. A database of target cepstral and polynomial features are generated to train a neural network which is then used for feature matching in the testing phase.

MFCC has been tested on a dataset of GPR B-scans and compared with regional feature technique. The data set introduced contain half of the B-scans with distinct strong hyperbolic reflections while the other half contained distorted reflections of incomplete hyperbolic shaped. Both regional feature technique and proposed method were able to distinguish 100% of the target reflections in the first half, but regional feature technique tend to fail in the second half because of the distorted shapes of the hyperbolas. On the other hand, the proposed method was able to distinguish most of the target signatures with very less error rate. This is mostly because the proposed method looks at the A-scans of the boxed region containing the reflection and is able to distinguish between target and non target reflections. It had also been noted that for the proposed system to work effectively a minimum number of at least 5 -10 A-scans from the target or non target are required to be ordered lexicographically hence introduction of a boxed region containing the blob. Experimental results show that the proposed approach is successfully able to extract target signatures from GPR data thus introducing a novel approach of image classification besides the traditional classification approaches of statistical and regional features. MFCCs have commonly been used in speech recognition but its application as a classification tool for GPR image processing has been introduced for the first time.

The dual fitting technique in this study incorporates two separate techniques in order to get the best possible results. The correct estimation of the hyperbolic major and minor axis is very important as wrong values would give wrong results

for GPR target parameters and therefore render the complete post processing stages useless. The current study makes use of two distinct hyperbolic fitting techniques that have the capability to fit a wide range of hyperbolas. The positive attributes of both fitters are combined into a single algorithm in which the best results are considered for further processing. Results show that the combined effect of the two fitters produce much more reliable target interpretation.

Chapter 5

Modelling and Parameter Estimation

This chapter describes the estimation of the target parameters from the extracted hyperbola. A general equation that is used to model a cylindrical reflection is explained in detail. This model takes into effect the target radius, depth and orientation angle in addition with the dielectric of the host medium.

The results from the hyperbola fitter are used in the model to estimate the target parameters and a 3D iterative procedure is discussed that is used for the correction of the estimated parameters. The chapter also discusses two distinct 3D line detection techniques.

5.1 Introduction

The last step in GPR data processing is the interpretation of the data in real world parameters. The estimation of the correct target parameters such as its depth, orientation and dimensions is the final stage. An error in these values could lead to disastrous consequences. Human intervention and assumptions lead to errors and is a blockade in the automated process and this involvement has not been satisfactorily resolved. Researchers have tried addressing these problems and to certain extent they have been successful in introducing robustness and consistency in the estimation of the dielectric properties of the medium [100], [43]. Also improvements have been shown in estimation of target parameters in certain specific cases [1] but improvement of overall results for a variety of data sets is still an issue. The reason for the uncertainty is usually because visibly the reflections of some non targets can be very similar to that of targets hence creating confusion. This problem is usually overcome by making assumption of the system and host medium sometimes even without a priori knowledge which gives inaccurate results.

The conventional target signature estimation methods relied on various assumptions such as target having zero radius, the dielectric of the medium above the target being homogeneous in nature, the antenna radiation is two-dimensional, the buried target is normal to the scan direction and parallel to the surface of the ground etc. All of these assumptions impede in the correct estimation of the target parameters as they change the position of the target object therefore any values resulting would definitely have some error.

The hyperbolic signature of a cylindrical target detected by GPR are influenced by a number of factors for example environmental factors such as the dielectric

and conductivity of the host medium, system related factors such as the antenna polarisation and radiation patterns and target related parameters such as the target depth, velocity of the wave through the medium, orientation of the target and the angle the target makes with the scan angle.

This study used a mathematical model that is dependent on the target position, its depth, propagation velocity, orientation angle and target radius [1]. An overview of the development of this model from the classical models is shown and the results from GPR data are shown.

The parameters estimated from the model are then introduced in an iterative 3D technique developed to refine the results. Two methods have been used. The first one is an improved technique using Applied non-Accumulative Hough Transform (ANHT) and the other one is a novel technique known as Angle-based 3D line detection which is much more efficient then ANHT in terms of computation time and performance.

5.2 Standard Signature Model

The reflection from a cylindrical object such as pipes or electrical cables is presented as a downward opening hyperbola in GPR data. Researchers have been investigating the relationship between the shape of the hyperbola and the geometric configuration of the target object as the study of this hyperbola can provide valuable information about the nature of the target. The detected two way travel time t is related to the horizontal position x and the propagation velocity v as in

Equation 5.1 [5].

$$\left(\frac{t}{t_0}\right)^2 - \left(\frac{x - x_0}{\frac{v}{2}t_0}\right)^2 = 1 \tag{5.1}$$

where (x_0, t_0) are the coordinates of the apex of the hyperbola in the image (space-time) plane. This basic model is of a cylinder buried in homogeneous material in a plane that is perpendicular to the direction of the GPR scan. This equation is similar to the equation of vertically opening hyperbola centered at (x_0, y_0) and represented as

$$\left(\frac{y - y_0}{a}\right)^2 - \left(\frac{x - x_0}{b}\right)^2 = 1 \tag{5.2}$$

By comparing Equation 5.1 and Equation 5.2 the values of a and b can be given by

$$a = t_0 \tag{5.3}$$

$$b = \frac{v}{2}t_0 \tag{5.4}$$

This model lacks the contribution of the cylinder radius, horizontal and vertical orientation, hence a new model given by Shihab in [1] was used which is a modified version of this model and incorporates the cylinder radius as well as vertical and horizontal orientation.

5.2.1 Modified Signature Model

The model given in Equation 5.1 relies on the assumption that the cylinder has zero radius hence the reflections are from a point source but in reality this is not the case. The cylinder has a fixed finite radius. A more generalised equation is thus used that takes the effect of the cylinder radius. Figure 5.1 is an example of a scan taken over a cylinder of radius R. Using simple pythagoras theorem we get

$$(z + R)^2 = (z_0 + R)^2 + (x - x_0)^2 \tag{5.5}$$

where z_0 is the depth to the top of the cylinder, z is the apparent depth of the reflection from the cylinder at a position x displaced from the position of the cylinder x_0.

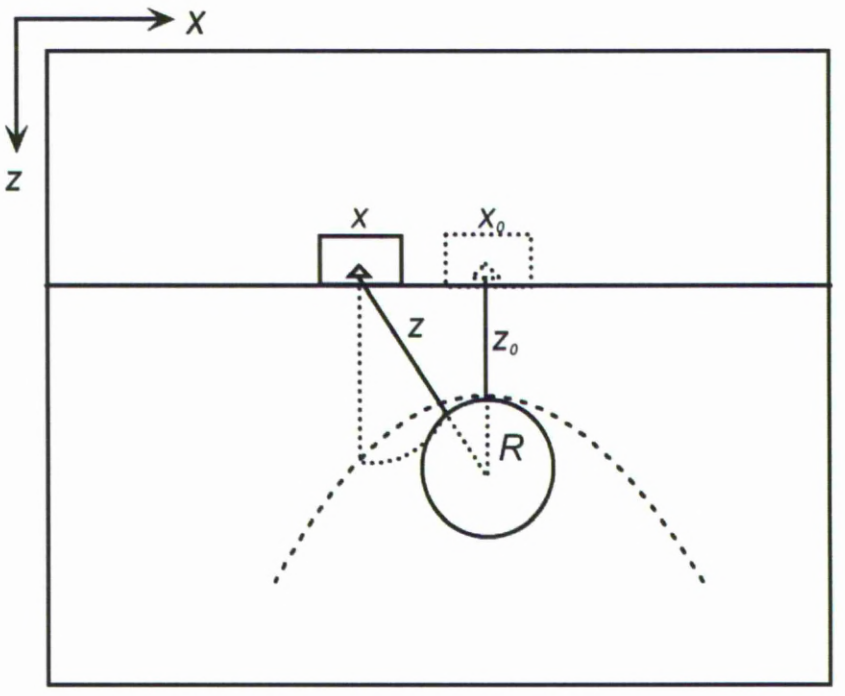

FIGURE 5.1: Effect of changing the value of R on the resulting hyperbola [1]

Substituting z with $\frac{vt}{2}$ and z_0 with $\frac{vt_0}{2}$ in Equation 5.5 and manipulating it gives

$$\left(\frac{t+\frac{2R}{v}}{t_0+\frac{2R}{v}}\right)^2 - \left(\frac{x-x_0}{\frac{v}{2}t_0+R}\right)^2 = 1 \tag{5.6}$$

By comparing this with Equation 5.6, then values of a and b are given by

$$a = t_0 + \frac{2R}{v} \tag{5.7}$$

$$b = \frac{v}{2}t_0 + R \tag{5.8}$$

It can be seen here that the radius of the cylinder plays an important role in the shape of the hyperbola. It should also be noted that when a scan is taken at an angle perpendicular to the scan direction we get a hyperbola but in a case when the scan is taken along the length of the pipe a horizontal reflection is seen. If the angle between the scan direction and pipe orientation is changed in intervals from 90^0 to 0^0, the hyperbola tends to expand which means the the orientation angle also has significant involvement in determining the shape of the hyperbola. In a typical GPR survey the orientation of the target is unknown. Even though a hyperbolic signature can be achieved, there is no way of telling the exact angle between the target and the scan. An assumption in this case could lead to incorrect results.

Shihab [1] modified his first model and incorporated the effect of cylinder orientation. It is shown in Appendix E that the normal distance between the antenna and a cylinder oriented at an angle γ is reduced by a factor of $\sin\gamma$ compared to

the normal case above. The signature will still be hyperbolic, but Equation 5.6 is modified as follows

$$\left(\frac{t+\frac{2R}{v}}{t_0+\frac{2R}{v}}\right)^2 - \left(\frac{(x-x_0)\sin\gamma}{\frac{v}{2}t_0+R}\right)^2 = 1 \tag{5.9}$$

The value of a is the same as given in Equation 5.7, while the value of b is modified by a factor of $\frac{1}{\sin\gamma}$, which will in turn influence the eccentricity of the hyperbola and the inclination of its asymptotes.

$$b = \frac{\frac{v}{2}t_0+R}{\sin\gamma} \tag{5.10}$$

It can be seen here that if only one value of R, v, or γ is known, the other two values can be accurately calculated. For example, if the dielectric constant of the host medium is known, and hence the value of v is known, then the value of R can then be calculated from

$$R = \frac{v}{2}(a-t_0) \tag{5.11}$$

or

$$R = b\sin\gamma - \frac{v}{2}t_0 \tag{5.12}$$

Then γ can be calculated as

$$\gamma = \arcsin\left(\frac{\frac{v}{2}t_0+R}{b}\right) \tag{5.13}$$

5.2.1.1 Azimuthal and vertical Orientation

The orientation of the buried cylinder should be in terms of inclination angle and azimuthal orientation rather than just simply the angle between cylinder axis and radar scan. Therefore, the angle γ is decomposed into two such angles.

The azimuth orientation is defined here as the acute angle between projection of the buried cylinder onto the ground (radar) plane and the direction of scanning of the GPR, and will be referred to here as α, whereas the inclination angle β is the acute angle between the cylinder and its projection onto the ground plane [1]. Each of these angles has a separate and identifiable effect on the ray-path, and hence on the shape of the hyperbolic signature.

Referring to Figure 5.2, the relationship between the three angles can be derived. Assuming the radar scan direction to be along the $x-$axis, and assuming $z = 1$, the length of the side h which is common to two triangles can be expressed as

$$h^2 = y^2 + 1 = \rho^2 + x^2 - 2\rho x \cos\gamma \tag{5.14}$$

where $x = \frac{\cos\alpha}{\tan\beta}$, $y = \frac{\sin\alpha}{\tan\beta}$, and $\rho = \frac{1}{\sin\beta}$.

Substituting in Equation 5.14 gives

$$\frac{\sin^2\alpha\cos^2\beta}{\sin^2\beta} + 1 - \frac{1}{\sin^2\beta} - \frac{\cos^{\alpha}\cos^2\beta}{\sin^2\beta} - 2\frac{1}{\sin\beta}x\cos\gamma = 0 \tag{5.15}$$

Manipulating the above leads to

$$\frac{\sin^2\alpha\cos^2\beta + \sin^2\beta - 1 - \cos^2\alpha\cos^2\beta + 2\cos\alpha\cos\beta\cos\gamma}{\sin^2\beta} = 0 \tag{5.16}$$

$$\sin^2\alpha\cos^2\beta + \sin^2\beta - 1 - \cos^2\alpha\cos^2\beta + 2\cos\alpha\cos\beta\cos\gamma = 0 \tag{5.17}$$

$$\sin^2\alpha\cos^2\beta - \cos^2\beta - \cos^2\alpha\cos^2\beta + 2\cos\alpha\cos\beta\cos\gamma = 0 \tag{5.18}$$

$$-\cos^2\beta(1 - \sin^2\alpha + \cos^2\alpha) + 2\cos\alpha\cos\beta\cos\gamma = 0 \tag{5.19}$$

$$-2\cos^2\beta\cos^2\alpha + 2\cos\alpha\cos\beta\cos\gamma = 0 \tag{5.20}$$

This will result in the following final compact relation

$$\cos\gamma = \cos\alpha\cos\beta \tag{5.21}$$

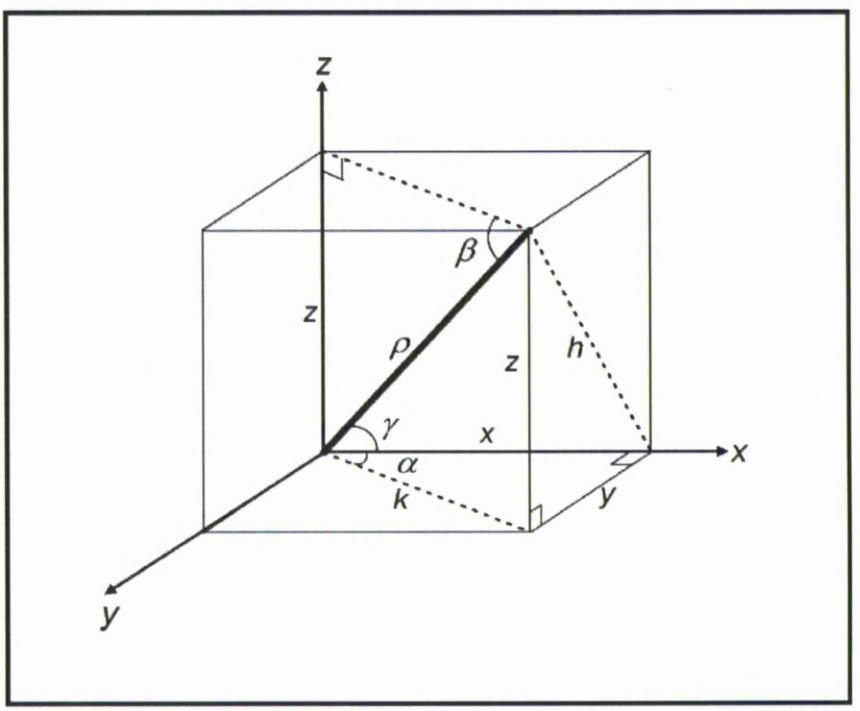

FIGURE 5.2: Geometric relationship between the angles α, β and γ [1]

Thus Equation 5.9 can be modified to include both components α and β.

$$\left(\frac{t+\frac{2R}{v}}{t_0+\frac{2R}{v}}\right)^2 - \left(\frac{(x-x_0)\sqrt{1-\cos^2\alpha\cos^2\beta}}{\frac{v}{2}t_0+R}\right)^2 = 1 \tag{5.22}$$

This demonstrates that the signature of a buried cylinder is unique to a single geometrical configuration consisting of a finite radius R, and angle γ, buried in a medium of dielectric constant $\varepsilon_r = \left(\frac{c}{v}\right)^2$ where c is the speed of light in vacuum.

5.3 The Use of 3D Line Detection in GPR Data

The model presented in the above section gives us the major and minor axis of hyperbola as in Equation 5.7 and 5.10. The major and minor axis a and b can be found by using a hyperbola fitter on the signature, therefore the remaining unknowns are R, v, and γ. If any one of these three unknowns is known the other two can be calculated using equation 5.7 and 5.10. Since all three values are unknown therefore one of these values would have to be assumed but assumptions lead to error in the results. This error would be dependent on how close the assumption is to the true value. It has also been shown in [1] that

$$\cos\gamma = \cos\theta\cos\phi \tag{5.23}$$

It is shown that the orientation angle is dependent on the azimuth angle θ and vertical angle ϕ of the target. In order to calculate these angles the GPR data has to be observed from 3D perspective thus the use of 3D line detection comes in the picture. In a 2D GPR image the vertical axis is the z-axis and the horizontal

axis is the x-axis. In order to find the correct parameters of the target an iterative cycle is created. Initially the value of gamma is assumed to be zero and the values of v, R and apex of the hyperbola are calculated. The apexes of all the hyperbolas in adjacent B-scans are then plotted into 3D space. Using 3D line detection, those points that are in a straight line or are within a certain threshold range of a straight line are considered to be part of the same target object.

In the case of utility detection the following points can be made of use in 3D space:

- In 3D space the target pipes are moving along the y-axis, therefore hyperbolas that are in line on the x-axis or z-axis can not be grouped together because they do not belong to the same target pipe.
- The radius of targets in different B-scans of the same cylindrical pipe would be nearly the same, thus in detecting lines those detected linear points with nearly the same calculated radius should be considered part of the same target. If the radius of the detected linear points is different then that line should not be considered as part of the same target. They can be parts of two different pipes.

Once the lines are detected and targets are located the values of θ and ϕ are converted into γ using Equation 5.23. The corresponding orientations are used to correct the values of R, ϑ and ε_r for each detected cylinder via

$$R = \frac{b(a - t_0)\sin\gamma}{a} \tag{5.24}$$

$$\vartheta = \frac{2b\sin\gamma}{a} \tag{5.25}$$

$$\varepsilon_r = \left(\frac{c}{\vartheta_s}\right)^2 \tag{5.26}$$

the depths is calculated as

$$D = \frac{v_s t_{s0}}{2} \tag{5.27}$$

where ϑ_s is given by

$$\vartheta_s = \frac{\vartheta \times \texttt{samples\_per\_scan}}{\texttt{scans\_per\_meter} \times \texttt{range}} \tag{5.28}$$

and t_{s0} is given by

$$t_{s0} = \frac{t_0 \times range}{samples\_per\_scan} \tag{5.29}$$

These new values are used to re-map the detected apices according to the calculated orientation, the iterations are repeated until change in gamma is significantly small or a fixed number of iterations are set. After the system settles, the final values of the relative permittivity of each detected apex are used to generate the permittivity profile of the site via fitting a surface of the form $\varepsilon_r = f(x,y)$ to the dielectric constant values obtained at the detected target points. This fitting is based on the Delaunay triangulation [101].

5.4 Adaptive Non-Accumulative Hough Transform (ANHT)

A straight line in 3D space through the point (x_1, y_1, z_1) and having the direction vector (a,b,c) can be described by the equation

$$\frac{x - x_1}{a} = \frac{y - y_1}{b} = \frac{z - z_1}{c} (a \neq 0, b \neq 0, c \neq 0) \tag{5.30}$$

This equation can be expressed in vector form as

$$\mathbf{r} = (x, y, z) = r_1 + t\,\overrightarrow{l} \tag{5.31}$$

where $\mathbf{r}$ is the position vector relative to the origin O, $\mathbf{r}_1$ is a given point on the line, l is the direction vector and t is a number dependent on the position of the point in the line. If $\mathbf{r}_1 = (x_1, y_1, z_1)$ and $\boldsymbol{l}$ = (a,b,c), Equation 5.31 can be rewritten as

$$\mathbf{r} = (x, y, z) = (x_1, y_1, z_1) + t(a, b, c) \tag{5.32}$$

For any value of t there is a unique point $P(x,y,z)$ on the line. So a given point and a direction vector can fully describe a line in 3D space.

For a given line in 3D there is only one plane $\prod$ through the origin perpendicular to the line $\boldsymbol{l}$. Let n be the normal-vector of the plane $\prod$, B a fixed point on the plane and $P(x_t, y_t, z_t)$ any point on the plane. Taking O as the origin, let $\overline{OB}$=$\boldsymbol{r}_1$,

$\overline{OP}$=$\boldsymbol{r}$ Thus

$$BP.n = 0 \tag{5.33}$$

Since

$$BP = \mathbf{r} - \mathbf{r}_1 \tag{5.34}$$

Hence

$$(\mathbf{r} - r_1).n = 0 \tag{5.35}$$

The plane $\prod$ is passing through the origin therefore the origin can be set as the fixed point B. Hence $\overline{OB}$=$\mathbf{r}_1$=(0,0,0). Therefore eq 5.35 can be written as

$$r.n = 0 \tag{5.36}$$

Since the line is perpendicular to the plane $\prod$, the direction vector of the line is the normal-vector of the plane. Let P be the intersection of the plane $\prod$ and the line l. We have

$$[(x_1, y_1, z_1) + t(a, b, c)].(a, b, c) = 0 \tag{5.37}$$

solving the equation we get value of t as

$$t = \frac{-(ax_1 + by_1 + cz_1)}{a^2 + b^2 + c^2} \tag{5.38}$$

therefore the intersection P can be obtained by

$$P = (x_1, y_1, z_1) + t(a, b, c) \tag{5.39}$$

Let the direction-vector of the line be the unit vector, we have

$$a = \sin\phi.\cos\theta \tag{5.40}$$

$$b = \sin\phi.\sin\theta \tag{5.41}$$

$$c = \cos\phi \tag{5.42}$$

where ϕ and θ are the orientation of the line l in spherical form.

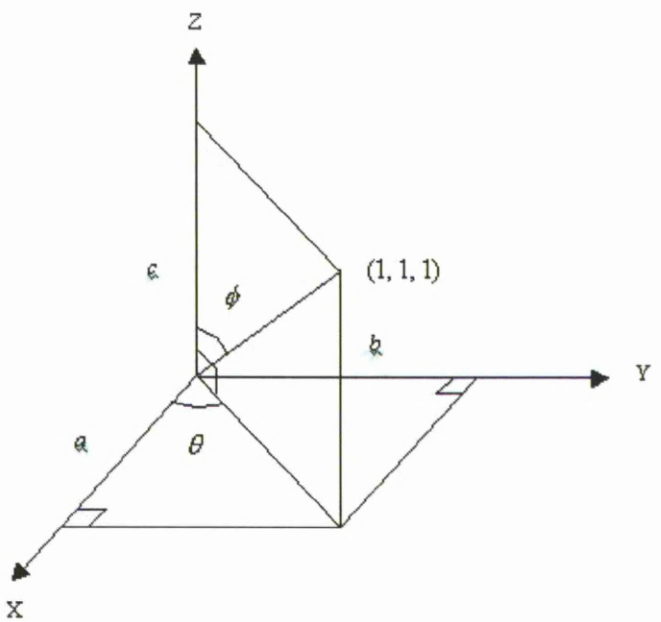

FIGURE 5.3: Cartesian and spherical coordinates

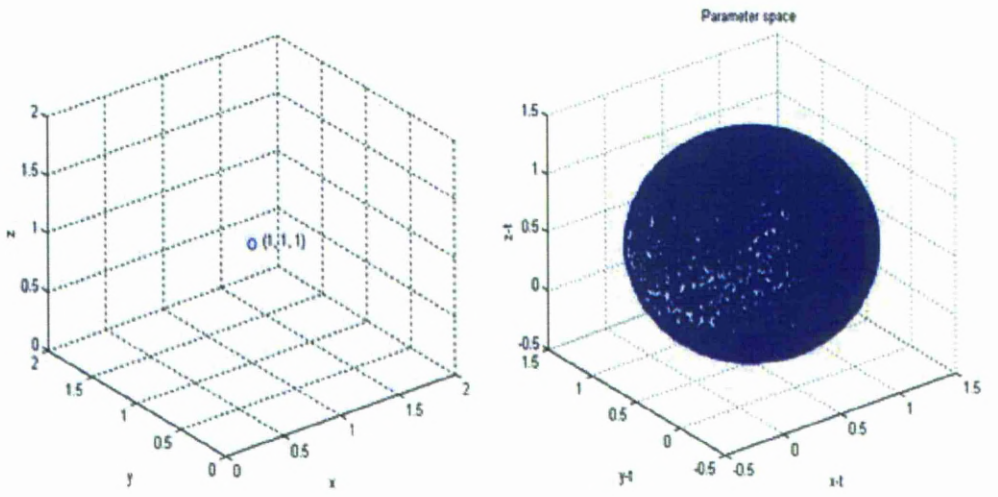

FIGURE 5.4: Mapping of a point from 3D space to parameter space (a) 3D space (b) parameter space

Substituting values of a,b and c into eq 5.39

$$P = (x_1, y_1, z_1) + t(\sin\phi.\cos\theta, \sin\phi.\sin\theta, \cos\phi) \tag{5.43}$$

where

$$t = -(\sin\phi.\cos\theta.x_1 + \sin\phi.\sin\theta.y_1 + \cos\phi.z_1) \tag{5.44}$$

The use of this representation shows that a straight line can be parameterised by 5 parameters, its point of intersection $P(x_t, y_t, z_t)$ with a plane through the origin perpendicular to it and its two direction angles in spherical form (ϕ, θ). Each 3D point (x, y, z) generates a hyper-surface $(x_t, y_t, z_t, \phi, \theta)$ in parameter space. The intersection of hyper-surfaces generated by many 3D points show that they are linear.

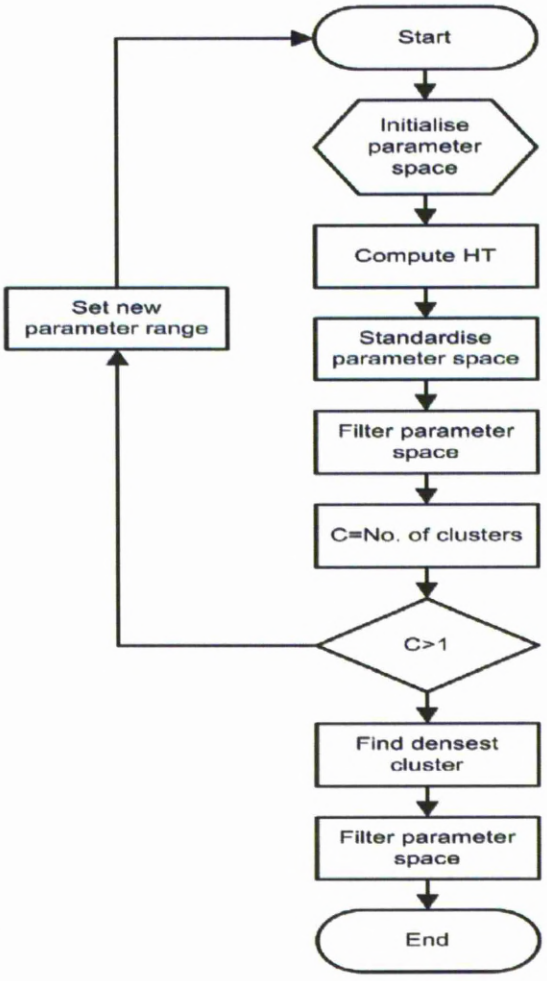

FIGURE 5.5: Flow chart of line detection algorithm

5.4.1 ANHT Algorithm

This section presents the details about the ANHT algorithm. Figure 5.5 shows the flow chart of the control strategy used to identify an instance of a 3D linear object.

The ANHT algorithm consists of four key ideas:

1. Filtering parameter space to reduce the effect of outliers.

2. Automatic estimation of the number of significant clusters in parameter space

3. Using competitive learning neural network to find the intersection so that the use of finely quantised accumulator can be avoided.

4. Intelligently redefining the parameter range so that the interesting area can be investigated in greater detail and the use of a small parameter size becomes possible, consequently the computer storage requirement can be reduced considerably.

The data may consist of more than one line therefore an iterative procedure is used to find all lines as the algorithm detects one line per iteration. If an instance of linear objects has been detected, the points identified as belonging to this instance will be removed from the list of candidate points. Then a search for another linear object instance can be made. Data containing multiple linear objects is therefore processed until there is no significant structure in it.

The algorithm is discussed in greater detail in the following subsections

5.4.1.1 Standardising the Parameter Space

The five parameters generated by HT are in different scales and different ranges, since the further stages of ANHT involve calculating distance between the parameter points therefore it is necessary to re-scale these parameters. It is common to standardise each dimension to the same standard deviation.

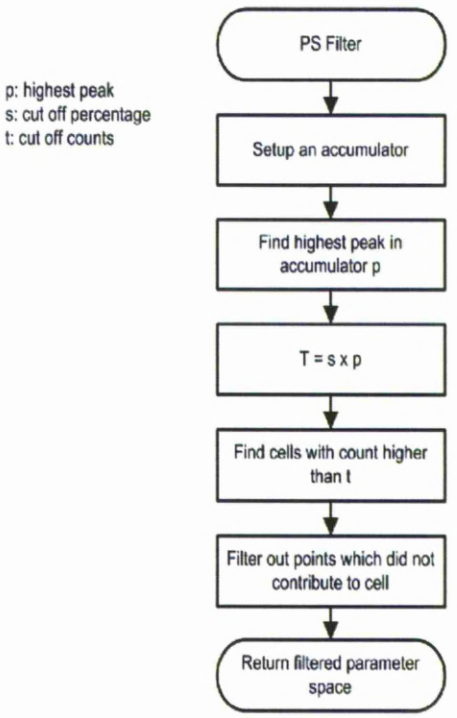

FIGURE 5.6: Flow diagram for PS Filter

5.4.1.2 Filtering the Parameter Space

The effect of outliers in the parameter space is one of the major problems of implementing the ANHT algorithm. Therefore, it is necessary to filter these outliers. Figure 5.6 is a flow diagram for the Parameter Space (PS) filter. This scheme consists of accumulating the points of the parameter space in a small fixed size accumulator and using this information to filter the outliers out of the parameter space. The threshold chosen to filter outliers is calculated as a fixed fraction of the highest count found in a single accumulator bin. A typical value of the cutoff percentage is 0.9 %. Finally any point contributing to the cell which has a count less then the threshold is treated as an outlier and is filtered out. Figure 5.7 is a plot of the filtered parameter space corresponding to Figure 5.4.

Due to the number of points of each line being different one of the expected clusters

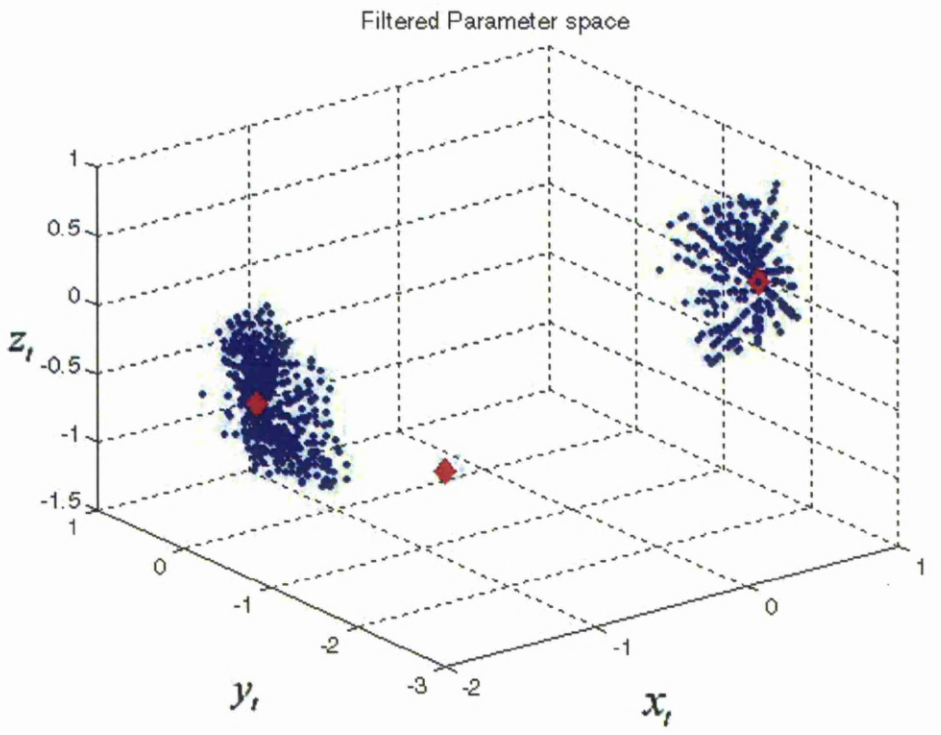

FIGURE 5.7: Filtered parameter

is missed in Figure 5.7, but this missed cluster would not affect the final result because the ANHT detects the most likely line in input data.

5.4.1.3 Cluster Analysis

The ANHT detects one line at a time therefore the densest cluster in the parameter space is clearly a representative of a line in 3D space. Prior to finding the densest cluster the total number of clusters in the parameter space is to be known. Therefore a method of estimating the number of clusters in the parameter space was implemented.

Several indices for estimating the true number of clusters in multivariate data have been proposed previously. Dubes has demonstrated two internal indices in

[102]. The first DB index is the Davies-Douldin statistics. The second MH index is a modified version of the Hubert gamma statistics. He has also shown that the MH index performs better than the DB index with higher reliability under all experimental conditions. The modified Hubert (MH) index is used in ANHT. The output results in 'C', the number of clusters, found by detecting the "significant knee" in the plot of MH index against the number of clusters. Figure 5.8 is the plot of MH index versus number of clusters. This input was the filtered parameter space shown in Figure 5.7.

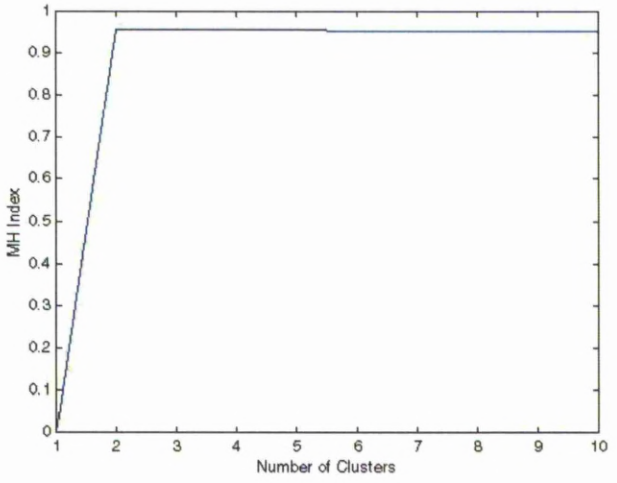

FIGURE 5.8: Plot of MH vs number of clusters

It is clear that the "significant knee" is formed at two. This means C, the number of clusters in the filtered parameter space is two which is identical to the results observed in Figure 5.7. Normally the resolution of the parameter space is already precise enough to distinguish very similar linear objects after two or three iterations, and the filter also could take the responsibility of providing the information for redefining the parameter range. One could set a threshold, D, of the capability

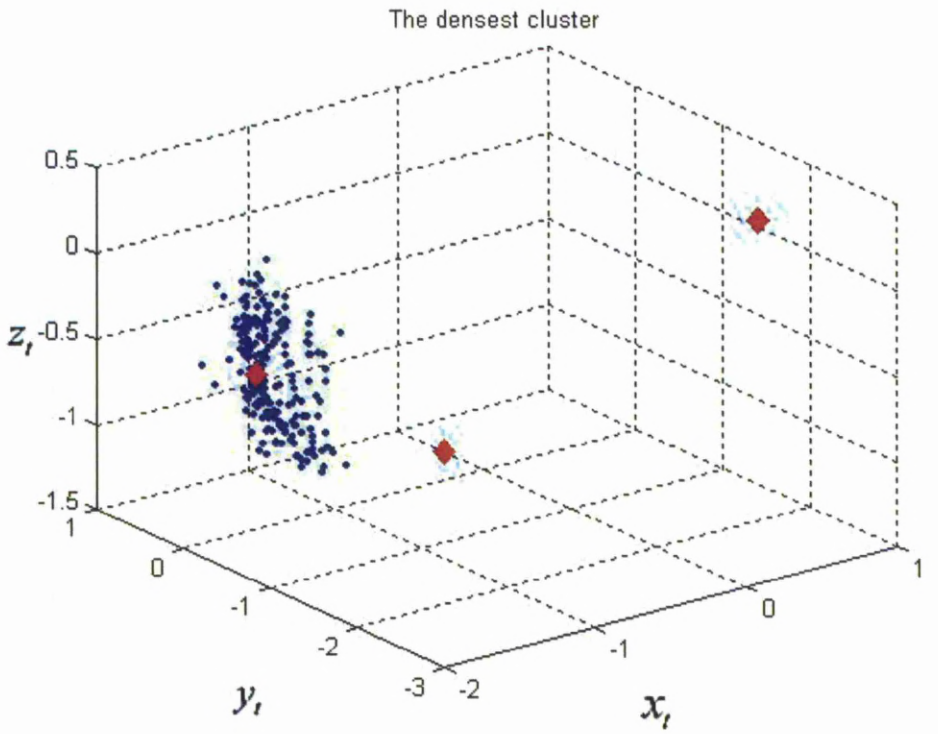

FIGURE 5.9: Plot of densest cluster in the filtered parameter space

of the ANHT for distinguishing similar linear objects in the 3D space. It is a user defined parameter. If D was set to 1^o, It would mean that the ANHT could distinguish the linear objects that only have 1^o difference.

After the number of clusters has been found the densest cluster is easily found by calculating the density of each cluster in the parameter space. Figure 5.9 is a plot of the densest cluster found in the filtered parameter space shown in Figure 5.7.

Once the densest cluster has been found the new parameter range can be defined for $(x_t, y_t, z_t, \phi, \theta)$ by measuring the range of the densest cluster. The new parameter range is defined independently for each parameter dimension and therefore this method can select appropriate precision for each parameter. This method lets the parameter space to be calculated at a very high resolution and the effect of outliers

is dramatically reduced.

5.4.1.4 Implementation of Neural Networks to Find Barycentre

competitive learning neural network is used to perform the detection of the barycentre of the densest cluster in the parameter space. Competitive learning implies an unsupervised learning scheme with no prior knowledge of what the output should be for any given input. The output neurons of a competitive learning neural network compete with each other and only a single output neuron is active at any one time (winner). The weights of the winning neuron are adjusted with the competitive learning rule so the winning neuron whose weight was closer to that of the input vector is updated to be even closer. As more and more inputs are presented, each neuron in the layer closest to a group of input vectors adjust its weight accordingly towards the input vectors. Eventually, every cluster of similar input vector will have a neuron which wins when a vector in the cluster is presented while losing at all other times [103]. If the densest cluster found is treated as a group of the input vectors of a competitive learning neural network and set the number of neurons to one, then the neuron in the network wins all the time and its weight vector tends towards the barycentre of the input vector since the barycentre is the most powerful point to classify the input vector as a single cluster.

5.4.1.5 Algorithm Terminating Criteria

The ANHT algorithm is an iterative process that detects the linear objects within the 3D space one by one, the detected linear points are then stored in another

location and eliminated from the data set so that the next linear object can be detected. One terminating criteria is when the number of linear objects is known so the code is repeated that number of times and ended. In case the number of linear objects is not known the algorithm compares the total number of points in the data sets with the previous number of points. Since in every cycle a linear object is deleted from the data sets, at the end only the noise will be left, when the algorithm compares the noise of two cycles and find them to be the same it terminates.

5.5 Experimental Results

In this section, the performance of the ANHT was tested on simulated 3D data and GPR data. Single and multiple line data within noiseless and noisy background was detected accurately. The experiments were performed on single line as shown in Figure 5.10, multiple lines in noiseless background Figure 5.11 and on multiple lines in noisy background as in Figure 5.12. The (*) indicate the original points in 3D space while the red line is the result of ANHT.

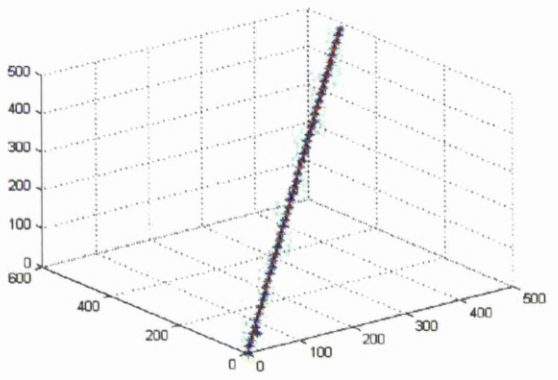

FIGURE 5.10: Single line noiseless background

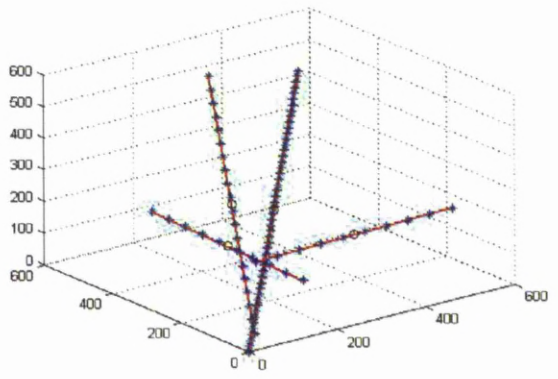

FIGURE 5.11: Multiple lines noiseless background

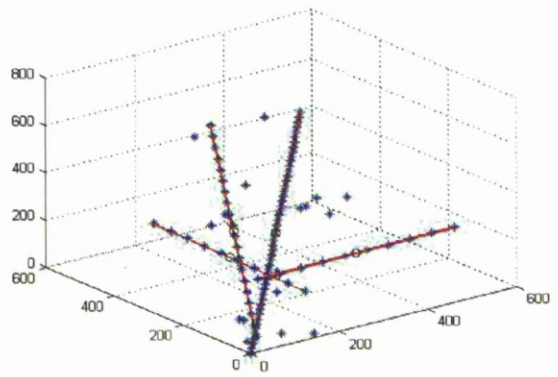

FIGURE 5.12: Multiple-line noisy background

5.6 Angle-based 3D Line Detection

ANHT is based on Hough Transform (HT) which is a powerful technique used to detect lines in images [104]. Hough transform consists of parameterizing the features in image space, an accumulator array of these parameters is generated and for each transform result its value in the accumulator is incremented. The peaks in the array correspond to line segments [105]. A difficult pattern detection problem is thus converted into a simple peak detection in parameter space [28]. The size of the accumulator depends on the required resolution. A finely quantised accumulator will lead to a higher resolution and a better accuracy in determination of individual parameters. A fine quantization always leads to a very large accumulator array, especially when the standard 2D HT is employed to detect 3D patterns.

The problem of a large accumulator array for 3D was solved by the development of Adaptive Non-accumulative Hough Transform [40] (ANHT) that converts the data into parameter space using the Hough Transform and then instead of a large accumulator array uses neural networks to detect barycenter of clusters that contribute to a linear line. This method gives accurate results most of the time but it is also very time consuming. On an average ANHT take 6 to 10 minutes to detect one linear line therefore larger the data set the more time consuming this process would be. The reason for ANHT to be so time consuming is that it detects one line per iteration and each iteration involves time expensive procedures like conversion to parameter space, cluster analysis, filtering, use of neural networks to find barycenter and generating line information. The accumulation of these time consuming processes would require 15 to 20 mins in order to detect a noisy data set involving four lines.

The importance of time efficiency and output accuracy has led us to the development of a novel idea which is the Angle based 3D line detection technique. This method takes the azimuth and vertical angles each data point makes with the other as the origin and combine points of similar angles into one line. The experimental results have shown remarkable improvement in computational time and memory usage therefore proving that Angle-based 3D line detection technique is ideal for detection of lines in 3D space.

In order to understand the concept of Angle based 3D Line Detection technique let us consider a point P in 3D space at a distance L from the origin as shown in Figure 5.13. B is the projection of the point P on the xy plane. The azimuth angle which is on the xy plane is given by θ while the angle between the xy plane and z axis with respect to the origin is ϕ. Since z axis is perpendicular to the horizontal xy plane, let us call ϕ the vertical angle. Let us now consider the right angled triangle $\angle AOB$ where $\overline{OA} = x$ and $\overline{AB} = y$ hence using basic trigonometry the hypotenuse of the triangle is given by $\overline{OB} = \overline{O'P} = \sqrt{x^2 + y^2}$. The angle theta can be calculated by:

$$\tan\theta = \frac{y}{x} \tag{5.45}$$

$$\theta = \arctan\frac{y}{x} \tag{5.46}$$

In right angle triangle $\angle B'OC$ the angle ϕ can be calculated as

$$\phi = \arctan\frac{\sqrt{x^2 + y^2}}{z} \tag{5.47}$$

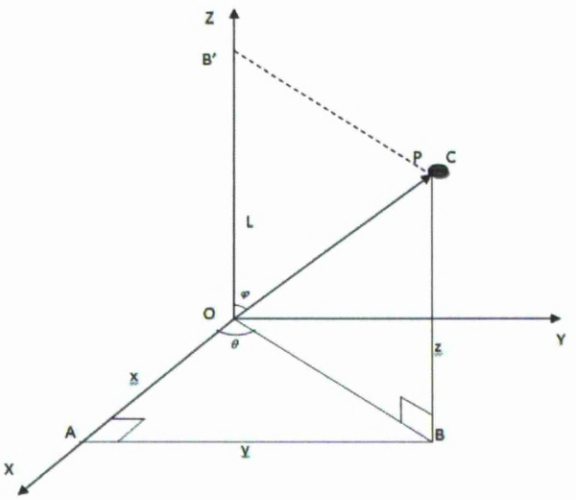

FIGURE 5.13: Single point in 3D space

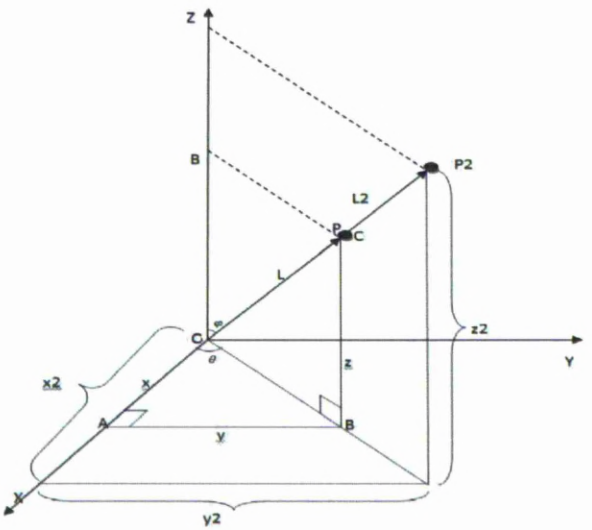

FIGURE 5.14: Two points in 3D space angled with reference to origin

In this case the angles were calculated from the origin, now let us suppose another point P2 at a distance L2 from the previous point P and at a distance of (x2,y2,z2) from the origin as shown in Figure 5.14. It can be seen that both the points P and P2 are in line with the origin. Therefore the angles θ and ϕ are the same. This shows that two linear points that are on the same line from the origin will have the same angles from the origin.

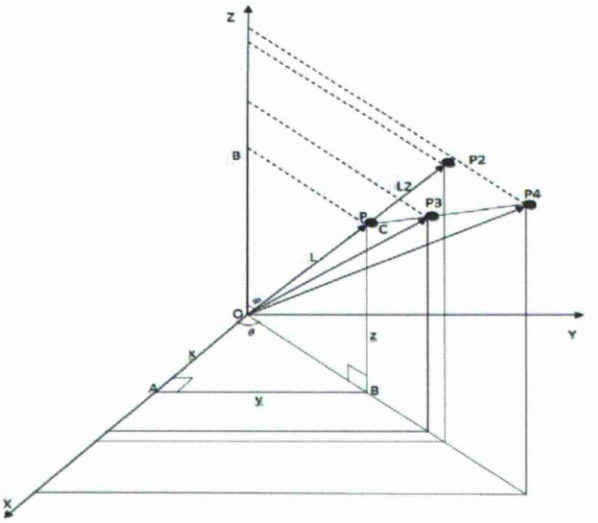

FIGURE 5.15: Four points in 3D space angled with reference to origin

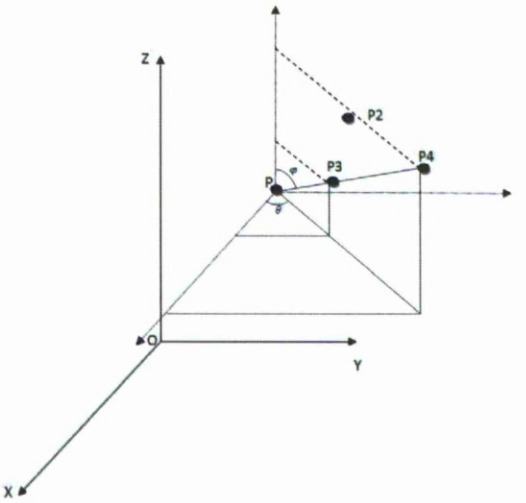

FIGURE 5.16: P3, P4 angles with reference to P taken as origin

Now let us consider a third case in which there are two more points P3 and P4 that are in line with the point P as shown in Figure 5.15. It can be seen here that the points have different angles from the origin but since they are in line with point P. Therefore, if the point P is to be taken as the origin then the points P3 and P4 will have the same angles from point P as shown in Figure 5.16.

Now let us consider the case shown in Figure 5.17, here we have the three points

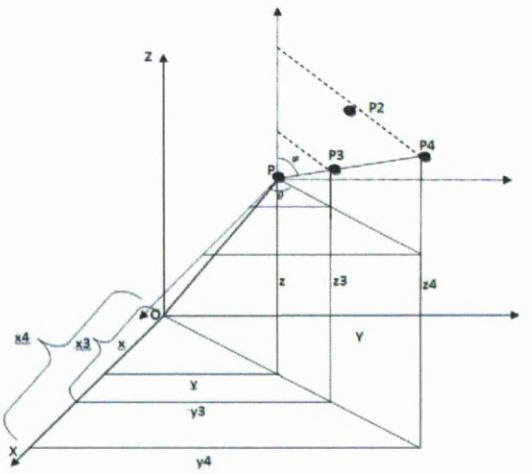

FIGURE 5.17: Points in 3D space with same origin and angles with reference to P

P, P3,P4 with respect to the origin. The axis length of the points from the origin is (x,y,z) for P, $(x3,y3,z3)$ for P3 and $(x4,y4,z4)$ for P4. If we were to calculate the angles of the point P3 from the origin we could simply replace the (x,y,z) values in the above equations with $(x3,y3,z3)$ or $(x4,y4,z4)$, but if we want to find out the angles with reference to P as the origin, then the difference between the coordinates of the two points is the axis length and thus

$$\theta_3 = \arctan \frac{(y3 - y)}{(x3 - x)} \tag{5.48}$$

$$\phi_3 = \arctan \frac{\sqrt{(x3 - x)^2 + (y3 - y)^2}}{(z3 - z)} \tag{5.49}$$

Similarly we can find out the angles of P4 with P as the origin by

$$\theta_4 = \arctan \frac{(y4 - y)}{(x4 - x)} \tag{5.50}$$

$$\phi_4 = \arctan \frac{\sqrt{(x4 - x)^2 + (y4 - y)^2}}{(z4 - z)} \tag{5.51}$$

Since the points are in line with each other therefore $\theta_3 = \theta_4$ and $\phi_3 = \phi_4$ which can also be verified by looking at Figure 5.17. From the above equations it can be seen that if we have N number of points we can standardise the formula as

$$\theta_i = \arctan \frac{(y_i - y)}{(x_i - x)} \tag{5.52}$$

$$\phi_i = \arctan \frac{\sqrt{(x_i - x)^2 + (y_i - y)^2}}{(z_i - z)} \tag{5.53}$$

where i= 1,2,.....N

Figure 5.17 also shows that the three points are exactly in line with each other therefore we can say that the points are exactly linear also the angles θ and ϕ are equal. This is the basic concept of the Angle-based 3D line detection and can be stated as: "The vertical and azimuth angles of exactly linear points are the same".

5.6.1 Special Cases

The special cases for calculating θ and ϕ are as follows;

1. If x_i-x=0, y_i-y=0 and z_i-z=0; In this case the point is looking at itself and thus this case is ignored.

2. If x_i-x=0, y_i-y≠0 and z_i-z≠0; this would mean that second point is on the 'yz' plane. Therefore θ should be 90^o if y_i-y is positive or -90^o if y_i-y is negative. In this case, we consider θ to be positive 90^o because all the points would lie on the same line and by doing so they would be treated as a single line. The case where θ is considered positive for values of y_i-y greater then zero and negative for values of y_i-y less then zero all the points would still be considered linear, but they will be represented by two separate lines one in the positive axis and the other in the negative axis direction. ϕ would be the same as in equation 5.53.

3. If y_i-y=0, x_i-x≠0 and z_i-z≠0; this would mean that the second point is on the 'xz' plane and since the y axis point lies on the origin therefore the angle θ between x and y will be 0, while ϕ would be the same as in equation 5.53.

4. If z_i-z=0; this would mean that the second point is on the 'xy' plane therefore ϕ would be 0, while θ would be the same as in equation 5.52.

5. If x_i-x=0 and y_i-y=0; this would mean that the second point is on the z axis therefore θ would be zero and ϕ would be 90^o.

6. If x_i-x=0 and z_i-y=0; this would mean that the second point is on y axis therefore θ would be 90^o while ϕ would be zero.

7. If y_i-y=0 and z_i-z=0; this would mean that the second point is on the x axis therefore θ and ϕ both will be zero.

8. If all the above cases are false then θ and ϕ are treated as in equation 5.52 and 5.53.

5.6.2 3D Line Detection

Hough Transform [106] is a very accurate way of line detection in 2D and 3D space, but it involves conversion into parameter space, a quantised 5D array and detection of peaks within the array involves computational processing and is expensive in terms of memory storage. ANHT has solved the problem of detecting individual peaks by detecting bary-center of cluster of peaks but it is also very time consuming and sometimes it is unable to detect certain lines. Therefore, it is necessary to develop a technique which is both memory and time efficient.

Angle-based 3D line detection compares the angles that all the points in 3D space make with each other. Let us have some randomly scattered points in 3D space as shown in Figure 5.18. The total number of points are 14. Points 1,2,3,4 are on the same line. Therefore, these are the linear points which we have to detect. The first step is to take each point as origin and calculate the angles the other points make with it. Since we have 14 points in this example therefore we will make two empty arrays of '14 X 14' elements, one for θ and the other for ϕ. The angles calculated by taking each point as origin are stored in these arrays. The index of the array corresponds to each point.

Once all the angles are calculated, they are to be compared with each other therefore another loop is executed in which it is checked that how many points make the same angle with the reference point. If two or more points make the same angle with that point then they are considered to lie on the same line. Those points are marked. After each cycle the points detected and the angles those points make with the other points are removed from the 2D array data set in order to save time on unnecessary computation. In the example given the angles that 'P1' will

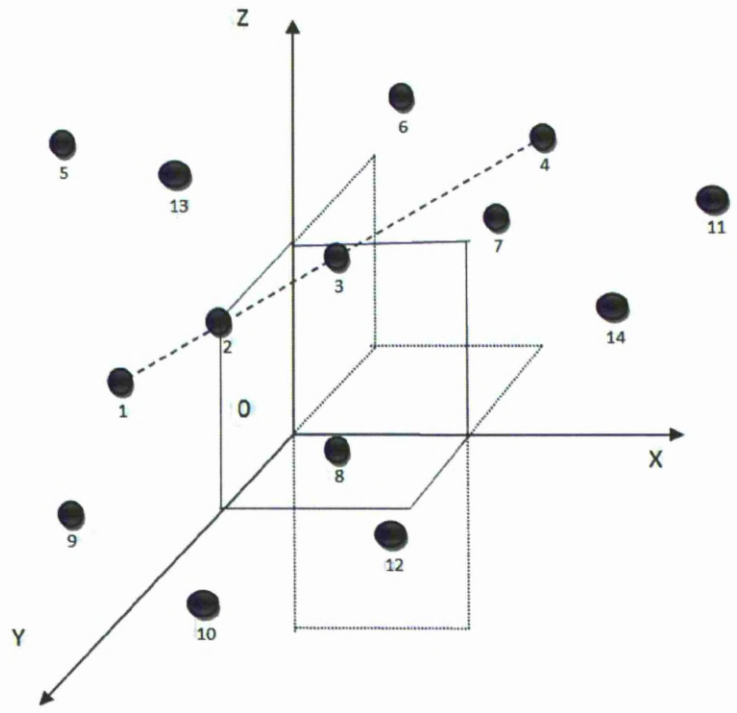

FIGURE 5.18: Points in 3D space

make with P2, P3 and P4 will be same therefore they would be stored and there angles with all the other points would be removed from the data set so that the loop directly jumps to P5 and does not waste any time in comparing the angles of P2, P3 and P4.

All the points contributing to linear lines are stored separately. After the line detection procedure these points are plotted to show the results.

The angles are calculated for all points with each point taken as reference, thus if we have 'N' number of points we get a 2D array of 'N X N' elements for θ and ϕ. It can be seen here that the more number of points there are the bigger will be the 2D array and more time would be required for the computation but when compared to other 3D line detection techniques the total time is significantly less.

5.6.3 GPR Applicability

The GPR B-scans are solved individually for target depth, radius and propagation velocity by assuming γ to be zero. The apexes are then plotted into 3D space using the depth and checked for linearity using Angle-based 3D line detection along the y direction and keeping in mind the linear points with similar radius.

It should be noted here that the plotted apexes are not perfectly linear because they have noise of there own which tend to displace them from their true linear position. This noise is caused because of human/equipment error while data acquisition, difference of soil condition over a stretch of area etc. In order to compensate for this problem the 3D line detection method should be made flexible. A threshold limit has to be introduced while comparing the θ and ϕ angles of the points. This threshold is selected by the user depending on the quality of data. Therefore all those points corresponding to angles that come within the threshold range are considered to be on the same linear line. Once three or more linear points have been detected an imaginary line is assumed throughout the 3D space and another factor is introduced which is the distance of all the points from that line.

Let us assume we have a point outside our 3D line given as P(x_p,y_p,z_p). The first step is to find a point on the line which is closest to this point P and then use the distance formula to find the distance between the two points. Let us have two known points on the line L given by A(x_{l1},y_{l1},z_{l1}) and B(x_{l2},y_{l2},z_{l2}), there is a point on the line that is closest to point P given as C(x_{l3},y_{l3},z_{l3}). The minimum distance between the point and the line is the perpendicular distance therefore the the line joining C and P would be perpendicular to the line L. In vector geometry,

two vectors are perpendicular if and only if their dot product is zero. We find the vector direction of a line by subtracting two points on the line. So we'll have two equations:

$$((x_p, y_p, z_p) - (x_{l3}, y_{l3}, z_{l3}).((x_{l1}, y_{l1} n z_{l1}) - (x_{l2}, y_{l2}, z_{l2})) = 0 \tag{5.54}$$

and for some value k we have

$$(x_{l1}, y_{l1} n z_{l1}) + k((x_{l2}, y_{l2}, z_{l2}) - (x_{l1}, y_{l1} n z_{l1})) = (x_{l3}, y_{l3}, z_{l3}) \tag{5.55}$$

Equation 5.55 says that the point C is somewhere on the line L. By simplifying Equation 5.54 we get

$$(x_p - x_{l3}, y_p - y_{l3}, z_p - z_{l3}).(x_{l1} - x_{l2}, y_{l1} - y_{l2}, z_{l1} - z_{l2}) = 0 \tag{5.56}$$

solving Equation 5.55 gives us the following

$$(x_{l1}, y_{l1} n z_{l1}) + k(x_{l2}, y_{l2}, z_{l2}) - k(x_{l1}, y_{l1} n z_{l1}) = (x_{l3}, y_{l3}, z_{l3}) \tag{5.57}$$

$$(x_{l1}(1-k) + kx_{l2}, y_{l1}(1-k) + ky_{l2}, z_{l1}(1-k) + kz_{l2}) = (x_{l3}, y_{l3}, z_{l3}) \tag{5.58}$$

Hence

$$x_{l3} = x_{l1}(1-k) + kx_{l2} \tag{5.59}$$

$$y_{l3} = y_{l1}(1-k) + ky_{l2} \tag{5.60}$$

$$z_{l3} = z_{l1}(1-k) + kz_{l2} \tag{5.61}$$

Therefore we have these three equations and Equation 5.56 making total of four equations and four unknowns x_{l3}, y_{l3}, z_{l3} and k. By solving these equations we can estimate point C on the line L which is perpendicular to the point P.

The distance between these two points can then be calculated by using the distance formula given as

$$r_d = \sqrt{(x_p - x_{l3})^2 + (y_p - y_{l3})^2 + (z_p - z_{l3})^2} \tag{5.62}$$

this formula can be generalised for all the points as

$$r_d = \sqrt{(x_i - x_l)^2 + (y_i - y_l)^2 + (z_i - z_l)^2} \tag{5.63}$$

where $i = 1,2,3....N$ and $l =$ points on the detected line perpendicular to the points in space.

All those points that are within a certain threshold distance from the line are also introduced as part of the line. The values of θ and ϕ are then calculated for the line, which are used to find out the value of γ. γ is then introduced in the hyperbolic equation and again the values of R, v and apex of hyperbola are calculated. These iterations tend to continue until the change in γ is zero or significantly small or a specific number of iterations is set.

5.6.4 Comparison with ANHT and Test Results

ANHT produces good results, but it is very time consuming and in dense noisy data it sometimes skips a line. The reason for that is use of too many control variables

like number of iterations, threshold of resolution, threshold of dissimilarity of two lines and threshold of distance of a point from detected lines. Once all these variable have been tuned for a specific data set it performs very well and gives accurate results but the setting up of variable causes operator intervention which stops the method to be used in an automated system. Certain modifications have been made to the method in order to automate it like setting up a check to keep on detecting lines until no more linear points are available, and to reduce the time consumption the neural net can be set to meet a performance goal so that it does not have to workup to the total number of epochs for each iteration but still there is a need of setting up the other parameters.

TABLE 5.1: ANHT and angle-based comparison

S No.	Time(min)	Time(sec)	Lines Detected	Lines Detected
-	ANHT	Angle-based	ANHT	Angle-based
1	1.46 min	0.7937 sec	1/1	1/1
2	3.27 min	0.76 sec	1/1	1/1
3	6 min	1.64 sec	1/1	1/1
4	6.07 min	0.93 sec	1/1	1/1
5	2.62 min	1.21 sec	1/1	1/1
6	2.018 min	0.7139 sec	1/1	1/1
7	11.88 min	4 sec	3/4	4/4
8	14.15 min	7.26 sec	2/4	4/4

ANHT has been used before the development of Angle based 3D line detection therefore test results have been shown in Table 5.1 for comparison purposes. The test data in which ANHT had failed to detect lines has been selected along with the output of Angle based 3D line detection in order to demonstrate the performance of the new technique. It is also worth noticing that the time for the detection procedure has reduced tremendously.

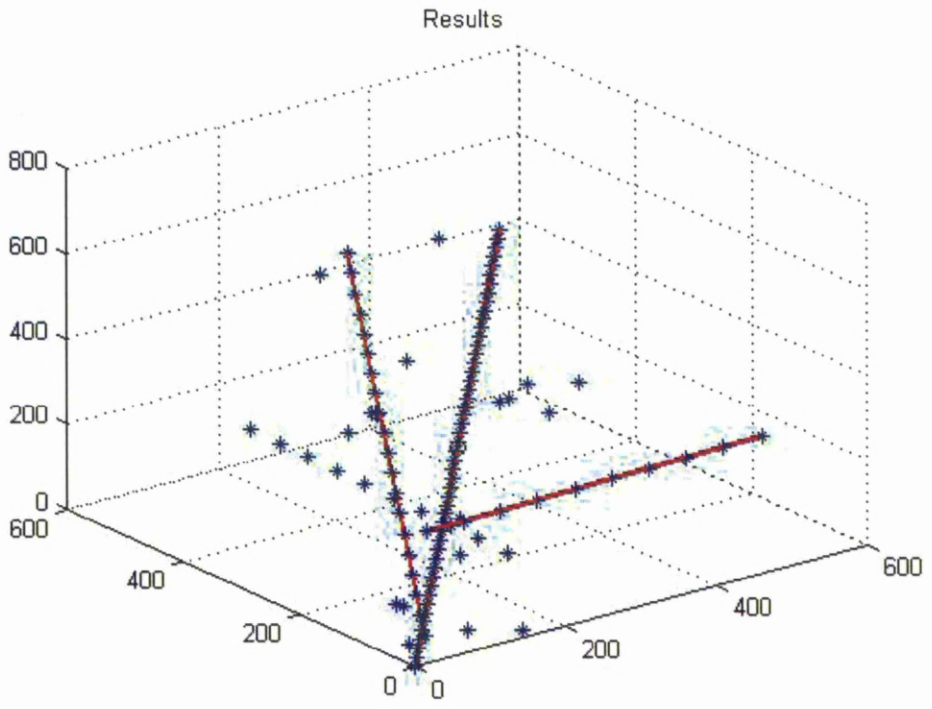

(a)

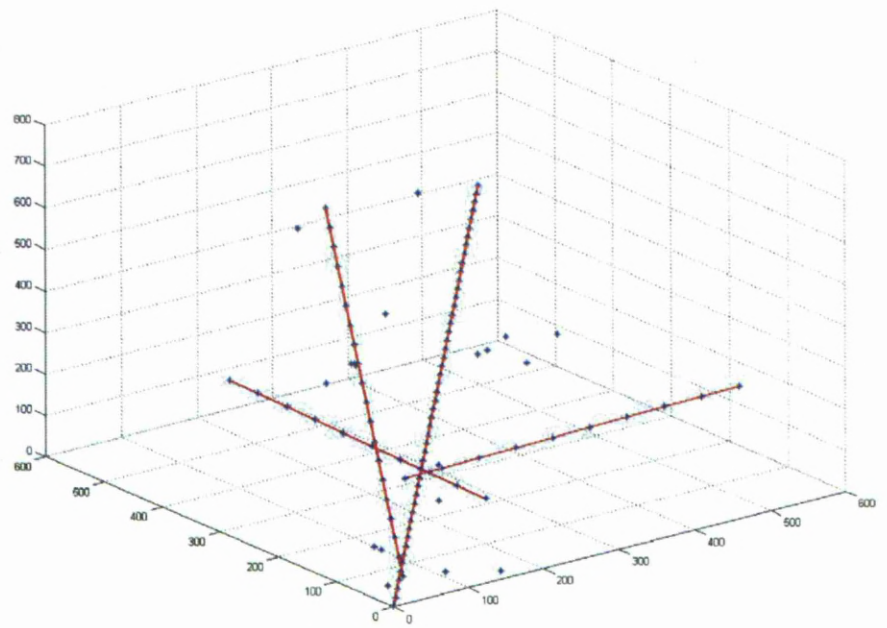

(b)

FIGURE 5.19: Results of exp 7, (a) ANHT (b) Angle-based line detection

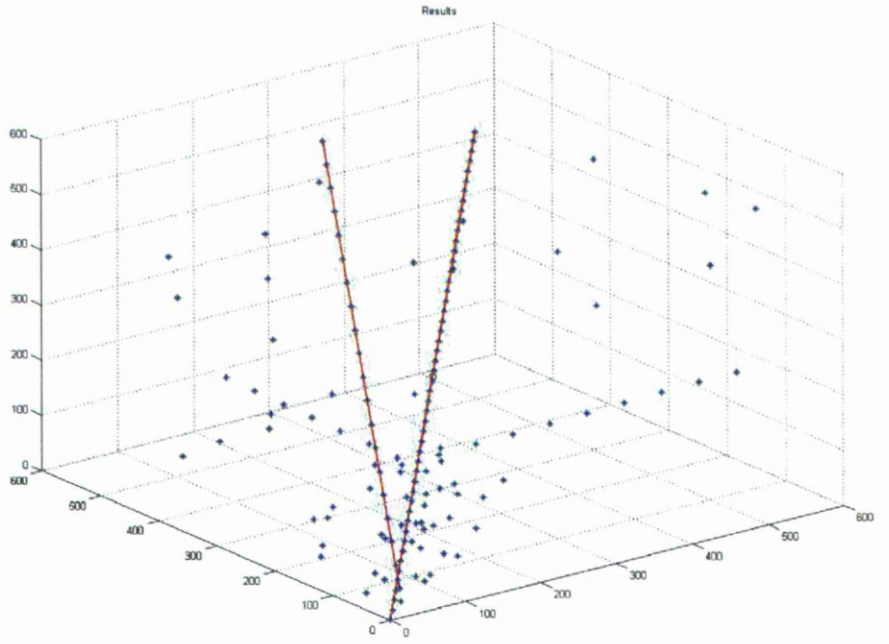

(a)

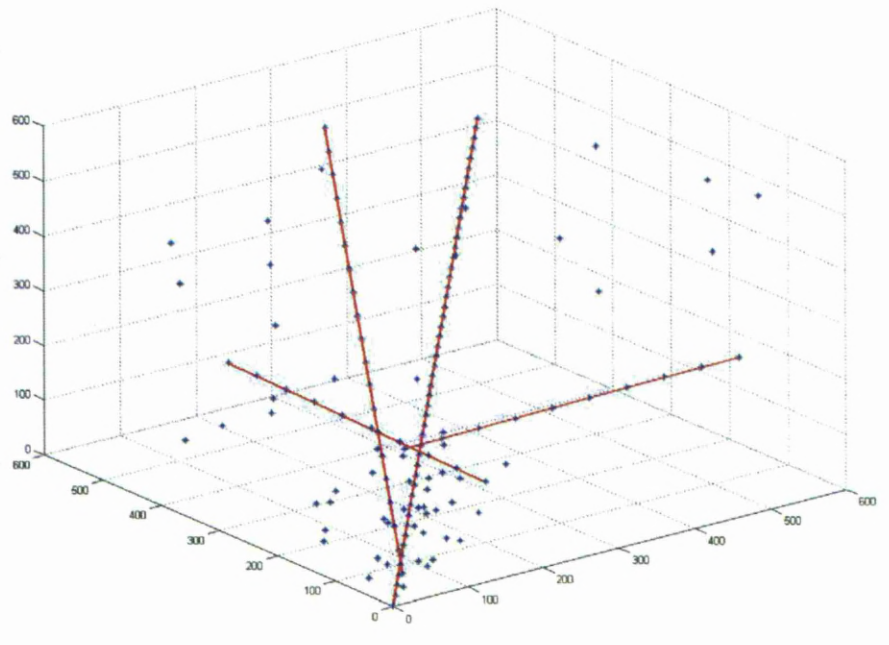

(b)

FIGURE 5.20: Results of exp 8, above ANHT below Angle-based line detection

The outputs of some of the experiments in Table 5.1 are shown in Figures 5.19 and 5.20.

5.7 GPR Data Results

In order to verify the effectiveness of the methods, the procedure was applied to a GPR data set. The radius of the target pipe was 27 cm. The hyperbolic signature of the pipe was extracted from the data set using standard thresholding and classification techniques. Hyperbola fitting was applied to the signature in order to extract the major and minor axis; assuming gamma to be zero and using equation 3 and 4 the depth and radius were calculated. The points were then plotted into 3D space and using 3D line detection technique a line was drawn through the points. The values of θ and ϕ are calculated and using these values in equation 5.23 gamma is calculated. Using this value of gamma in the Equation 5.7 and 5.10 gives us the new value of depth and radius. The results are shown in the Table 5.2 for ANHT and Table 5.3 for angle-bsaed technique.

TABLE 5.2: GPR data results for ANHT

File	True R (cm)	Initial R (cm)	% Error	R after iteration (cm)	% Error
18	27	28.15	4.26	28.09	4.04
19	27	27.92	3.41	27.87	3.22
20	27	27.6	2.22	27.55	2.04
21	27	27.19	0.70	27.14	0.52
28	27	27.21	0.78	27.16	0.59

TABLE 5.3: GPR data results for angle-based 3D line detection technique

File	True R (cm)	Initial R (cm)	% Error	R after iteration (cm)	% Error
18	27	28.15	4.26	27.96	3.56
19	27	27.92	3.41	27.74	2.74
20	27	27.6	2.22	27.42	1.56
21	27	27.19	0.70	27.01	0.04
28	27	27.21	0.78	27.03	0.11

5.8 Summary

This chapter has discussed a mathematical model that takes into account not only the depth, velocity and radius information but also the orientation of the target to the scan angle. The dangers of ignoring these parameters could result in disastrous consequences.

The estimation of the GPR parameters using the model is just the first step afterwards the data is subjected to an iterative 3D line detection technique that refines the estimated parameters. Two 3D line detection techniques have been used. One is the ANHT and the other is a novel technique known as the Angle-based 3D line detection.

ANHT uses Hough transform for line detection. Employing the standard Hough Transform in a high dimensional parameter space requires huge amount of computer memory. To solve this problem Adaptive Non-accumulative Hough Transform (ANHT) is used. Its performance has been demonstrated by the detection of 3D linear objects and shown that the method retains the desired HT characteristics of robustness to extraneous data. The amount of computer storage used by this method is much less than standard HT, and it can easily detect single and

multiple lines. Therefore it can be considered an important tool in underground utility radius correction process of GPR data.

Angle-based 3D line detection technique is a novel technique developed to replace ANHT. The results indicate that this method is very robust and efficient. It can detect lines in 3D space in significantly less time as compared to existing 3D line detection techniques which makes it ideal for processing of huge amount of data. The technique involves less number of control variable, It can easily detect noisy data by setting up of a specified threshold. This method is ideal for use in automatic inspection of GPR data. It reduces the processing time for utility detection along with better results.

Chapter 6

Near Real Time Site Data Processing

The scope of this study is to produce an automatic data interpretation system for GPR in near real time. In order to perform this task, some novel techniques have been developed that are more efficient in terms of time consumption as well as being accurate also the existing techniques have been modified to attain the goal.

The data site in this study is the University of Liverpool campus. Details about the site, targets, location and maps have been discussed in Chapter 2 and Appendix B. Since this is a very large data site, it is impractical to show results of the complete site. Therefore, a small selection has been shown in this study.

This chapter discusses the collaboration of all the techniques and methodologies that have been presented in the previous chapters in order to come up with a near real time data processing system. Results have been shown for the new system and a time comparison has been made to a previous study given in [1].

6.1 Near Real Time Processing System

The proposed system works in two ways. The first method is scan by scan processing in which data processing is performed on each individual scan and the results are estimated. This method gives near real time results however, the results may not be very accurate. For more accurate results, processing can be performed on a number of scans and this mode of operation is called multiple scan processing. The later stage require multiple scans to be taken so the operator can collect the data first and after a number of scans have been taken the data can be introduced to the processing system which would do on site processing and give results.

6.1.1 Scan by Scan Processing

In this mode of processing each scan is processed individually, all files need to go through the basic post processing stages in order to estimate the depth and radius. Since the files are being processed individually, this method does not estimate the orientation angle and the results are obtained on the assumption of the scan angle to be 90 degrees. Each file is subject to stages involving background removal, segmentation,classification, hyperbola fitting and result estimation using hyperbolic model.

The current study is compared to a previous study [1], results indicate that the procedures involved in the current study are superior to the previous study in terms of accuracy and time consumption. Three unique methods have been adopted to obtain these results. The background removal technique used here is the novel background removal technique using Eigenvalues, the details and methodology of

the technique has already been discussed in Chapter 4. Even though this technique takes slightly more time than the mean background removal technique, the resulting image is much more refined and the clutter and noise effects are tremendously removed hence less time is consumed in the classification and segmentation of the image.

Classification and segmentation consumes the major portion of time in the GPR data processing. This study recommends the use of two different classification approaches depending on the quality of data. The first approach is classification on the basis of regional features. This approach is very efficient in terms of speed and can accurately identify good hyperbolic shapes however if the target signature is distorted it tends to fail. On the other hand, a novel approach has been developed that uses Mel frequency cepstral coefficients (MFCC) to extract target signatures [58]. This technique is slightly slower than the regional feature based method but is able to identify not only the good hyperbolic shapes but also the distorted target reflections. MFCC has been explained in detail along with results and its comparison with regional feature based method in [107].

The classified hyperbolic signature is then subject to a fitting. This study uses a combination of two different fitters rather then a single fitter used in the predecessor study [1]. Therefore, the current fitter uses more time then the traditional fitting technique but the results are far better then the traditional fitter, hence, the suggested fitting technique is highly recommended.

The final stage involves introducing the fitting results into the hyperbolic model and estimating the target parameters. The results for plastic and steel pipes using single scan processing are shown in Table 6.1 these results can be compared to an example of a predecessor study [1] given in Table 6.2. The time estimation of

the techniques in this study and the previous study are also shown for comparison purposes. Table 6.3 is a time comparison for a 512 samples per scan by 600 scans image. It can be seen that in single scan processing the current study consumes slightly more time than the previous study but there is improvements in the estimated results.

6.1.2 Multiple-Scan Processing

The scan by scan processing methodology works on the assumption of scan angle being perpendicular to the orientation of the pipe hence assuming an orientation angle to be 90^0, but in reality this may not be the case. A better estimation of the orientation angle can be achieved by taking into consideration multiple radargrams. This can be performed by first scanning the data site for a number of scans and then using the proposed algorithm in estimating the target parameters.

The target pipes discussed in the previous section have been processed using this methodology and the results are shown in Tables 6.4 and 6.5. A set of seven to ten consecutive radargrams having a grid spacing of 1 m have been selected. each radargram had been processed individually first for the extraction of the hyperbolic signature and apex. The major and minor axis are also calculated using the hyperbolic model. The apex points in terms of target depth, grid spacing and horizontal placement from the grid start line are plotted into 3D space. A 3D line detection approach is then used in order to find linear points. This study has discussed two approaches for 3D line detection. One approach uses Applied Non-Accumulative Hough transform, this procedure has also been implemented in a previous study. ANHT is computationally expensive as well as time costly

TABLE 6.1: Pipe parameters resulted from current study

	True Depth	True radius	Fitter Results			Calculated Results		Error %	
	(cm)	(cm)	a	b	t0	Depth	Radius	Depth	Radius
Target 1 (Metal)	70	5	174.32	46.2	162	70.56	5.4	0.80	8.00
Target 2 (Metal)	70	5	180.07	44.68	169	69.89	4.56	-0.16	-8.80
Target 3 (Metal)	96.52	27	355.96	73.72	277	95.62	27.26	-0.93	0.96
Target 4 (Metal)	96.52	27	362	73.95	282	96.01	27.24	-0.53	0.89
Target 5 (Plastic)	73.66	15.5	223.71	53.29	184	73.06	15.77	-0.81	1.74
Target 6 (Plastic)	73.66	15.5	214.21	53.82	183	76.63	13.07	4.03	-15.68

TABLE 6.2: Pipe parameters resulted from previous study [1]

Parameters	True Depth (cm)	Calc Depth (cm)	Error (%)	True Radius (cm)	Calc Radius (cm)	Error (%)
Target 1 Metal	70	72.3	3.29	5	5.56	11.2
Target 2 Metal	70	65.55	6.36	5	5.64	12.8

TABLE 6.3: Time consumption for a single scan of 512 x 600

	Previous Study Time (sec) [1]	Current Study Time (sec)
Background Removal	0.0077	1.99
Classification and Segmentation	16.34	15.9476
Hyperbola Completion	0.0236	0.0508
Thinning and Skeletonisation	0.1456	0.113
Fitting and Parameter estimation	0.2536	1.0931
Total time	16.77	19.19

therefore the new Angle-based 3D line detection approach has been presented and selected for the study because of its less time consumption along with better accuracy. The results indicate that the error in the depth and radius has been improved after the first iteration.

Table 6.6 shows the total time consumed for the complete processing. This time involves the hyperbola extraction, fitting and modeling of each radargram within the data set, application of the 3D line detection technique and new parameter estimation. Overall it is clearly seen that the proposed techniques are well suited for a near real time processing system.

TABLE 6.4: Depth correction using multiple-scan processing

Parameters	True Depth (cm)	Calc Depth (cm)	Error (%)	Depth after 1st Iteration(cm)	Error (%)
Pipe 1 Metal	96.52	95.62	0.93	96.12	0.41
Pipe 1 Metal	96.52	96.01	0.53	96.4	0.12
Pipe 2 Plastic	73.66	73.06	0.81	73.26	0.54
Pipe 2 Plastic	73.66	76.63	4.03	74.20	0.73

TABLE 6.5: Radius correction using multiple-scan processing

Parameters	True Radius (cm)	Calc Radius (cm)	Error (%)	Radius after 1st Iteration(cm)	Error (%)
Pipe 1 Metal	27	27.26	0.96	26.96	0.14
Pipe 1 Metal	27	27.24	0.89	27.12	0.44
Pipe 2 Plastic	15.5	15.77	1.74	15.72	1.41
Pipe 2 Plastic	15.5	13.07	-15.68	14.53	6.25

TABLE 6.6: Time consumed by multiple-scan processing

	Previous Study Time	Current Study Time
Individual Processing of data set	3 min 20 Sec	3 Min 44 Sec
3D Line Detection and new parameter estimation	6 Min 7 Sec ANHT	1.64 Sec Angle-Based
Total Time	9 Min 27 Sec	3 Min 46 Sec

6.2 Summary

This chapter presents the complete overview of the study by sequentially explaining the processes that will be involved in the presented near real time data interpretation system. Results have been shown from one section of the data site that involves a metallic pipe and a plastic pipe.

The current study uses two modes. The first mode gives scan by scan results and

is done on the assumption that the orientation angle of the target is perpendicular to the scan angle; this assumption how ever introduces error into the results. The second mode is called multiple-scan processing and can be performed on site after collection of a number of scans. The introduction of the novel techniques for background removal, classification, fitting and 3D line detection not only gives improved results, but they have been compared in terms of time with a predecessor study and it is shown that the time consumption is reduced to nearly one third.

Chapter 7

Conclusions and Recommendations

This study addresses the task of near real time automatic detection and interpretation of GPR data. The techniques have been implemented on a data site containing water pipes as targets. Novel techniques were developed that treated the radar data keeping the time cost and accuracy of results in view. A general overview of existing techniques and methodologies have also been explained in the study for comparison purposes.

A large GPR database has been created around the University of Liverpool campus. Two different radars had been used to collect data using 900MHz and 400MHz antenna. The radar systems are the GSSI Sir-3000 and the GSSI Sir-2 system. A variety of signal and image processing approaches have been discussed along with the introduction of novel approaches for optimised and accurate results.

7.1 Conclusions

GPR is a non destructive technique for the investigation of the subsurface. A cylindrical object such as pipe would yield an inverted hyperbolic signature in an ideal case but unfortunately due to the diversity of the subterraneous environment and the nature of the electromagnetic configuration this is not the case. We might often get part of a hyperbola or no reflection at all depending on the ground conditions. More over non target reflections might often be confused as targets by in experienced personnel.

Artificial sites may provide better conditions to get a clear target reflection but real sites provide a much challenging environment and the main objective of a well constructed system is to operate successfully in a real environment. In this study data has been collected from a real site. Chapter 2 discusses the site selected for this study. A pipe laying project had been undertaken by the University of Liverpool in order to lay water pipes around the campus. Through out this project data had been collected in pictorial form, precise and accurate measurements of target position, dimensions and depth have been recorded. Data had been collected using two radar systems which are the GSSI Sir-2 and GSSI Sir-3000, more over extra surveys had been taken by the ORFEUS radar and DUO radar.

Chapter 3 discusses some existing GPR processing techniques, the aim of these target detecting techniques is to discriminate between targets and non targets. This stage is the most computationally expensive and serves as a bottle neck for a near real time GPR processing system. Neural networks are used to classify target from non targets based on certain features. Regional features have been found to

be most effective in this genre as they are not as computationally expensive as other techniques such as B-scan statistics and A-scan statistics and are more robust.

Chapter 4 is an introduction to some novel GPR processing techniques which are reliable, computationally inexpensive and overcome the high time cost of traditional approaches. Classification and segmentation of data into hyperbolic and non hyperbolic targets consumes the major portion of data processing time. The more noise and clutter the data has the more time will be consumed in processing, therefore a novel Eigen based background removal technique has been developed that produces a refined image with less clutter than the existing background removal techniques. Hence less target and non target reflections are passed on to the classification stage thus reducing the time cost. The data is then thresholded and converted into binary, the resulting image is then passed through a miniature blob deletion filter that rejects the small reflections which would not classify as reflection from a target and would consume extra time in the classification process. The minimum dimension values are set by the operator and depends on the data resolution. The third stage is the actual classification.

This study uses a novel classification approach that uses cepstral and polynomial coefficients for classification. Even though this approach is quite common in speech signal processing its use in GPR image processing has been introduced for the first time. The methodology of this approach has been discussed in detail in Chapter 4. A new fitting approach that is combination of two unique hyperbola fitters is presented in this study. Results from both the fitters are compared to the data points and the one having more accuracy is selected. The fitter gives accurate results for a wide range of hyperbolas.

Chapter 5 discusses the modelling and parameter estimation procedure. 3D line

detection approach has been used to correct the error in parameters. Some improvements have been suggested to a conventional 3D line detection approach that uses Applied Non-accumulative Hough Transform but the procedure is computationally expensive especially in cases where multiple targets are in close proximity with each other. A novel 3D line detection technique known as Angle-based 3D line detection has therefore been developed that is faster and much more accurate than ANHT.

Chapter 6 is a compilation of the selected methods and results are shown. The time consumption of each stage is also discussed and compared with a previous study. The results clearly show the superiority and accuracy of the proposed near real time automatic interpretation system.

7.2 Further Work

This study is a development of a near real time GPR interpretation system. Novel techniques have been developed keeping the time cost in mind. These techniques are background removal, MFCC classifier, hyperbola fitter and 3D line detection techniques. These approaches can be expanded to other GPR applications such as archeological surveys or land mine detection.

The Eigen based background removal process performs very well for strong targets from underground pipes however in certain cases the method might saturate weak target reflections. These reflections can be from underground cables and ducts. One solution to this problem is to stop the process after stage one in which results are nearly the same as in average background removal. Stopping the process

manually will hurdle the automatic process. Future work in this area requires the study of techniques that would make the weak reflections sharper and then merging with the Eigen based background removal technique. Doing so will also affect the clutter in the same manner. Therefore, an optimum balance needs to be achieved.

The MFCC classification technique requires further study as it could prove to be a very useful tool in GPR data classification. Liu *et. al.*[108] used MFCC's in a recent study for classification of hyperspectral images. It has been shown that, in standard MFCC calculations, only the power information is considered and the phase information is discarded. The standard MFCC can be improved by reintroducing the phase information. In this thesis polynomial coefficients have been used to reduce the sensitivity to mismatches or time shifts between training and testing data. Future work involves the addition of phase information as it may lead to further improved results.

MFCC's prove to be useful in target classification, however the cepstrum analysis itself has not been studied in detail and may lead to good results. Future work involves the study of cepstrum analysis for GPR data classification. A recent study by Sardar and Enis [109] used Mel-cepstral analysis for image representation. 2D cepstrums were used for face recognition and classification. An important characteristic of 2D cepstrum is its symmetry. This symmetry characteristic may be useful for hyperbolic shape classification that could lead to better results.

The study has presented two modes of operation one is the scan by scan processing that could be adopted onto the radar system and could do real time interpretation after each and every scan. Mode two is a multiple scan processing method that needs a set of radargrams to reduce the error in the estimated parameters of mode

one. This could be done by setting up a wireless link of the radar CPU with another system. The data can be sent to the second system after each scan, the data collection system can do mode one processing at the end of each scan while the secondary system can collect the scans through the wireless link and once a certain number of scans have been received the system can automatically process them in mode two and give the end results.

Most of the work done in this study is on 2D radargrams. However, tools and techniques can be developed for 3D data processing. Scans taken with different angles over an area can be arranged in a 3D grid. Targets such as pipes and cables are cylindrical in shape and would yield a distinct 3D shape. The 2D mathematical model used in this study can be modified for a 3D hyper-surface that involves all three axis. Doing this would require the modification of all the techniques involved from 2D to 3D. A 3D background removal technique can be developed to eliminate clutter. Also the classification technique should be able to extract the desired 3D shape from the data set. Inputs to the mathematical model would require the results from a 3D hyper-surface fitter. Future work involves the study of methods and applications that could result to these objectives and if successful will open a whole new area of research in GPR data analysis.

These novel techniques have been used for underground utility investigation however their use is not restricted to this application and they can be incorporated in other GPR applications such as land mine detection and archeological studies. The background removal, hyperbola classifier and fitter and 3D line detection techniques can also be used as image processing applications.

Bibliography

[1] S. Shihab. *Automatic Detection and Characterisation of Cylindrical Objects using Ground Penetrating Radar.* PhD thesis, University of Liverpool, March 2005.

[2] Remke L. Van Dam. Three-dimensional stratigraphic models of sedimentary deposits using full-resolution ground-penetrating radar. Technical report, Michigan State University, 2009.

[3] Howard Scott. Liverpool university campu test trials. Technical report, ORFEUS Project, 2009.

[4] Harry M. Jol. *Ground penetrating radar: theory and applications.* Elsevier Science, 2009.

[5] W. Al-Nuaimy. *Automatic feature detection and interpretation in ground penetrating radar data.* PhD thesis, University of Liverpool, 1999.

[6] GSSI. *SIR System-20 User's Manual.* Geophysical Survey Systems, Inc., 13 Klein Drive, P.O. Box 97, North Salem, NH 03073-0097, 2003.

[7] David J. Daniels. *Ground Penetrating Radar - 2nd Edition.* The Institution of Electrical Engineers, London, UK, 2nd edition, 2004.

[8] J. W. Brooks. *The Detection of Buried Non-Metallic Anti-Personnel Land Mines.* PhD thesis, The University of Alabama in Huntsville, August 2000.

[9] D. J. Daniels, D. J. Gunton, and H.F. Scott. Introduction to surface radar. In *Commuication, Radar and Signal Processing*, page 135, Aug 1988.

[10] D. J. Daniels, R. Roberts, and M. Vendi. Ground penetrating radar for the detection of liquid contaminents. *Journal of Applied Geophysics*, 33:195–207, 1995.

[11] S. B. Costello, D. N. Chapman, C. D. F. Rogers, and N. Metje. underground asset locations and condition assessment technologies. *Tunnelling and Underground space technology*, 22:525–542, 2007.

[12] Nigel J. and Cassidy. *Ground Penetrating radar Theory and Applications*, chapter Chapter 5-Ground Penetrating Radar Data Processing, Modelling and Analysis, pages 141–176. Elsevier B.V., 2009.

[13] S. J. Radzevicius and J. J. Daniels. Ground penetrating radar polarization and scattering from clylinders. *Journal of Applied Geophysics*, 45:111–125, 2000.

[14] B. J. Allred, N. R. Fausey, Chi-Chih Chen, L. Peters, Jr., and H. Youn. Dpr detection of drainage pipes in farmlands. In *tenth international conference on ground penetrating radar*, 2004.

[15] B. Sai and L. Ligthart. Improved gpr data preprocessing for detection of various landmines. In *Eighth International Conference on Ground Penetrating Radar, Proceedings of SPIE*, pages 80–84, 2000.

[16] A. Merwe, I. Gupta, and L. Peters. Jr. A clutter reduction technique for gpr data from mine like targets. In *Processdings of SPIE*, volume 3710, pages 1094–1106, 1999.

[17] D. Carevic, I. Chant, and T. Caelli. Feature extraction and classification of minelike targets from gpr data using gaussian mixture models. In *Information, Decision and Control Conference proceedings*, pages 329–334, 1999.

[18] B. Ulug, J. Zhao, and S. Ahalt. Feature based classification of sar data using rbf network. In *Conference on Signal Processing, Sensor Fusion and target recognition IV, Proceedings of SPIE*, pages 583–594, 1995.

[19] Y. Nagashima, H. Saito, S. Kobayashi, and M. Jun-ichi. Automatic recognition of hyperbolic pattern in underground cross-sectional image. *Technical report of IEICE. SANE*, 95:959–956, 1996.

[20] R. J. Chignell and H. S. Dabis. A pipe detection radar with automatic three dimensional mapping. In *Sixth International Conference On Ground Penetrating Radar, Sendai, Japan*, pages 511–514, 1996.

[21] T. C. Molyneaux, S. G. Millard, J. H. Bungey, and J. Q. Zhou. Radar assessment of structural concrete using neural networks. *NDT&E International*, 28(5):281–288, 1995.

[22] R. Lotlikar and R. Kothri. Bayes-optimality motivated linear and multilayered perceptron-based dimensionality reduction. *IEEE Transactions on Neural Networks*, 11(2):452–463, 2000.

[23] P. Gamba and S. Lossani. Neural detection of pipe signatures in ground penetrating radar images. *IEEE Transactions on Geoscience and remote sensing*, 38(2):790–798, 2000.

[24] W Al-Nuaimy, Y. Huang, V. Nguyen, and A. A. Eriksen. Automatic feature selection for unsupervised image segmentation. *Applied Physics Letters*, 77(8):1230–1232, 2000.

[25] H. Youn and C. Chen. Neural detection for buried pipe using fully polarimetric gpr. In *Tehth International Conference on Ground Penetrating Radar*, June 2004.

[26] G. Grandjean and H. Durand. A complete package for gpr data processing. *Journal of Computer and Geosciences*, 25:141–149, 1999.

[27] B. B. Chaudhuri and G.P. Samanta. Elliptic fit of objects in two and three dimensions by moment of inertia optimization. *Pattern Recongnition Letters*, 12(1):315–335, 1992.

[28] J. Illingworth and J. Kittler. A survey of the hough transform. *Computer vision, graphics and image processing*, 44(1):87–116, 1988.

[29] F. Bookstein. Fitting conic sections to scattered data. *Computer Graphics and Image Processing*, 9:56–71, 1979.

[30] A. Fitzgibbon, M. Pilu, and R. Fisher. Direct least square fitting ellipses. *IEEE transactions on Pattern Analysis and Machine Intelligence*, 21(5):476–480, May 1999.

[31] J. Porrill. Fitting ellipses and predicting confidence envelopes using a bias corrected kalman filter. *Image and Vision computing*, 8(1):37–41, 1990.

[32] M. Pilu, A. Fitzgibbon, and R. Fisher. Ellipse-specific direct least square fitting. In *In Proceedings of International Conference on Image processing, (ICIP06)*, volume 3, 1996.

[33] H. Chen and A. G. Cohn. Probabilistic robust hyperbola mixture model for interpreting ground penetrating radar data. In *Proceedings of the 2010 IEEE congress on computational intelligence (WCCI10)*, 2010.

[34] O Leary P. and Zsomber-Murray. Direct and specific least square fitting of hyperbolae and ellipses. *Journal of Electronic Imaging*, 13(3):492–503, 2004.

[35] S. Shihab and W. Al-Nuaimy. Radius estimation for cylindrical objects detected by ground penetrating radar. *Sensing and Imaging: An International Journal*, 6(2):151–166, 2005.

[36] S. Shihab, W. Al-Nuaimy, and A. Eriksen. Radius estimation for subsurface cylindrical objects detected by ground penetrating radar. In *Proceedings of the tenth International conference on ground penetrating radar*, 2004.

[37] S. Shihab, W. Al-Nuaimy, Y. Huang, and A. Eriksen. Neural network target identifier based on statistical features of gpr signals. In *Ninth international conference on ground penetrating radar*, pages 135–138, 2002.

[38] S. Shihab, W. Al-Nuaimy, and A. Eriksen. Image processing and neural network techniques for automatic detection and interpretation of ground penetrating radar data. In *Proceedings of the 6th WSEAS International Multiconference on Circuits, Systems, Communications and Computers*, 2002.

[39] S. Shihab, W. Al-Nuaimy, Y. Huang, and A. Eriksen. Neural network classifier for detecting subsurface objects. In *Proceedings of IEE/EPSRC Joint National Conference PREP 2002*, 2002.

[40] W. Al-Nuaimy, H.Lu, S. Shihab, and A. Eriksen. Automatic mapping of linear structure in 3-dimensional space in ground penetrating radar data. In

Proceedings of IEEE/ISPRS Joint Workshop on Remote Sensing and Data Fusion Over Urban Areas, Rome, pages 198–201, 2001.

[41] L. E. Bernold, L. Venkatesan, and S. Survarna. A multi-sensory appriach to 3d mapping of underground utilities. In *International Symposium on Automation and Robotics in Construction, 19th (ISARC). Proceedings*, pages 525–530, 2002.

[42] C. Stolte and K. Nick. Eccentricity-migration: a method to improve the imaging of pipes in radar reflection data. In *The Fifth International Conference on Ground Penetrating Radar*, pages 723–733, 1995.

[43] G. Olhoeft. Maximising the information return from ground penetrating radar. *Journal of Applied Geophysics*, 43:175–187, 2000.

[44] Aleksander Vasi Ristic, Dusan Petrovacki, and Miro Govedarica. A new method to simultaneously estimate the radius of a cylindrical object and the wave propagation velocity from gpr data. *Computers and Geosciences*, 35:1620–1630, 2009.

[45] L. Capineri, P. Grande, and J. temple. Advanced image processing technique for real-time interpretation of ground penetrating radar images. *International Journal of Imaging Systems and technology*, 9(1):51–59, 1998.

[46] Gary R. Olhoeft. Automatic processing and modeling of gpr data for pavement thickness and properties. In *Eighth International Conference on Ground Penetrating Radar*, April 2000.

[47] Peter A. Torrione, Chandra S. Throckmorton, and Leslie M. Collins. Performance of an adaptive feature-based processor for a wideband ground penetrating radar system. *IEEE Transactions on aerospace and electronics systems*, 42:644–658, 2006.

[48] R. Roberts and D. Cist. Enhanced target imaging in 3d using gpr data from orthogonal profile lines. In *Ninth International conference on ground penetrating radar, Proceedings of SPIE*, pages 256–261, 2002.

[49] J. Binningbo, E. Eide, and J. Hjelmstad. 3d migration of gpr array antenna data. In *Eighth International Conference on Ground Penetrating Radar*, pages 459–463, 2000.

[50] W. Al-Nuaimy, H. Lu, S. Shihab, and A Eriksen. Automatic 3-dimensional mapping of features using gpr. In *Ninth International Conference on Ground Penetrating Radar. S.Barbara, CA*, May 2002.

[51] T. Sato. Automatic data processing procedure for ground probing radar. *IEICE transactions on communication, E77-B*, 6:831–837, June 1994.

[52] S. M. Shrestha and I. Arai. High resolution image reconstruction by gpr using music and sar processing method for landmine detecion. In *Geoscience and Remote Sensing Symposium, IGARSS'03. Proceedings, IEEE*, volume 4, pages 2921–2923, 2003.

[53] Jiang Wei, Pennock Steve, and Shepherd Peter. Novel short-time music in non-linear fmcw gpr signal analysis. In *13th International Conference on Ground Penetrating Radar (GPR), 2010*, 2010.

[54] A. Zarkhidze and E. Lemenager. Case study - use of 3d gpr technologies for utility mapping in paris. In *Tenth International conference on Ground penetrating radar*, 2004.

[55] Dusan Petrovacki and Aleksandar Ristic. Mapping process of kikinda area gas line network by use of gpw and subterrestrial detection technologies. In *4th International Conference on recent problems in geodesy and related fields with international importance*, Feb 2007.

[56] Umar S. khan and W. Al-Nuaimy. Angle-based 3d line detection and its application for radius correction of underground utilities in gpr data. In *International Workshop of Advanced Ground Penetrating Radar, IWAGPR*, 2009.

[57] Umar S. Khan, W. Al-Nuaimy, and H. Lu. 3d line detection using adaptive non-accumulative hough transform and its application for radius correction of underground utilities in gpr data. In *International Workshop of Advanced Ground Penetrating Radar, IWAGPR*, 2009.

[58] Umar S. Khan, Abd El-Samie. Fathi, and W. Al-Nuaimy. Detection of land mine and underground utilities from acoustic and gpr images with a cepstral approach. *Journal of Visual Communication and Image Representation, JVCI*, 21:731–740, 2010.

[59] Umar S. Khan and W. Al-Nuaimy. Background removal from gpr data using eigenvalues. In *13th International Conference on Ground Penetrating Radar, Lecce, Italy*, 2010.

[60] W. Al-Nuaimy, S. Shihab, U. Khan, and Y. Huang. An iterative technique for the characterisation of the geometry of buried utilities in a non-uniform

medium. In *Proceedings of the 12th International Conference on Ground Penetrating radar*, 2008.

[61] GSSI. *SIR System-2 Operation Manual.* Geophysical Survey Systems Inc., 13 Klein Drive, P.O. Box 97, North Salem, NH 03073-0097, USA, June 1994.

[62] GSSI. *SIR 3000 Users Manual.* Geophysical Survey Systems, Inc., 12 Industrial Way, Salem, NH 03079-4843, July 2009.

[63] Massimiliano Pieraccini, Fillippo Parrini, Gaetano De Pasquale, and Howard Scott. The orfeus project (optimised radar for finding every utility in the street). In *IEEE Geoscience and remote sensing symposium, IGARSS*, volume 2, pages 9–12, July 2008.

[64] A. M. Thomas, C. D. F. Rogers, N. Metje, and D. N. Chapman. A stakeholder led accuracy assessment system for utility location. In *Workshop on Advanced Ground Penetrating Radar, Naples*, 27-29 June 2007.

[65] G. Manacorda, H. F. Scott, P. D. Loach, J. J. Kazik, D. Pinchbeck, M. Rameil, J. Capdeville, and P. Fournier. The european giga project. In *Proceedings of the Tenth International Conference on Ground Penetrating radar*, volume 1, pages 355–358, Delft, Neitherland, 2004.

[66] Fawzy Abujarad, Andreas J., and A.S.Omar. Clutter removal for landmine using different signal processing techniques. In *Tenth International Conference on Ground Penetrating Radar*, pages 697–700, June 2004.

[67] Li Ting-jun, Kong ling jiang, and Zhou Zheng-ou. Symmetry filtering method for gpr clutter reduction. In *ICMMT Proceedings*, 2008.

[68] Huo Zhihua and Wang Minghui. The application of kl transform to remove direct wave in ground penetrating radar records. In *Fourth International Conference on Image and Graphics*, 2007.

[69] B. Cagnoli and T.J. Ulrych. Singular value decomposition and wavy reflections in ground-penetarting radar images of base surge deposits. *Journal of Applied Geophysics*, 48:175–182, July 2001.

[70] R. Gonzalez and H.woods. *Digital Image Processing.* Addison Wesley, 1992.

[71] A. Papoulis. *Probabilit and Random Variables and Stochastic Processes.* McGraw-Hill, USA, 1984.

[72] E. R. Kanasewich. *Time Sequence Analysis in Geophysics.* University of Alberta Press, Canada, 1975.

[73] M. Bartlett. *Periodogram analysis and continous spectra.* Nature, 1948.

[74] P. Castigliono. *Wigner-Ville Distribution. Encyclopedia of Biostatistics.* John Wiley and Sons, England, 2005.

[75] L. Cohen. *Time-Frequency Analysis.* Prentice Hall, USA, 1995.

[76] L. Cohen. *Time-Frequency Analysis.* Prentice Hall, 1995.

[77] Daubechies. Time frequency localisation and signal analysis. *IEEE Transactions Information Theory*, 36(5):961–1005, 1990.

[78] F. Tomita and S. Tsuji. *Computer Analysis of Visual Textures.* Kluwer Academic Publishers, USA, 1990.

[79] M. Tuceryan and A. Jain. *Handbook of pattern recognition and computer vision.* Scientific Publisher Company, Singapore, 1993.

[80] J. Sklansky. Image segmentation and feature extraction. *IEEE Transactions on Systems, Man and Cybernetics*, 8:237–247, 1978.

[81] P. Ohanian and R. Dubes. Performance evaluation for four classes of textural features. *Pattern Recognition Society*, 25(8):819–833, March 1992.

[82] R. Conners and A. Harlow. A theoretical comparison of texture algorithms. *Digital Image Processing and Analysis, IEEE Compter Society*, 2:323–341, 1985.

[83] Simon Haykins. *Neural Networks: A Comprehensive Foundation (2nd Edition)*. Prentice Hall, 1998.

[84] W. McCulloch and W. Pitts. A logical calculus of the ideas immanent in nervous activity. *Bulletin of Mathematical Biophysics*, 7:115–133, 1943.

[85] Gilbert Strang. *Linear Algebra and Its Application*. Wellesley-Cambridge Press, Orlando, 3rd edition, 2009.

[86] Freire, S.L.K., and T.J. Ulrych. Application of singular value decomposition to vertical seismic profiling. *Geaophysics*, 53:778–785, 1988.

[87] T. J. Ulrych, M.D. Sacchi, and S.L.M. Freire. Eigenimages processing of seismic section. In *Covariance Analysis for Seismic Signal Processing. Soc. Explor. Geophys., Tulsa*, pages 241–274, 1999.

[88] R. Chengalvarayan and L. deng. Speech trajectory discrimination using the minimum classification error learning. *IEEE transaction on Speech and Audio processing*, 6:505–515, 1998.

[89] P. D. Polur and G. E. Miller. Experiments with fast fourier transform, linear predictive and cepstral coefficients in dysarthic speech recognition algorithms

using hidden markov model. *IEEE transactions on Neural Systems and Rehabilitation Engineering*, 13:558–561, 2005.

[90] S. Dharanipragada, U. H. Yapanel, and B. D. Roa. Robust feature extraction for continuous speech recognition using mvdr spectrum estimation method. *IEEE Transaction on Audio, Speech and Language processing*, 15:223–234, 2007.

[91] T. Kinnunen. *Spectral Features For Automatic Text-Independent Speaker Recognition.* PhD thesis, University of Joensuu, Department of computer science, Finland, 2003.

[92] D. Pullella. Speaker identification using higher order spectra. Master's thesis, Dissertation of Bachelor of Electrical and Electronic Engineering, University of Western Australia, 2006.

[93] S. Furui. Cepstral analysis technique for automatic speaker verification. *IEEE Transactions on Acoustics, Speech, And Signal Processing*, ASSP-29, No. 2:254–272, 1981.

[94] R. Gandhiraj and P. S. Sathidevi. Auditory-based wavelet packet filterbank for speech recognition using neural network. In *Proceedings of the 5th international conference on Advanced Computing and Communication*, pages 666–671, 2007.

[95] A. I. Galushkin. *Neural Networks Theory.* Springer-Verlag Berlin Heidelberg, 2007.

[96] G. Dreyfus. *Neural Networks Methodology and Applications.* Springer-Verlag Berlin Heidelberg, 2005.

[97] H. Hedberg and P. Nilsson. A survey of various discrete transforms used in digital image compression algorithms. In *Proceedings of the Swedish System-On-Chip Conference*, pages 13–14, 2004.

[98] S. Shihab and W. Al-Nuaimy. A comparison of segmentation techniques for targets extraction in ground penetrating radar data. *Near-Surface Geophysics*, 2(1):49–57, 2004.

[99] R. Haralick. *Computer and Robot Vision.* Addison-Wesley, 1992.

[100] W. Al-Nuaimy, Y. Huang, M. Fang, V. Nguyen, and A. Eriksen. Automatic detection of buried utilities and solid objects with gpr using neural networks and pattern recognition. *Journal of Applied Geophysics*, 43:157–165, 2000.

[101] A. Dwyer. A faster divide and conquer algorithm for constructing delaunay triangulation. *Algorithmica*, 2:137–151, 1989.

[102] Richard C. Dubes. How many clusters are best?—an experiment. *Pattern Recogn.*, 20(6):645–663, 1987.

[103] Howard Demuth, Mark Beale, and Martin Hagan. *Neural Network Toolbox 6 User's Guide.* The Mathworks, Inc, March 2008.

[104] P. V. C. Hough. A method and means for recognizing complex patterns. *U.S. Patent*, 3:654, 1965.

[105] A. L. Kesidis and N. Papamarkov. A windows-based inverse hough transform. *Pattern recognition*, 33:1105–1117, 2000.

[106] J. Illingworth and J. Kittler. The adaptive hough transform. *IEEE Trans. Pattern Anal. Mach. Intell.*, 9(5):690–698, 1987.

[107] Umar S. Khan, Abd El-Samie. Fathi, and W. Al-Nuaimy. Identification of underground utility signatures in ground penetrating radar data using mel frequency cepstral coefficients. IET Radar Sonar and Navigation.

[108] D. Liu, X. Wang, J. Zhang, and X. Huang. Feature extraction using mel frequency cepstral coefficients for hyperspectral image classification. *Applied Optics*, 49(14):2670–2675, 2010.

[109] Serdar Cakir and A. Enis Cetin. Mel-cepstral feature extraction methods for image representation. *Optical Engineering*, 49(9), 2010.

[110] Markt G. Subsurface characterisation of hazardous waste sites using ground penetrating radar. In *Second International Symposium on Geotechnical applicatoins of Ground Penetrating Radar*, page 41, 1988.

Appendices

Appendix A

GSSI SIR® -2 and SIR® -3000 Specifications

Following are the detailed specifications of Geophysical Survey Systems Inc. Surface Impulse Radar System 2 [61]:

Hardware

Radar Processor	Motorola DSP 562002
Display	21cm 640x480 Colour Active Matrix LCD VGA
	for real time display
CPU	80486 DX
Memory	16Mb RAM
Hard Drive	Upto 450 Mb Internal IDE
Input/Output	Antenna Input (Including survey wheel)
	Fiber Optic Transmit Trigger
	Parallel:
	12V DC Input, 3LED Indicators,
	Multifunction Connector: RS 232, VGA
	Keyboard, NTSC/PAL Video (optional)
Printer	Optional thermal plotter for real time or playback
	hard copy of wiggle plot or gray scale line scan data

Electrical

Antennae	Operates all GSSI surface and air-coupled antennae:
	Dipoles:
	Unshielded: 15, 20, 30, 40,80, 120 MHz
	Shielded: 100, 200, 300, 400, 500, 900, 1000 MHz
	Monostatic: 80, 100, 120, 300, 500, 900, 1000 MHz
	Bistatic: 15, 20, 30, 40, 80, 100, 120, 300 MHz
	TEM Horns:
	1.0 GHz, 2.5 GHz (bistatic, unshielded)
Dynamic Range	24 bit (144 dB unstacked)
A/D Conversion	8 or 16 bit
Input Power	12V DC (3 Amps or 36 Watts)

Mechanical

Dimensions	29 x 27 x 14 cm
Weight	6.3 Kg

Operational

Temperature	0C to +40C (operating),
	-25C to +60C (storage)
Humidity	0 - 100%(RH)
Environmental	Radar control unit is environmentally sealed
	Can be used in inclement weather

Software

Data Collection	Continuous profiling with manually or survey wheel-emplaced horizontal reference marks. Point stacking either during continuous collection by stacking sequential scans or in stationary point collection mode
Display mode	User selected: colour/gray scale line scan, wiggle plot or oscilloscope formats
Range Gain	100 dB automatic or user selected; range gain prior to digitisation for maximum system dynamic range
Filters	Automatic or user selected vertical and horizontal filtering in real-time or post-acquisition processing
Stacking	Automatic or user selected
Transmit Rate	Automatic or user selected up to 64KHz
Scan Rate	Automatic or user selected, 8 to 64 scans per second
Sampling	Automatic or user selected, 128, 256, 512, 1024, 2048 samples/scan
Range	Automatic or user selected: 5 to 2000 nanoseconds
Data Transfer	Through parallel port to PC with bi-directional parallel port
Post Processing	Optional RADAN software can be installed for additional post processing and colour printing

Following are the detailed specifications of Geophysical Survey Systems Inc. Surface Impulse Radar System 3000 [62] :

System

Display	8.4; TFT, 800 x 600 resolution, 64K
Display modes	Line scan, O-scope, 3D
Data Storage	Internal memory 2GB, Accepts CF Memory upto 2GB(using FAT 16 format)
Number of Channels	1 (one)
Antennas	Compatible with all GSSI antennas
Languages	English, French, Italian, German, Spanish, Japanese, Chinese

Software

Data Format	RADAN (.dzt)
Scan Rate Example	220 scans/sec at 256 samples/scan, 16 bit and 120 scans/sec at 512 samples
Scan Interval	User-selectable
Number of samples per scan	256, 512, 1024, 2048, 4096, 8192
Operating Modes	Free run, survey wheel, point mode
Time Range	0 - 8,000 nanoseconds full scale, user selectable
Gain	Manual or Automatic, 1-5 gain points (-20 to +80 dB)
Filters	Vertical: Low Pass, High Pass IIR and FIR, Horizontal: Stacking, Background removal

Mechanical

Dimensions	12.4(l) x 8.7(w) x 4.1(h) in (31.5 x 22 x 10.5 cm)
Weight	9 lbs (4.1 Kg) Including battery
Environmental	Water Resistant

Operational

Temperature	-10C to +40C
Charge Power Requirements	15V DC, 4 Amps
Battery	10.8V DC, Internal
Transmit Range	Upto 100KHz
Environmental	Radar control unit is environmentally sealed. Can be used in inclement weather.

Input/Output

Available Ports	Antenna input, DC Power input, Serial RS232 (GPS port), Compact Flash memory, USB master slave

Appendix B

University of Liverpool test Site

At the end of year 2007 water pipes were laid around the University of Liverpool campus. The campus was devised into three sections *i.e.* North Campus, South Campus and Central Campus. The pipes used in were metallic in nature with an outer insulation and the outer most boundary was or hard rubber as seen in the samples given in Figure 1.

FIGURE 1: Sample of target pipes

TABLE 1: Nominal diameters of pipes used in the site

Inner Dia (mm)	Outer Dia (mm)	Outer Casing Dia (mm))
20	26.9	90
25	33.7	90
32	42.4	110
40	48.3	110
50	60.3	125
65	76.1	140
80	88.9	160
100	114.3	200
125	139.7	225
150	168.3	250
200	219.1	315

The nominal outer and inner diameter of the pipes used through out the site is given in Table 1.

The trenches dug for the pipes were at least three to four feet wide and a pair of two pipes were going through as shown in Figure 2. The depth of the trench varied from place to place from 3 feet to 5 feet.

FIGURE 2: Sample of target pipes through trench

The backfilling was done using red sand and gravel. The order of the pipes and backfill material was such that the water pipes were laid at the base of the trench

and they were covered using red sand, after that hollow plastic pipes were laid on top for electrical cables to pass through and another thing layer of red sand was put on top. Over this layer a layer of gravel was set which was pressed and leveled. On top of that the original surface was remade. The original surfaces were of different material as the pipes were spread across a large area. These surfaces were asphalt roads for road crossings and parking areas, granite tiles and concrete slabs for walkways and pavements and clay for grassy meadows. Figure 3 shows an area where the backfill is shown in progress. The dielectric characteristics of these materials can be seen in Appendix 3.

FIGURE 3: Backfill in progress

At many places the trenches are being intersected with already existing utilities such as pipes and cables of different sizes and materials. The measurements of all the intersecting pipes have also been recorded along with the target pipes. Figure 4 show an area where already existing utilities are intersecting the trench.

The sites are composed of parking areas, road intersections, walkways and grass. Site one is mostly of walkway for students, its surface has been made by bricks

FIGURE 4: Existing utilities intersecting the trench

and granite marbles and benches have been placed at certain locations. Site two involves two parking areas, a meadow with tall grass, concrete slabs and walkway. Site three is mostly car parking and an area with grassy meadow at the end. Figure 5, 6 and 7 are maps of the areas according to the buildings.

An accurate map of the target locations and measurements including depth profile and other utility crossings is available in CAD format. Samples of which can be seen in Figure 8, 9 and 10.

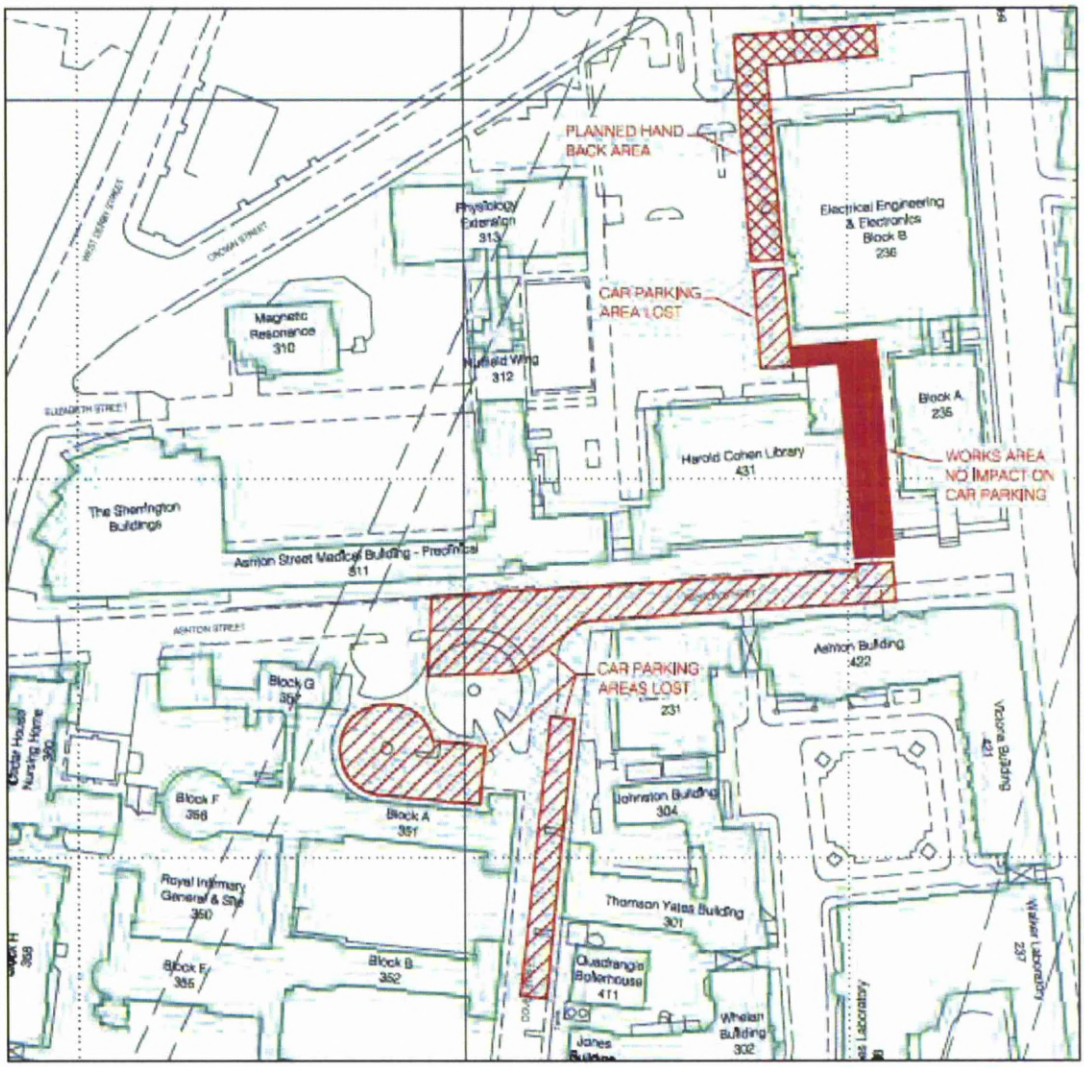

FIGURE 5: Site 1, North campus

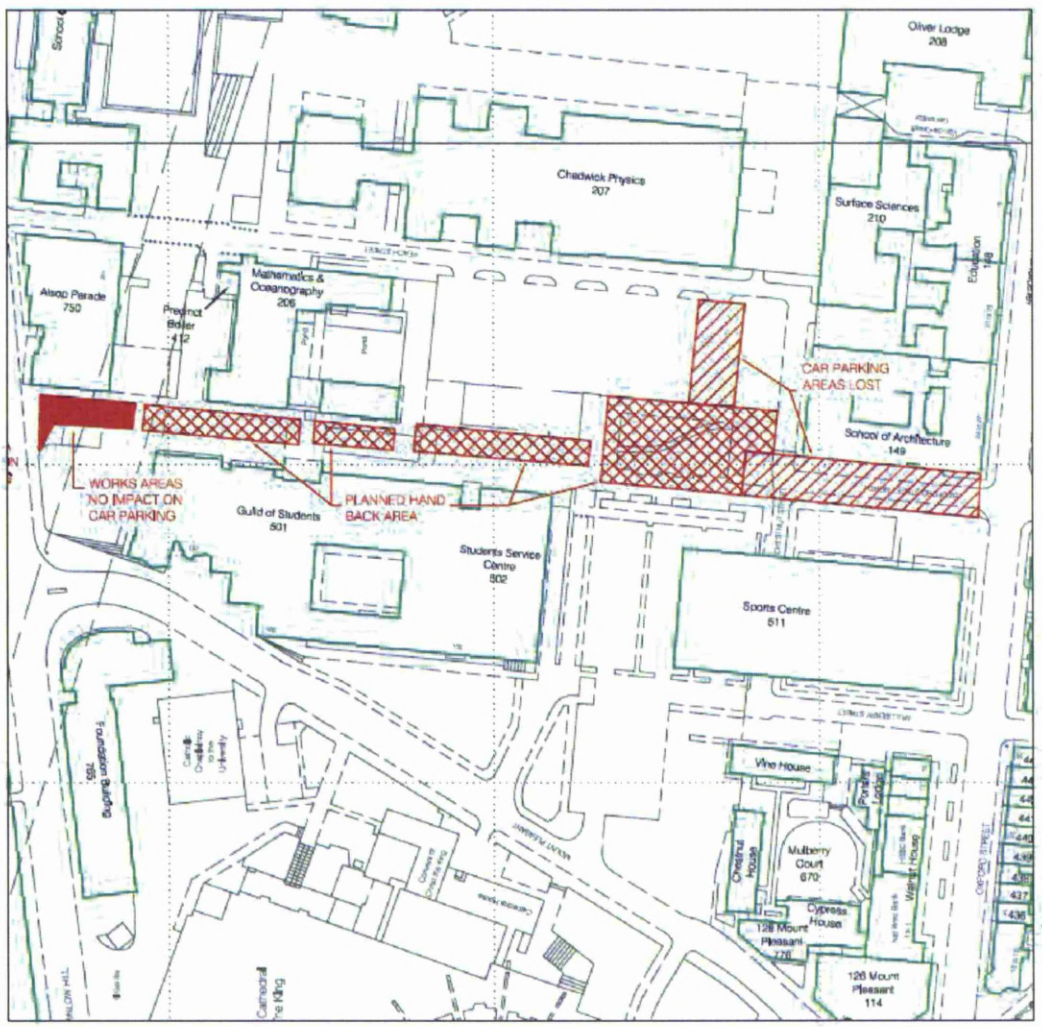

FIGURE 6: Site 2, Central campus

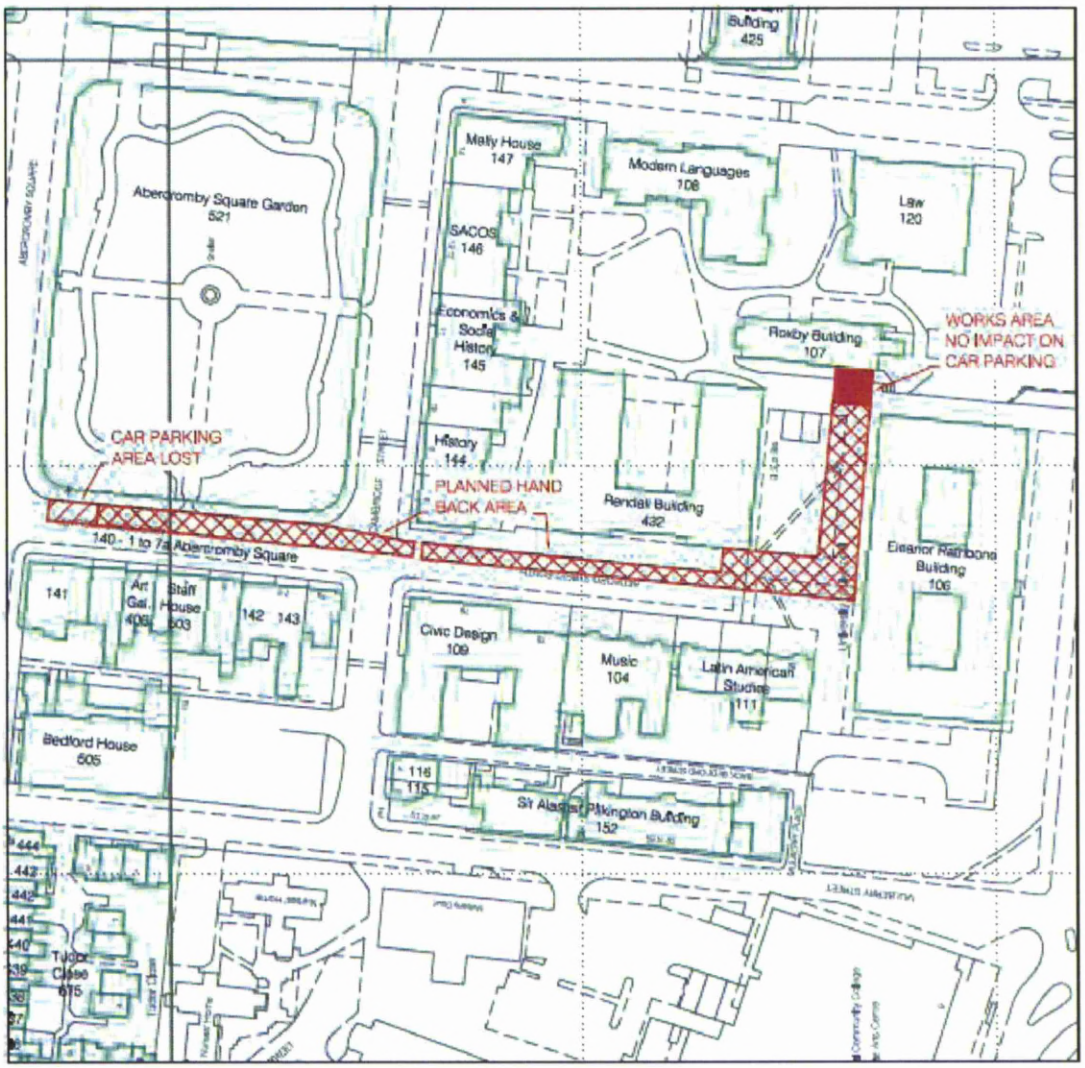

FIGURE 7: Site 3, South campus

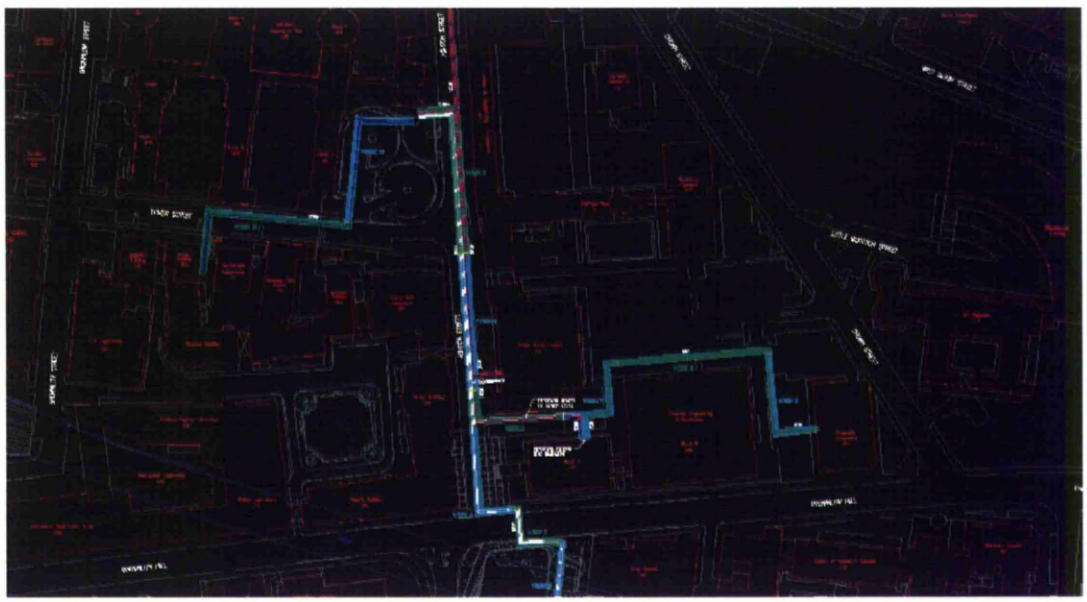

FIGURE 8: Site 1, North campus

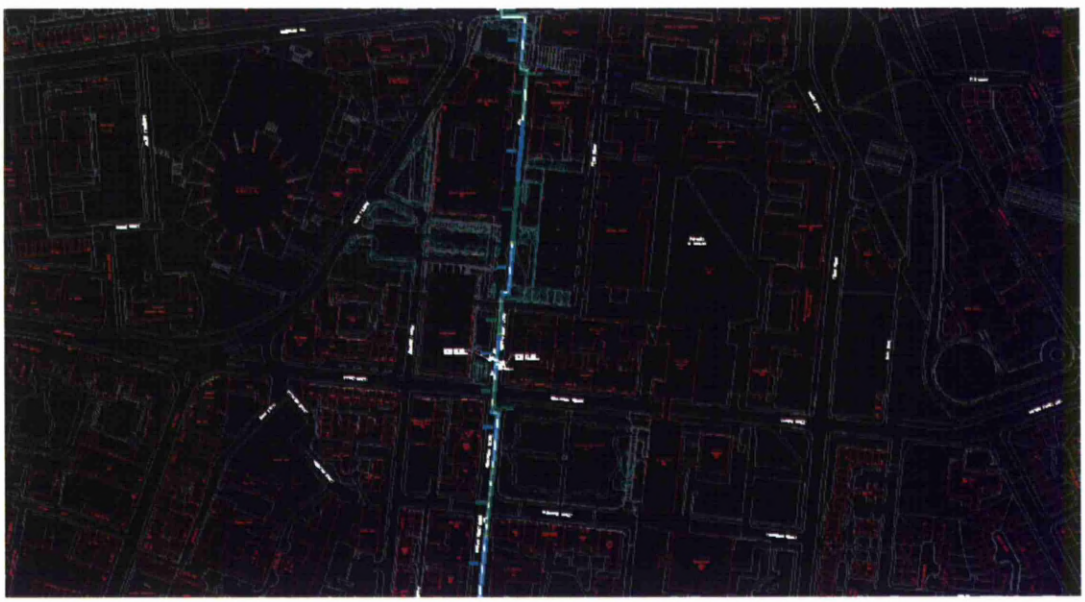

FIGURE 9: Site 2, Central campus

FIGURE 10: Site 3, South campus

Appendic C

GSSI SIR® File Format

GSSI radar systems are stored in binary as a binary block of data preceded by a file header containing information about the site, the data acquisition settings, the system configuration and on-board processing parameters. The detailed format of the header structure for these files, which are given the extension *.dzt*, is given below in Tables 2 and 3, as published by GSSI in the RADAN®processing software manual [61]. If tightly packed, the header portion will occupy 1024 bytes (1 kilobyte) of memory.

TABLE 2: DZT data structure

Data type	Field name			Description
unsigned	sec2	:	5	Second/2 (0-29)
unsigned	min	:	6	Minute (0-59)
unsigned	hour	:	5	Hour/2 (0-23)
unsigned	month	:	5	Day/2 (1-31)
unsigned	year	:	4	Year-1980(0-127)

TABLE 3: DZT header structure

Data type	Field name	Description
unsigned short	dzt_hdr_id	OxOOFF if header
unsigned short	offset_to_data	Offset to data in bytes (1024)
unsigned short	samples_per_scan	Samples per scan
unsigned short	bits_per_sample	Bits per data word
unsigned short	amp_midpoint	Offset to data mid-point
float	scans_per_second	Scans per second
float	scnas_per_metre	Scans per meter
float	metres_per_mark	meters per mark
float	start_time_offset	Position (ns)
float	total_time_range	Range (ns)
unsigned short	number_passes	Number of passes for 2D files
long	create_date	Creation date and time
long	modified_date	Last modification date and time
unsigned short	offset_to_gain	Offset to range gain function
unsigned short	sizeof_rgain	Size of range-gain function
unsigned short	offset_to_text	Offset to text
unsigned short	sizeof_text	Size of text
unsigned short	offset_proc_hist	Offset to processing history
unsigned short	sizeof_proc_hist	Size of processing history
unsigned short	number_of_channels	Number of channels
float	ave_rel_diel_perm	Average dielectric constant
float	top_in_metres	Top position in metres
float	range_in_metres	Range in metres
char	reserved	Reserved
unsigned short	scans_per_pass	Scans per pass
unsigned short	line_num	line number
unsigned short	start_x	Initial line number
unsigned short	start_y	Initial station number
unsigned short	end_x	Final line number
unsigned short	end_y	Final station number
character	dtype	Data type
character	antenna	Antenna name
unsigned short	channel_mask	Active channel mask
integer	checksum	Checksum for header
character	variable	Range gain, comments & history

Appendix D

Dielectric Characteristics

The velocity of electromagnetic wave propagation is governed by the electrical permittivity of the medium material, which depends primarily upon its water content. Over the range of frequencies over which GPR operates, water has a relative permittivity ϵ_r of approximately 80, while the solid constituents of most soils have dry relative permittivities between 2 and 9. Although these permittivities vary to an extent with frequency, they remain relatively constant for most materials in the microwave frequency range. Table 4 shows the conductivity and relative permittivity of a number of common materials, measured at 100 MHz [7], [110].

The time taken by a radar wave to travel down and back through one meter (or foot) of a particular material is known as the two-way slowness of the subsurface material and Table 5 shows the two way slowness for different materials. These two way slowness values are just estimate and the exact value of the sites may vary [61].

TABLE 4: Typical range of dielectric characteristics of various materials

Material type	**Conductivity (S/m)**	**Relative permittivity**[§]
Air	0	1
Asphalt, dry	$10^{-3} - 10^{-2}$	$2 - 4$
Asphalt, wet	$10^{-2} - 10^{-1}$	$6 - 12$
Clay, dry	$10^{-3} - 10^{-2}$	$2 - 6$
Clay, saturated	$10^{-1} - 1$	$15 - 40$
Coal, dry	10^{-2}	3.5
Coal, wet	10^{-1}	8
Concrete, dry	$10^{-3} - 10^{-2}$	$4 - 10$
Concrete, wet	$10^{-2} - 10^{-1}$	$10 - 20$
Freshwater	$10^{-4} - 10^{-2}$	81
Freshwater ice	10^{-3}	4
Granite, dry	$10^{-8} - 10^{-6}$	5
Granite, wet	$10^{-3} - 10^{-2}$	7
Limestone, dry	$10^{-9} - 10^{-6}$	7
Limestone, wet	$10^{-2} - 10^{-1}$	8
Permafrost	$10^{-5} - 10^{-2}$	$4 - 8$
Rock salt, dry	10^{-4}	$4 - 7$
Sand, dry	$10^{-7} - 10^{-3}$	$4 - 6$
Sand, saturated	$10^{-4} - 10^{-2}$	$10 - 30$
Sandstone, dry	$10^{-9} - 10^{-6}$	$2 - 3$
Sandstone, wet	$10^{-5} - 10^{-6}$	$5 - 10$
Seawater	4	81
Seawater ice	$10^{-2} - 10^{-1}$	$4 - 8$
Shale, saturated	$10^{-2} - 10^{-1}$	$6 - 9$
Snow, firm	$10^{-6} - 10^{-5}$	$8 - 12$
Soil, sandy, dry	$10^{-4} - 10^{-2}$	$4 - 6$
Soil, sandy, wet	$10^{-2} - 10^{-1}$	$15 - 30$
Soil, loamy, dry	$10^{-4} - 10^{-3}$	$4 - 6$
Soil, loamy, wet	$10^{-2} - 10^{-1}$	$10 - 20$
Soil, clayey, dry	$10^{-4} - 10^{-1}$	$4 - 6$
Soil, clayey, wet	$10^{-1} - 1$	$10 - 15$

[§] The permittivity of free-space, $\epsilon_0 = 8.854 \times 10^{-12}\,\mathrm{Fm}^{-1}$

TABLE 5: Typical range of two way slowness values of various materials

Material type	**S (ns/meters)**	**S (ns/feet)**
Air	6.5	2
Ice	13	4
Snow Firn	8	2.5
Water	59	18
Asphalt	14	4.5
Dry Concrete	15	4.5
Wet Concrete	23	7
Dry Sand	13	4
Wet Sand	25.5	7.5
Saturated Sand	33	10
Dry Sand and Gravel	15.5	4.5
Frozen Sand and Gravel	14.5	4.5
Dry Loamy/Clayey Soils	10.5	3
Dry Mineral/Sandy Soils	16	5
Organic Soils	52.5	16
Wet Sandy Soils	32	9.5
Frozen Soil/Permafrost	16	5
Tills	22	6.5
Peats	51.5	15.5
Wet Clay	34	10.5
Dry Clay	13	4
Dry Granite	14.5	4.5
Wet Granite	16.5	5
Wet Basalt	19	6
Volcanic Ash	23.5	7
Potash Ore	15.5	4.5
Dry Bauxite	33	10
Syenite Porphyry	16	5
Travertine	18.5	5.5
Coal	14	4
Dry Limestone	15.5	4.5
Wet Limestone	18.5	5.5
Wet Sandstone	16	5
Dry Salt	16	5

Appendix E

Effect of Orientations on Hyperbolic Signature

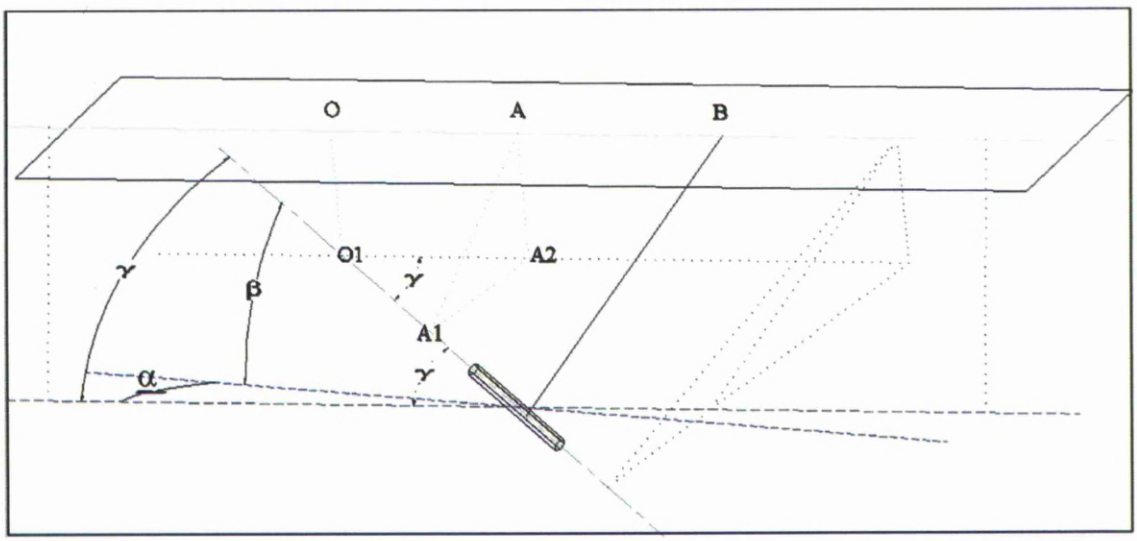

FIGURE 11: 3D presentation of a buried cylinder with azimuth and vertical orientations

Figure 11 shows a subsurface cylinder of radius R in 3D-space with an azimuth orientation angle α and vertical inclination angle β.

From Figures 11 and 12, from the right-angled triangle AA_1A_2:

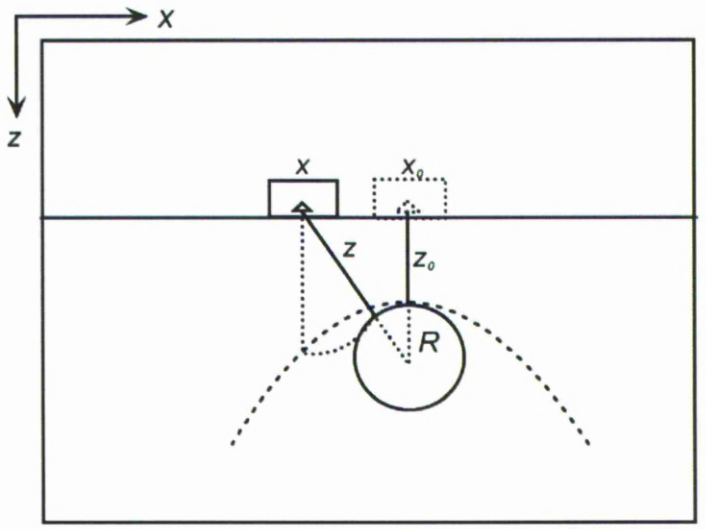

FIGURE 12: Side view of the buried cylinder in Figure 12

$$(AA_1)^2 = (A_1A_2)^2 + (AA_2)^2 \tag{1}$$

where

$$AA_1 = Z + R \tag{2}$$

$$AA_2 = OO_1 = Z_0 + R \tag{3}$$

since $Z = \frac{vt}{2}$ then:

$$AA_1 = \frac{vt}{2} + R \tag{4}$$

and

$$OO_1 = \frac{vt_0}{2} + R \tag{5}$$

and

$$A_1A_2 = (x - x_0)\sin\gamma \tag{6}$$

Substituting Equations 4, 4, and 4 into Equation 1 tog get:

$$\left(\frac{vt}{2} + R\right)^2 = \left(\frac{vt_0}{2} + R\right)^2 + ((x - x_0)\sin\gamma)^2 \tag{7}$$

Manipulating Equation 7 leads to:

$$\left(\frac{t + \frac{2R}{v}}{t_0 + \frac{2R}{v}}\right)^2 - \left(\frac{(x - x_0)\sin\gamma}{\frac{v}{2}t_0 + R}\right)^2 = 1 \tag{8}$$

It was shown in Chapter 4 that the relation between α, β, and γ is:

$$\cos\gamma = \cos\alpha\cos\beta \tag{9}$$

In the special case when $\alpha = 0$, then this means that the three points: A, A_1, and A_2 are aligned do not form a triangle anymore. Consequently, the relation in Equation 1 is not valid. Instead the new assumption will be:

$$AA_1 = A_1A_2 + AA_2 \tag{10}$$

Substituting for the values of AA_1, AA_2, and A_1A_2 leads to:

$$\frac{vt}{2} + R = \frac{vt_0}{2} + R + (x - x_0)\sin\gamma \tag{11}$$

Since $\alpha = 0$ then $\gamma = \beta$, with manipulation, then Equation 11 becomes:

$$t = \frac{2}{v}(x - x_0)\sin\beta + t_0 \tag{12}$$

It can be seen that Equation 12 is of a straight line, which means that the resulting signature will not be hyperbolic and hence will not be detected as a target.

Appendix F

Optimised Radar to Find Every Utility in the Street (ORFEUS) Field Trials [3]

LIVERPOOL UNIVERSITY CAMPUS TEST TRIALS

27/28 August 2009

SUMMARY

1 Introduction

This report describes the results of the measurement sessions carried out in Liverpool University Campus (UK) on august 27/28. The aim of this trial was to evaluate the performances of the ORFEUS radar, which has been developed within the European union 6th FP. The ORFEUS radar is a CW-SF (Continuous Wave – Stepped Frequency) GPR (Ground Penetrating Radar), which was developed using innovative technologies aimed at providing better performances than present pulsed GPR system. One of the most important characteristics for GPR radar is the penetration depth. This parameter can be determined as the maximum depth of the target that can be detected by the radar. The aim of the ORFEUS project is to develop a radar whose penetration depth performance was better than standard pulsed GPR. The performances assessment is done comparing the results achieved by ORFEUS with those obtained with a state-of-the-art pulsed GPR, called DUO®, commercialized by I.D.S. s.p.a. This radar is a pulsed GPR, which uses two different radiating antennas in the same case, with centre frequency respectively at 200MHz and a 600MHz. The radar uses the 200MHz antenna to detect deep target, while the 600MHz is used to obtain high-resolution image of shallow targets.

In this trials 5 different sites have been inspected, named site A, B, C, D and E, the position of each of these sites is sketched in Figure 1. There are targets whose position and depth are documented all along the 5 sites described above. It is a couple of pipe buried at approximately 1 meter deep, which is indicated with the red line in the map. This target, along with others, has been used for the performance assessment.

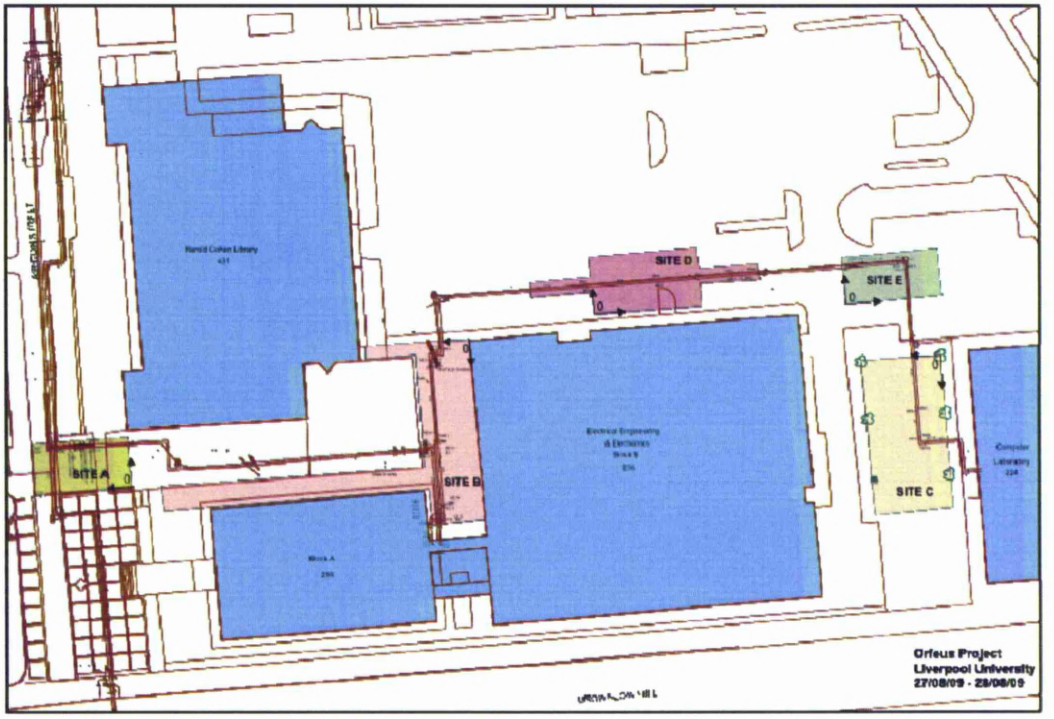

Figure 1 - View of the Campus with test sites

In next pages, each of the sites will be described. For every site a dense grid of sweeps has been done, but here only the more significant ones, where interesting target can be found, will be reported.

2 Site A

Site A is located in front of the main entrance of the Electrical Engineer and Electronics Department Building. In Figure 2 the global view of the site is shown. This site is located in a pedestrian area in front of the main entrance of the Electrical Engineer Dept. The pavement in this area is made by granite tiles. Figure 3 shows the ORFEUS and the DUO radars during a measurement session.

Figure 2 - View of the Site A

Figure 3 – ORFEUS radar and DUO during measurement session

Figure 4 represents the map of the surveyed area. Red arrow shows sweep length and orientation. In next pages the comparison between ORFEUS and DUO B-scans will be shown. The comments of these maps can be found at the end of the last Site A measurement.

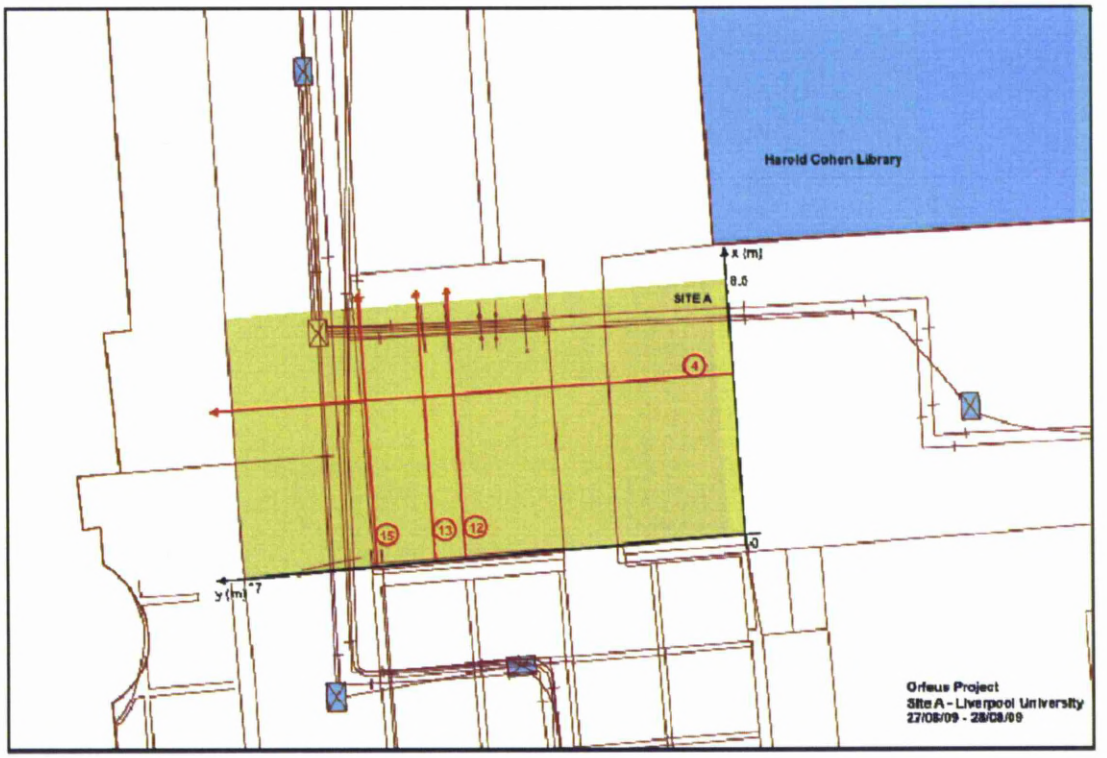

Figure 4 - Site A map and sweep location

2.1 LIVERPOOL - SITE A – POSITION 4

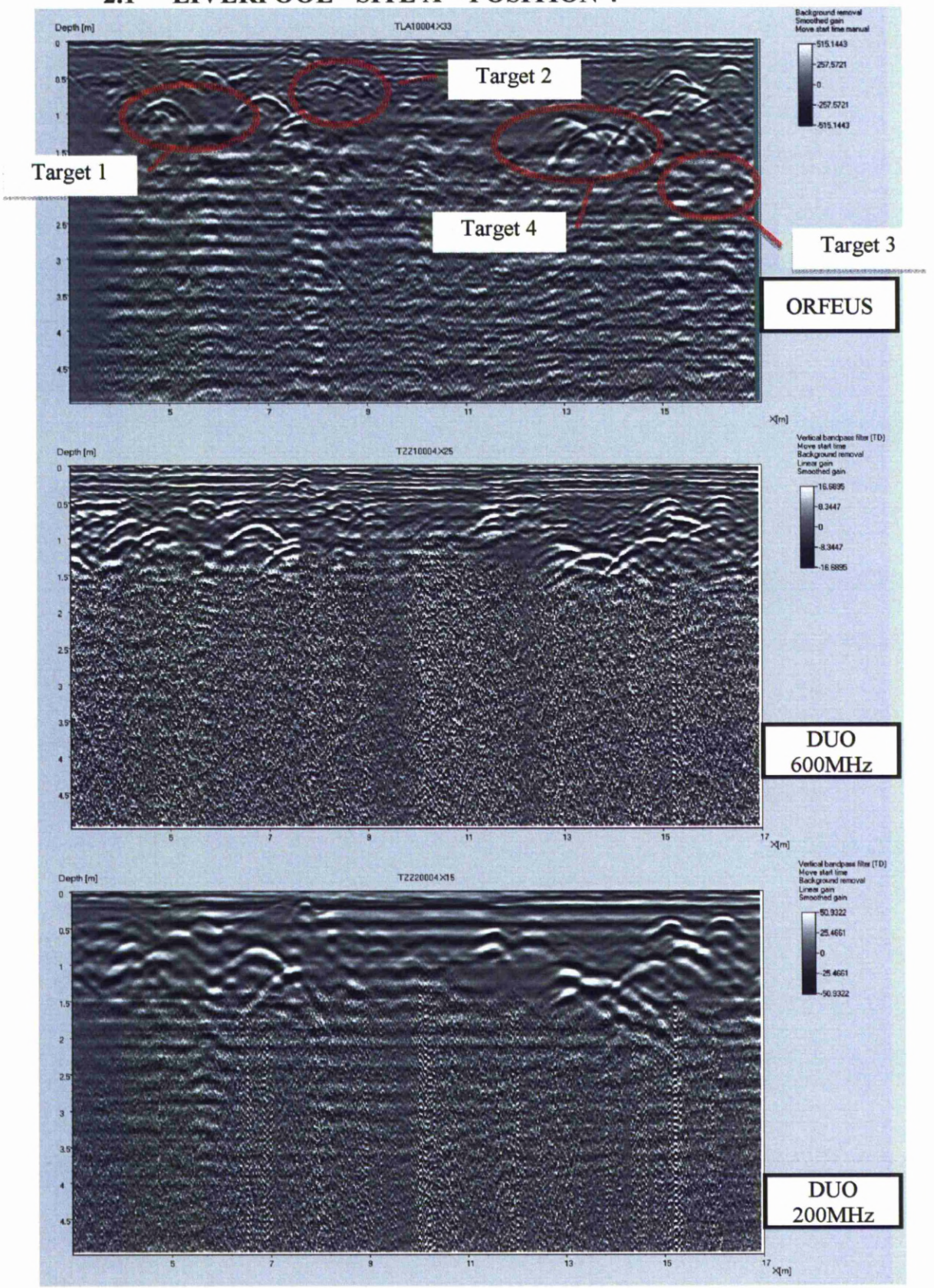

2.2 LIVERPOOL - SITE A – POSITION 12

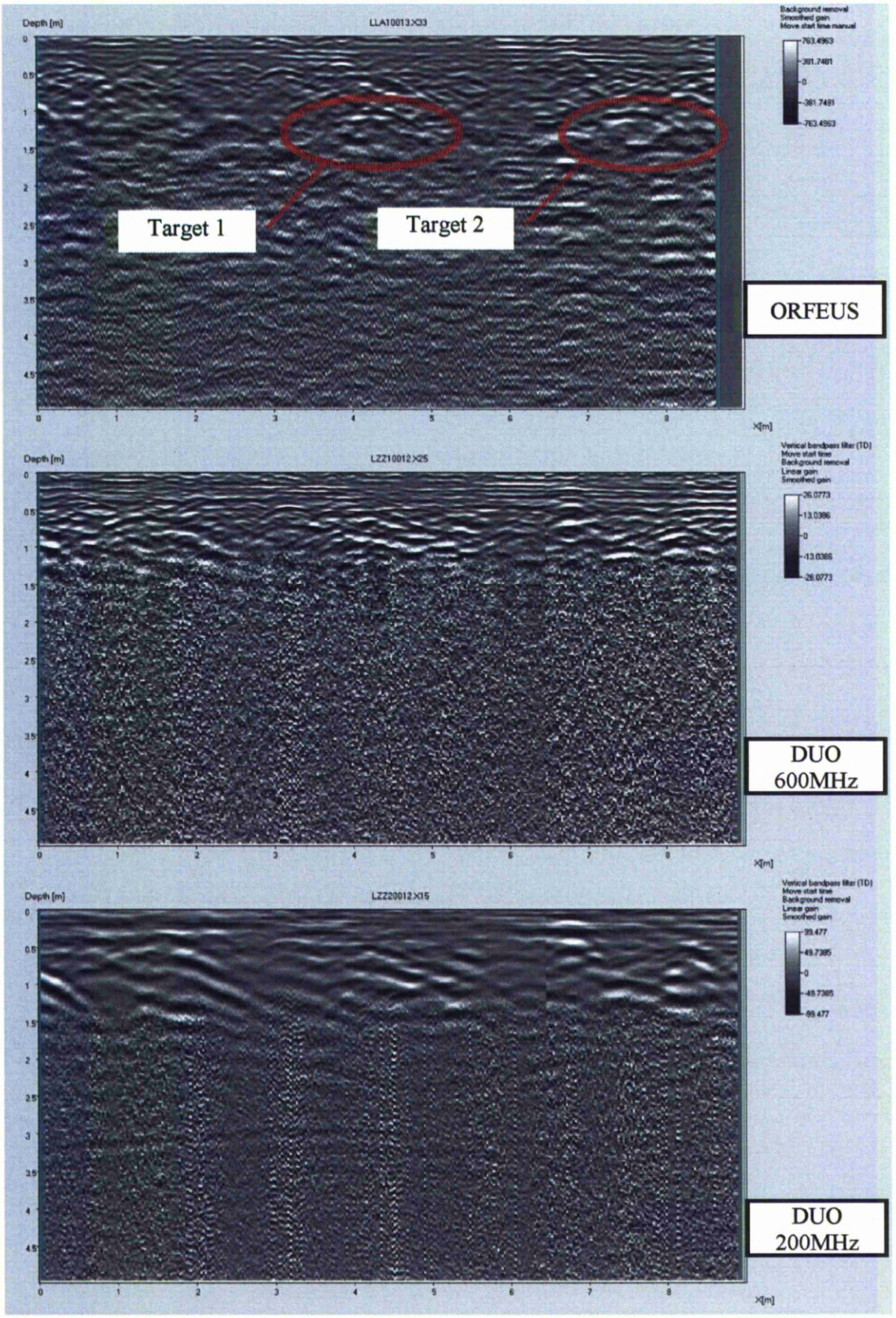

2.3 LIVERPOOL - SITE A – POSITION 13

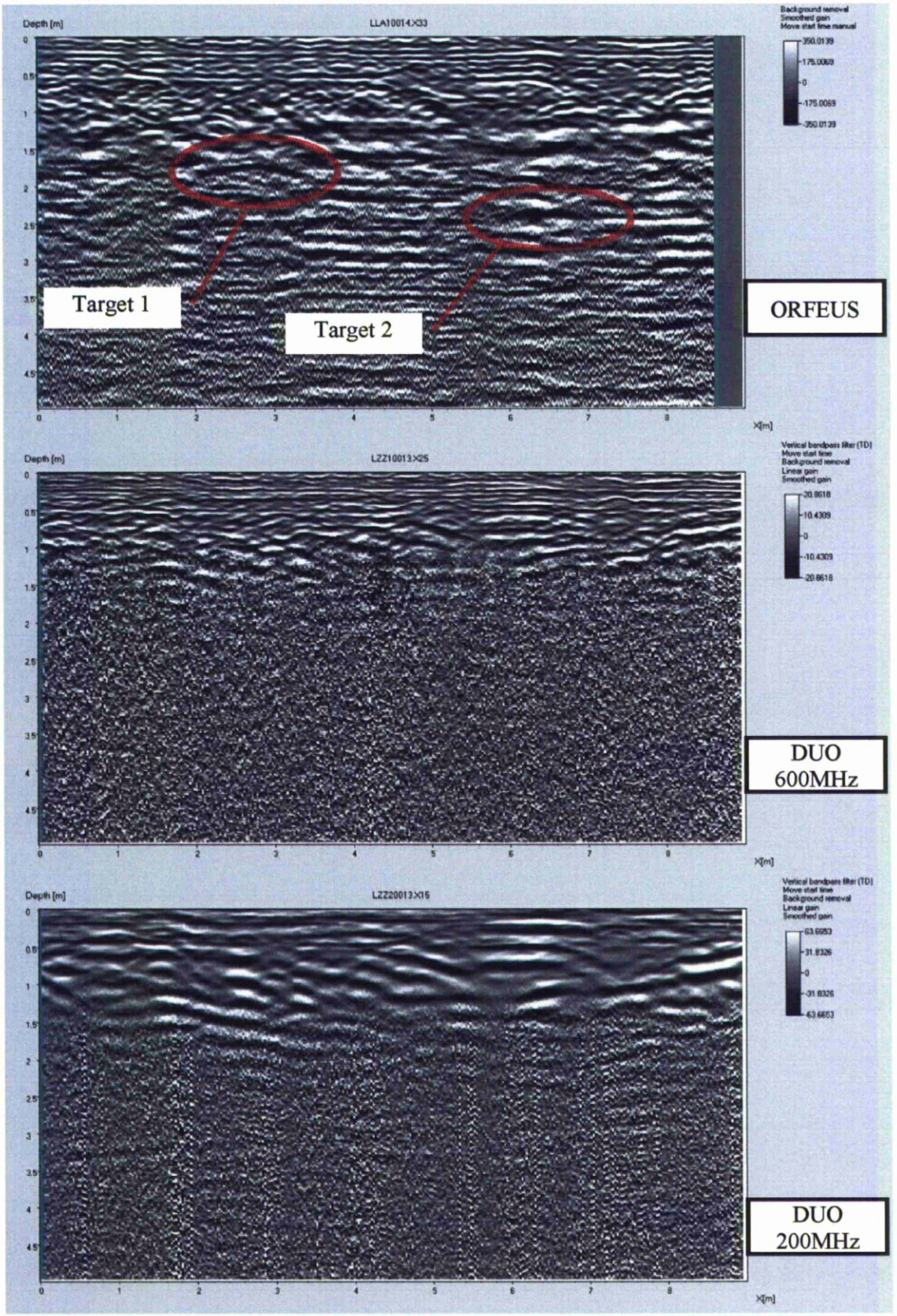

2.4 LIVERPOOL - SITE A – POSITION 15

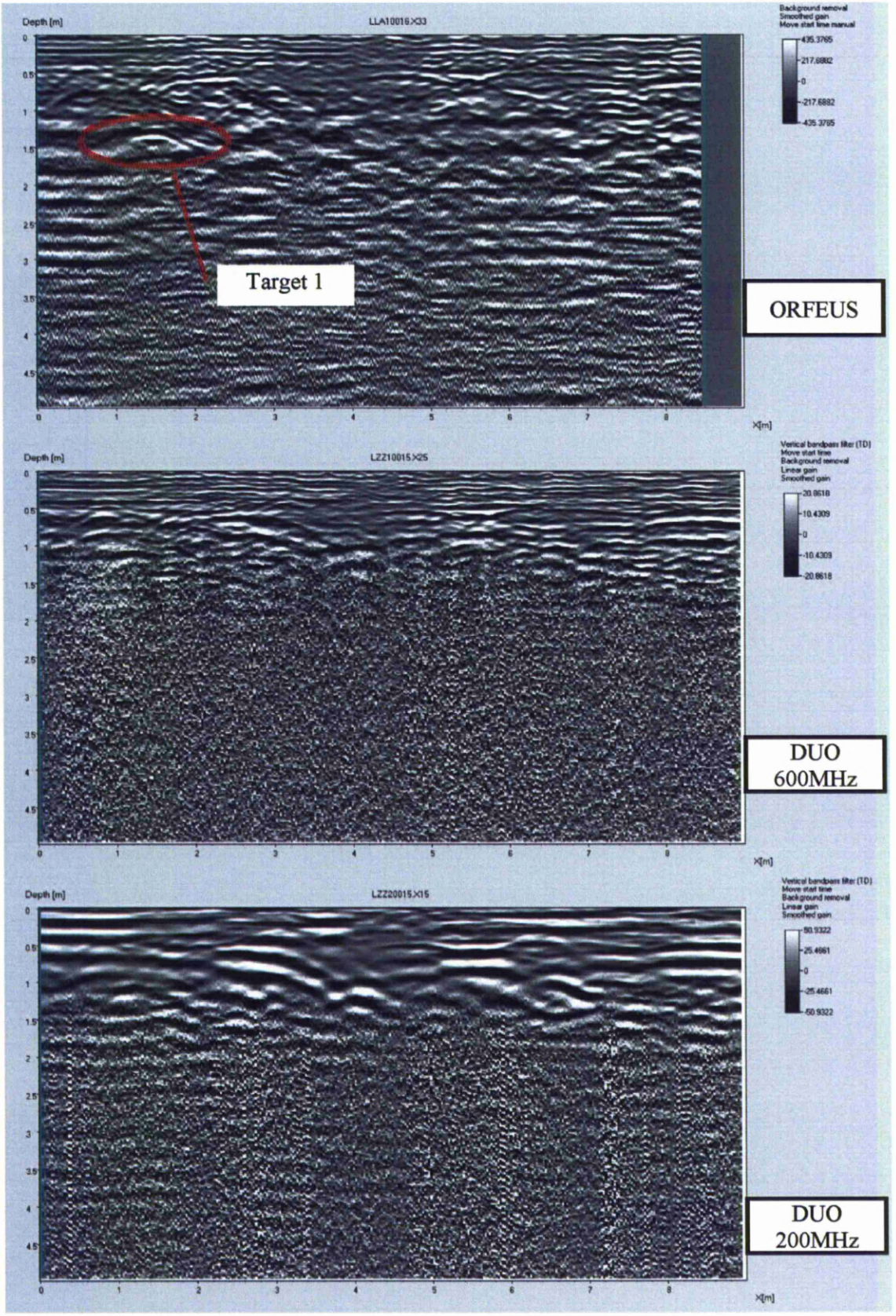

2.5 Site A – Target identification

Site A – Position 4

Target 1 – in this area ORFEUS B-Scan shows a more detailed hyperbola compared to both DUO 200 and DUO 600

Target 2 – in this case this shallow target (0.5 meter deep considering a soil with propagation velocity of 10^8 m/s) can only be detected with ORFEUS radar

Target 3 – this target is deeper than others (about 2 meter deep) and can only be detected with ORFEUS radar.

Site A – Position 12

Target 1 and 2 – these targets exhibit the same hyperbola at 1 meter deep and can be clearly detected with ORFEUS radar. Even if these targets are only 1 meter deep, due to the high medium loss, pulsed GPR B-scans are affected by very high noise level starting from about 1.2-1.5 meter. In these conditions these targets are only partially visible by DUO200.

Site A – Position 13

Target 1 – this target is near the noise level of the ORFEUS radar (1.7 meter deep) and can only be detected with ORFEUS radar, in both DUO 200 and DUO 600 is covered by noise.

Target 2 – another tweak target appears in ORFEUS B-scans. This target is very deep (about 2.25m) and is absolutely not visible in DUO B-scans.

Site A – Position 15

Target 1 – in this case this target (1.2 meter deep) can be clearly detected with ORFEUS radar. In pulsed GPR B-scans only the top of the hyperbola is slightly detectable: in this condition, the detection of this target should be impossible without the aid of ORFEUS B-scan.

2.6 Site A – Range performance evaluation.

Generally speaking, pulsed GPR radar system are affected by high noise level due to UWB receiver architecture. This aspect is clearly visible in B-scan where increasing the deepness, the map starts to shown so called *salt and pepper* noise that compromise the target detection capability at high depth. Due to the tuned receiver architecture, ORFEUS Surface GPR exhibits very low noise level, for this reason ORFEUS B-scan are slightly affected by salt and pepper.

In the previous site A B-scans, salt and pepper noise appears in DUO 200 and DUO 600 at about 1.5m and 1.2m depth respectively, while this level is about 2m in ORFEUS B-scans.

Moreover another instrument is employed in order to compare the overall performance: the power sweep graph. This graph represents the mean signal level measured during a whole B-scan coming from each different range bin (that is from each depth layer).

Power level is an integral contribution due to:

- *antenna coupling*
- *targets*
- *ground clutter cell noise*
- *system thermal noise (average)*
- *range energy spreading (mainly due to antenna ringing effects)*

Following in the next graph (Figure 4) we observe that at deep range ORFEUS power image exhibits a better performances with respect to DUO200 and DUO600. Since the antenna is the same of DUO200 we can estimate that the dynamic range is increased of about 10dB at 3mt depth and about 20dB at greater depth.

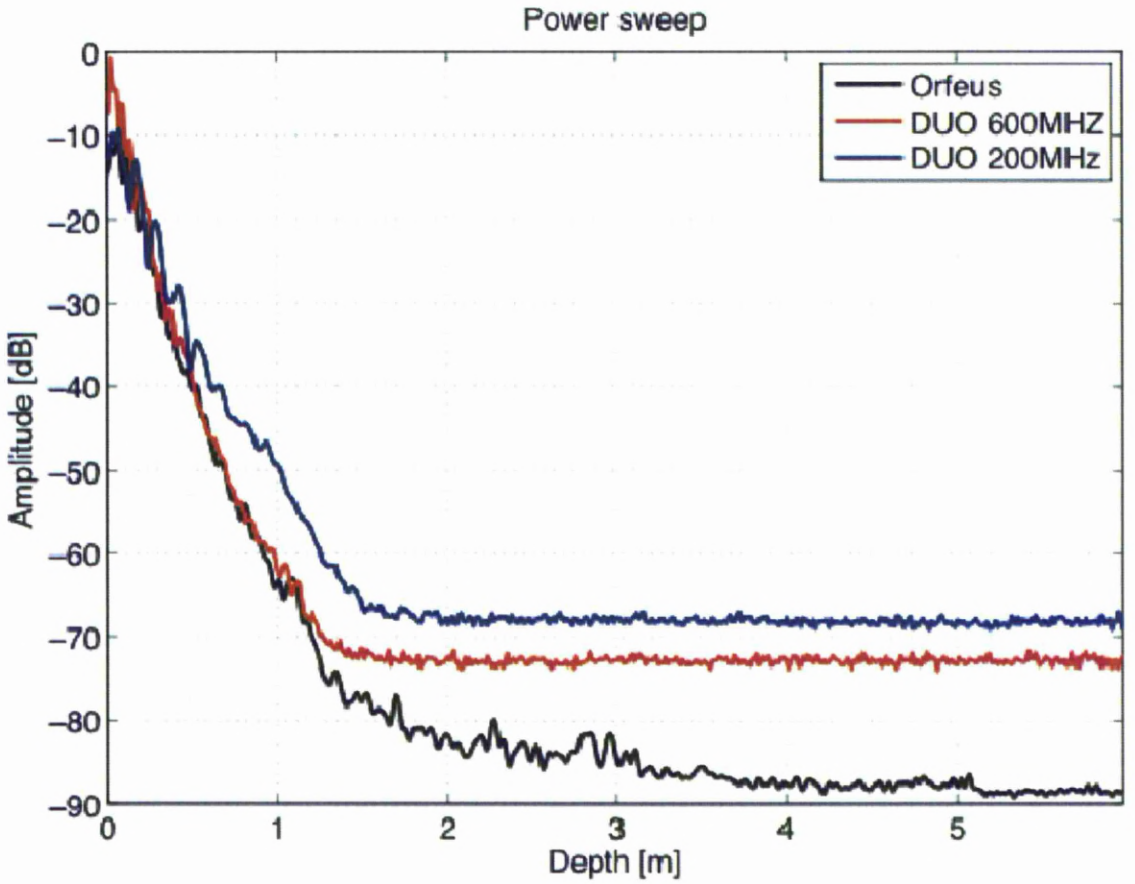

Figure 5 - Received power diagram for Site A - position 4

3 Site B

Site B is located between the Electronic Engineer Department Block A and the rear parking, in this area the pavement is made by concrete tiles; lower, a reinforced mesh is present in some small areas.

Figure 6 – Partial view of the site B

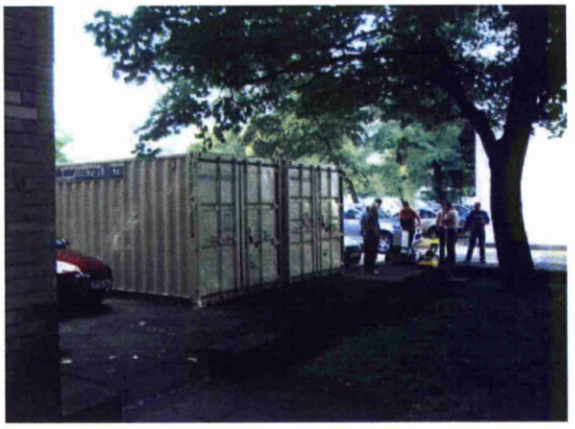

Figure 7 – ORFEUS and DUO during measurements

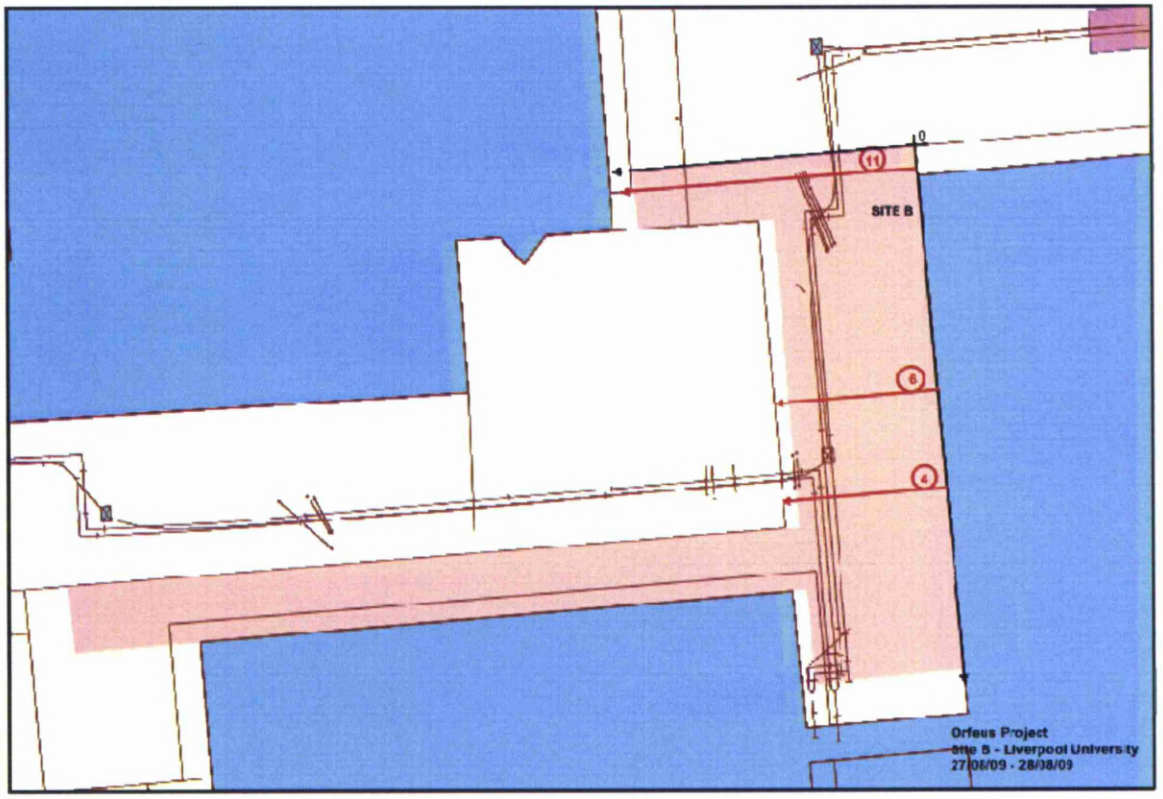

Figure 8 - Site B map and sweep location

3.1 LIVERPOOL - SITE B – POSITION 4

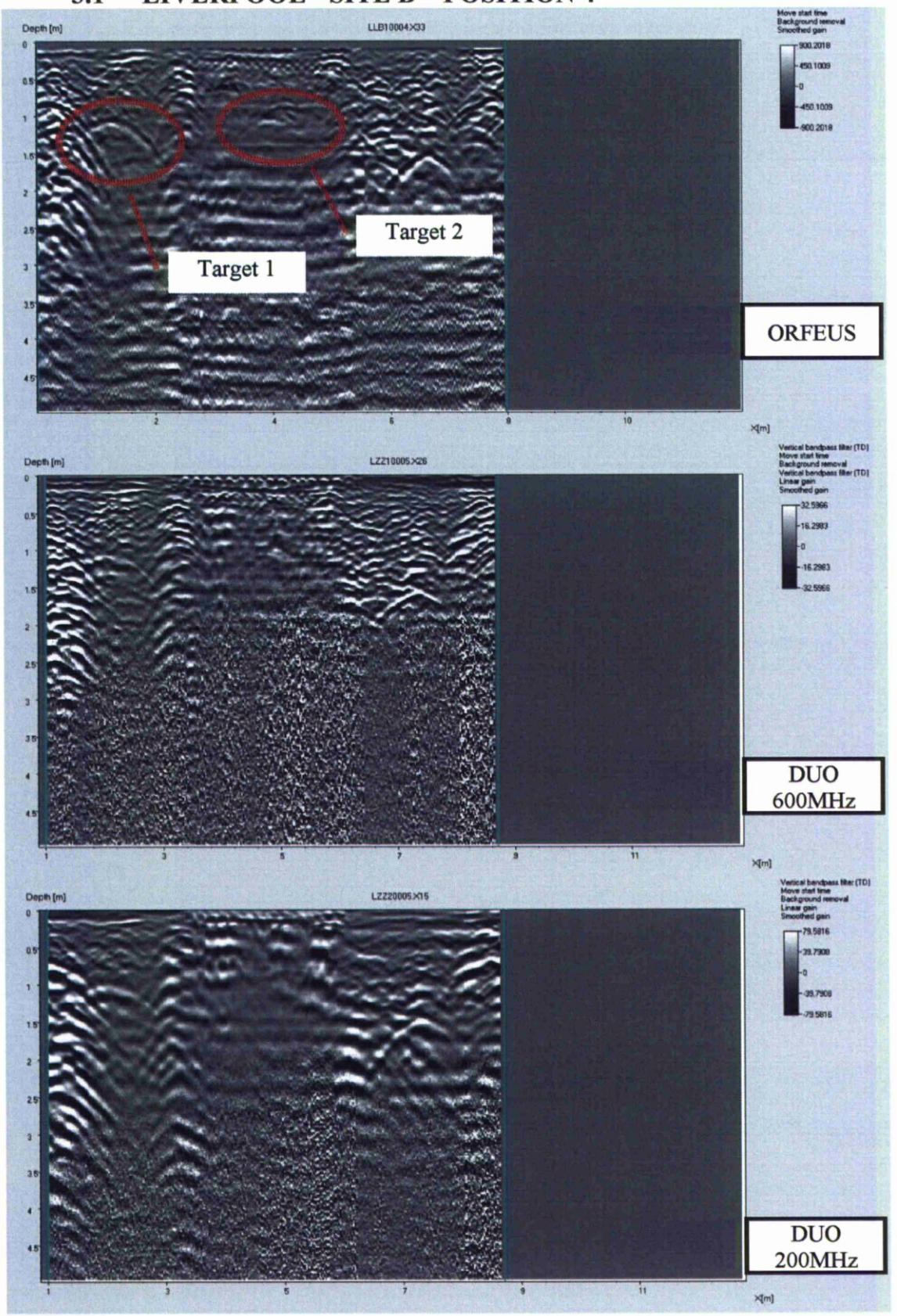

3.2 LIVERPOOL - SITE B – POSITION 6

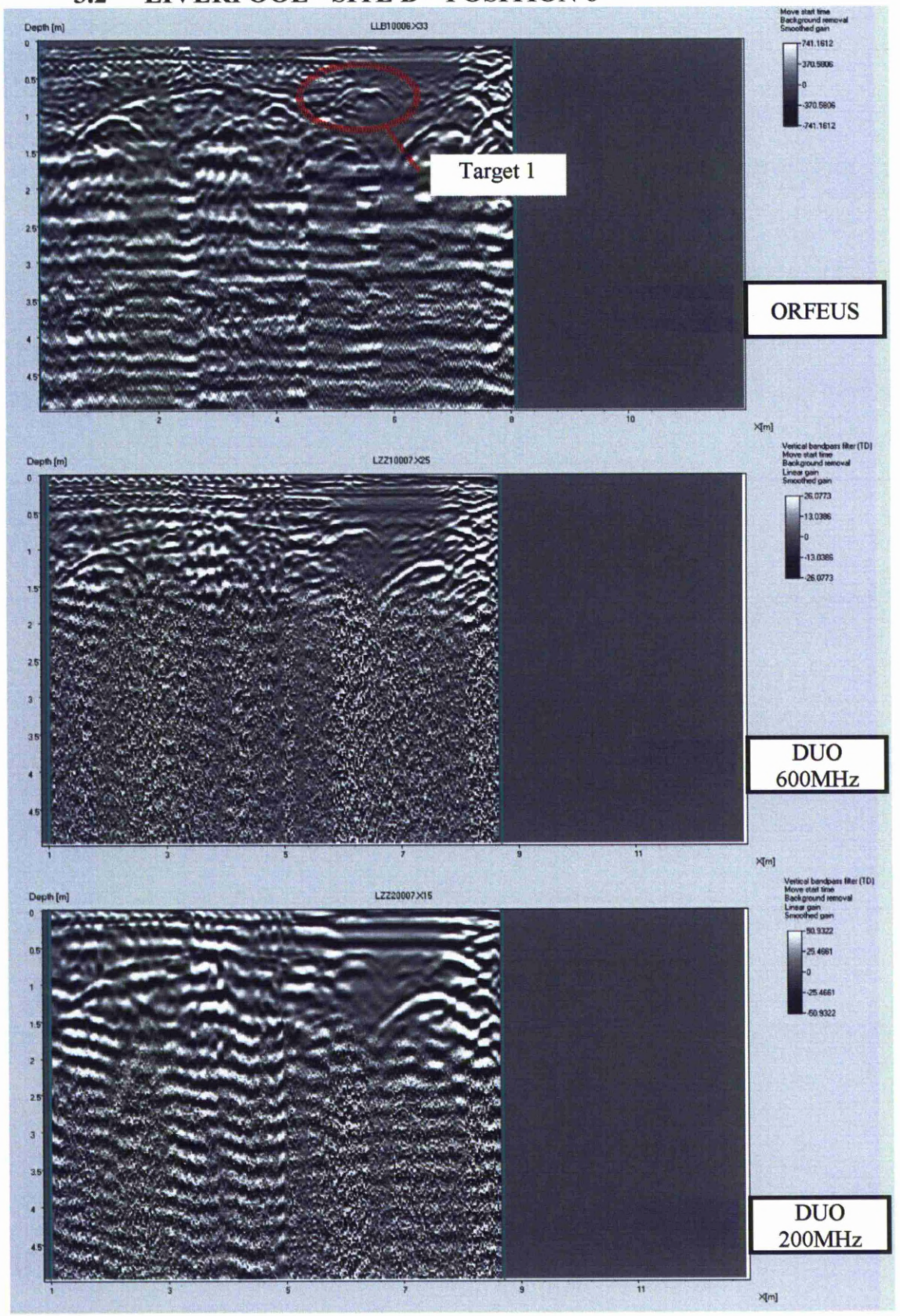

3.3 LIVERPOOL - SITE B – POSITION 11

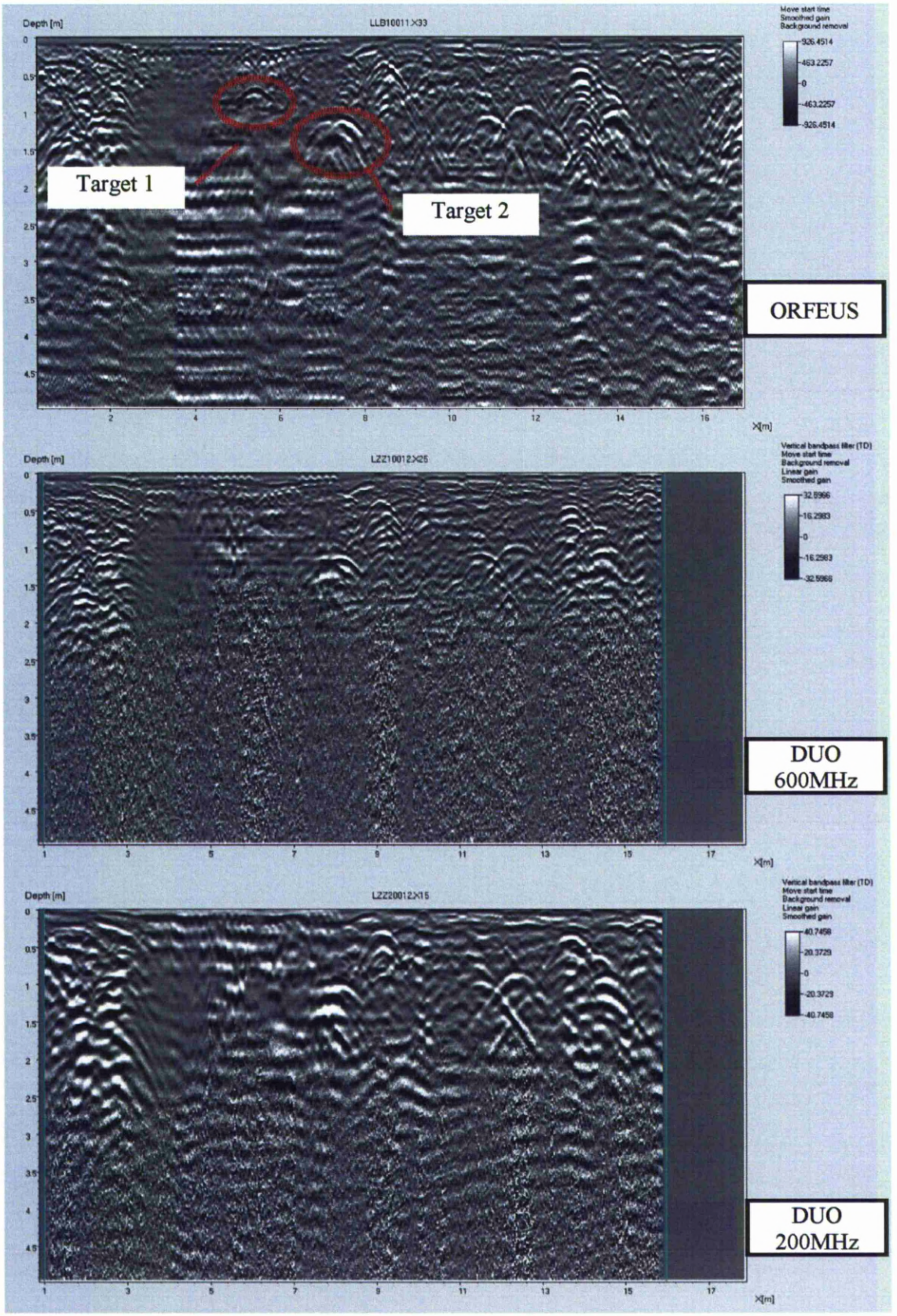

3.4 Site B – Target identification

Site B – Position 4

Target 1 – in this case this target (1 meter deep) can be clearly detected with ORFEUS radar. The same target is not as clearly detectable with either DUO200 or DUO600.

Target 2 – this target is located under the reinforced mesh and is detectable only in ORFEUS B-scan. Probably the ORFEUS UWB capability aid to reduce the impact of hyperbola generated by reinforced mesh, allowing to detect target that are present under this structure.

Site B – Position 6

Target 1 – focusing the attention on the top of target 1 hyperbola, DUO200 and DUO600 exhibits a flat top, while ORFEUS, having higher resoultion, exhibits a slightly sinking phenomenon. This is due to the presence of two targets close together that generates a coupled of closely spaced hyperbola that are mixed together by low range resolution radar systems.

Site B – Position 11

Target 1, Target 2 – these targets are clearly visible in ORFEUS B-Scan although they are under some reinforcement bars. The former, that is 0.7m deep, is hardly visible in both DUO600 and DUO200 B-scans. The latter, that is 1m deep, is detectable also in both DUO600 and DUO200 B-scans, even if with lower resolution. ORFEUS B-scans shows that the so called Target 2 actually encompasses two closed targets. Their hyperbolas are slightly distinguishable in DUO600 while beeing completely mixed together in DUO200 B-scan due to low resolution capability.

3.5 Site B – Range performance evaluation.

Following in the next graph (Figure 9) we observe that at deep range ORFEUS power image exhibits a better performances with respect to DUO200 and DUO600. Since the antenna is the same of DUO200 we can estimate that the dynamic range is increased of about 10dB at 3mt deep and about 15-20 dB at greater deep.

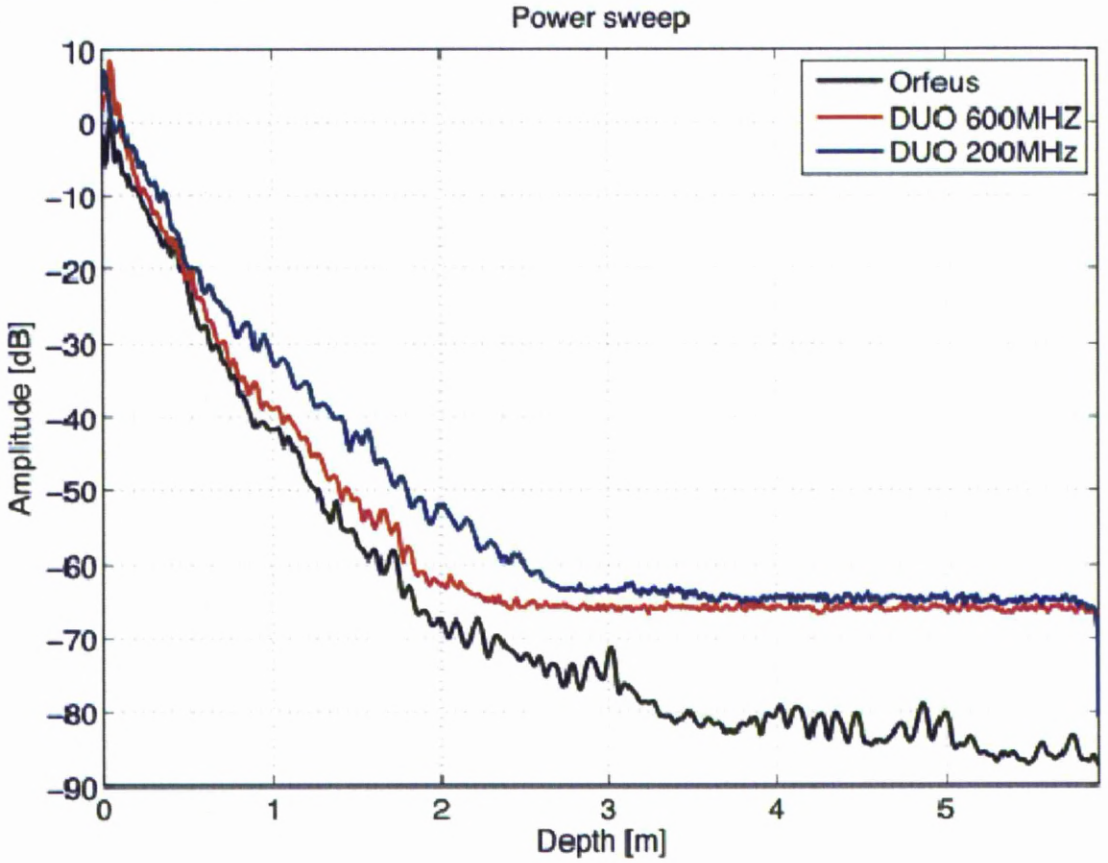

Figure 9 - Received power diagram for Site B - position 11

4 Site C

Site C is located between the Electronic Engineer Department Block B and the Computer Laboratory, this area is a meadow with tall grass.

Figure 10 – View of site C

Figure 11 – ORFEUS and DUO is preparing to scan

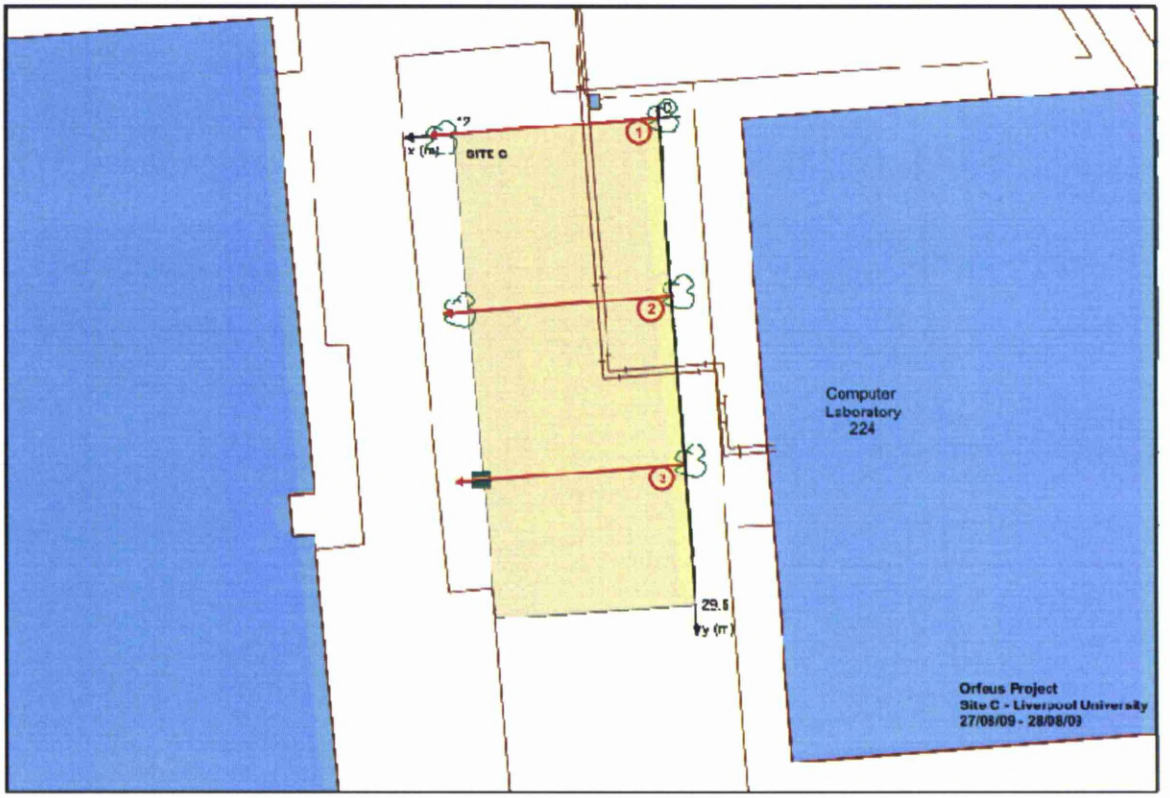

Figure 12 - Site C map and sweep location

4.1 LIVERPOOL - SITE C – POSITION 1

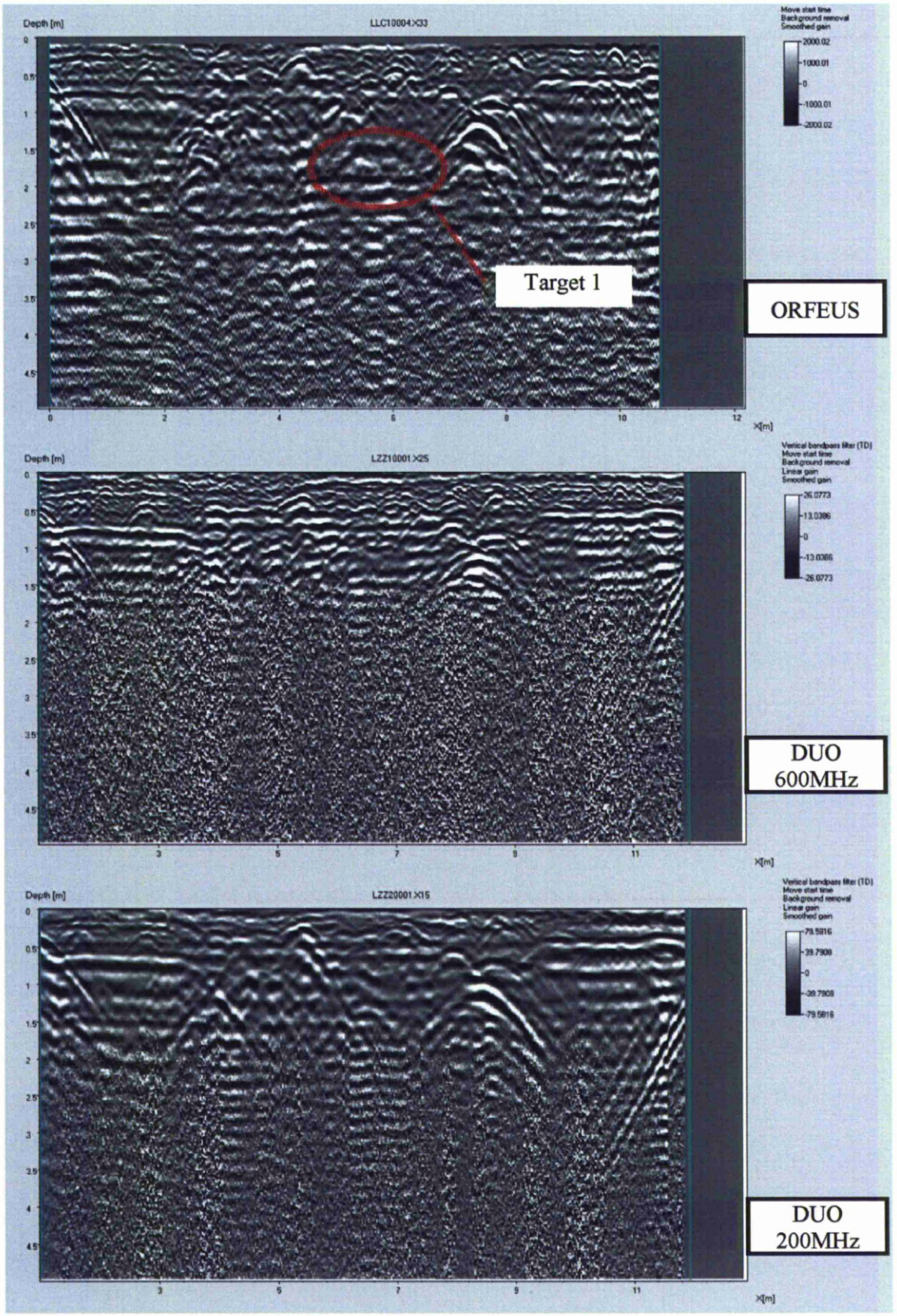

4.2 LIVERPOOL - SITE C – POSITION 2

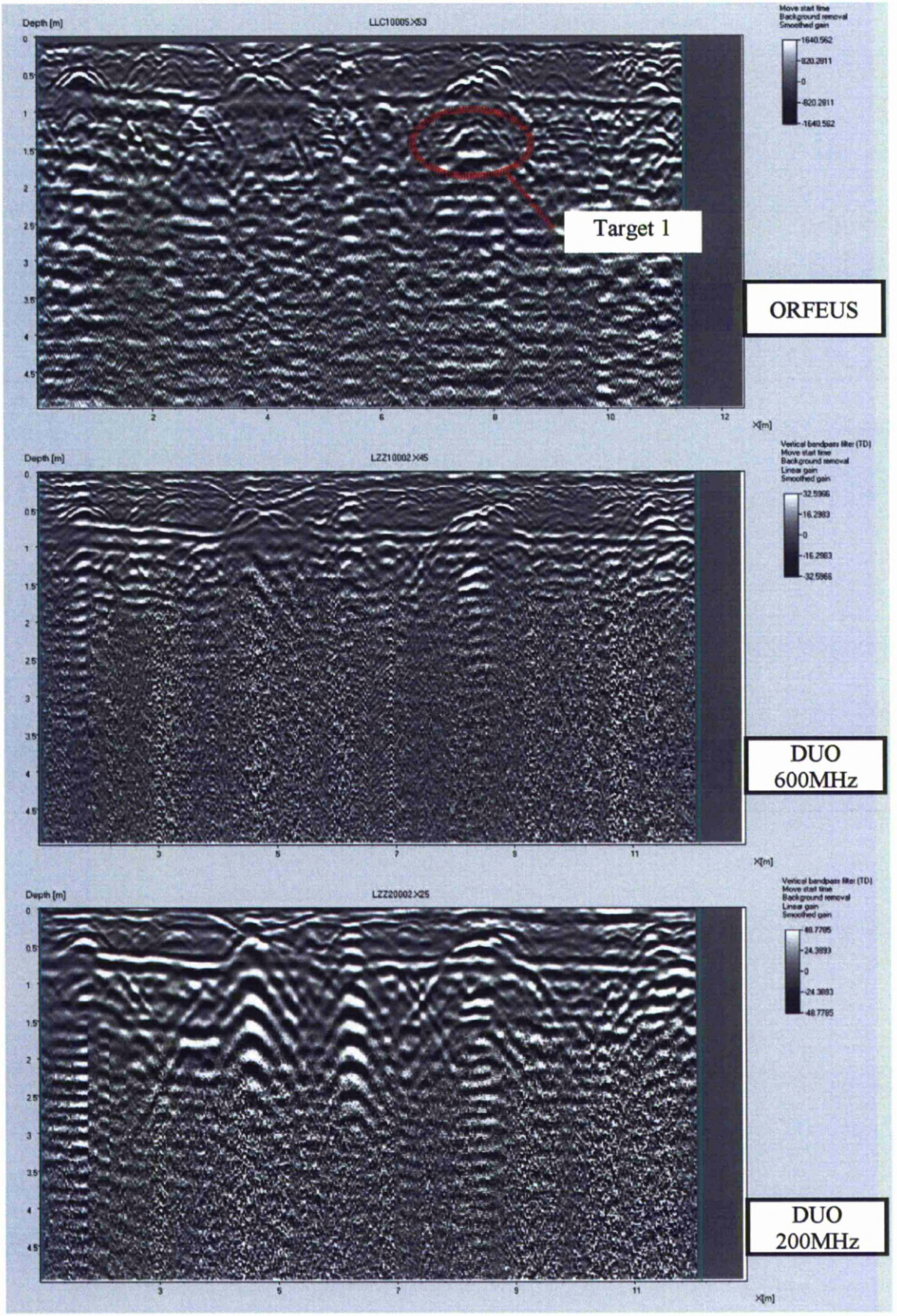

4.3 LIVERPOOL - SITE C – POSITION 3

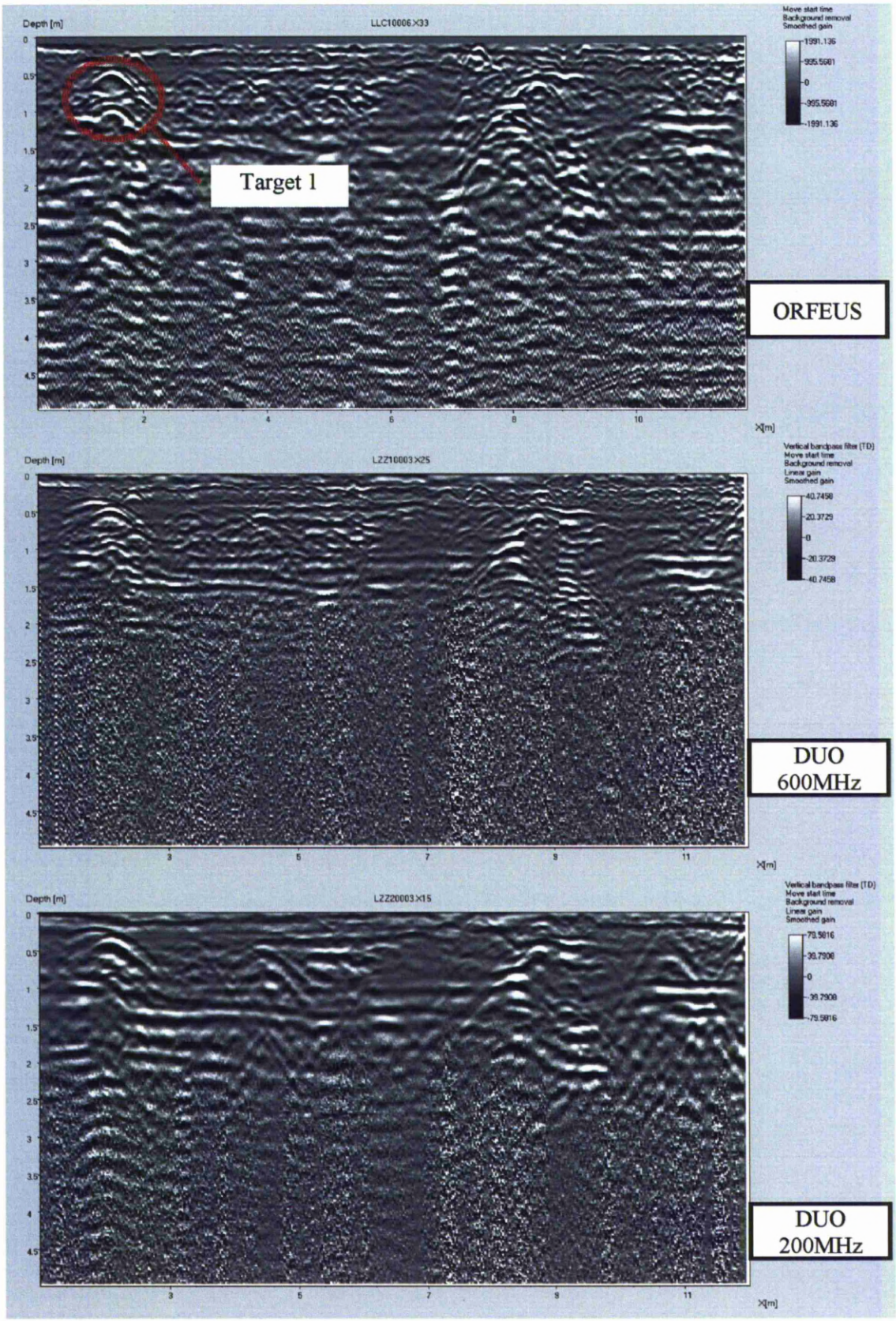

4.4 Site C – Target identification

Site C – Position 1

Target 1 – this target (1.5 meter deep) can be detected with ORFEUS B-scan and partially with DUO 200.

Site C – Position 2

Target 1 – in this area we can see a target at about 1meters deep. ORFEUS B-Scan shows a more clearly detectable hyperbola compared to both DUO 200 and DUO 600.

Site C – Position 3

Target 1 – in this area we can see a shallow target (0.5 meters deep) followed by another reflection at 1m depth. ORFEUS B-Scan shows more detailed hyperbolas compared to both DUO 200 and DUO 600.

4.5 Site C – Range performance evaluation.

Following in the next graph (Figure 13) we observe that at deep range ORFEUS power image exhibits a better performances with respect to DUO200 and DUO600. Since the antenna is the same of DUO200 we can estimate that the dynamic range is increased of about 10-15dB at 3mt deep and about 20-25 dB at greater deep.

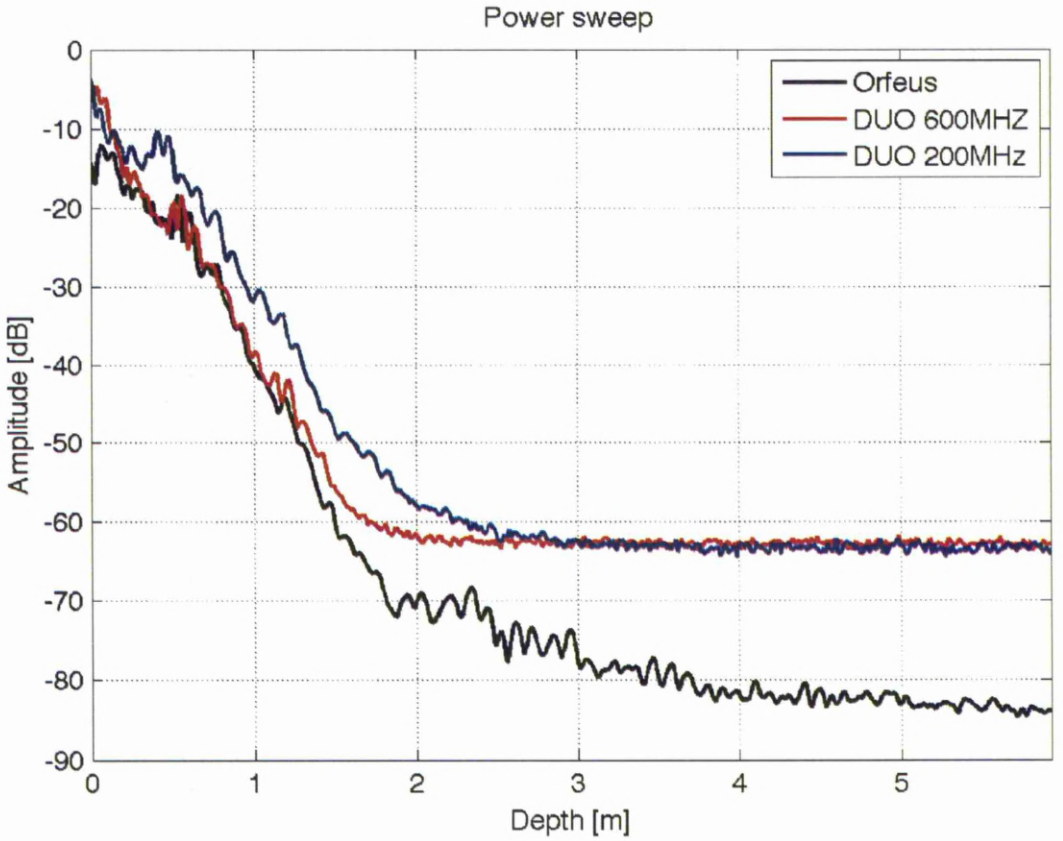

Figure 13 - Received power diagram for Site C - position 1

5 Site D

Site D is located in the parking alongside the rear of Electronic Engineer Department; in this area the pavement is made by asphalt.

Figure 14 – Partial view of site D

Figure 15 – Partial view of site D

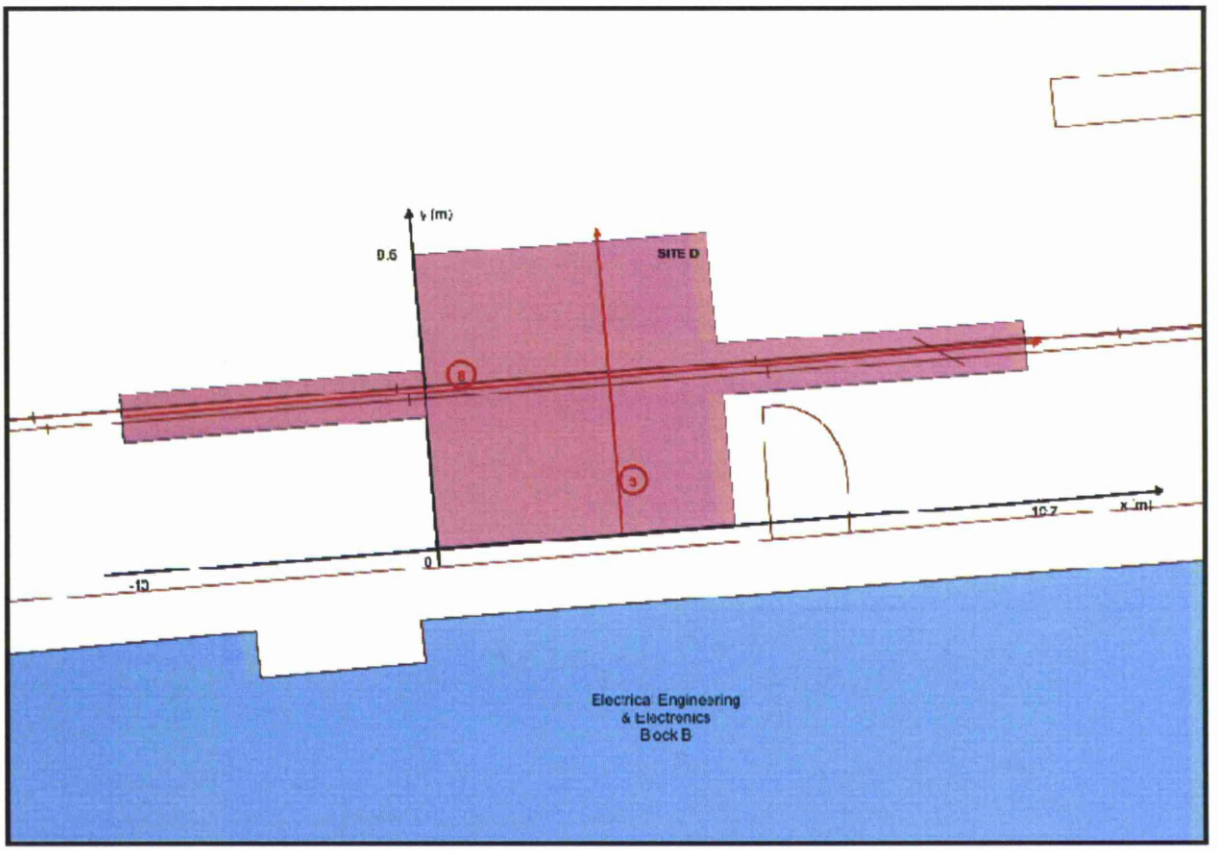

Figure 16 – Site D map and sweep location

5.1 LIVERPOOL - SITE D– POSITION 3

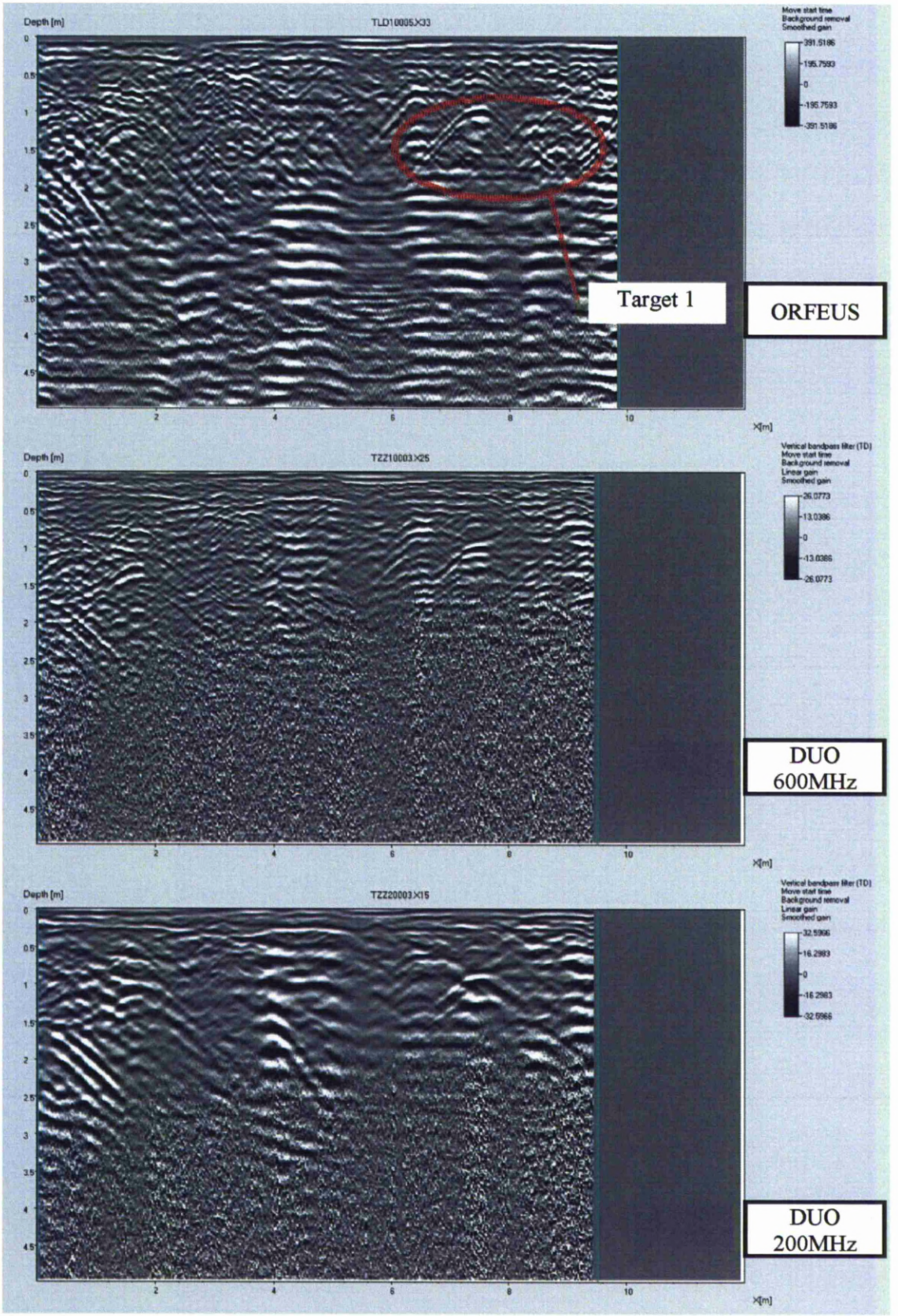

5.2 LIVERPOOL - SITE D– POSITION 8

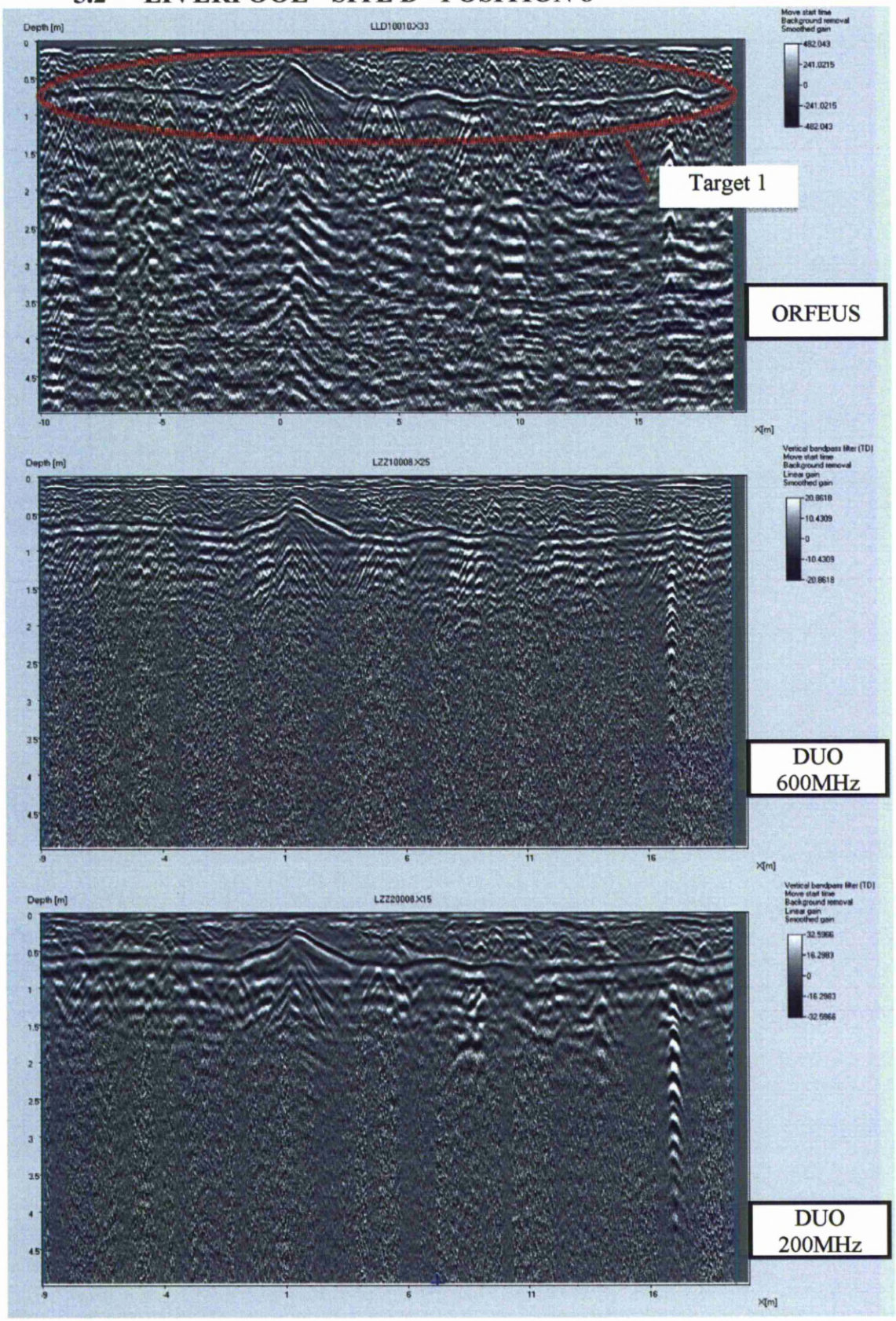

5.3 Site D – Target identification

Site D – Position 3

Target 1 – in this area we can see a target at about 1 meters deep. ORFEUS B-Scan shows a more detailed hyperbola compared to both DUO 200 and DUO 600.

Site D – Position 8

Target 1 – here we can see pipes running along the sweep direction, that in B-Scan result in a layer at about 0.7 meters deep. At X=0 in the ORFEUS B-scan we can see an interference with a shallower orthogonally intersecting target.

5.4 Site D – Range performance evaluation.

Following in the next graph (Figure 17) we observe that at deep range ORFEUS power image exhibits a better performances with respect to DUO200 and DUO600. Since the antenna is the same of DUO200 we can estimate that the dynamic range is increased of about 10-15dB at 3mt depth and about 20-25 dB at greater depth.

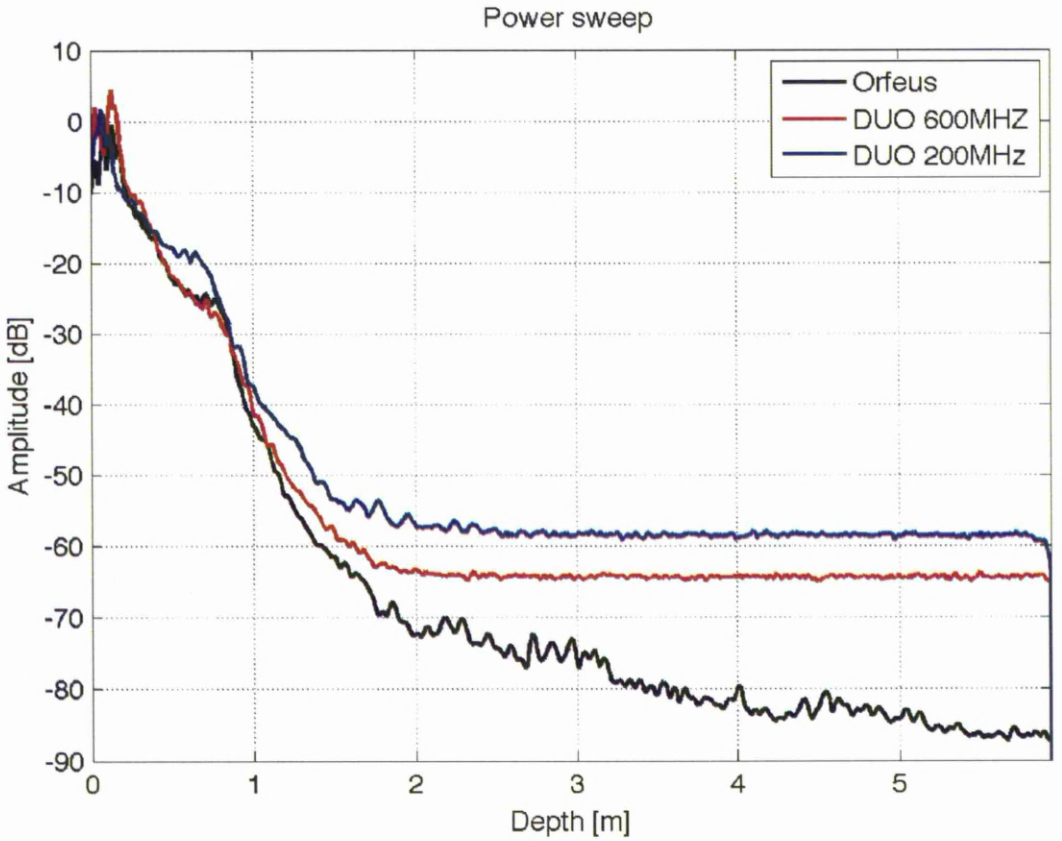

Figure 17 – Received power diagram for Site D - position 8

6 Site E

Site E is located in the parking behind the Computer Laboratory, in this area the pavement is made by asphalt. As shown in Figure 19 and Figure 20, because of the presence of a manhole in the center of the surveyed area, a longitudinal scans was splitted in two measures.

Figure 18 – View of site E

Figure 19 – Partial view of site E, the manhole

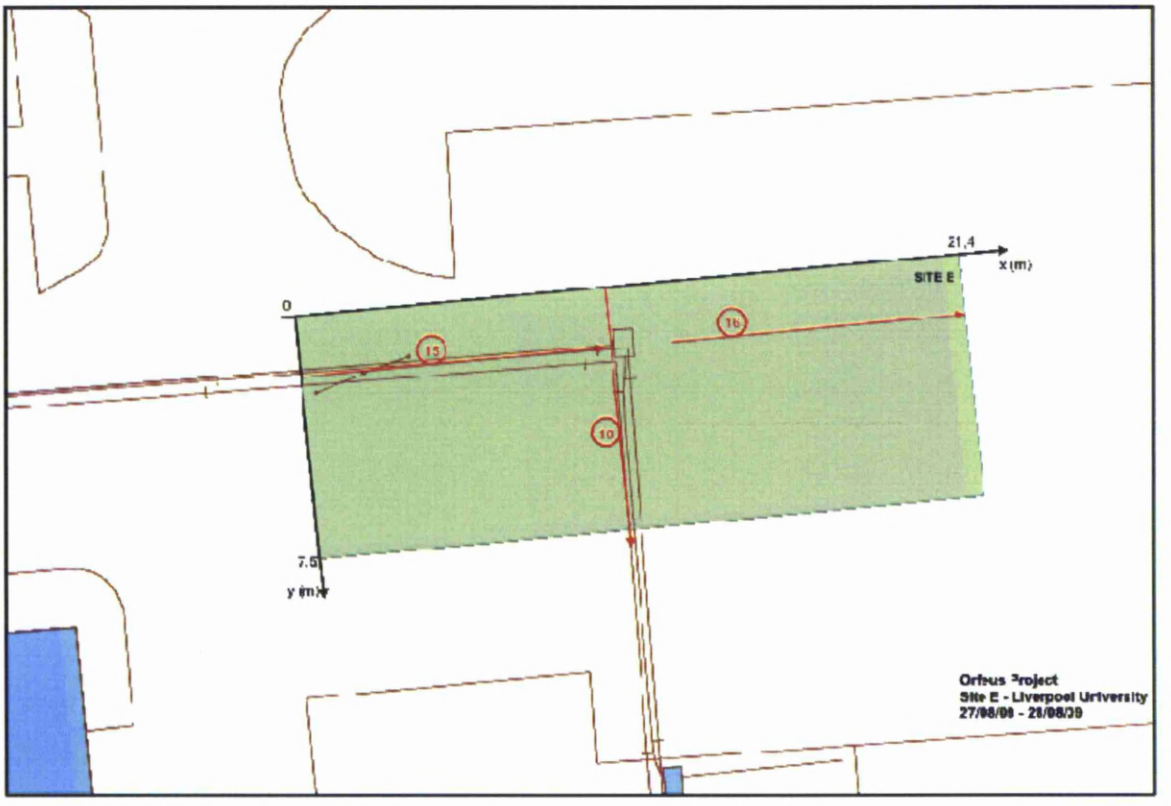

Figure 20 - Site E map and sweep location

6.1 LIVERPOOL - SITE E – POSITION 10

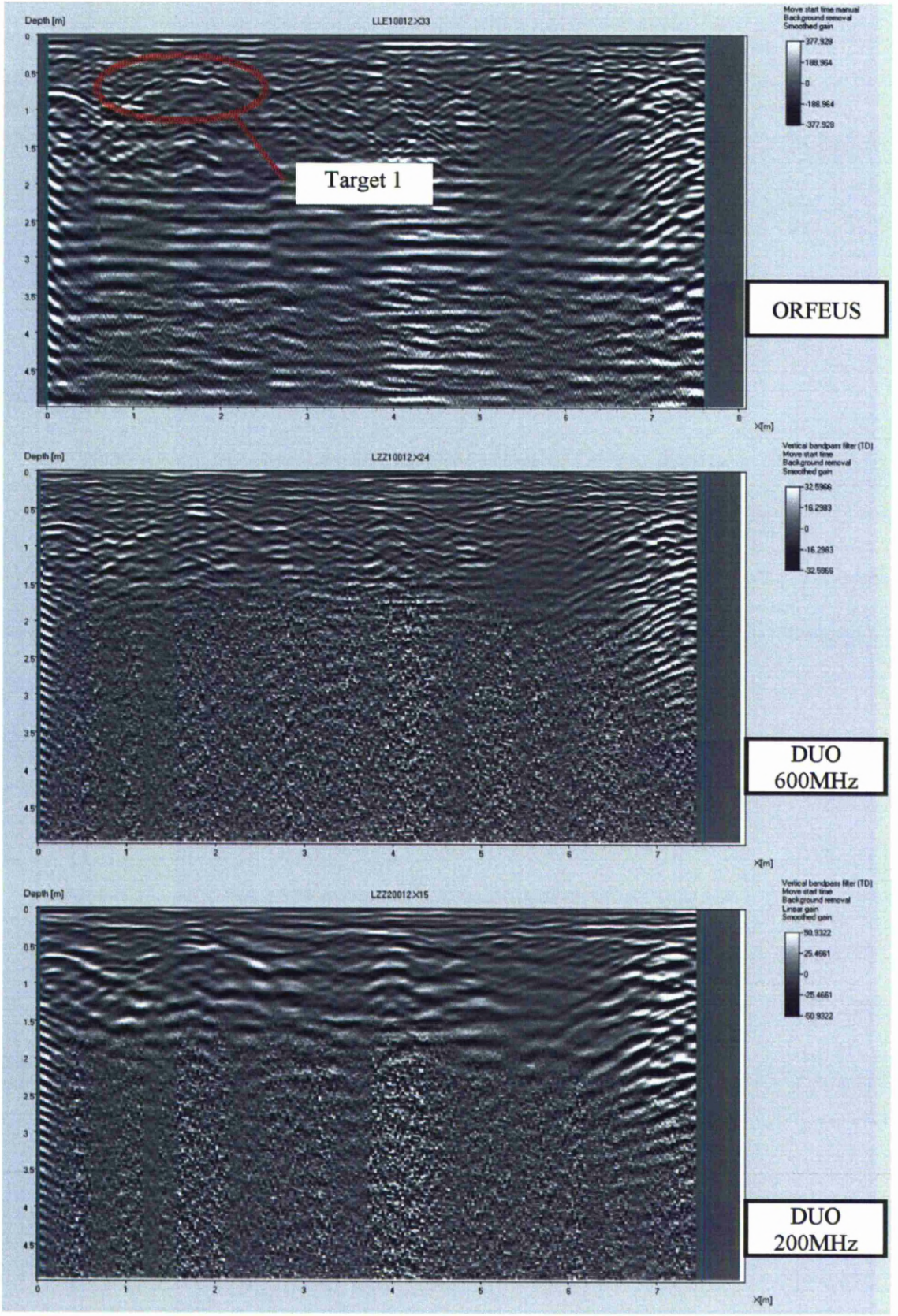

6.2 LIVERPOOL - SITE E – POSITION 15

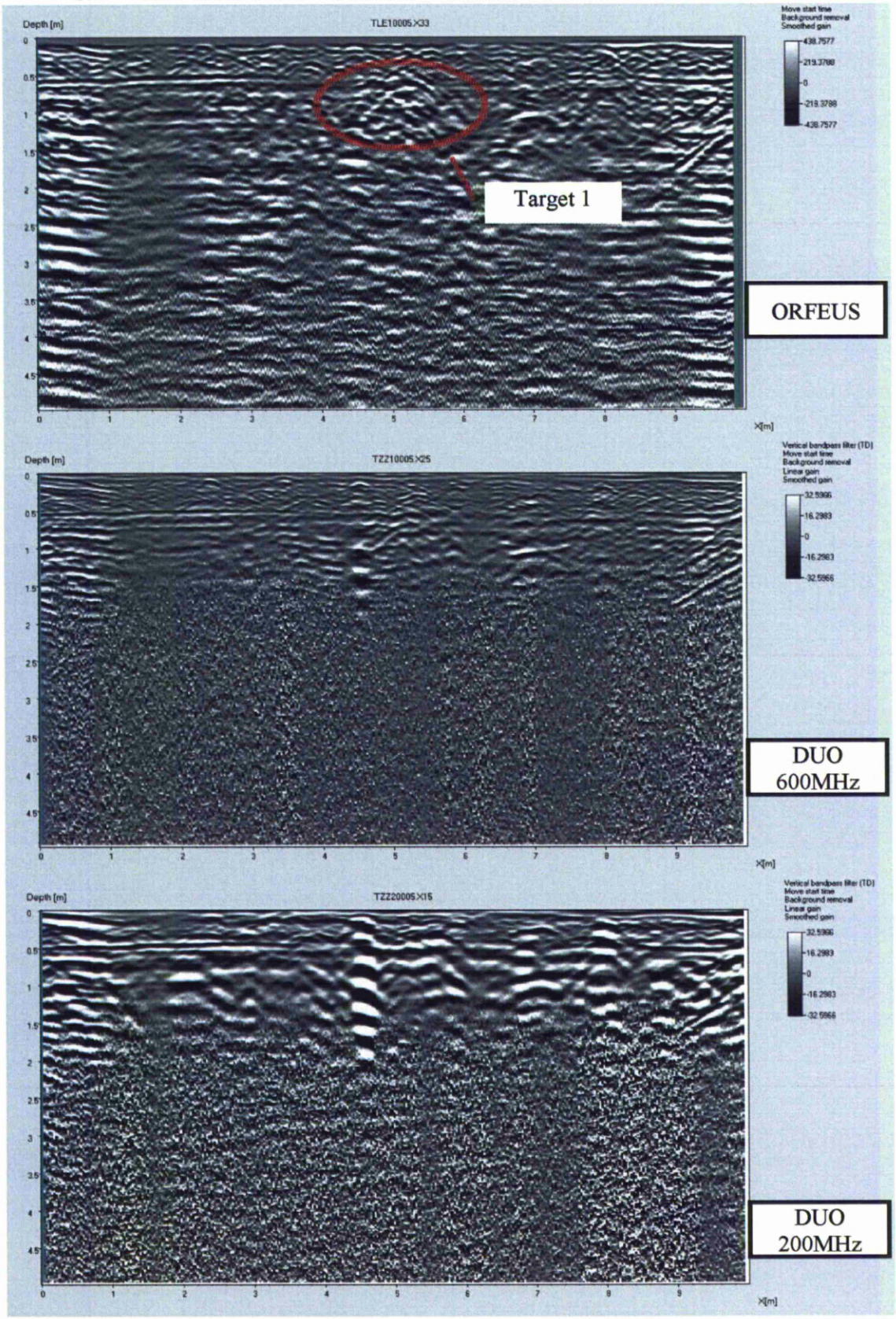

6.3 LIVERPOOL - SITE E – POSITION 16

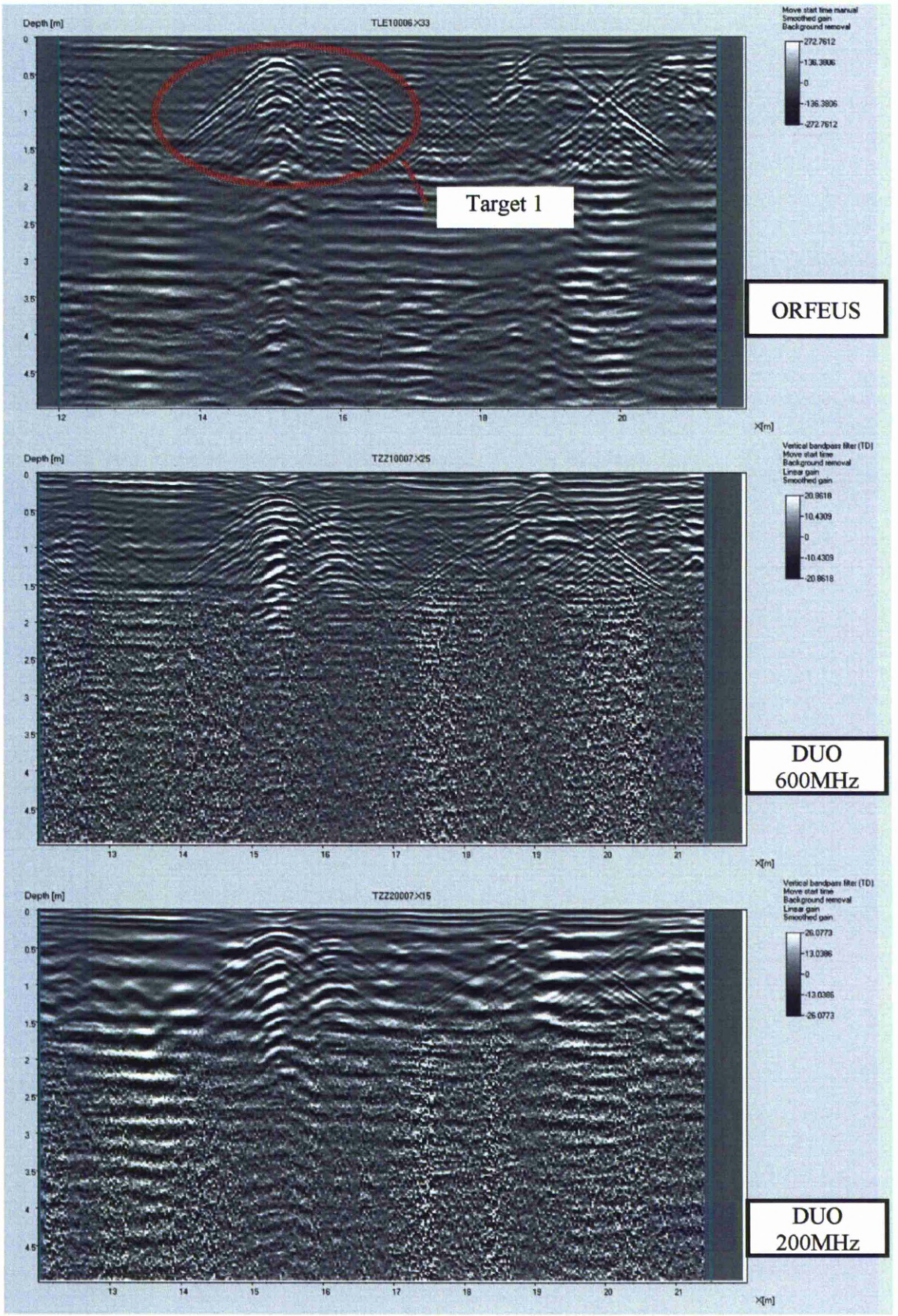

6.4 Site E – Target identification

Site E – Position 10

Target 1 – in this area we can see distinguish three targets at about 0.5 meters deep. ORFEUS B-Scan clearly exhibits better resolution compared to both DUO 200 and DUO 600 ones, in which a unique target is detectable.

Site E – Position 15

Target 1 – in this area ORFEUS B-Scan shows a more detailed hyperbola compared to both DUO 200 and DUO 600.

Site E – Position 16

Target 1 – in this area ORFEUS B-Scan shows a more detailed hyperbola compared to both DUO 200 and DUO 600.

6.5 Site E – Range performance evaluation.

Following in the next graph (Figure 21) we observe that at deep range ORFEUS power image exhibits a better performances with respect to DUO200 and DUO600. Since the antenna is the same of DUO200 we can estimate that the dynamic range is increased of about 10dB at 3mt deep and about 20 dB at greater deep.

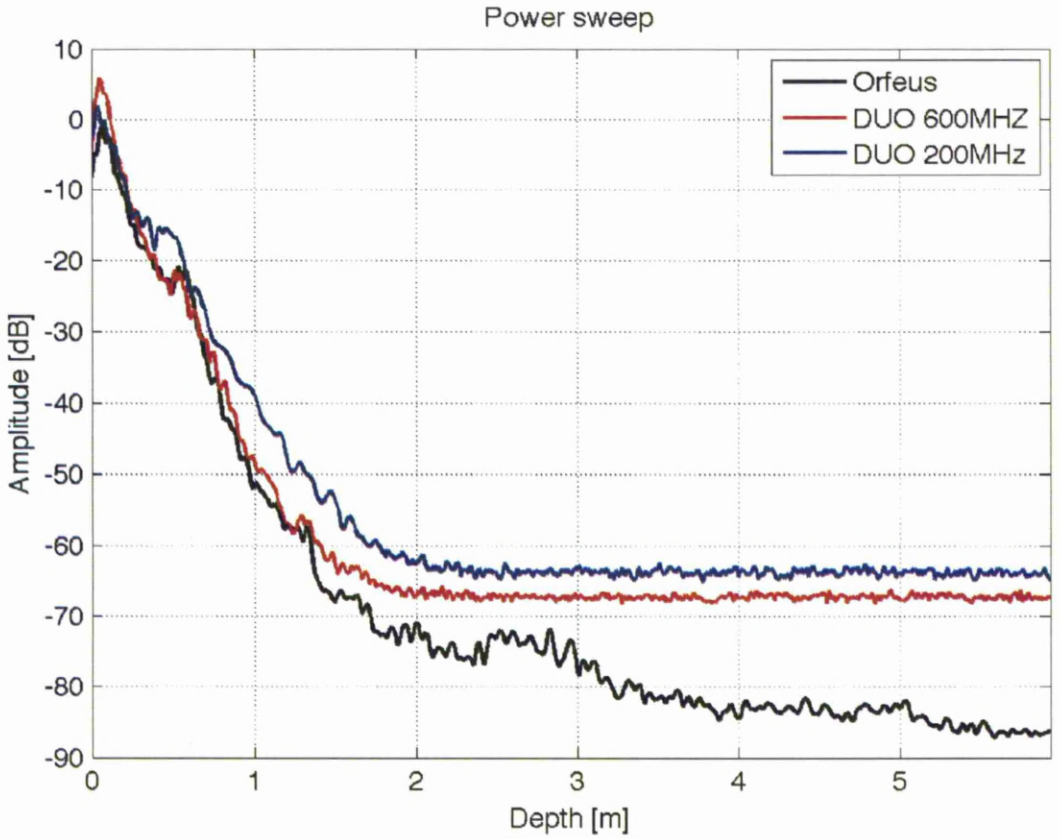

Figure 21 - Received power diagram for Site E - position 15